Guest entrapment, uptake and release in metal-azole based frameworks and complexes

James Stuart Wright

A thesis submitted to The University of Sheffield in partial fulfilment of the requirements for the degree of Doctor of Philosophy

Department of Chemistry
University of Sheffield
Sheffield S3 7HF

February 2016

It’s turtles all the way down.

Thesis summary & chapter abstracts

The work in this thesis is generally concerned with the crystal engineering of azole or azolate containing coordination compounds, either in molecular clusters or within metal-organic frameworks. The intermolecular interactions that halogenated azole/azolate coordination compounds are capable of supporting in the solid state are explored. The functionality of molecular materials and metal-organic frameworks containing azole/azolates is also examined.

Chapter 1 introduces the concept of crystal engineering, and the intermolecular interactions and coordination chemistry which it utilises. Coordination polymers, metal-organic frameworks (MOFs) and other supramolecular structures which are polymeric are introduced, and the applications of coordination polymers and MOFs are outlined.

Chapter 2 introduces a family of 'stellated' cluster compounds, of the general formula $[M_x(\text{halopyrazolate})_y]$. The roles of hydrogen bonding and halogen bonding on the packing of these clusters in the solid state are explored, including in a family of dihalomethane solvates. The packing arrangement and intermolecular interactions formed by the stellated clusters was shown to be highly solvent dependent.

Chapter 3 describes the desolvation of one of the stellated cluster compounds from chapter 2, **2.1·MeCN**, $[Pd_3(\text{4-bromopyrazolate})_6]\cdot 3MeCN$, and demonstrates the successful structure solution of the resulting compound **2.1**, $[Pd_3(\text{4-bromopyrazolate})_6]$ from X-ray powder diffraction data. The effect of CO_2 gas pressure and N_2 pressure on the stellated cluster **2.1** is explored through *in situ* X-ray powder diffraction, and suggests a selective uptake of CO_2 over N_2 by crystals of cluster **2.1**.

Chapter 4 describes the design and synthesis of a chiral/racemic pair of MOFs [Zn(benzenedicarboxylate)(cyclohexane-1,2-bis(1',2',4'-triazole))], **4.1** and **4.2**. The desolvation of the MOFs is explored, and the uptake of CO_2 within both MOFs is followed crystallographically and by gravimetric adsorption measurements. The enantioselectivity of the MOFs is explored through adsorption from both the vapour

phase and liquid phase. Chiral framework **4.2** is shown to selectively entrap *R*-phenylethanol in a 48% enantiomeric excess.

Chapter 5 introduces an attempt to synthesise an isostructural family of zeolitic imidazolate frameworks (ZIFs), some with halogen substituents. The brominated ZIF [Zn(NO_2im)(Brbim)], **5.3** is investigated for its uptake behaviour towards dihalomethane guests, and their presence in the pores of **5.3** is demonstrated and explored by solid-state NMR spectroscopy. The thermal degradation of **5.3**, initially suggested to be via loss of NO_2 is explored and shown not to occur upon heating of **5.3**.

Chapter 6 introduces two pyrazole/pyrazolate-containing coordination materials. One is a new phase of the previously reported flexible MOF [Co(bdp)], **6.1**, resulting from its synthesis from dimethylformamide, rather than diethylformamide. A coordination polymer based on the bipyrazole ligand **H_2bpz** is also reported and the hydrogen bonding within the structure is examined.

Author's declaration

The work described in this thesis was carried out at the Department of Chemistry at the University of Sheffield between October 2011 and December 2015. It is the original work of the author, except in cases of measurements obtained outside the University of Sheffield, as noted below. This work has not been submitted previously for a degree at this, or any other university. The views expressed in this thesis are those entirely of the author, and not the University of Sheffield.

Gravimetric gas sorption measurements were obtained by Craig McAnally and Ashleigh J Fletcher at the University of Strathclyde, Glasgow. Subsequent data analysis was conducted jointly between the two groups.

James Wright
December 2015

Acknowledgements

My first thanks go to Lee Brammer for his patient and continuous support over the course of this PhD project. Lee has constantly demonstrated that he cares about the development and individual goals of his students, and my PhD has been all the more valuable for it. When I mention the amount of individual attention and support I have received, students from other groups become unreasonably jealous.

The Brammer group members past and present as a whole also deserve great thanks for being fantastic company, good labmates and for being great to bounce ideas off of (whether or not the ideas are bad). Adrian, Craig, Danny, Elliot, Feifan, Iñigo, Isabel, Jason, John, Paul, Tom, Rebecca, Stefano – thank you for all these things and more. Particular thanks go to Iñigo Vitórica-Yrezábal, who supervised my MChem project in Lee's group and has continued to tolerate my questions even after he left Sheffield. The Ward group, Weinstein group and the GTA students also deserve thanks for both professional and personal support as labmates and good drinking buddies (in this context Ash, Jerry, Methers and Will merit specific mention). Thank you also to my MChem students John, Brice, Abhishek and Cat for giving me a chance to develop my teaching skills in a research context, and for along with Feifan advancing the silver carboxylates work (the project that keeps on giving) even further. Thanks are also owed to the many people who helped make data collection possible for this project, including Harry Adams for crystallography help and the beamline staff at Diamond Light Source and ESRF.

Through the GTA programme, teaching has been a very big part of my PhD. The guidance and support of the Teaching Fellows has given me the opportunity to develop skills and do things I hadn't even imagined at the start of this project, including teaching in China. Ed Warminski deserves recognition for helping to push my boundaries, and encouraging me to take on a wide range of teaching. My sincere thanks go also to Julie Hyde, for keeping me involved in the China project, and who has time and again shown faith in me and encouraged me to take new opportunities. Thank you Julie, for all your support.

One group of people deserves thanks and blame in equal measure, for keeping my grip on responsible adult life tenuous at best. Ethan, Nick, Rob, Adam, Moxon, Ron, Stef, Jamie, Charles, Ashley and others, thank you. Thanks for five years that have made this PhD so eventful and memorable, and thanks in particular to Ethan who has heard more about this thesis than most. Thank you for being amazing friends.

My final thanks go to my family, to whom this thesis is dedicated. Thanks for encouraging me to push myself and to do more, and for showing unfailing faith in me for 26 years. I wouldn’t have made it this far without you.

Table of contents

1. Introduction

Crystal engineering & metal-organic frameworks (MOFs)

2. Stellated halogenated cluster compounds:

Crystal engineering through halogen bonds

3. Stellated halogenated cluster compounds:

Towards porous molecular materials for selective gas sorption

4. A chiral/racemic pair of triazole-based MOFs:

Investigating gas uptake and chiral guest selectivity

5. Halogenated zeolitic imidazolate framworks:

Investigating dihalomethane uptake and thermal degradation

6. Metal pyrazolate coordination polymers:

Flexibility and hydrogen bonding

Abbreviations and acronyms

[α]	Specific rotation
bdc	1,4-benzenedicarboxylate
bim	benzimidazolate
bipy	4,4’-bipyrimidine
Brbim	5-bromobenzimidazolate
Brpz	4-bromopyrazolate
cbt	Cyclohexane-1,2-bis-(1’,2’,4’-triazole)
CCD	Charge-coupled device
CSD	Crystal structure database
DABCO	Diazobicyclo[2.2.2]octane
DCM	Dichloromethane
DBM	Dibromomethane
DEF	Diethylformamide
DIM	Diiodomethane
DMF	Dimethylformamide
DMSO	Dimethylsulfoxide
ee	Enantiomeric excess
GC	Gas chromatography
H-bond	Hydrogen bond
H_2bdc	1,4-benzenedicarboxylic acid
Hpz	Pyrazole
Ibim	5-iodobenzimidazolate
Mebim	5-methylbenzimidazolate
NH_2bdc	2-amino-1,4-benzenedicarboxylate
NO_2im	2-nitroimidazolate
Ipz	4-iodopyrazolate
MAC	Multi-analyser crystal
MIL	Materials Institute Levoisier
MOF	Metal-organic framework
MS	Mass spectrometry
NMR	Nuclear magnetic resonance
PXRD	Powder X-ray diffraction
pz	Pyrazolate
QCM	Quartz crystal microbalance
***RR*cbt**	(-,-)cyclohexane-1,2-bis-(1’,2’,4’-triazole)
***RR,SS*cbt**	(±)cyclohexane-1,2-bis-(1’,2’,4’-triazole)

R_{XA}	Reduced interaction distance
SBU	Secondary building unit
SCSC	Single-crystal to single-crystal
SCXRD	Single-crystal X-ray diffraction
SURMOF	Surface-bound MOF
TGA	Thermogravimetric analysis
THF	Tetrahydrofuran
X-bond	Halogen bond

Introduction:

Crystal engineering & metal-organic frameworks (MOFs)

Chapter One

1

1.1 Crystal engineering – an overview

Crystal engineering is a rapidly developing field, with the aim of studying, understanding and designing crystalline materials. Specific arrangement of discrete molecules in the solid-state facilitates the formation of new and functional materials, as perhaps first put forward by Pepinski in 1955,[1] and elaborated on by von Hippel in 1962 as "molecular engineering … the building of materials and devices to order".[2] This prediction has been widely realised and embraced, and at present the CSD (Cambridge Structural Database),[3] a database for crystal structures (many designed and arguably the products of crystal engineering) contains over 800,000 entries.[i]

Crystal engineering is integral to several important and emerging fields involving chemicals in their solid state. In pharmaceutical chemistry, the physicochemical properties of drugs delivered in solid form (i.e. their solubility) have been shown to greatly depend upon their crystalline form. Particularly in this context, the importance of understanding co-crystal formation is highlighted.[4–6] In the growing field of coordination polymers and metal-organic frameworks (see section 1.3), the structure-function relationships of these materials for application to catalysis,[7–18] gas or fuel storage,[19–25] the separation of complex mixtures (including mixtures of gases)[26–31] optical application [32–36] and magnetic[37–40] properties is also being elucidated. Important to both the field of pharmaceutical chemistry and coordination polymers is polymorphism, in which the possibility of multiple accessible crystalline forms of the same constituent molecules is shown to have effects on the solid-state properties of the resultant materials.[41–44] The already substantial range of applications shown in this relatively young research field promises many future exciting results and potential solution to real-world issues.

1.1.1 Intermolecular interactions in crystal engineering

Where organic chemists may synthesise small molecules based upon formation of new covalent bonds, crystal engineering uses intermolecular forces to arrange 'supramolecular' assemblies. This analogy was first employed by Lehn in 1988,[45] and highlights the need for firm understanding of the intermolecular interactions within

---

[i] *Correct as of October 2015.*

super-molecules, just as for the covalent bonds holding together molecular synthetic targets (see Figure 1.1).

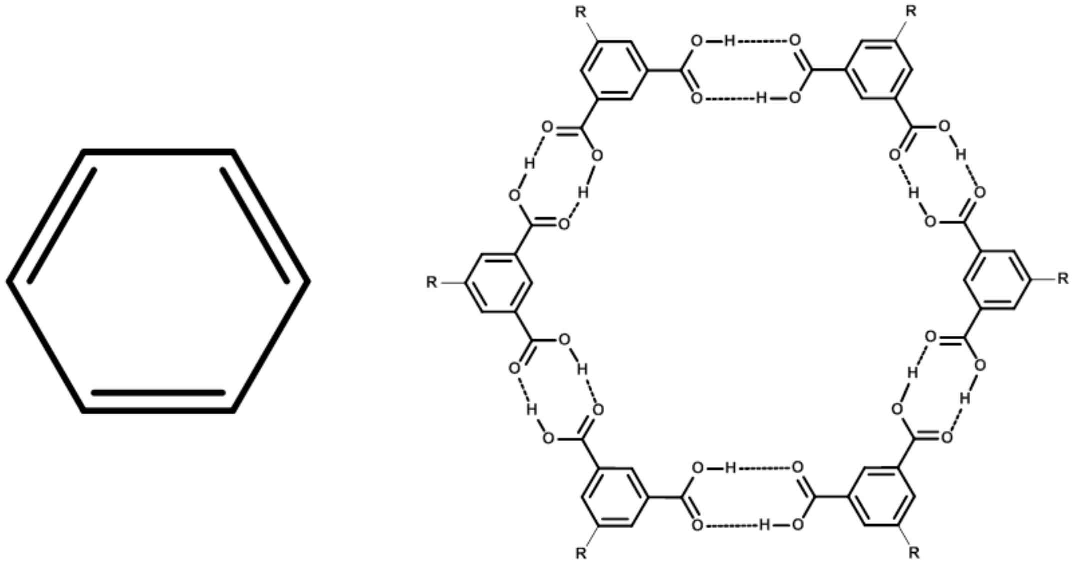

Figure 1.1. *A diagram illustrating the analogy between covalent bonds holding together a molecular species (left, benzene) and the intermolecular interactions holding together a supramolecular assembly (right, hexamer of substituted isophthalic acid).*[46]

Although perfect prediction of and control over the self-assembly of supramolecular structures is not currently achievable (though computational methods for the prediction of crystal structures have given promising initial results),[47] intermolecular interactions are a useful tool in directing self-assembly. To understand and manipulate these interactions is therefore a necessity. Directional (anisotropic) forces are arguably of most use to the crystal engineer (such as hydrogen bonds, halogen bonds, π-π stacking and coordination bonds), though use of isotropic forces has been made (van der Waals forces).[48,49]

As a further analogy to molecular synthesis, where synthons are used in organic retrosyntheses to assemble molecular targets, the term ‘supramolecular synthon’ (hereafter contracted to ‘synthon’) was coined by Desiraju[50] in describing the reliable, replicable intermolecular motifs that may be used in such a manner by the crystal engineer.

1.1.1.1 Hydrogen bonds

Ubiquitous in the natural world and the basis of many common natural phenomena, the non-covalent interaction between an electron-rich heteroatom and a hydrogen atom forms many motifs present in nature and biological structures that may be used as supramolecular synthons. Though a potentially strong intermolecular interaction (the strongest hydrogen bond being the $[FHF]^-$ unit, ~ 162 kJ mol^{-1}), the bond is still flexible and may be considered a weaker alternative to coordination bonds in self-assembly. The linearity of the hydrogen bond is one of the characteristics making it so applicable to crystal engineering. The θ(D–H···A) angle is generally close to 180°, as observed by Steiner's review of organic hydrogen bonds in the solid state in 2002,[51] or indeed now by anyone curious enough thanks to free access to the Cambridge Structural Database.

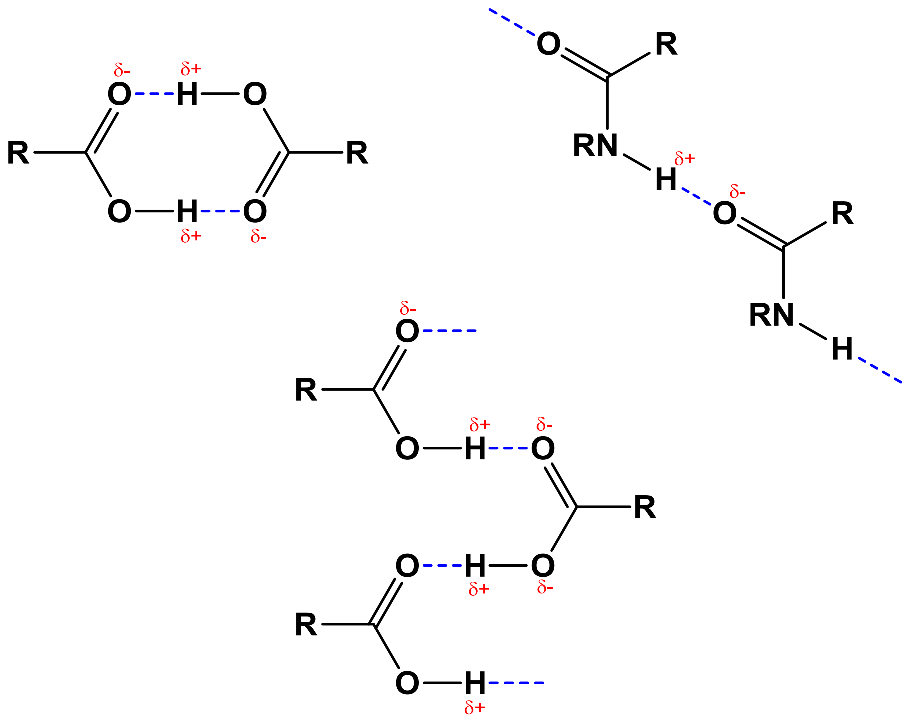

Figure 1.2. *Some simple hydrogen-bonding 'synthons' found in the solid state.*

The hydrogen bond has also proven useful in the construction of crystalline framework materials, and has already led to materials demonstrating potential for real-world application. Noteworthy useful hydrogen-bond-assembled materials include: porous guanidinium organodisulfonate materials made by Ward and co-workers, for the selective enclathration of xylene and methylnaphthalene isomers (commercially important), facilitating their easy isolation from mixtures;[26,52] as well as cucurbit[6]uril, which has also proven capable of capturing carbon dioxide at ambient temperature.[53]

1.1.1.2 π···π interactions

As ubiquitous with chemistry in biological systems as hydrogen bonding, yet much less well understood until recently, are π···π interactions. The combination of several energetically favourable effects (electrostatic interaction, charge induction and transfer, and the hydrophobic effect in the solution phase),[54] produces interaction energies around 65 kJ mol^{-1} (as reported for interaction between porphyrins).[54] The electronic effects of heteroatoms or substituents on aromatic rings may cause changes in the stacking behaviour, and this has been studied using computational chemistry, giving information on the angle and displacement distances of contact between rings.[55,56]

Though not as strong as coordination bonds, π···π interaction as secondary intermolecular interactions in self-assembly have been widely observed, both in organic (e.g. DNA) and in hybrid organic/inorganic materials.[57] For example DNA helices consist of supermolecules assembled through covalent bonds and hydrogen bonding (between chains), and then the base pairs π···π stack onto each other, producing an added structural dimension, complementary to the hydrogen bonds. The sextuple phenyl embrace (see Figure 1.3) is an example of a solely π···π interaction not directed also by hydrogen bonding or other intermolecular interactions.

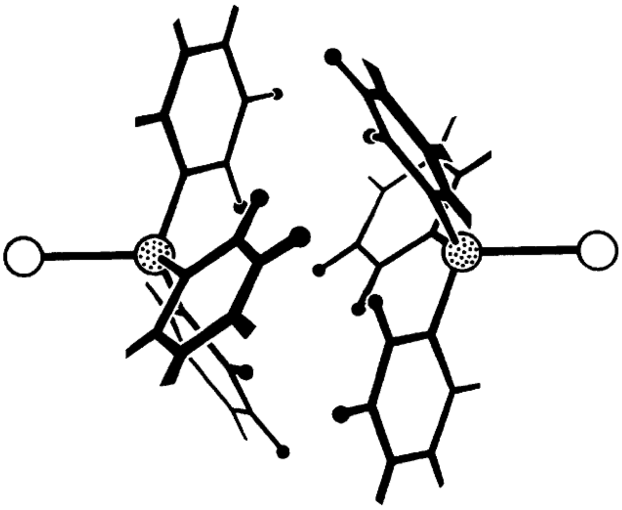

Figure 1.3. *A schematic of a sextuple phenyl embrace between [PPh$_3$R]$^+$ cations. Empty spheres represent an R-group, dot-filled spheres are phosphorus atoms and skeletal structures are phenyl rings. Figure reproduced from reference 57.*

1.1.1.3 Halogen interactions

As well as participating in hydrogen bonds as acceptors,[58] halogens may also interact attractively with each other, and with heteroatoms or lone-pairs in the solid state. These 'halogen bonds' are also present in nature,[59,60] though not as commonly as hydrogen bonds. The anisotropic electron density distribution about larger halogens (when covalently bonded to carbon atoms and/or electron withdrawing groups) creates an uneven distribution of electrostatic potential (see Figure 1.4). With increasingly larger halogens (I > Br > Cl), the polarisability is greater, creating a larger, stronger region of positive electrostatic potential (often called the 'σ-hole') available for interaction, as shown in Figure 1.4. As such, halogen-halogen interactions are found to be more prevalent for larger halogens.[61]

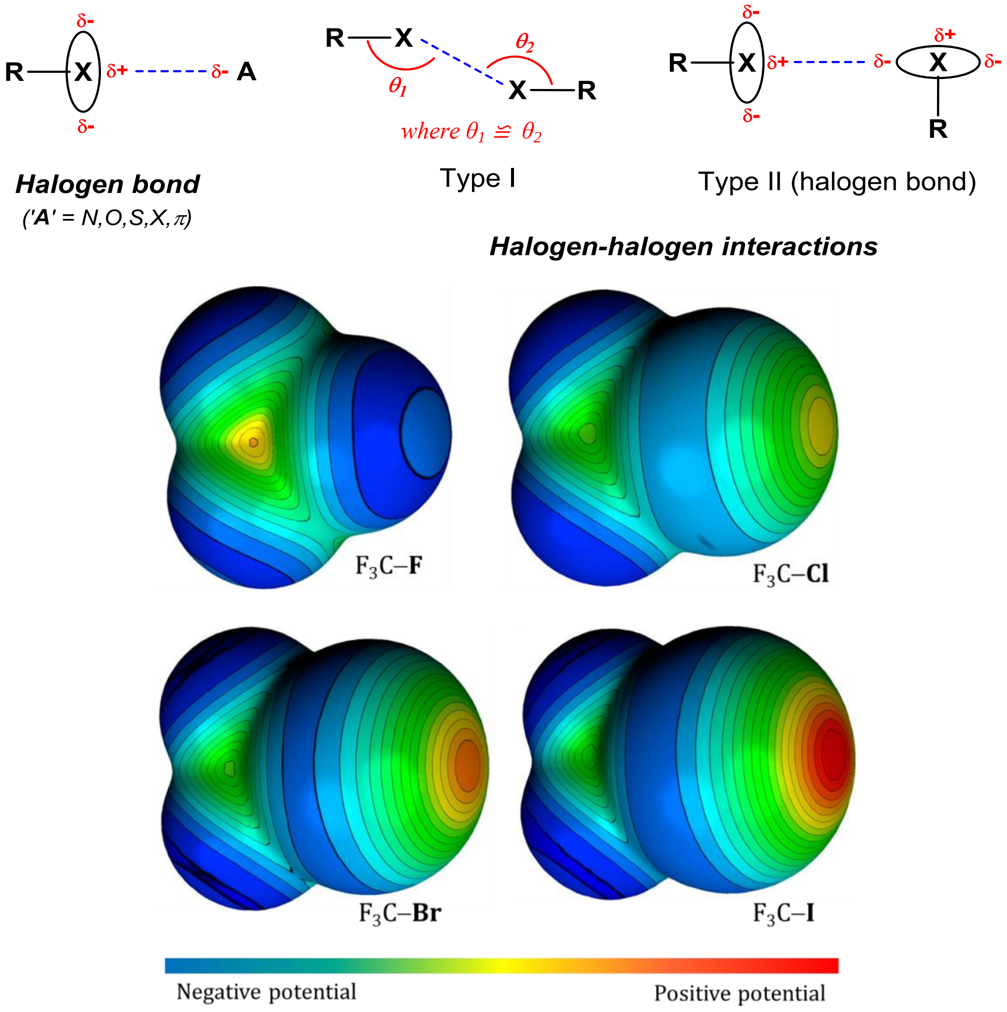

Figure 1.4.* *(Top) *Halogen bonding and attractive halogen-halogen interactions.* ***(Bottom)*** *Increasing regions of positive electrostatic potential (the 'σ-hole') on halogen substituents on trifluorohalomethane. Figure reproduced in part from reference 65.*

Type II halogen-halogen interactions have been noted for their relative strength (even affecting the mechanical properties of some solid materials),[62] and are considered to also fall under the term 'halogen bonds', though all the interactions in Figure 1.4 could be described as attractive. Halogen bonds have been found to have a range of energies, some comparable to hydrogen bonds. Halogen bonds between neutral organic species in solution have been found to have interaction energies ranging between 0 and 40 kJ mol^{-1}.[63] Due to their relative strength and greater directionality compared to hydrogen bonds (due to the uneven distribution of electrostatic potential about halogens, as opposed to hydrogen), halogen bonds and halogen-halogen interactions have seen increasing attention in the field of crystal engineering,[63–66] as well as in the solution phase.[67,68] Chapter 2 (section 2.1) introduces some of the applications of halogen bonding to the field of crystal engineering in further detail.

1.1.2 Coordination bonds in crystal engineering

Coordination of electron-rich atoms or functional groups (or even electron-rich chemical bonds) to metal ions provide perhaps the most important foundation for crystal engineering. These interactions may be considered strong and rigid, with set geometries and bond lengths determined by the properties of the metal ion. The coordination geometries of metals/metal ions strongly affect the arrangement of their ligands around them, and so strongly affect the packing of the resultant material in the solid state. This is particularly important in the case of coordination polymers (introduced further in section 1.2). Some typical coordination geometries for *d*-block metals are illustrated in Figure 1.5.

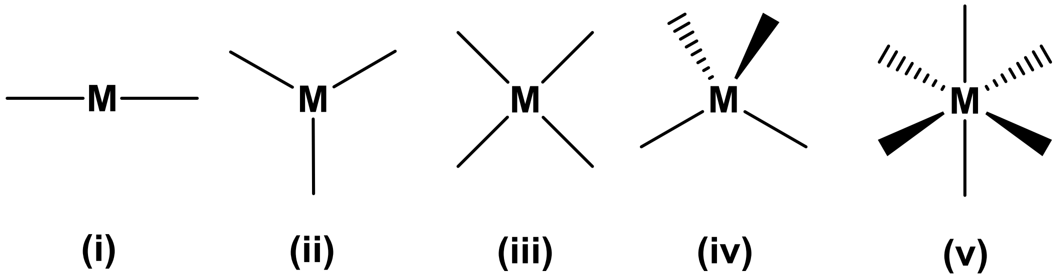

Figure 1.5. *Some typical coordination complex geometries, where 'M' is a transition metal ion:* ***(i)*** *Linear (e.g. Ag(I), Au(I)),* ***(ii)*** *Trigonal planar (e.g. Ag(I), Cu(I)),* ***(iii)*** *Square planar (e.g. Pd(II), Pt(II)),* ***(iv)*** *Tetrahedral (e.g. Zn(II), Ti(IV)),* ***(v)*** *Octahedral (e.g. Fe(II)).*

The coordination chemistry of transition metals is of particular use in crystal engineering (though examples of *s*-block metals in crystal engineering also exist)[69–71] as opposed to that of the *f*-block metals, where geometric coordination preference is reduced by the valence *f*-orbitals' contraction to the nuclei of those metals.

Although the rigidly-defined geometries of transition metals are very useful in directing the self-assembly of coordination materials in the solid state (see section 1.2), d^{10} metals have been shown to be useful in a different way. Substitution of hydrogen atoms with Cu(I), Ag(I) or Au(I) in hydrogen-bonded 'supramolecular synthons' has produced both novel and functional materials. Silver carboxylate coordination materials have featured extensively in the Brammer group's research on structurally dynamic materials,[72–76] and the substitution of the above metals into pyrazole trimers have given complexes with novel luminescence properties.

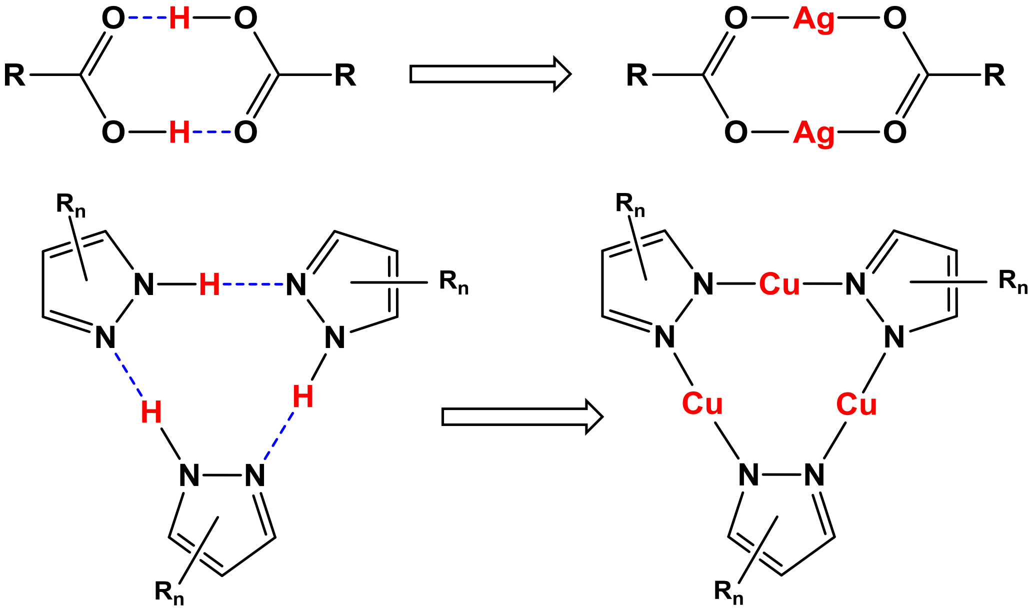

Figure 1.6. *Substitution of Ag(I) into carboxylate dimers,*[72] *or of Cu(I) into pyrazolate trimers.*[77]

1.2 Coordination polymers, metal-organic frameworks and other supramolecular polymers

1.2.1 Coordination polymers

The usefulness of metal ions in crystal engineering has led to their utilisation in many supramolecular systems. Perhaps the most diverse and promising such supramolecular structure type is the coordination polymer. Coordination polymers are infinitely extended in at least one dimension, and this is propagated by the coordination of multitopic ligands ('spacers') to metal ions or clusters ('nodes').

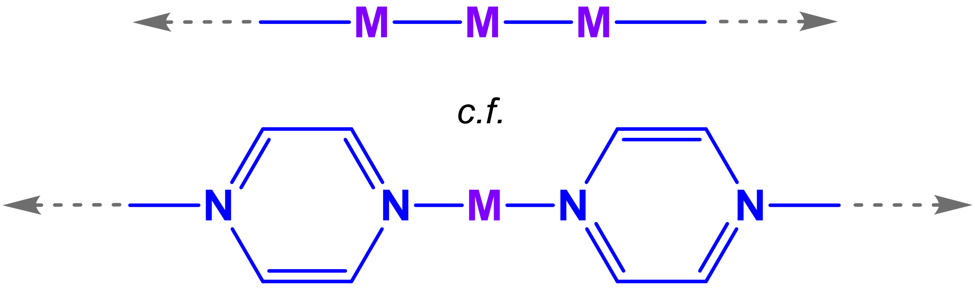

Figure 1.7. *A schematic of a one-dimensional coordination polymer consisting of simple metal ion 'nodes' (M) and linear, ditopic 'spacer' ligands (shown in blue).*

This 'node and spacer' approach allows the rational design of a great many polymer architectures. The ligand spacer may be varied by choosing the number of coordinating sites, changing the functional group used to coordinate, or by choosing either linear or angular 'spacers'. The metal ion (or cluster) used can be varied to create different 'node' geometries (as shown in Figure 1.5). The versatility of coordination polymers, and so their importance to the field of crystal engineering has been reviewed several times.[78–81]

One-dimensional or two-dimensional coordination polymers are most generally non-porous, however some have shown interesting potential for applications similar to porous materials. Gas sorption in inherently non-porous coordination polymers is introduced in greater detail in section 1.4.2. Three-dimensional coordination polymers, due to their inherently porous nature, have been studied much more extensively in this context.

1.2.2 Metal-organic frameworks (MOFs)

Metal-organic frameworks (or MOFs) may be considered as a subset of coordination polymers, which are generally of three-dimensional connectivity (though some two-dimensional coordination polymers have been considered MOFs), and they are generally (though not necessarily) porous (also called PCPs – porous coordination polymers). The exact hierarchy of terms for coordination network solids (including coordination polymers and MOFs) remains a topic of ongoing discussion.[82]

The porosity of MOFs is what dominates their interesting nature, and their main functionalities. The customisability of MOFs though changing the nodes and spacers enables the rational design of different pore environments. Perhaps the most well-known example of a metal-organic framework is MOF-5, $[Zn_4(\mu_4\text{-}O)(bdc)_3]$.[19] MOF-5 is a simple cubic porous material constructed from zinc-oxide tetrahedra (nodes) connected by linear benzene dicarboxylate ligands (spacers). Its hydrogen storage capacity (due to its high surface area and pore space)[19] and deliberate design (crystal engineering approach) led to it being the starting point for many other carboxylate-based MOFs in the literature.

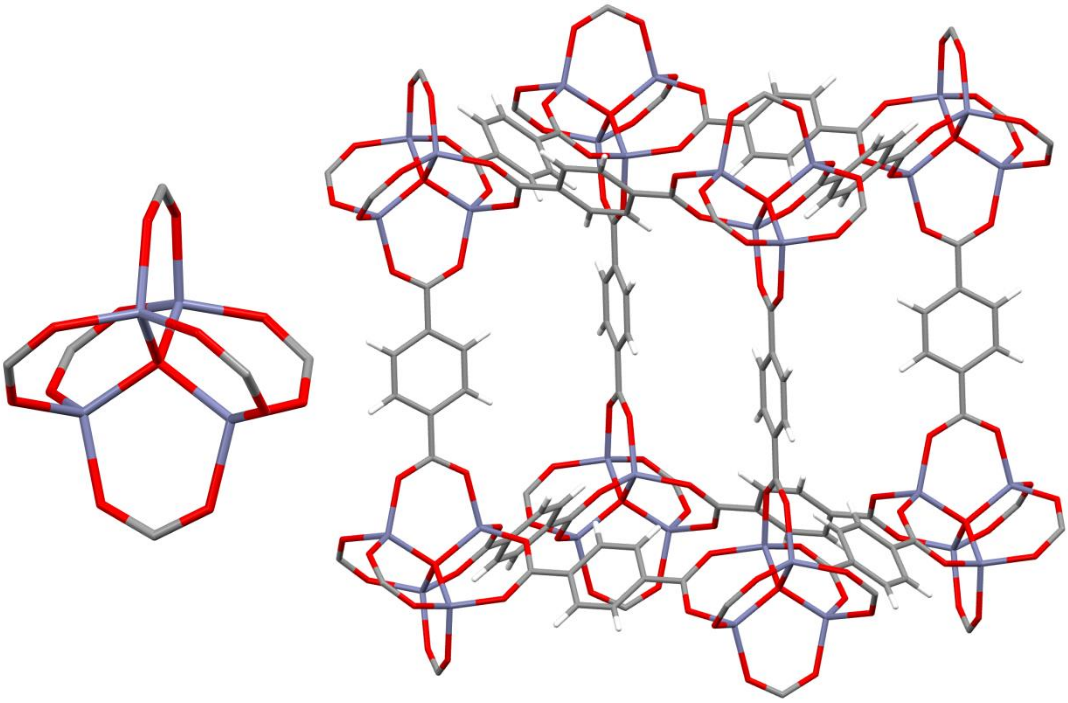

Figure 1.8. Left: *the 'node' of MOF-5 or* $[Zn_4(\mu_4\text{-}O)(bdc)_3]$*, showing the* μ_4*-oxo zinc cluster (with carboxylates coordinated).* ***Right:*** *the cubic pore environment within MOF-5.*

Despite the greater thermal and hydrolytic stability of zeolites (perhaps the most closely related class of porous materials to MOFs), the crystal engineering approach to MOF materials has led to their diverse, successful application in many ways. MOFs for gas and vapour capture, heterogeneous catalysis, proton conduction, chiral resolution and trapping of hazardous materials (among many other applications) have been identified so far. Examples of such applications are introduced and referenced in section 1.3.

1.2.3 Zeolitic imidazolate frameworks (ZIFs)

ZIFs may be considered a subset of metal-organic frameworks, which have enjoyed particular attention due to their enhanced thermal stability relative to MOFs based on carboxylate ligands. They are three-dimensional, generally porous coordination polymers, based on tetrahedral metal ions (not clusters), connected by imidazolate ligands. An example of a ZIF (which is introduced further in chapter 5) is shown in Figure 1.9.

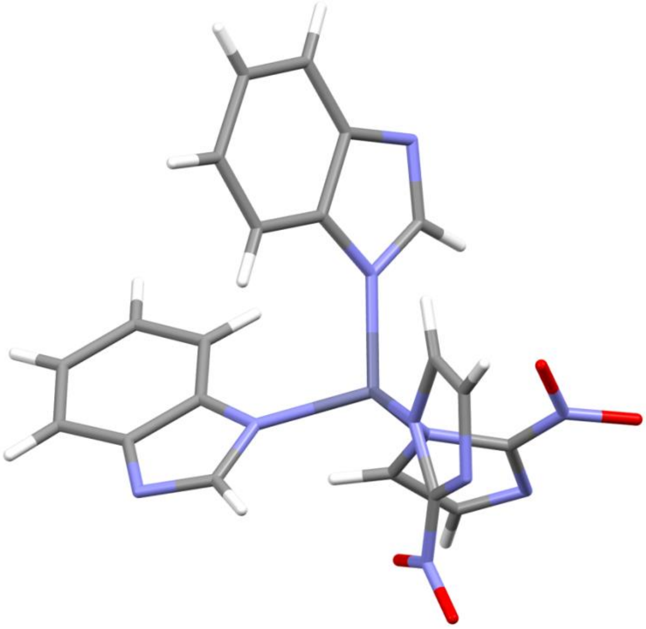

Figure 1.9. *The coordination environment in the mixed-ligand ZIF-69 [Zn(2-nitroimidazolate)$_2$(benzimidazolate)$_2$].*[83]

Whereas MOFs based on carboxylates offer generally much lower thermal and hydrolytic stability than zeolites, ZIFs possess much more favourable thermal and chemical stabilities (relative to MOFs). The variety of structures observed of ZIF materials, as well as their potential for structural flexibility has also been of recent interest, including the structural transformations, amorphisation and glass-like properties of some ZIF phases.[84–88]

1.2.4 Other supramolecular polymers

The prominence of MOFs and coordination polymers has led to the study of other network materials for similar applications. Covalent organic frameworks (COFs) have become the subject of a research field in their own right in recent years.[89–93] COFs are organic polymers, propagated by covalent bonds rather than coordination bonds. The use of rigid polyaromatic building blocks to engineer 2D or 3D polymers has led to a range of highly porous structures.

The high degree of porosity in COFs has been exploited for gas sorption as in MOF materials.[90–92] COFs also demonstrate a high degree of customisability (see sections 1.3.2 and 1.3.1 respectively).[89] However, due to their high porosity, poor crystallinity and lack of strong X-ray scattering elements, COFs have been difficult to characterise crystallographically, hindering the understanding of their structure-function relationships. To date only one example of 'complete', single-crystal diffraction characterisation of a COF exists.[93]

Porous supramolecular materials propagated by hydrogen bonds have also been described as polymeric. The acronym HOF (hydrogen-bonded organic framework) has been used to describe a related series of compounds which also display similar properties to MOFs and COFs despite being comprised of discrete molecules in the solid state. The porosity of these materials has been explored for gas sorption purposes.[94]

1.3 Synthesis and applications of metal-organic frameworks

As noted above, metal-organic frameworks are attractive materials to study, in particular due to their varied and potentially powerful applications arising from their porosity. Such applications which have received recent attention include the entrapment of gas (in some cases selectively),[95–97] the catalysis of reactions within their pores,[98] novel optical properties[99–101] and flexibility or dynamic structural behaviour in response to guests.[102–104] Specific noteworthy examples of MOF applications are introduced in section 1.3.2. The synthesis of MOFs and developments in solvent-free or multi-step synthesis are also introduced in section 1.3.1.

1.3.1 Synthesis of MOFs

1.3.1.1 The effect of solvent and self-assembly

The role of solvent in the self-assembly of coordination polymers (and MOFs) is highlighted in the review by Li and Du.[105] Slight variations in synthetic conditions (where perhaps solvent mixtures or heating regimes for syntheses are not identical) for MOFs could give potentially large numbers of polymorphs or alternative formulations in simple systems (for example combinations of Zn^{II} and terephthalate, the constituent components in MOF-5).

Mechanochemical (solvent-free or with very small quantities of solvent) synthesis of MOFs has been pursued in recent years, in particular by James and co-workers. Mechanochemical synthesis bypasses the effect of solvent (where none is used) as well as offering a more environmentally friendly approach to MOF synthesis. Research in the James group has successfully demonstrated the solvent-free synthesis of MOFs,[106–108] including several well-known and extensively studied MOFs, and is now the subject of one of the first MOF spin-out commercialisations.[ii] However, the absence of a crystallisation solvent can cause complications, leaving unreacted starting material (metal salts or ligand) present, giving a product which requires further purification before application.[109]

[ii] See www.moftechnologies.com/order.html (accessed November 2015).

1.3.1.2 Multi-step MOF synthesis and structural transformations of MOFs

Some one-dimensional and two-dimensional coordination polymers have been shown to transform into porous three-dimensional coordination polymers through multi-step reaction pathways. Work in the Brammer group demonstrated the flexibility of the common 'paddlewheel' coordination polymer node in a reversible chemical and structural transformation from a 2D coordination polymer to a 3D MOF.[110]

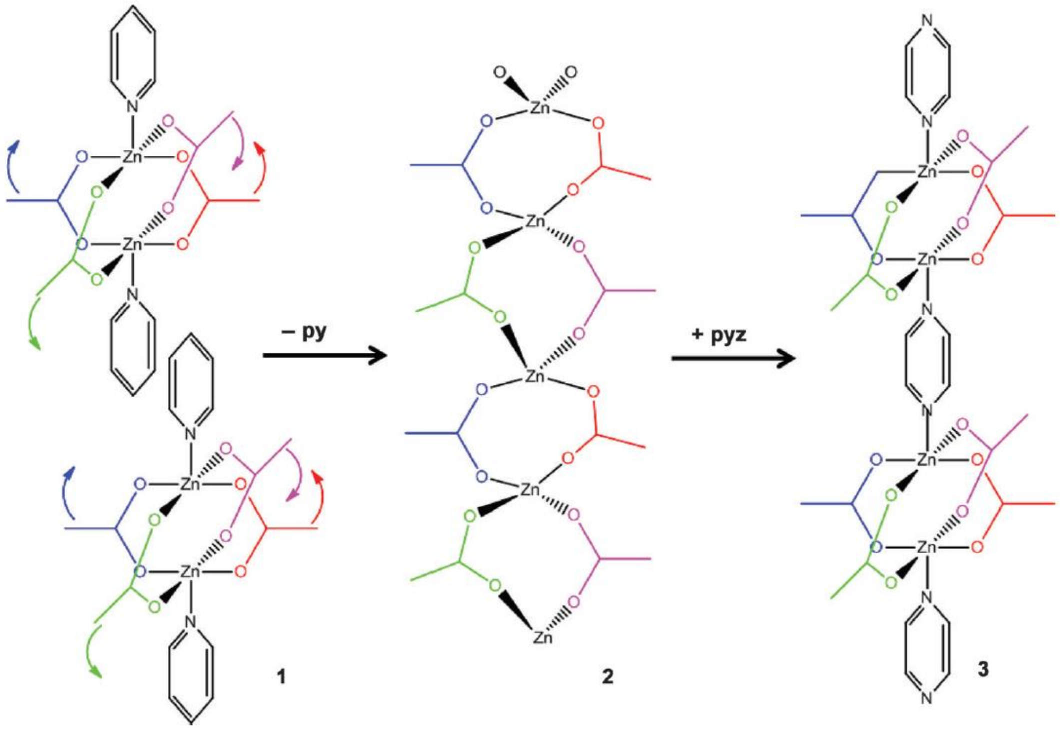

Figure 1.10. A mechanistic representation of removal of pyridine from a 2D coordination polymer, accommodated by rearrangement of the paddlewheel coordination polymer node, and its replacement with pyrazine to form a new 3D coordination polymer (MOF). Figure reproduced from reference 110.

The removal of pyridine (a capping ligand in the initial 2D coordination polymer) was compensated for by the rearrangement of the paddlewheel unit. Introduction of pyrazine enabled the formation of a 3D porous coordination polymer (MOF), due to the reformed paddlewheel nodes being connected in the third dimension by the pyrazines.

The removal of capping solvent molecules to enable propagation of a coordination polymer in an addition dimension was also shown, in work by Du and Vittal.[111] This was as part of a two-step transformation of a coordination polymer into a MOF (1D coordination polymer to 2D to 3D), although crystallographic evidence was not obtainable in this case.

The pores of as-synthesised MOFs are most often filled with the crystallisation solvent. To activate the materials for gas sorption (or other applications that depend on the pores being empty), this solvent must be removed. In the case of many rigid MOFs, this removal of solvent does not result in a collapse of the pores (for example 'MOF-5' introduced in section 1.2.2).[19] This type of porosity has been termed 'second-generation porosity' primarily by Kitagawa.[102,112,113] However, some MOFs have demonstrated a structural dependence on the solvent contained within them.[113–117] Removal of the solvent results in either a reversible structural rearrangement ('third-generation porosity' or 'soft-porous crystals') or a complete collapse of the pores (or even loss of crystallinity), which may be irreversible or reversible ('first-generation porosity'). This terminology will become increasingly important as MOFs which are not necessarily rigid and/or are solvent-structure dependent become more prominent. This terminology is also relevant to work in this project described in chapter **3** on molecular materials.

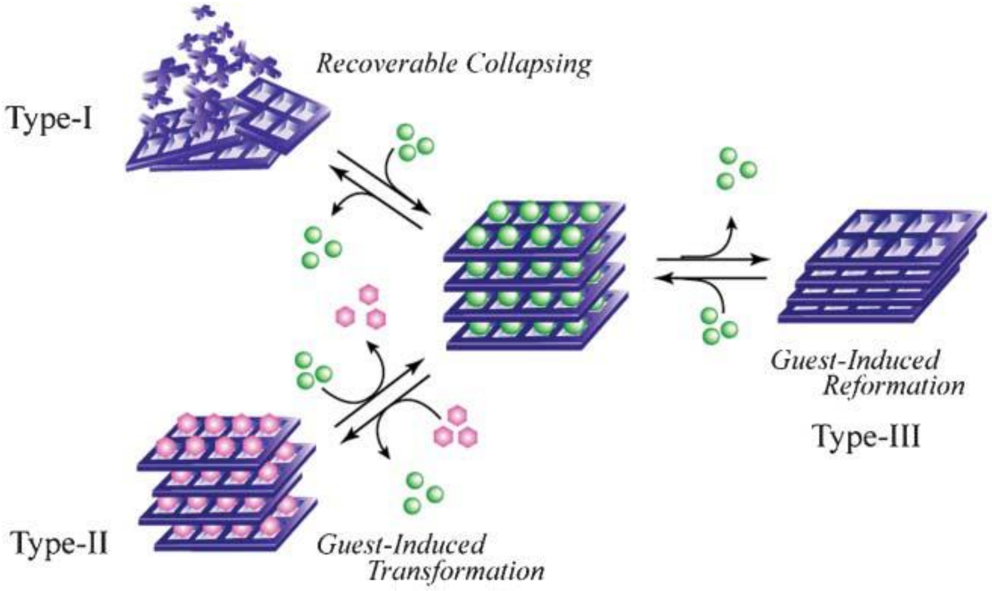

Figure 1.11. *The three 'types' of porosity classified by Kitagawa, describing traditionally rigid MOF systems (type II) and more flexible systems (types I and III). Figure reproduced from reference 113.*

1.3.1.3 Post-synthetic modification of MOFs

MOFs have been shown to be customisable not only during the synthesis (through the selection of metal and ligand) but after initial synthesis. Functional groups on ligands which point into the pore environment may undergo simple organic transformations, thereby modifying the pore space. This process has become known as post-synthetic modification (PSM).[118,119]

PSM is particularly useful in cases where a desired functional group cannot be used in the initial synthesis. Potentially coordinating functional groups may interfere with the initial self-assembly of the MOF (by competing with the intended coordinating functional group, and creating an unintended product). Post-synthetic modification has been reviewed Cohen.[118–120] A diagrammatic representation of the concept of PSM is shown in Figure 1.12.

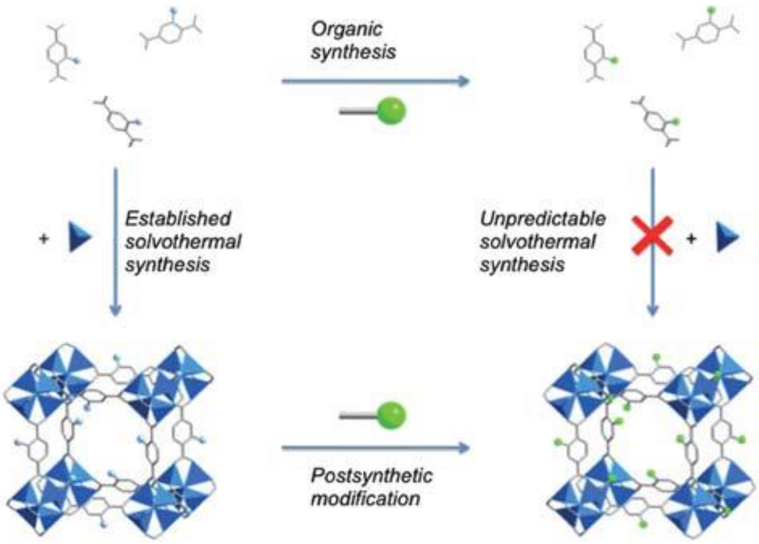

Figure 1.12. *Synthetic routes to functionalised MOFs, either through modifying the ligand and then mixing with metal salt (methods complex, unknown) (follow diagram from top left clockwise), or solvothermal synthesis and post-synthetic modification (follow diagram from top left anticlockwise). Figure reproduced from reference 120.*

The PSM strategy has been used by Rosseinsky and co-workers to introduce a coordinating 1,3-ketoimine functionality to a pore surface.[121] This allowed the complexation of a transition metal, which would not have been possible during the initial self-assembly.

Interestingly, the outcome of simple organic transformations has also been affected by conducting them within the pores of a MOF. The confined space and limited rotational freedom available to the ligands was shown to direct distereoselectivity of alkene bromination within a MOF (see Figure 1.**13**).[122]

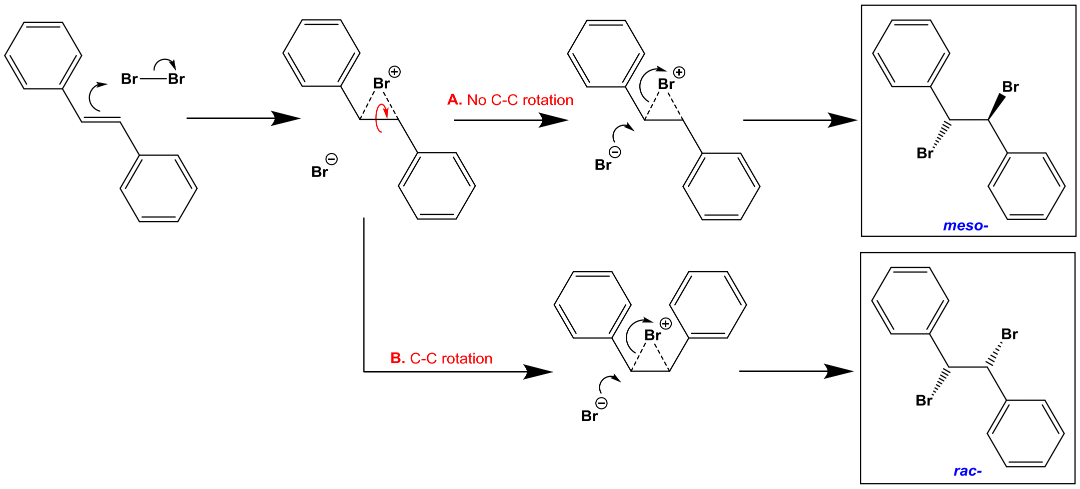

Figure 1.13. *Diastereoisomerism in the bromination of stilbene. The product formation is dependent upon the rotation of the C–C alkene bond during reaction (shown in red). Both the meso- and rac- products are accessible where rotation is possible (products in boxes with blue titles), but only the meso- product results where C–C bond rotation is not possible.*

The bromination of the stilbenedicarboxylate ligands of a MOF was shown to be affected by the lack of freedom of rotation. In a solution-phase reaction on molecular stilbene (or its derivatives), the stilbene unit would be free to rotate during the bromination, and so the bromination could proceed by either reaction route A or B shown in Figure 1.13, enabling formation of both diastereomers. The lack of rotational freedom when stilbenedicarboxylate is used as a ligand in a MOF, however, prevented reaction route B from taking place, and therefore gave a diastereoselective bromination reaction.

1.3.2 Gas storage/entrapment

The high internal surface area and high porosity of metal-organic frameworks has led to a considerable amount of study into their potential for storing or separating gases. This has been applied to the capture and storage of undesirable gases such as CO$_{2,}$ or the storage of fuel gases (or feed gases) such as H$_2$ or volatile organics for later use.

Further work on MOFs for gas storage by the Yaghi group has taken a crystal engineering approach to designing MOFs with massive internal pore space, by using extremely long ligand spacers between nodes. MOFs with internal void spaces of up to 90% were successfully synthesised by this approach (just 10% of the material volume is occupied) (See Figure 1.14).[22]

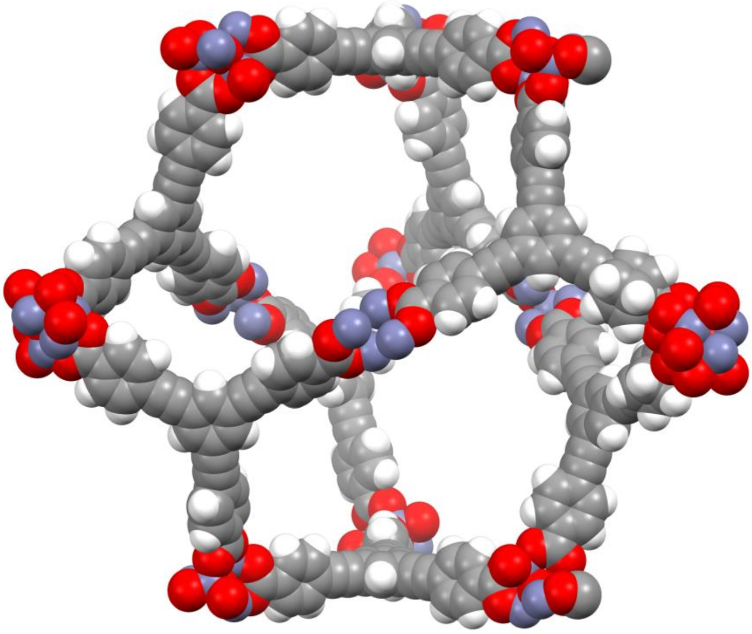

Figure 1.14. *Ultra-high porosity in* $[Zn_4(\mu_4\text{-}O)(L)_2]$ *(where L is 4,4',4''-(benzene-1,3,5-triyl-tris(ethyne-2,1-diyl))tribenzoate) presented by Yaghi and co-workers.*[22] *Atoms are shown as spheres representing their van der Waals radii.*

However, targeting such great porosity does not necessarily lead to better functionality. Materials for the entrapment of undesirable gases need to demonstrate some retention or selectivity for the target. Materials for the storage of fuel gases need to demonstrate good working capacity. Working capacity refers to the storage capability of the material above the 'working' pressure (a minimum of c. 5bar, at which most storage tanks are maintained even when 'empty') – see Figure 1.15.

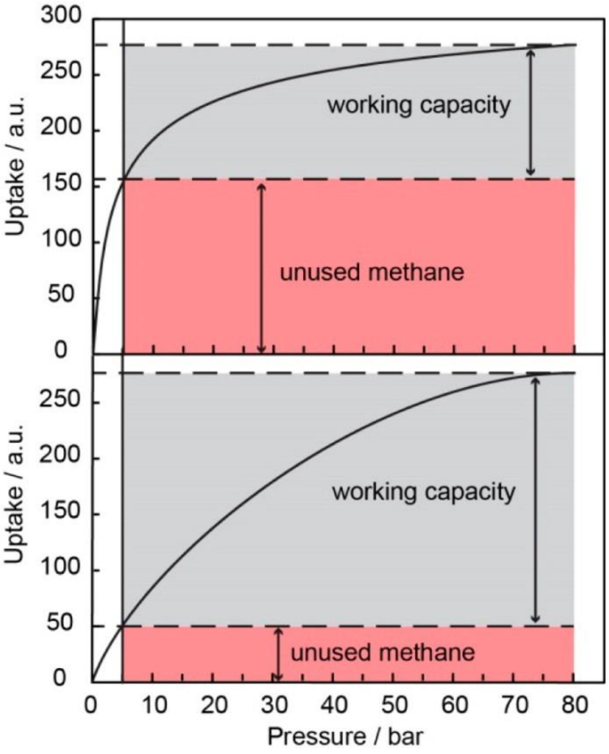

Figure 1.15. *A simple schematic of gas sorption isotherms for two different porous materials.* ***Top:*** *a material with poor working capacity, as most of the gas remains adsorbed below 5 bar.* ***Bottom:*** *a material with good working capacity, as most of the gas stored is removed from the material above 5 bar. Figure reproduced from reference 24.*

Selective entrapment of gases from a mixture is a more recently explored application of MOFs. Entrapment of CO_2 from a mixture (often from air/N_2) is particularly desirable, for its removal from flue gas streams in power plants. Several MOF systems have been used for the selective entrapment of CO_2,[25,123–132] many of them utilising amino groups decorating the pore surface.[125,126,132–134] This idea comes from the arrest of CO_2 in the liquid phase by carbamate formation ("scrubbing"), currently used in industry.[21]

However this is not the only method of inducing selectivity. Fluorinated MOF hosts have also been shown to be efficient at accommodating CO_2 (in some cases selectively over N_2 or CH_4), and MOFs with perfluorinated ligands have been used to this end.[28,135] In particular, work by the Farha group demonstrates the improvement of CO_2 uptake by using fluorinated MOFs.[135] An existing MOF (NU-1000) was modified post-synthesis (PSM) to feature perfluorinated alkyl chains (of varying lengths) decorating the pore surface (see Figure 1.16).

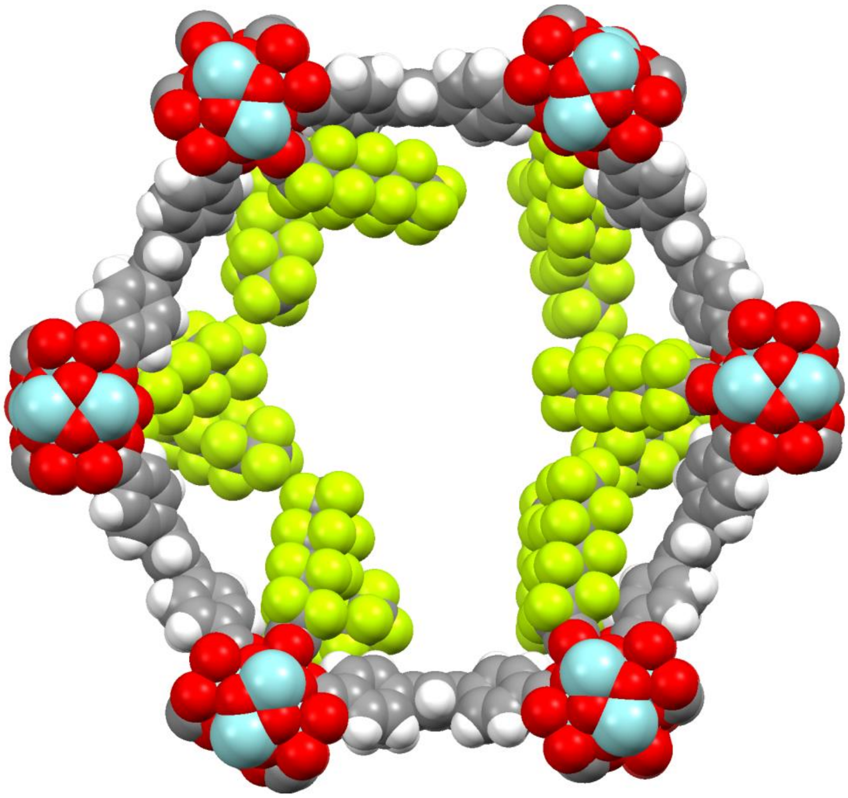

Figure 1.16. *The interior pore surface of the "NU-1000" MOF, which has been modified to contain perfluorononanoate chains. This particular MOF showed an increased* CO_2 *uptake at 0.15 bar* CO_2 *of 0.8* cm^3 cm^{-3} *over the unmodified parent material.*

It was gravimetrically observed that at low loading (p =0.15 bar) the CO_2 uptake of the fluorinated materials was increased over that of the non-fluorinated parent MOF. This, however, is accompanied by a loss of overall pore space due to the presence of the perfluorinated chains. The use of fluoroalkyl groups to selectively adsorb CO_2 has also been investigated in non-porous materials, and related work is introduced in section 1.4.2.

1.3.3 Capture/destruction of undesirable substances

While CO_2 has been a well-studied target for capture within MOFs, due to its role in anthropogenic global warming, the capture of other harmful anthropogenic gases has enjoyed less attention in the MOF field.

However, hydrophobic MOFs have been explored in recent years for their ability to capture volatile organic compounds (VOCs) from humid air.[136–139] In particular, Navarro and co-workers have reported promising results with azolate-based MOFs as highly hydrophobic hosts for a family of organic guests that mimic chemical warfare agents (CWAs) (see Figure 1.17).[137,138]

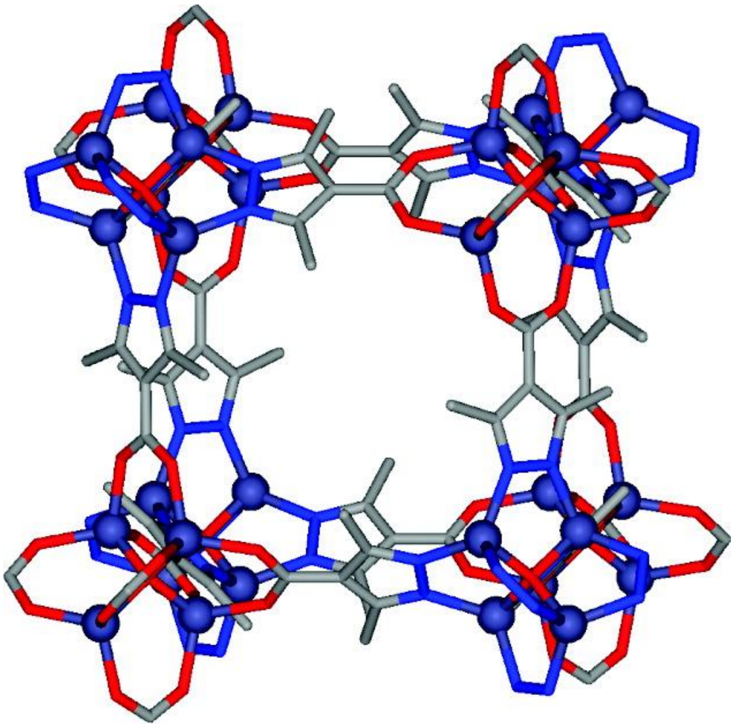

Figure 1.17. *A highly hydrophobic MOF (based on the MOF-5 type structure shown in Figure 1.8) for the capture of chemical warfare agent analogues (such as diethylsulfide). Figure reproduced from reference 138.*

The relative success in capturing these gases within MOFs, in cases better than in activated carbon, has led to attempts to destroy the CWAs captured within hydrophobic MOFs.[139] The addition of lithium alkoxide to the pores of the well-known hydrophobic MOF UiO-66 ($[Zr_6O_4(OH)_4(bdc)_6]$) by the Navarro group created a material capable of catalysing the destruction of CWA analogue compounds. This proceeded via the hydrolysis of the P–F, P–O and P–Cl bonds commonly present in CWAs. In fact, suspensions of these modified MOF materials were also successfully impregnated into silk, creating a porous fabric that demonstrably degraded CWA analogue compounds in the vapour phase. This shows potential for real-world application of active MOFs. An image of the MOF particles suspended on silk is shown in Figure 1.18**.**

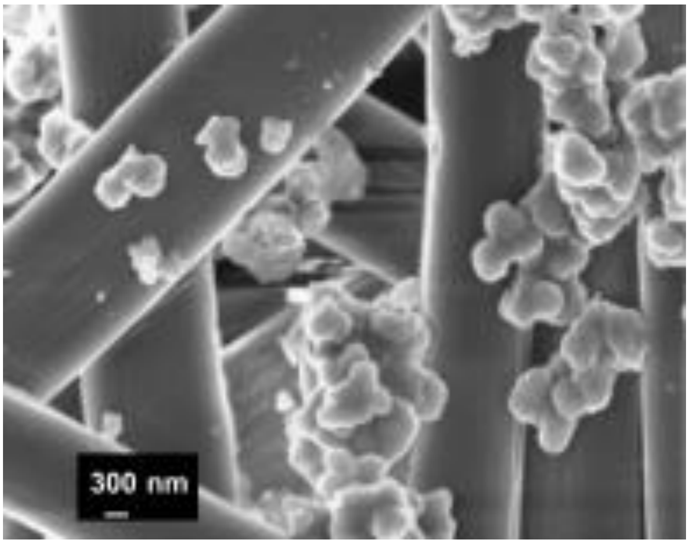

Figure 1.18. *Particles of the alkoxide-modified MOF* $[Zr_6O_4(OH)_4(bdc)_6](LiO^tBu)$ *on silk. Figure reproduced from reference 139.*

1.3.4 Catalysis

The potential of MOFs as heterogeneous catalysts has also been explored. Here the versatility of MOFs in comparison to zeolites is also advantageous. A variety of catalytically active MOFs have been designed, which may be catalytically active at an open metal site which is pointing into a pore,[7,140,141] where the ligands themselves have been activated as catalysts,[13,14] at a cluster or complex which has been impregnated into the MOF,[11,12,17,18] or by a combination of metal/ligand activity.[15,16]

A notable example of ligand-catalysed reactions in a MOF is the use of radical-containing ligands for MOF construction by Kitagawa and co-workers.[14] Their use of a ligand resembling TEMPO ((2,2,6,6-Tetramethylpiperidin-1-yl)oxyl) created a pore space lined with nitroxyl radicals (see Figure 1.19).

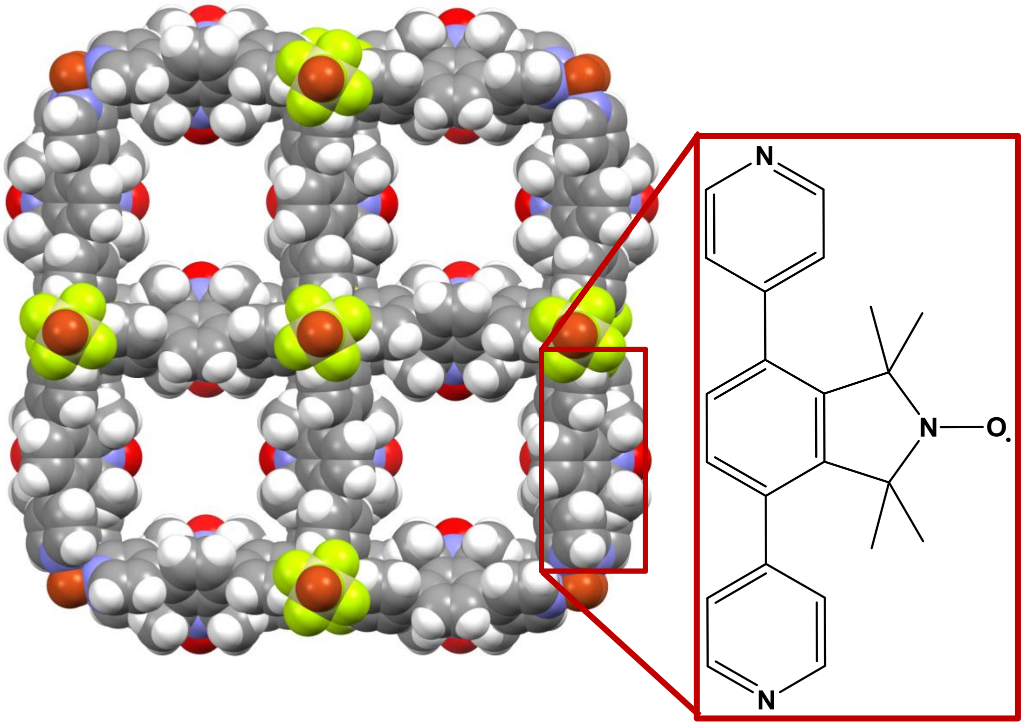

Figure 1.19. *Nitroxyl radicals lining the pores of a MOF designed for oxidation catalysis by Kitagawa and co-workers.*[14]

The nitroxyl-containing MOF was found to catalyse the oxidation of a broad range of simple alcohols, in comparable yields to reactions using TEMPO as a homogeneous catalyst. Moreover, the advantages of using a heterogeneous catalyst (i.e. a MOF) over homogeneous catalysts are also exemplified by this work, as the substrates after reaction were found to be easily removed from the MOF, and the authors noted that work-up was also simplified due to the absence of catalyst in solution.

Recent work has also looked at the application of MOFs as photocatalysts, in several cases for CO_2 reduction,[15,16] following on logically from the continuing interest in MOFs for the capture of CO_2 within their pores. A noteworthy example uses a combination strategy of utilising the MOF as a host for the CO_2, with ligands containing an iridium complex for the reduction of that CO_2. Again the advantages of heterogeneous catalysis are shown by the use of MOFs, as the catalytic MOF could be re-used by quenching of the iridium catalyst, and it's successful re-use with only a minor loss of activity over 5 cycles.

1.3.5 Optical properties

The luminescent properties of MOFs have also been explored, in particular by the group of Wenbin Lin. The Lin group have worked on tuning the optical properties of MOFs through interpenetration,[32] 'doping' of MOFs with luminescent ligands,[35] or more recently the tandem effect of metal clusters (nodes) and their ligands (spacers).[36] Perhaps most notable is the latter example, in which zirconium (or hafnium)-based MOFs of the same topology as the UiO series (see Figure 1.20) were shown to act as X-ray scintillators.

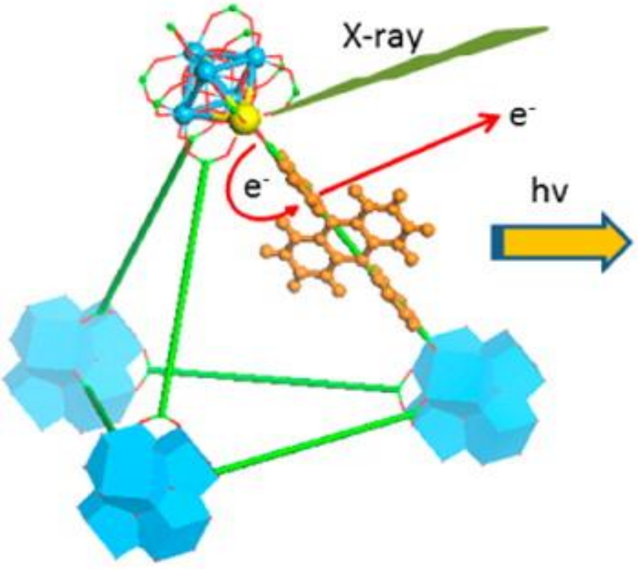

Figure 1.20. *X-ray scintillation by the tandem absorption of X-ray photons by heavy metal clusters and visible photon emission by anthracene-like ligands in* [$Hf_6O_4(OH)_4(ligand)_6$] *MOFs by the Lin group. Figure reproduced from reference 36.*

The X-ray scintillation was achieved by exploiting the X-ray absorption of heavy metals (the zirconium or hafnium in this case), and its conversion to fast electrons. The resultant excitation of the specifically designed anthracene-like spacers generated visible photons.

The visible (or near-visible) luminescence ability of MOFs has also been recently applied to the sensing of guests present within the pores.[33,142–150] This has been achieved through the introduction of either luminescent ligands which may either by excited[145,146] or quenched[33,142,143,148,149] by the presence of the target guest, or by the presence of open metal sites to bind the guests.[144] One promising example also demonstrates the value of using luminescent sensor molecules as ligands in MOFs, rather than as free molecules in the solution phase (see Figure 1.21).[146] In this case, the high cytotoxicity of a cyano-fucntionalised imidazole sensor molecule was found to be mitigated by its suspension within the framework as a ligand, preventing unintended reaction with components of the cell.

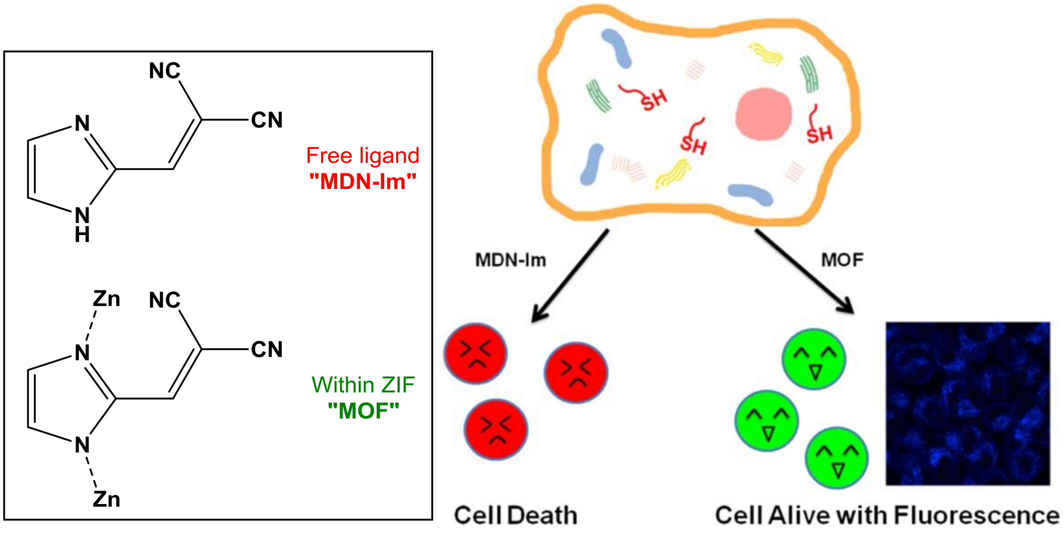

Figure 1.21. *Use of either the free ligand 2-((1-methyl-1H-imidazol-2-yl)methylene)malonitrile or the ZIF form [Zn(2-((1-methyl-1H-imidazol-2-yl)methylene)malonitrile)] as a thiol sensor in cells. Use of the free ligand results in cell death, but of the ZIF preserves the cell. Figure reproduced in part from reference 146.*

1.3.6 Other 'host' applications

The applications described in sections 1.3.1 to 1.3.5 above describe some of the most explored areas of MOF chemistry, but are by no means exhaustive. This section introduces some other notable applications of MOFs which do not entirely match the paradigms previously introduced.

1.3.6.1 The 'crystalline sponge' crystallographic method

Using a MOF host containing the electron-rich element iodine in the framework, the Fujita group have crystallographically characterised small molecules which do not normally form crystals, by encapsulating them as guests within the crystalline MOF.[151,152] This has helped identify the structure of synthetic organic targets which may only be isolable in microgram quantities, and the absolute configuration of enantiomerically pure compounds.[153] The presence of heavy atoms in the framework has helped bypass the need for heavy elements in the guest molecule, enabling solution of the phase problem where it may not be possible for light organic structures containing only C,H,N.

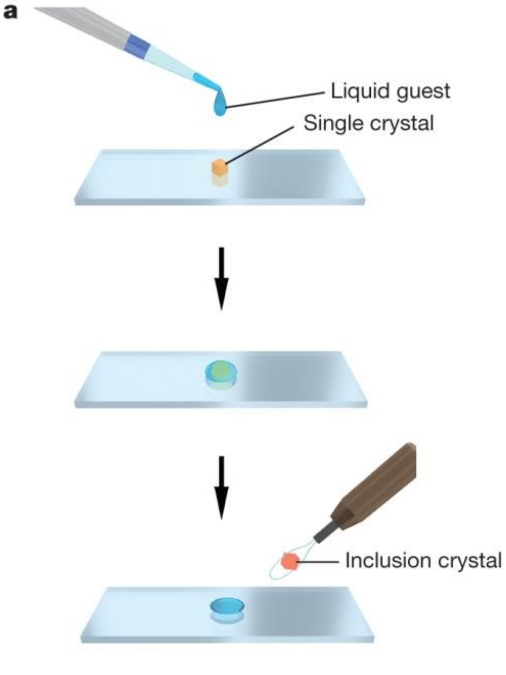

Figure 1.22. *The 'crystalline sponge' method for obtaining crystal structures of small compounds. Section **a** shows the general method for inclusion of the guest, and sections **b** and **c** show the crystal structures of the host MOF (shown in wireframe) and the guests contained within (shown in space-fill view, then also with thermal ellipsoids at the 50% probability level). Figure reproduced from reference 151.*

1.3.6.2 Templated polymerisation

Two interesting variations on the application of MOFs to polymer synthesis have been shown, involving the pre-organisation of monomers.

The first involves using the ligands of the MOF as monomers. Sada and co-workers demonstrated the templating of porous organic polymers by this method.[154] In their work, ligands which contained pendant polymerisable groups (see Figure 1.23) were reacted with metal salts to produce MOFs of various architectures. The monomer ligands were then polymerised by the introduction of cross-linking guests (see also Figure 1.23), and the MOFs digested using acid. This left behind porous organic polymers with architectures that were templated by the MOF phase previously present.

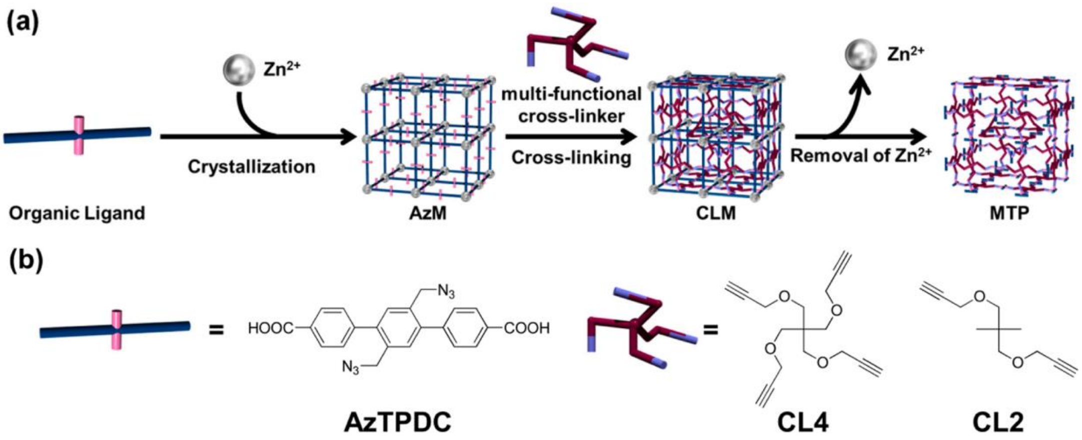

Figure 1.23. *Schematic of templated polymer synthesis, using monomers which are pre-organised as ligands within a MOF. 'Click'-able cross linkers are added to the crystals to initiate polymerisation, followed by removal of the metal nodes with acid. Figure reproduced from reference 154.*

Secondly, work by the Kitagawa group utilised MOFs as hosts for the polymerisation of a monomer guest.[155] They demonstrated that the bulky, normally un-polymerisable monomer 2,3-dimethylbutadiene (DMB) could be polymerised within the channels of several MOF hosts, due to the suppression of termination reactions within the pores. The restrictive pore channel environment of the MOFs used pre-organised the monomers such that cyclisation termination routes or other branching reactions could not occur. Moreover, by using different sized pore channels, the group were able to restrict the extent of (or stop completely) the polymerisation by restricting the space available for the reaction to take place. This approach also enabled the microstructure (branching) of the polymer formed to be altered.

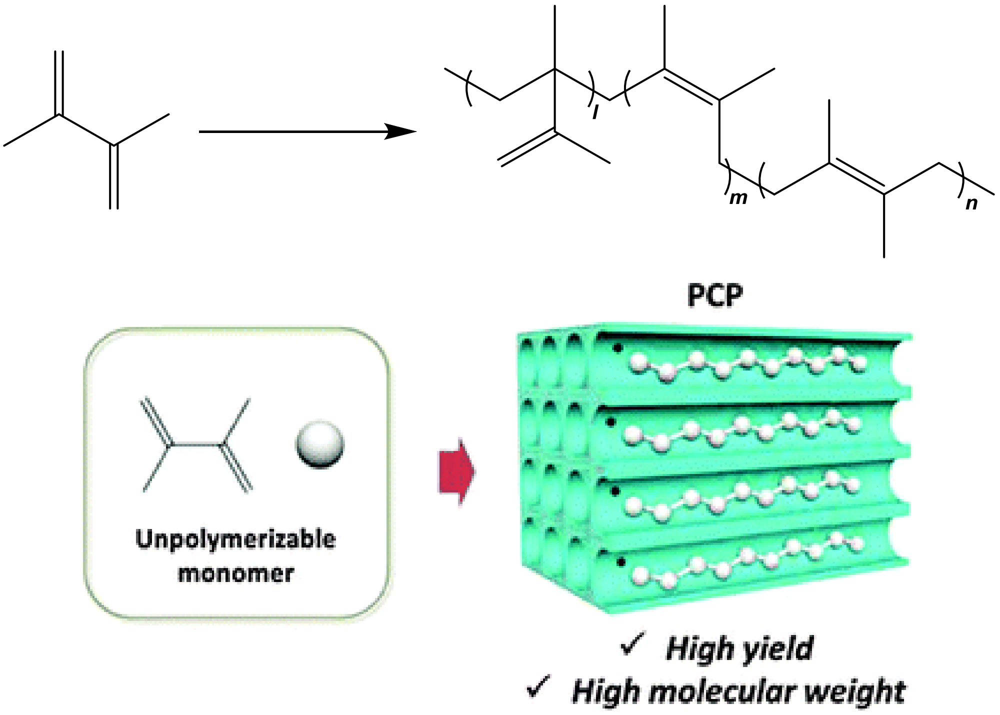

Figure 1.24. Top: *Potential polymerisation products of dimethylbutadiene (DMB), giving polymers with different microstructures (branching), denoted by regions* ***l***, ***m*** *and* ***n***. ***Bottom:*** *Schematic representation of the polymerisation of DMB within one-dimensional channels of a MOF. Figure reproduced from reference 155.*

1.4 Non-porous coordination polymers and molecular crystals: solvent effects and latent porosity

In the context of the results introduced in sections 1.3.1 (crystal engineering aspects of MOFs) and 1.3.2 (gas sorption and selectivity in MOFs), related work with non-porous coordination polymers (and in cases, molecular materials) is introduced briefly here.

1.4.1 Crystal engineering – solvent effects

Crystal engineering of non-porous materials relates closely to the work described by chapter 2. Previous crystal engineering work by the Brammer group has focussed on halogen bonding in molecular crystals[156–161] and coordination polymers of silver.[72–76]

The importance of the effect of crystallisation solvent on the packing of molecules in the solid state is shown to have a dramatic effect on competitive co-crystallisation.[162] Work by the Metrangolo and Resnati groups on a ternary competitive co-crystallisation system (a hydrogen bond donor, a halogen bond donor and a hydrogen/halogen bond acceptor) demonstrated that halogen-bonded co-crystal formation could be supported by the use of a relatively polar crystallisation solvent, keeping the third component (the hydrogen bond donor) in solution (see Figure 1.25).

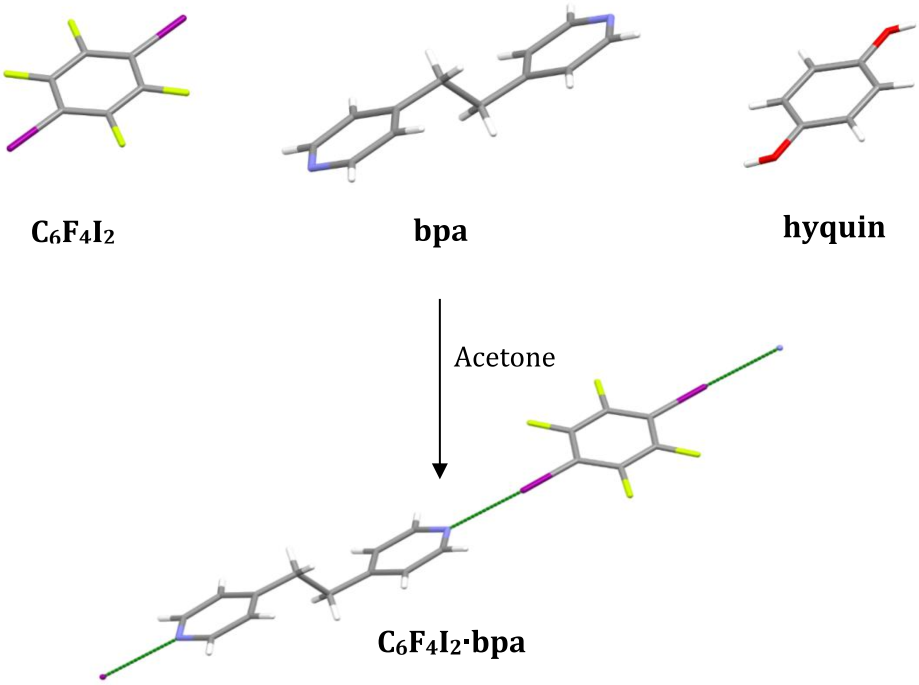

Figure 1.25. *Competitive crystallisation of a halogen-bonded co-crystal* ***$C_6F_4I_2$·bpa*** *from a ternary mixture of 4,4'-bispyridyl-1,2-ethane (bpa), para-diiodoperfluorobenzene ($C_6F_4I_2$) and hydroquinone (hyquin), in acetone.*[162]

The effect of solvent on the self-assembly of coordination polymers (previously noted in the literature in review by Li and Du)[105] has also been highlighted through the Brammer group's work with silver coordination polymers. The choice of arene solvent in the synthesis of a family of non-porous coordination polymers was shown to affect the architecture (1D or 2D) of the resultant coordination polymers, which are polymorphic (see Figure 1.26).[76]

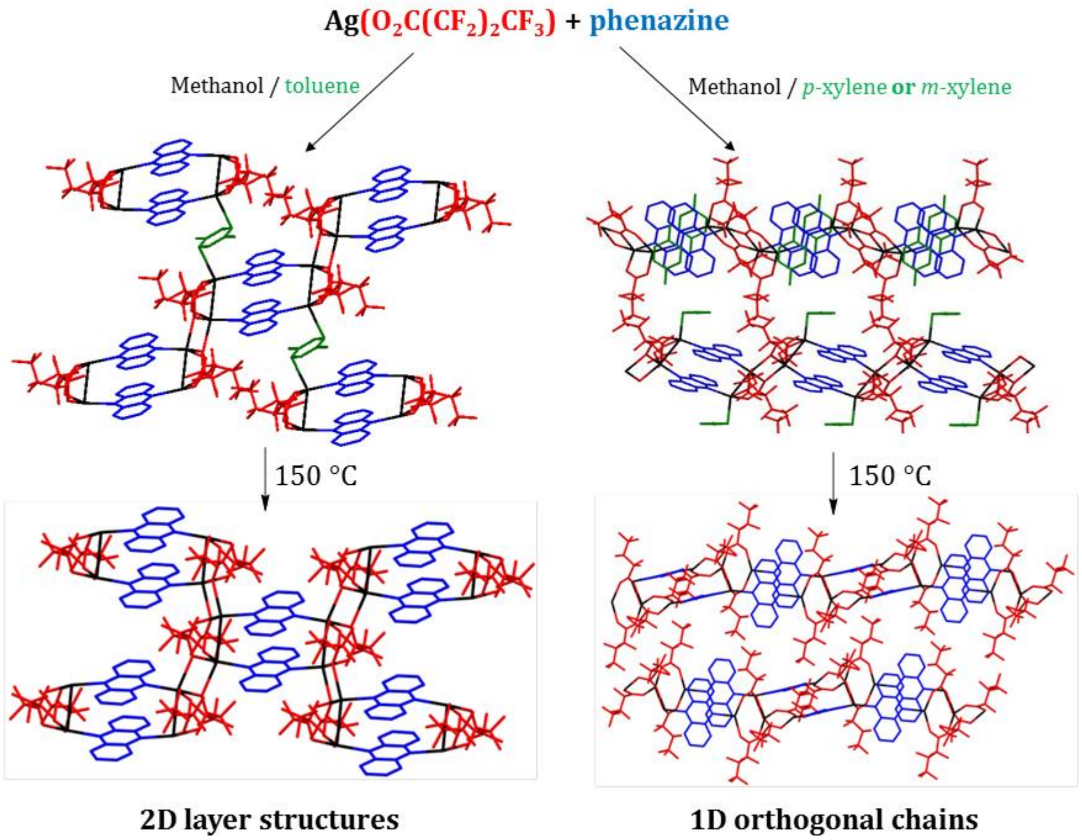

Figure 1.26. *Different coordination polymer architectures afforded by coordinating arene solvent in two related silver coordination polymers. The pre-arrangement of the coordination polymers into 2D sheets or 1D orthogonal chains is preserved after removal of the solvent thermally.*[76]

Moreover, this pre-arrangement of the coordination polymer chains by the crystallisation solvent was shown to affect the product of heating the coordination polymers, resulting in solvent loss. The resultant coordination polymers upon heating were of the same topology as their precursors (e.g. 2D coordination polymers gave 2D coordination polymers upon heating, 1D coordination polymers gave 1D coordination polymers upon heating). This was despite the considerable amount of structural rearrangement of the coordination node involved in the solvent loss.

The role of crystallisation solvent on the arrangement of molecules in the solid state, in particular its presence as a solvate within the crystal, is explored and discussed in chapter 2.

1.4.2 Gas sorption in coordination polymers

The potential for uptake of gas in inherently non-porous materials relates closely to work described in chapter 3.

The uptake of CO_2 into fluorous host compounds has not only been observed in MOFs, but also in non-porous coordination polymers. Work in the Kitagawa group used a fluoroalkyl-functionalised ligand (similar to the strategy described for MOF NU1000 in section 1.3.2) to create an inherently non-porous coordination polymer which possessed densely-packed regions of fluoroalkyl chains between coordination polymer layers (see Figure 1.27).[163]

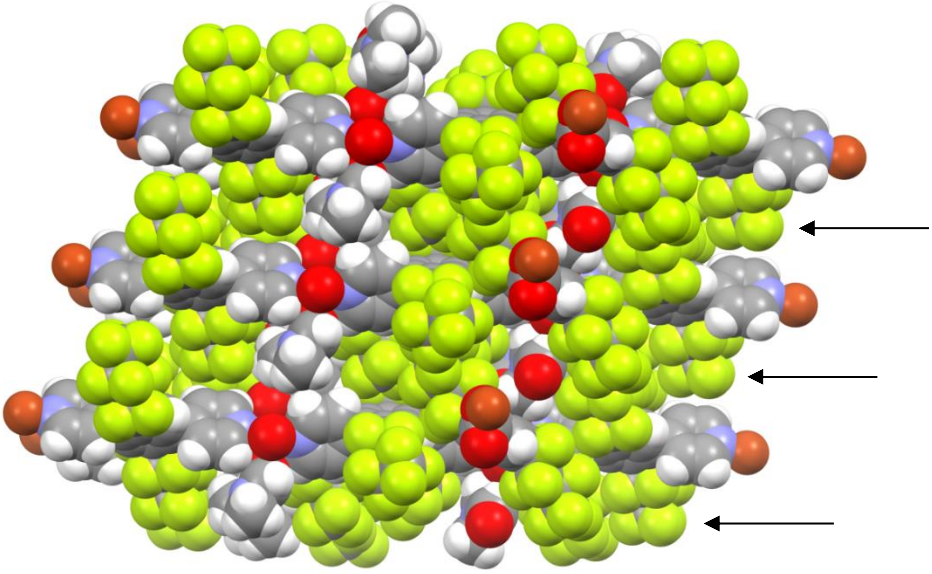

Figure 1.27. *Layers of fluoroalkyl chains between 2D coordination polymers in an inherently non-porous material, described by Kitagawa and co-workers. Fluorous layers created by perfluoroalkyl chains are highlighted with arrows.*[163]

Despite not appearing to be porous, this material was found to take up CO_2. This uptake was also shown to be selective, as for the modified NU1000 MOF shown in section 1.3.2. It appears that conformational rearrangement of the fluoroalkyl chains accommodates CO_2 selectively, but does not permit the entry of CO, O_2 or N_2. Work on the fluorinated non-porous coordination polymers of silver (I) in the Brammer group has also demonstrated the selective uptake of CO_2, potentially within the highly fluorinated domains between coordination polymers, as shown in the example in Figure 1.27.[75]

1.5 References

1 R. Pepinski, *Phys. Rev.*, 1955, **100**, 971.

2 A. R. von Hippel, *Science*, 1962, **138**, 91–108.

3 I. R. Thomas, I. J. Bruno, J. C. Cole, C. F. MacRae, E. Pidcock and P. A. Wood, *J. Appl. Crystallogr.*, 2010, **43**, 362–366.

4 O. Almarsson and M. J. Zaworotko, *Chem. Commun.*, 2004, 1889–1896.

5 N. Blagden, M. de Matas, P. T. Gavan and P. York, *Adv. Drug Deliv. Rev.*, 2007, **59**, 617–630.

6 N. Schultheiss and A. Newman, *Cryst. Growth Des.*, 2009, **9**, 2950–2967.

7 R. Tannenbaum, *Chem. Mater.*, 1994, **6**, 550–555.

8 B. Gomez-Lor, E. Gutierrez-Puebla, M. Iglesias, M. A. Monge, C. Ruiz-Valero and N. Snejko, *Inorg. Chem.*, 2002, **41**, 2429–2432.

9 A. Hu, H. L. Ngo and W. Lin, *Angew. Chem. Int. Ed. Engl.*, 2003, **42**, 6000–6003.

10 W. Xuan, C. Ye, M. Zhang, Z. Chen and Y. Cui, *Chem. Sci.*, 2013, **4**, 3154–3159.

11 D. T. Genna, A. G. Wong-Foy, A. J. Matzger and M. S. Sanford, *J. Am. Chem. Soc.*, 2013, **135**, 10586–10589.

12 Q.-L. Zhu, J. Li and Q. Xu, *J. Am. Chem. Soc.*, 2013, **135**, 10210–10213.

13 Z. Zhang, Y. R. Ji, L. Wojtas, W.-Y. Gao, S. Ma, M. J. Zaworotko and J. C. Antilla, *Chem. Commun.*, 2013, **49**, 7693–7695.

14 L. Li, R. Matsuda, I. Tanaka, H. Sato, P. Kanoo, H. J. Jeon, M. L. Foo, A. Wakamiya, Y. Murata and S. Kitagawa, *J. Am. Chem. Soc.*, 2014, **136**, 7543–7546.

15 S. Wang, W. Yao, J. Lin, Z. Ding and X. Wang, *Angew. Chem. Int. Ed. Engl.*, 2014, **53**, 1034–1038.

16 L. Li, S. Zhang, L. Xu, J. Wang, L.-X. Shi, Z.-N. Chen, M. Hong and J. Luo, *Chem. Sci.*, 2014, **5**, 3808–3813.

17 D. Yang, S. O. Odoh, T. C. Wang, O. K. Farha, J. T. Hupp, C. J. Cramer, L. Gagliardi and B. C. Gates, *J. Am. Chem. Soc.*, 2015, **137**, 7391–7396.

18 X. Yu and S. M. Cohen, *Chem. Commun.*, 2015, **51**, 9880–9883.

19 H. Li, M. Eddaoudi, M. O'Keefe and O. M. Yaghi, *Nature*, 1999, **402**, 276–279.

20 A. R. Millward and O. M. Yaghi, *J. Am. Chem. Soc.*, 2005, **127**, 17998–17999.

21 D. M. D'Alessandro, B. Smit and J. R. Long, *Angew. Chem. Int. Ed. Engl.*, 2010, **49**, 6058–6082.

22 H. Furukawa, N. Ko, Y. B. Go, N. Aratani, S. B. Choi, E. Choi, A. O. Yazaydin, R. Q. Snurr, M. O'Keeffe, J. Kim and O. M. Yaghi, *Science*, 2010, **329**, 424–428.

23 X. Rao, J. Cai, J. Yu, Y. He, C. Wu, W. Zhou, T. Yildirim, B. Chen and G. Qian, *Chem. Commun.*, 2013, **49**, 6719–6721.

24 F. Gándara, H. Furukawa, S. Lee and O. M. Yaghi, *J. Am. Chem. Soc.*, 2014, **136**, 5271–5274.

25 S. A. Basnayake, J. Su, X. Zou and K. J. Balkus, *Inorg. Chem.*, 2015, **54**, 1816–1821.

26 A. M. Pivovar, K. T. Holman and M. D. Ward, *Chem. Mater.*, 2001, **13**, 3018–3031.

27 F. Vermoortele, M. Maes, P. Z. Moghadam, M. J. Lennox, F. Ragon, M. Boulhout, S. Biswas, K. G. M. Laurier, I. Beurroies, R. Denoyel, M. Roeffaers, N. Stock, T. Düren, C. Serre and D. E. De Vos, *J. Am. Chem. Soc.*, 2011, **133**, 18526–18529.

28 S. D. Burd, S. Ma, J. A. Perman, B. J. Sikora, R. Q. Snurr, P. K. Thallapally, J. Tian, L. Wojtas and M. J. Zaworotko, *J. Am. Chem. Soc.*, 2012, **134**, 3663–3666.

29 H. Wang, K. Yao, Z. Zhang, J. Jagiello, Q. Gong, Y. Han and J. Li, *Chem. Sci.*, 2014, **5**, 620–624.

30 L. R. Nassimbeni, N. B. Báthori, L. D. Patel, H. Su and E. Weber, *Chem. Commun.*, 2015, **51**, 3627–3629.

31 X. Chen, A. M. Plonka, D. Banerjee, R. Krishna, H. T. Schaef, S. Ghose, P. K. Thallapally and J. B. Parise, *J. Am. Chem. Soc.*, 2015, **137**, 7007–7010.

32 O. R. Evans and W. Lin, *Acc. Chem. Res.*, 2002, **35**, 511–522.

33 J.-M. Zhou, W. Shi, N. Xu and P. Cheng, *Inorg. Chem.*, 2013, **52**, 8082–8090.

34 K. Sokołowski, W. Bury, I. Justyniak, D. Fairen-Jimenez, K. Sołtys, D. Prochowicz, S. Yang, M. Schröder and J. Lewiński, *Angew. Chem. Int. Ed. Engl.*, 2013, **52**, 13414–13418.

35 C. Wang, D. Liu, Z. Xie and W. Lin, *Inorg. Chem.*, 2014, **53**, 1331–1338.

36 C. Wang, O. Volotskova, K. Lu, M. Ahmad, C. Sun, L. Xing and W. Lin, *J. Am. Chem. Soc.*, 2014, **136**, 6171–6174.

37 S. Goswami, A. Adhikary, H. S. Jena, S. Biswas and S. Konar, *Inorg. Chem.*, 2013, **52**, 12064–12069.

38 L. D. Earl, B. O. Patrick and M. O. Wolf, *Inorg. Chem.*, 2013, **52**, 10021–10030.

39 J. J. Baldoví, E. Coronado, A. Gaita-Ariño, C. Gamer, M. Giménez-Marqués and G. Mínguez Espallargas, *Chem. Eur. J.*, 2014, **20**, 10695–10702.

40 D. Di Sante, A. Stroppa, P. Jain and S. Picozzi, *J. Am. Chem. Soc.*, 2013, **135**, 18126–18130.

41 B. Moulton and M. J. Zaworotko, *Chem. Rev.*, 2001, **101**, 1629–1658.

42 J. Bauer, S. Spanton, R. Henry, J. Quick, W. Dziki, W. Porter and J. Morris, *Pharm. Res.*, 2001, **18**, 859–866.

43 J.-P. Zhang, X.-C. Huang and X.-M. Chen, *Chem. Soc. Rev.*, 2009, **38**, 2385–2396.

44 D.-K. Bučar, R. W. Lancaster and J. Bernstein, *Angew. Chem. Int. Ed. Engl.*, 2015, **54**, 6972–6993.

45 J. M. Lehn, *Angew. Chem. Int. Ed. Engl.*, 1988, **27**, 90–110.

46 J. Yang, J.-L. Marendaz, S. J. Geib and A. D. Hamilton, *Tetrahedron Lett.*, 1994, **35**, 3665–3668.

47 R. M. Bhardwaj, A. Johnston, B. F. Johnston and A. J. Florence, *CrystEngComm*, 2015, **17**, 4272–4275.

48 M. W. Hosseini and A. De Cian, *Chem. Commun.*, 1998, 727–733.

49 J. L. Atwood, L. J. Barbour and A. Jerga, *Science*, 2002, **296**, 2367–2369.

50 G. R. Desiraju, *Angew. Chem. Int. Ed. Engl.*, 1995, **34**, 2311–2327.

51 T. Steiner, *Angew. Chem. Int. Ed. Engl.*, 2002, **41**, 48–76.

52 J. Kim, S.-O. Lee, J. Yi, W.-S. Kim and M. D. Ward, *Sep. Purif. Technol.*, 2008, **62**, 517–522.

53 J. Tian, J. Liu, J. Liu and P. K. Thallapally, *CrystEngComm*, 2013, **15**, 1528.

54 C. A. Hunter and J. K. M. Sanders, *J. Am. Chem. Soc.*, 1990, **112**, 5525–5534.

55 C. Janiak, *Dalt. Trans.*, 2000, 3885–3896.

56 S. Beg, K. Waggoner, Y. Ahmad, M. Watt and M. Lewis, *Chem. Phys. Lett.*, 2008, **455**, 98–102.

57 S.-Q. Liu, T. Kuroda-Sowa, H. Konaka, Y. Suenaga, M. Maekawa, T. Mizutani, G.-L. Ning and M. Munakata, *Inorg. Chem.*, 2005, **44**, 1031–1036.

58 L. Brammer, E. A. Bruton and P. Sherwood, *Cryst. Growth Des.*, 2001, **1**, 277–290.

59 P. Metrangolo, H. Neukirch, T. Pilati and G. Resnati, *Acc. Chem. Res.*, 2005, **38**, 386–395.

60 M. R. Scholfield, C. M. Vander Zanden, M. Carter and P. S. Ho, *Protein Sci.*, 2013, **22**, 139–152.

61 G. R. Desiraju and R. Parthasarathy, *J. Am. Chem. Soc.*, 1989, **111**, 8725–8726.

62 P. Metrangolo and G. Resnati, *IUCrJ*, 2014, 5–7.

63 L. C. Gilday, S. W. Robinson, T. A. Barendt, M. J. Langton, B. R. Mullaney and P. D. Beer, *Chem. Rev.*, 2015, **115**, 7118–7195.

64 P. Metrangolo and G. Resnati, *Chem. Eur. J.*, 2001, **7**, 2511–2519.

65 T. Clark, M. Hennemann, J. S. Murray and P. Politzer, *J. Mol. Model.*, 2007, **13**, 291–296.

66 B. Ji, W. Wang, D. Deng and Y. Zhang, *Cryst. Growth Des.*, 2011, **11**, 3622–3628.

67 C. C. Robertson, R. N. Perutz, L. Brammer and C. A. Hunter, *Chem. Sci.*, 2014, **5**, 4179–4183.

68 M. J. Langton, S. W. Robinson, I. Marques, V. Felix and P. D. Beer, *Nature Chem.*, 2014, **6**, 1039–1043.

69 K. Sumida, M. R. Hill, S. Horike, A. Dailly and J. R. Long, *J. Am. Chem. Soc.*, 2009, **131**, 15120–15121.

70 K. Sumida, C. M. Brown, Z. R. Herm, S. Chavan, S. Bordiga and J. R. Long, *Chem. Commun.*, 2011, **47**, 1157–1159.

71 K. G. S. Ranmohotti, E. Josepha, J. Choi, J. Zhang and J. B. Wiley, *Adv. Mater.*, 2011, **23**, 442–460.

72 L. Brammer, M. Burgard and C. Rodger, *Chem. Commun.*, 2001, 2468–2469.

73 L. Brammer, M. Burgard, M. D. Eddleston, C. S. Rodger, N. P. Rath and H. Adams, *CrystEngComm*, 2002, **4**, 239–248.

74 S. Libri, M. Mahler, G. Mínguez Espallargas, D. C. N. G. Singh, J. Soleimannejad, H. Adams, M. Burgard, N. P. Rath, M. Brunelli and L. Brammer, *Angew. Chem. Int. Ed. Engl.*, 2008, **120**, 1717–1721.

75 I. J. Vitórica-Yrezábal, G. Mínguez Espallargas, J. Soleimannejad, A. J. Florence, A. J. Fletcher and L. Brammer, *Chem. Sci.*, 2013, **4**, 696–708.

76 J. S. Wright, I. J. Vitórica-Yrezábal, H. Adams, S. P. Thompson, A. H. Hill and L. Brammer, *IUCrJ*, 2015, **2**, 188–197.

77 C. V. Hettiarachchi, M. A. Rawashdeh-Omary, D. Korir, J. Kohistani, M. Yousufuddin and H. V. R. Dias, *Inorg. Chem.*, 2013, **52**, 13576–13583.

78 C. Janiak, *Dalt. Trans.*, 2003, 2781–2804.

79 L. Brammer, *Chem. Soc. Rev.*, 2004, **33**, 476–489.

80 D. Braga, L. Brammer and N. R. Champness, *CrystEngComm*, 2005, **7**, 1–19.

81 M. D. Allendorf and V. Stavila, *CrystEngComm*, 2015, **17**, 229–246.

82 S. R. Batten, N. R. Champness, X.-M. Chen, J. Garcia-Martinez, S. Kitagawa, L. Ohrstrom, M. O'Keefe, M. Paik Si and J. Reedijk, *CrystEngComm*, 2012, **14**, 3001–3004.

83 R. Banerjee, H. Furukawa, D. Britt, C. Knobler, M. O'Keeffe and O. M. Yaghi, *J. Am. Chem. Soc.*, 2009, **131**, 3875–3877.

84 T. D. Bennett, A. L. Goodwin, M. T. Dove, D. A. Keen, M. G. Tucker, E. R. Barney, A. K. Soper, E. G. Bithell, J.-C. Tan and A. K. Cheetham, *Phys. Rev. Lett.*, 2010, **104**, 115503.

85 T. D. Bennett, P. Simoncic, S. A. Moggach, F. Gozzo, P. Macchi, D. A. Keen, J.-C. Tan and A. K. Cheetham, *Chem. Commun.*, 2011, **47**, 7983–7985.

86 T. D. Bennett and A. K. Cheetham, *Acc. Chem. Res.*, 2014, **47**, 1555–1562.

87 E. F. Baxter, T. D. Bennett, C. Mellot-Draznieks, C. Gervais, F. Blanc and A. K. Cheetham, *Phys. Chem. Chem. Phys.*, 2015, **17**, 25191–25196.

88 M. T. Wharmby, S. Henke, T. D. Bennett, S. R. Bajpe, I. Schwedler, S. P. Thompson, F. Gozzo, P. Simoncic, C. Mellot-Draznieks, H. Tao, Y. Yue and A. K. Cheetham, *Angew. Chem. Int. Ed. Engl.*, 2015, **54**, 6447–6451.

89 A. Nagai, Z. Guo, X. Feng, S. Jin, X. Chen, X. Ding and D. Jiang, *Nature Commun.*, 2011, **2**, 536–538.

90 H. Ma, H. Ren, S. Meng, Z. Yan, H. Zhao, F. Sun and G. Zhu, *Chem. Commun.*, 2013, **49**, 9773–9775.

91 H. Ren, T. Ben, F. Sun, M. Guo, X. Jing, H. Ma and K. Cai, *J. Mat. Chem.*, 2011, **21**, 10348–10353.

92 Y. Zhang, B. Li, K. Williams, W. Gao and S. Ma, *Chem. Commun.*, 2013, **49**, 10269–10274.

93 Y.-B. Zhang, J. Su, H. Furukawa, Y. Yun, F. Gándara, A. Duong, X. Zou and O. M. Yaghi, *J. Am. Chem. Soc.*, 2013, **135**, 16336–16339.

94 X.-Z. Luo, X.-J. Jia, J.-H. Deng, J.-L. Zhong, H.-J. Liu, K.-J. Wang and D.-C. Zhong, *J. Am. Chem. Soc.*, 2013, **135**, 11684–11687.

95 J. Liu, P. K. Thallapally, B. P. McGrail, D. R. Brown and J. Liu, *Chem. Soc. Rev.*, 2012, **41**, 2308–2322.

96 J. A. Mason, M. Veenstra and J. R. Long, *Chem. Sci.*, 2014, **5**, 32.

97 A. Das and D. M. D'Alessandro, *CrystEngComm*, 2015, **17**, 706–718.

98 A. H. Chughtai, N. Ahmad, H. A. Younus, A. Laypkov and F. Verpoort, *Chem. Soc. Rev.*, 2015, **44**, 6804–6849.

99 M. D. Allendorf, C. A. Bauer, R. K. Bhakta and R. J. T. Houk, *Chem. Soc. Rev.*, 2009, **38**, 1330–1352.

100 Y. Cui, Y. Yue, G. Qian and B. Chen, *Chem. Rev.*, 2012, **112**, 1126–1162.

101 L. E. Kreno, K. Leong, O. K. Farha, M. Allendorf, R. P. Van Duyne and J. T. Hupp, *Chem. Rev.*, 2012, **112**, 1105–1125.

102 S. Horike, S. Shimomura and S. Kitagawa, *Nature Chem.*, 2009, **1**, 695–704.

103 L. Sarkisov, R. L. Martin, M. Haranczyk and B. Smit, *J. Am. Chem. Soc.*, 2014, **136**, 2228–2231.

104 A. Schneemann, V. Bon, I. Schwedler, I. Senkovska, S. Kaskel and R. A. Fischer, *Chem. Soc. Rev.*, 2014, **43**, 6062–6096.

105 C.-P. Li and M. Du, *Chem. Commun.*, 2011, **47**, 5958–5972.

106 A. Pichon, A. Lazuen-Garay and S. L. James, *CrystEngComm*, 2006, **8**, 211–214.

107 W. Yuan, A. Lazuen-Garay, A. Pichon, R. Clowes, C. D. Wood, A. I. Cooper and S. L. James, *CrystEngComm*, 2010, **12**, 4063–4065.

108 D. Crawford, J. Casaban, R. Haydon, N. Giri, T. McNally and S. L. James, *Chem. Sci.*, 2015, **6**, 1645–1649.

109 R. Rattanakam, *Rational design, synthesis and characterisation of coordination networks based on carboxylate ligands (PhD Thesis, University of Sheffield)*, 2014.

110 P. Smart, C. A. Mason, J. R. Loader, A. J. H. M. Meijer, A. J. Florence, K. Shankland, A. J. Fletcher, S. P. Thompson, M. Brunelli, A. H. Hill and L. Brammer, *Chem. Eur. J.*, 2013, **19**, 3552–3557.

111 R. Medishetty, R. Tandiana, J. Wu, Z. Bai, Y. Du and J. J. Vittal, *Chem. Eur. J.*, 2015, **21**, 11948–11953.

112 S. Kitagawa and K. Uemura, *Chem. Soc. Rev.*, 2005, **34**, 109–119.

113 K. Uemura, R. Matsuda and S. Kitagawa, *J. Solid State Chem.*, 2005, **178**, 2420–2429.

114 S. Kitagawa and M. Kondo, *Bull. Chem. Soc. Jpn.*, 1998, **71**, 1739–1753.

115 C. Serre, F. Millange, C. Thouvenot, M. Noguès, G. Marsolier, D. Louër and G. Férey, *J. Am. Chem. Soc.*, 2002, **124**, 13519–13526.

116 D. J. Tranchemontagne, J. R. Hunt and O. M. Yaghi, *Tetrahedron*, 2008, **64**, 8553–8557.

117 L. Chen, J. P. S. Mowat, D. Fairen-Jimenez, C. A. Morrison, S. P. Thompson, P. A. Wright and T. Düren, *J. Am. Chem. Soc.*, 2013, **135**, 15763–15773.

118 Z. Wang and S. M. Cohen, *Chem. Soc. Rev.*, 2009, **38**, 1315–1329.

119 S. M. Cohen, *Chem. Sci.*, 2010, **1**, 32–36.

120 Z. Wang and S. M. Cohen, *Chem. Soc. Rev.*, 2009, **38**, 1315–1329.

121 M. J. Ingleson, J. P. Barrio, J.-B. Guilbaud, Y. Z. Khimyak and M. J. Rosseinsky, *Chem. Commun.*, 2008, 2680–2682.

122 S. C. Jones and C. A. Bauer, *J. Am. Chem. Soc.*, 2009, **131**, 12516–12517.

123 J.-P. Zhang and X.-M. Chen, *J. Am. Chem. Soc.*, 2009, **131**, 5516–5521.

124 J.-B. Lin, J.-P. Zhang and X.-M. Chen, *J. Am. Chem. Soc.*, 2010, **132**, 6654–6656.

125 B. Yuan, D. Ma, X. Wang, Z. Li, Y. Li, H. Liu and D. He, *Chem. Commun.*, 2012, **48**, 1135–1137.

126 T. Li, J. E. Sullivan and N. L. Rosi, *J. Am. Chem. Soc.*, 2013, **135**, 9984.

127 W. M. Bloch, R. Babarao, M. R. Hill, C. J. Doonan and C. J. Sumby, *J. Am. Chem. Soc.*, 2013, **135**, 10441.

128 E. Coronado, M. Giménez-Marqués, G. M. Espallargas, F. Rey and I. J. Vitórica-Yrezábal, *J. Am. Chem. Soc.*, 2013, **135**, 15986.

129 W.-Y. Gao, Z. Zhang, L. Cash, L. Wojitas, Y.-S. Chen and S. Ma, *CrystEngComm*, 2013, **15**, 9320–9323.

130 M. Wriedt, J. P. Sculley, W. M. Verdegaal, A. A. Yakovenkob and H.-C. Zhou, *Chem. Commun.*, 2013, **49**, 9612–9614.

131 M. Du, C. P. Li, M. Chen, Z. W. Ge, X. Wang, L. Wang and C. Sen Liu, *J. Am. Chem. Soc.*, 2014, **136**, 10906–10909.

132 P. Deria, S. Li, H. Zhang, R. Q. Snurr, J. T. Hupp and O. K. Farha, *Chem. Commun.*, 2015, **51**, 12478–12481.

133 A. Demessence, D. M. D'Alessandro, M. L. Foo and J. R. Long, *J. Am. Chem. Soc.*, 2009, **131**, 8784–8786.

134 P. Smart, *Design and synthesis of metal-organic frameworks and their characterisation by single crystal and powder diffraction (PhD Thesis, University of Sheffield)*, 2012.

135 P. Deria, J. E. Mondloch, E. Tylianakis, P. Ghosh, W. Bury, R. Q. Snurr, J. T. Hupp and O. K. Farha, *J. Am. Chem. Soc.*, 2013, **135**, 16801–16804.

136 S. Galli, N. Masciocchi, V. Colombo, A. Maspero, G. Palmisano, F. J. López-Garzón, M. Domingo-García, I. Fernández-Morales, E. Barea and J. A. R. Navarro, *Chem. Mater.*, 2010, **22**, 1664–1672.

137 C. Montoro, F. Linares, E. Quartapelle Procopio, I. Senkovska, S. Kaskel, S. Galli, N. Masciocchi, E. Barea and J. A. R. Navarro, *J. Am. Chem. Soc.*, 2011, **133**, 11888–11891.

138 N. M. Padial, E. Quartapelle Procopio, C. Montoro, E. López, J. E. Oltra, V. Colombo, A. Maspero, N. Masciocchi, S. Galli, I. Senkovska, S. Kaskel, E. Barea and J. A. R. Navarro, *Angew. Chem. Int. Ed. Engl.*, 2013, **52**, 8290–8294.

139 E. López-Maya, C. Montoro, L. M. Rodríguez-Albelo, S. D. Aznar Cervantes, A. A. Lozano-Pérez, J. L. Cenís, E. Barea and J. A. R. Navarro, *Angew. Chem. Int. Ed. Engl.*, 2015, **54**, 6790–6794.

140 W. Xuan, C. Ye, M. Zhang, Z. Chen and Y. Cui, *Chem. Sci.*, 2013, **4**, 3154–3159.

141 X. Zhang, L. Fan, W. Zhang, Y. Ding, W. Fan and X. Zhao, *Dalt. Trans.*, 2013, **42**, 16562–16568.

142 R.-B. Lin, F. Li, S.-Y. Liu, X.-L. Qi, J.-P. Zhang and X.-M. Chen, *Angew. Chem. Int. Ed. Engl.*, 2013, **52**, 13429–13433.

143 H. Jiang, D. Feng, K. Wang, Z. Gu, Z. Wei, Y. Chen and H. Zhou, *J. Am. Chem. Soc.*, 2013, **135**, 13934–13938.

144 N. B. Shustova, A. F. Cozzolino, S. Reineke, M. Baldo and M. Dincă, *J. Am. Chem. Soc.*, 2013, **135**, 13326–13329.

145 N. Wei, Y.-R. Zhang and Z.-B. Han, *CrystEngComm*, 2013, **15**, 8883–8886.

146 H. Li, X. Feng, Y. Guo, D. Chen, R. Li, X. Ren, X. Jiang, Y. Dong and B. Wang, *Sci. Rep.*, 2014, **4**, 4366.

147 L. Wang, Y. Li, F. Yang, Q. Liu, J.-P. Ma and Y. Dong, *Inorg. Chem.*, 2014, **53**, 9087–9094.

148 S. S. Nagarkar, A. V Desai and S. K. Ghosh, *Chem. Commun.*, 2014, **50**, 8915–8918.

149 D. Liu, K. Lu, C. Poon and W. Lin, *Inorg. Chem.*, 2014, **53**, 1916–1924.

150 E. X. Chen, H. Yang and J. Zhang, *Inorg. Chem.*, 2014, **53**, 5411–5413.

151 Y. Inokuma, S. Yoshioka, J. Ariyoshi, T. Arai, Y. Hitora, K. Takada, S. Matsunaga, K. Rissanen and M. Fujita, *Nature*, 2013, **495**, 461–466.

152 Y. Inokuma, S. Yoshioka, J. Ariyoshi, T. Arai and M. Fujita, *Nature Protoc.*, 2014, **9**, 246–252.

153 S. Yoshioka, Y. Inokuma, M. Hoshino, T. Sato and M. Fujita, *Chem. Sci.*, 2015, **6**, 3765–3768.

154 T. Ishiwata, Y. Furukawa, K. Sugikawa, K. Kokado and K. Sada, *J. Am. Chem. Soc.*, 2013, **135**, 5427–5432.

155 T. Uemura, R. Nakanishi, S. Mochizuki, Y. Murata and S. Kitagawa, *Chem. Commun.*, 2015, **51**, 9892–9895.

156 F. Zordan, G. M. Espallargas and L. Brammer, *CrystEngComm*, 2006, **8**, 425–431.

157 G. Mínguez Espallargas, L. Brammer and P. Sherwood, *Angew. Chem. Int. Ed. Engl.*, 2006, **45**, 435–440.

158 F. Zordan and L. Brammer, *Cryst. Growth Des.*, 2006, **6**, 1374–1379.

159 G. Mínguez Espallargas, L. Brammer, J. van de Streek, K. Shankland, A. J. Florence and H. Adams, *J. Am. Chem. Soc.*, 2006, **128**, 9584–9585.

160 L. Brammer, G. Mínguez Espallargas and S. Libri, *CrystEngComm*, 2008, **10**, 1712–1727.

161 G. Mínguez Espallargas, F. Zordan, L. Arroyo Marín, H. Adams, K. Shankland, J. van de Streek and L. Brammer, *Chemistry*, 2009, **15**, 7554–68.

162 E. Corradi, S. V. Meille, M. T. Messina, P. Metrangolo and G. Resnati, *Angew. Chem. Int. Ed. Engl.*, 2000, **39**, 1782–1786.

163 H. J. Jeon, R. Matsuda, P. Kanoo, H. Kajiro, L. Li, H. Sato, Y. Zheng and S. Kitagawa, *Chem. Commun.*, 2014, **50**, 10861–10863.

Stellated halogenated cluster compounds:

Crystal engineering through halogen bonds

Chapter Two

2.1 Introduction

2.1.1 Halogen bonding for crystal engineering purposes

Hydrogen bonding has been noted as a useful, directional interaction in crystal engineering several times, particularly by Gutaram Desiraju, as noted in chapter 1, section 1.1.1.1.[1–4] However, halogen bonds also are highly directional in nature, and indeed can possess strength and directional character comparable to hydrogen bonds.[5] The anisotropic distribution of electrostatic potential around larger halogen atoms enables them to behave as either electrophilic or nucleophilic intermolecular interaction sites. The region of positive electrostatic potential on larger halogens, parallel to the axis of their bond with another atom, may be referred to as the 'σ-hole'.

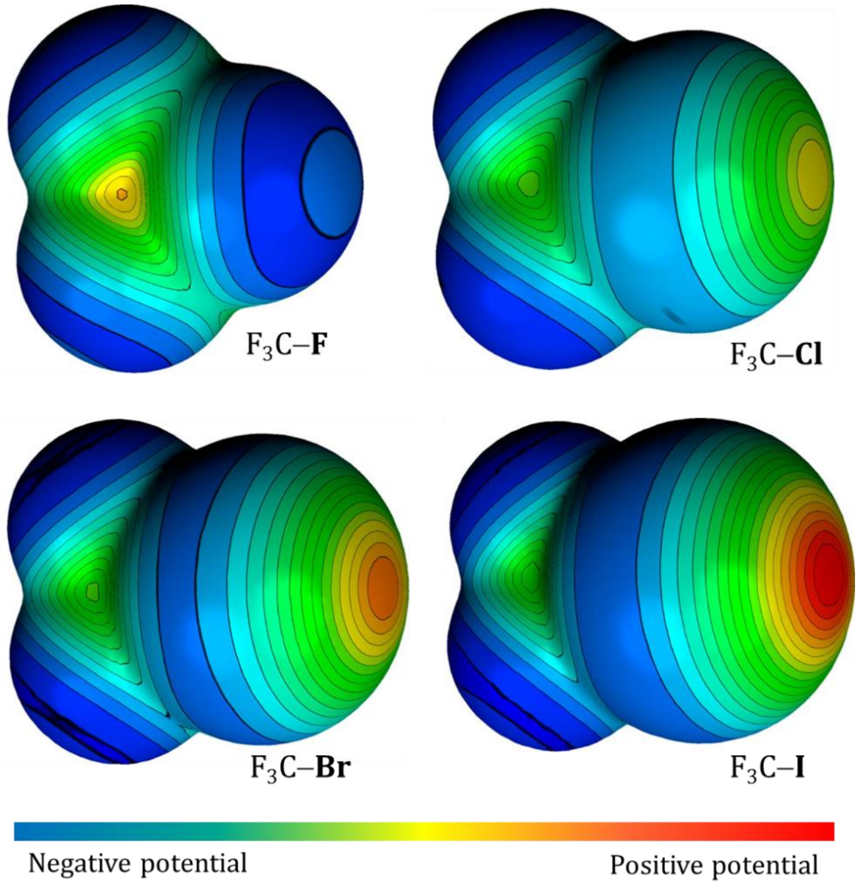

Figure 2.1. *The electrostatic potential computed, and plotted on the van der Waals surfaces for trifluorohalomethane with successive halogens (F, Cl, Br, I). This demonstrates the increasing size of the 'σ-hole' region of positive electron potential with increasing halogen size. Figure reproduced from reference 5.*

Indeed, halogen bonds have been successfully used to direct the packing of molecules in the solid state. Work by Metrangolo and Resnati has repeatedly demonstrated this, particularly in the self-assembly of novel co-crystal materials.[6–11] In particular, they have shown that halogen bonds form in a highly directional nature in the solid state, as with hydrogen bonds (see example shown in Figure 2.2). Specifically, the linear nature of halogen bonds formed where the halogen acts as an electrophilic species through the 'σ-hole' is useful in creating linear chains of halogen-bonded materials.

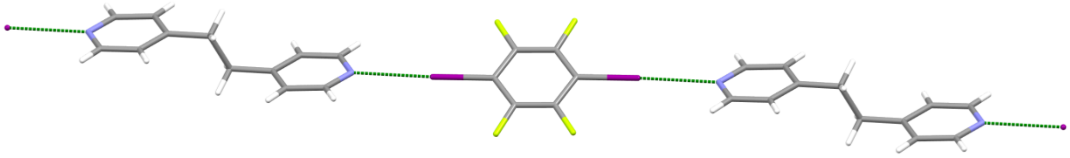

Figure 2.2. *Halogen-bonded co-crystal material [$C_6F_4I_2$][bpa], demonstrating the designed formation of 1D halogen-bonded chains in a crystalline material.*[6]

Work in the Brammer research group has also highlighted the important role of halogen bonding in supramolecular chemistry, including the ability of 'inorganic' halogens (those bound directly to a metal cation) to form strong intermolecular interactions in the solid state,[12] and in solution.[13]

Exploration of the halogen bond has expanded to its applications in host-guest chemistry, with impressive results both in the solid state, and solution phase. In the solid state Nassimbeni and co-workers have quantified the effect of tuneable halogen bonding on guest entrapment, and demonstrated that stronger halogen bonds create (understandably) more strongly binding hosts.[14] In the solution phase, Beer and co-workers demonstrate the superiority of halogen bonding over hydrogen bonding in the recognition of halide ions in solution.[15]

Halogen bonds are clearly an underexplored, but interesting area of supramolecular chemistry to explore, particularly in the solid state.

2.1.2 Halogen-bonded clusters in crystal engineering

Previous crystal engineering work in the Brammer group has looked at the halogen bonding in halobenzoate paddlewheel clusters, and the control that can be exerted over their solid state structures by changing the components involved in their self-assembly.[16–18] These discrete paddlewheel clusters contain four halogens, pointing away from the cluster either at the corners of a square (4-substituted benzoate) or at four vertices of a cuboid (3-substituted benzoate), as also shown in Figure 2.3.

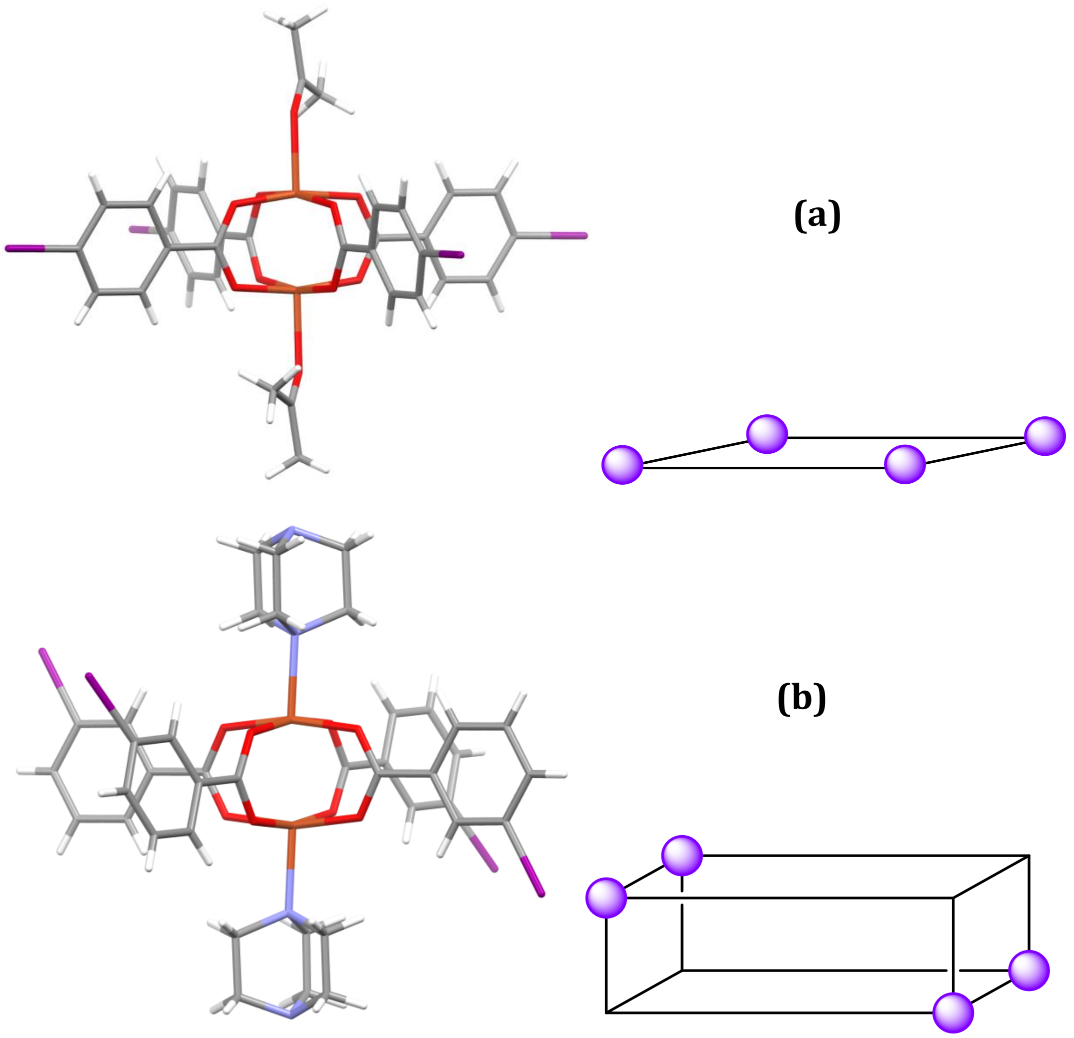

Figure 2.3. *Copper (II) paddlewheel halobenzoate clusters:* ***a)*** *based on 4-iodobenzoate, giving a cluster with halogens at all corners of a square;*[18] *and* ***b)*** *based on 3-iodobenzoate, giving a cluster with halogens at four vertices of a cuboid.*[16]

A commonly recurring motif in the study of the square-based 4-halobenzoate clusters was the C–X···π motif, in which pairs of clusters form dimers through such halogen bonds (shown in Figure 2.4). This was found to be a persistent motif in the formation of these clusters, creating 2D layers of clusters connected by halogen bonding.[18]

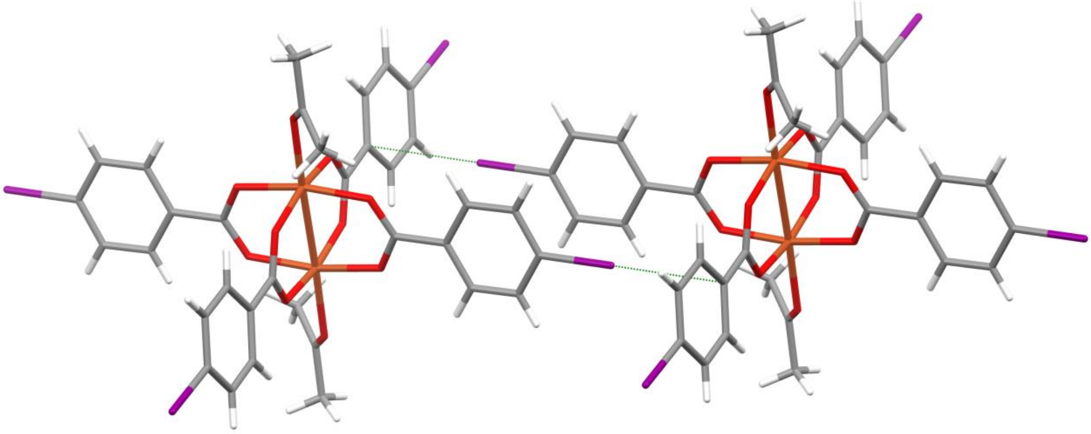

Figure 2.4. *Dimers of clusters in [Cu_2(4-iodobenzoate)$_4$(acetone)$_2$] connected by the C–X···π halogen bonding motif.*[18]

It was also demonstrated that, through adjusting the components in the self-assembly of halobenzoate-containing materials, the formation of either a coordination polymer or discrete, halogen-bonded clusters could be directed (see Figure 2.5).[16] When 3-halobenzoates were mixed with copper salts and a series of linker ligands, it was found that linkers of different lengths gave either discrete halogen-bonded clusters or one-dimensional coordination polymers. The linker ligands were linear, ditopic neutral ligands which occupied the axial sites at the carboxylate paddlewheel unit (where acetone is shown to be in Figure 2.4). Shorter linker ligands (i.e. DABCO, which is a good halogen-bond acceptor) gave discrete clusters, which were connected by N···I–C halogen bonds from the linker ligand to the halobenzoate (see Figure 2.5). Longer ligands did not form halogen bonds but instead gave linear 1D coordination polymers (see Figure 2.5).

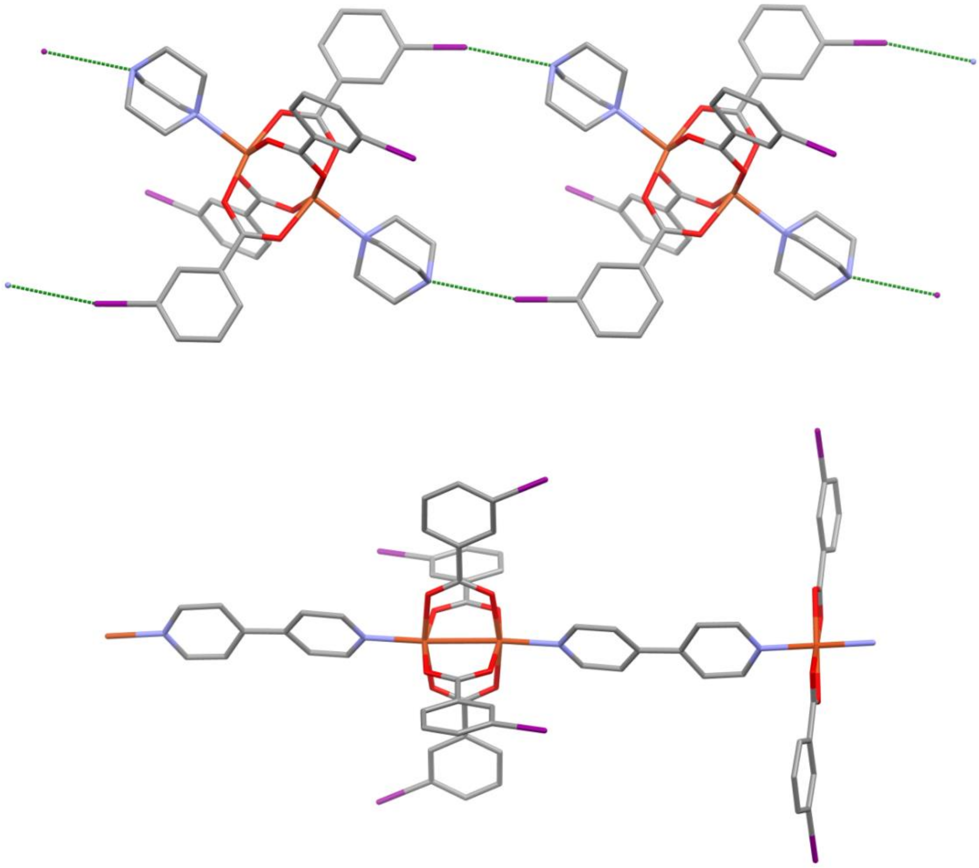

Figure 2.5. Top: *Discrete, halogen-bonded clusters of* $[Cu_2(3\text{-iodobenzoate})_4(DABCO)_2]$ *formed using DABCO in crystallisation.* ***Bottom:*** *1D coordination polymers of* $[Cu_3(3\text{-iodobenzoate})_6(bipy)]$ *formed using 4,4'-bipyridine in crystallisation, demonstrating control over the formation of different networks in the solid state.*[18]

A cluster with a greater number of interaction sties (more halogens on vertices, *cf.* the diagrams in Figure 2.3) may serve as an interesting point of comparison to the established clusters containing halobenzoates, in particular examining the persistence of the C–X···π motif in the presence of a greater number of halogen atoms (which may act as both electrophile and nucleophile).

Pyrazolate clusters based on palladium and platinum reported by Umakoshi and co-workers may provide such a point of comparison.[19] In the case of $[Pd_3(pz)_6]$ (see Figure 2.6), the authors show a cluster which contains six ligands, pointing away from the centre toward the vertices of an hourglass-like shape based on a trigonal prism. Another, based on a cube is $[Pt_2Ag_4(pz)_8]$ (see Figure 2.6), which has eight ligands, again each pointing away from the centre of the cluster in a symmetric manner, along the vertices of the cube.

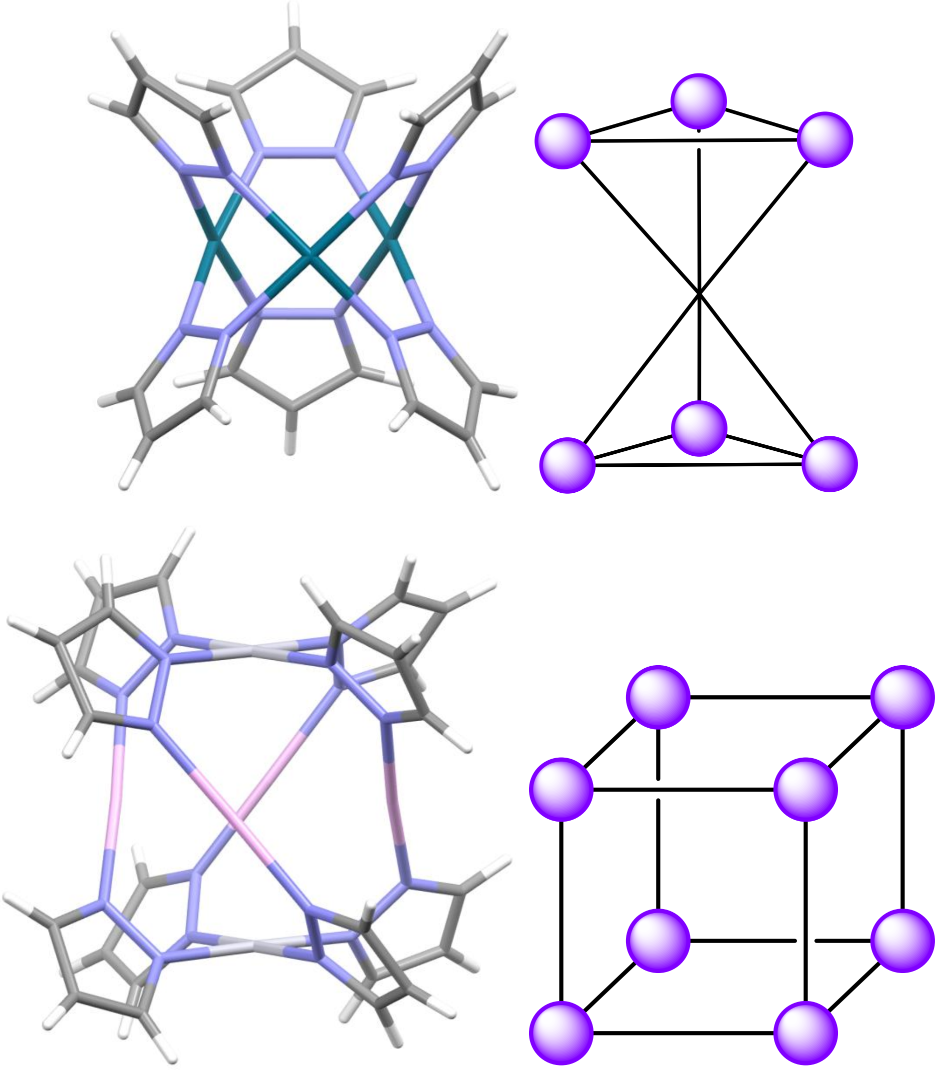

Figure 2.6. Top: *Trigonal prism cluster [$Pd_3(pz)_6$] and a schematic showing the terminal 4-substitution sites pointing towards the vertices of the cluster.* ***Bottom:*** *Cubic cluster [$Pt_2Ag_4(pz)_8$] and a schematic showing the terminal 4-substitution sites pointing to the vertices of that cube.*[19]

Analogous clusters to these, using 4-substituted pyrazoles (Cl, Br, I) would therefore be interesting to pursue, in the context of crystal engineering using halogen bonds. The halogen bonding motifs formed by these highly halogenated clusters (particularly the trigonal prismatic cluster) are (to the best of the author's knowledge) so far unexplored.

2.1.3 'Stellated clusters'

Clusters like the trigonal prismatic [$Pd_3(pz)_6$] with benzoates have also been described in the literature.[20,21] These clusters are based on the tris-chromium(III)-oxo building unit, which forms the basis of the MIL (Materials Institute Lavoisier) series of MOFs.[22–24] These clusters also feature six ligands, where the 4-substituent points toward a vertex of the trigonal prism created (see Figure 2.7).

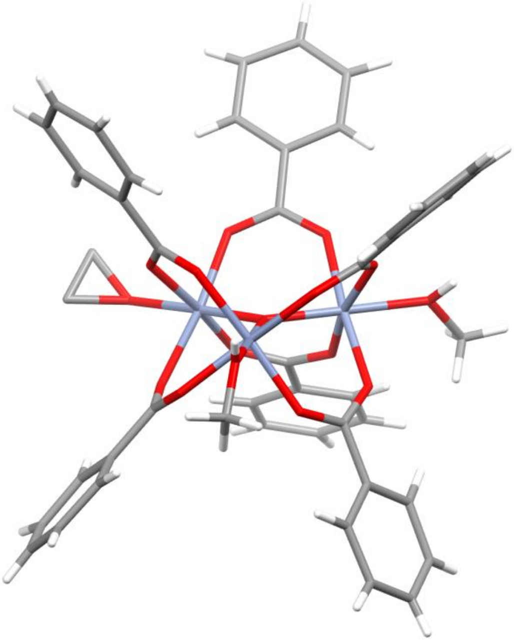

Figure 2.7. *The [$Cr_3(\mu_3\text{-}O)(benzoate)_6(MeOH)_3$] cluster (nitrate counter-ion and non-coordinated solvent from crystal structure are not shown for clarity) previously studied in the literature.*[20,21]

This type of cluster, along with the [$Pd_3(pz)_6$] cluster represent a particularly interesting avenue of study in crystal engineering due to their 'stellated' (star-like) nature. This star-like shape makes the individual molecules difficult to pack in the solid state, and as such the solvent in the crystal structures of the clusters is shown to be important in their packing, for example through hydrogen bonding with the cluster. The effect of solvent on the packing of these clusters in the solid state is therefore also of interest in these cases, as has been highlighted in the context of self-assembly.[25]

2.1.4 Chapter aims

The work described by this chapter aimed to apply halogen bonding (and hydrogen bonding) to a designed approach to materials in the solid state, using the clusters shown in Figure 2.6. A family of such materials were to be synthesised and their novel intermolecular interactions explored, as well to extent to which control over their packing in the solid state could be achieved. This was to be pursued through both changing the halogen substituent on the cluster and crystallising the trigonal prismatic cluster $[Pd_3(pz)_6]$ from a series of related solvents, to determine their effect on the packing.

2.2 Experimental

2.2.1 Crystal syntheses

All reactants were purchased from Fluorochem, Aldrich or Fisher Scientific and used as received without further purification. Containers of palladium and platinum salts (which are hygroscopic) were flushed with argon after each use and stored in a desiccator between uses. Silver salts and all experiments using silver salts were wrapped in aluminium foil and stored in a dark cupboard to prevent precipitation of silver solid.

$[Pd_3(Brpz)_6]\cdot 3MeCN$, (2.1·MeCN)

$PdCl_2$ (47 mg, 0.26 mmol) was dissolved in warm MeCN (100 mL), and 100 μL NEt_3 was added. The yellow solution was allowed to cool to ambient temperature and 1*H*-4-bromopyrazole (BrpzH) (117 mg, 0.80 mmol) was added in a single portion.

This effected the immediate appearance of fine, white powder which could not be collected even on a grade 4 sinter, and is suggested by Umakoshi and co-workers to be the coordination polymer $[Pd(R\text{-pyrazolate})]_n$, the kinetic product.[19]

The solution was covered with Parafilm^R, which was pierced to allow slow evaporation of the solvent. Yellow crystals of **2.1·MeCN** formed within three days (10 mg, 15.2 μmol, 9% yield). CHN expected: C 21.87%, H 1.61%, N 15.94%; anal. found: C 21.98%, H 1.71%, N 15.74%.

$[Pd_3(Ipz)_6]\cdot 2MeCN$, (2.2·MeCN)

$PdCl_2$ (47 mg, 0.26 mmol) was dissolved in warm MeCN (100 mL), and 100 μL NEt_3 was added. The yellow solution was allowed to cool to ambient temperature and 1*H*-4-iodopyrazole (IpzH) (155 mg, 0.80 mmol) was added in a single portion.

This effected the immediate appearance of fine, white powder which could not be collected even on a grade 4 sinter, and is suggested by Umakoshi and co-workers to be the coordination polymer $[Pd(R\text{-pyrazolate})]_n$, the kinetic product.[19]

The solution was covered with Parafilm^R, which was pierced to allow slow evaporation of the solvent. Yellow crystals of **2.2·MeCN** formed within three days (22 mg, 14 μmol, 16% yield). CHN expected: C 16.95%, H 1.16%, N 12.58%; anal. found: C 17.16%, H 1.27%, N 12.41%.

$[Pd_3(Brpz)_6]$·1.5DCM, (2.1·DCM)

Crystals of compound **2.1·MeCN** were recrystallised from the minimum amount of boiling dichloromethane (DCM), and the cooled solution was sealed in a small vial to prevent solvent evaporation. Crystals of **2.1·DCM** formed overnight (without the presence of the white by-product), but although sufficient in amount for single-crystal structure determination, were insufficient in amount for bulk analysis.

$[Pd_3(Brpz)_6]$·DBM, (2.1·DBM)

Crystals of compound **2.1·MeCN** were recrystallised from the minimum amount of boiling dibromomethane (dibromomethane), and after allowing the solution to cool to ambient temperature, a seal of Parafilm^R was used to cover the recrystallization flask, then was pierced three times to allow slow evaporation of solvent. Crystals of **2.1·DBM** formed overnight (without the presence of the white by-product), but although sufficient in amount for single-crystal structure determination, were insufficient in amount for bulk analysis.

$[Pd_3(Brpz)_6]$·2DIM, (2.1·DIM)

Crystals of compound **2.1·MeCN** (with 30 molar equivalents of diiodomethane (DIM), delivered by Gilson pipette) were recrystallised from the minimum amount of boiling dichloromethane, and the cooled solution was sealed to prevent rapid evaporation. Crystals of **2.1·DIM** formed within two days (without the presence of the white by-product), but although sufficient in amount for single-crystal structure determination, were insufficient in amount for bulk analysis.

$[Pd_3(Brpz)_6]$·bipm, (2.1·bipm)

2,2'-bipyrimidine (bipm) was prepared by Tom Roseveare, according to literature procedure.[26]

Crystals of compound **2.1·MeCN** (with 100 molar equivalents of 2,2'bipyrimidine solid) were recrystallised from the minimum amount of boiling dichloromethane, and the cooled solution was placed in a sealed vial to prevent solvent evaporation. Crystals of **2.1·bipm** formed within one week (without the presence of the white by-product), but although sufficient in amount for single-crystal structure determination, were insufficient in amount for bulk analysis.

$PdCl_2(HBrpz)_2$, (2.3)

$PdCl_2$ (44 mg, 0.25 mmol) was dissolved in warm MeCN (100 mL). The yellow solution was allowed to cool to ambient temperature and 1*H*-4-bromopyrazole (110 mg, 0.75 mmol) was added in a single portion. A seal of Parafilm^R was used to cover the reaction flask, then was pierced three times to allow slow evaporation of solvent. Orange needle-like crystals of **2.3** were obtained within four days (91 mg, 77%). CHN expected: C 15.29%, H 1.28%, N 11.89%, anal. found: C 15.46%, H 1.40%, N 11.72%.

$PdCl_2(HIpz)_2$, (2.4)

$PdCl_2$ (44 mg, 0.25 mmol) was dissolved in warm MeCN (100 mL). The yellow solution was allowed to cool to ambient temperature and 1*H*-4-iodopyrazole (146 mg, 0.75 mmol) was added in a single portion. A seal of Parafilm^R was used to cover the reaction flask, then was pierced three times to allow slow evaporation of solvent. Pale yellow needle-like crystals of **2.4** were obtained within two days (80 mg, 56%). CHN expected: C 12.75%, H 1.07%, N 9.91%, I 44.90%; anal. found: C 12.92%, H 1.16%, N 9.82%, I 44.93%.

***cis*-[$PdCl_2$(4-chloro-1-amidinopyrazol-)], 2.5**

$PdCl_2$ (44 mg, 0.25 mmol) was dissolved in warm MeCN (100 mL). The yellow solution was allowed to cool to ambient temperature and 1*H*-4-chloropyrazole (77 mg, 0.75 mmol) was added in a single portion. A seal of Parafilm^R was used to cover the reaction flask, then was pierced three times to allow slow evaporation of solvent. Clusters of hair-like, pale yellow crystals of the title compound were obtained within two weeks (18 mg, 23%). CHN expected (for the formula given above, from the single crystal structure): C 18.77%, H 1.58%, N 13.14%, Cl 33.25%; anal. found: C 19.07%, H 1.75%, N 14.34%, Cl 35.04%; (calculated for the expected [$PdCl_2(HClpz)_2$] complex is C 18.85%, H 1.58%, N 14.65%, Cl 37.09%).

[$Pt_2Ag_4(Brpz)_8$]·3MeCN, 2.6

$PtCl_2$ (10 mg, 0.03 mmol) and silver nitrate (5 mg, 0.03 mmol) were dissolved in warm MeCN (100 mL). The clear solution was allowed to cool to ambient temperature and 1*H*-4-bromopyrazole (44 mg, 0.3 mmol) was added in a single portion. A seal of Parafilm^R was used to cover the reaction flask, then was pierced three times to allow slow evaporation of solvent. A few colourless block-like crystals suitable for X-ray analysis were formed within one week, but were not sufficient in quantity for further analysis.

[$Pt_2Ag_4(Ipz)_8$], 2.7

$PtCl_2$ (10 mg, 0.03 mmol) and silver nitrate (5 mg, 0.03 mmol) were dissolved in warm MeCN (100 mL). The clear solution was allowed to cool to ambient temperature and 1*H*-4-iodopyrazole (60 mg, 0.3 mmol) was added in a single portion. A seal of Parafilm^R was used to cover the reaction flask, then was pierced three times to allow slow evaporation of solvent. A few colourless block-like crystals suitable for X-ray analysis were formed within one week, but were not sufficient in quantity for further analysis.

2.2.2 Single crystal X-ray diffraction

Single crystal X-ray diffraction data were collected for all compounds on Bruker *APEX-2* diffractometers, using Mo-Kα radiation, or on a Bruker D8 *VENTURE* diffractometer, equipped with a PHOTON 100 CMOS detector, using Cu-Kα radiation (as noted in Table 2.8).

All data were corrected for absorption using empirical methods (*SADABS*), based on symmetry-equivalent reflections combined with measurements at different azimuthal angles.[27,28] Crystal structures were solved and refined against all F^2 values, using the *SHELXTL* program suite,[29,30] or using *Olex2*.[31] Non-hydrogen atoms were refined anisotropically (except as noted below), and hydrogen atoms placed in calculated positions refined using idealised geometries (riding model) and assigned fixed isotropic displacement parameters.

Atoms in solvent molecules, particularly disordered solvent found within **2.1·MeCN**, **2.2·MeCN** and **2.6·MeCN** were modelled isotropically. In addition, poor X-ray data quality for compound **2.1·bipm** due to small, weakly diffracting crystals meant that not all atoms in these models could be refined anisotropically without causing the appearance of non-positive definite thermal ellipsoids. Single crystals of compound **2.5** proved difficult to isolate. The sample analysed was found to have a twin component, which was removed in data processing. As such, an R_{int} value could not be determined for this data set. Data collection and refinement parameters for all collections are provided in Table 2.8. Crystallographic information files for all structures in Table 2.8 are provided in the digital appendix.

Table 2.8 (continues on next page). *Data collection, structure solution and refinement parameters for crystal structures in chapter 2.*

	2.1·MeCN	**2.2·MeCN**	**2.1·DCM**
Radiation type:	*Cu-Kα*	*Mo-Kα*	*Mo-Kα*
Crystal habitat	Plate	Plate	Plate
Crystal colour	Yellow	Yellow	Yellow
Crystal size (mm)	0.24 x 0.10 x 0.10	0.36 x 0.34 x 0.06	0.27 x 0.17 x 0.03
Crystal system	Orthorhombic	Monoclinic	Monoclinic
Space group	P bcm	$P\,2_1/n$	$C\,2/c$
a (Å)	15.3853 (14)	10.3901 (7)	24.651 (2)
b (Å)	15.5134 (14)	10.5699 (7)	10.2026 (7)
c (Å)	15.1858 (13)	34.160 (2)	27.543 (2)
α (°)	90	90	90
β (°)	90	90.741 (2)	96.499 (4)
γ (°)	90	90	90
V (Å^3)	3624.5 (6)	3751.2 (4)	6822.5 (8)
Density (Mg m^{-3})	2.37	2.615	2.319
Temperature (K)	100	100	100
$\mu_{(\text{Mo-Ka})}$ (mm^{-1})	19.974	6.388	8.557
θ range (°)	5.744 to 144.076	2.384 to 55.618	2.976 to 55.092
Reflns. collected	20251	29259	41258
Independent reflns. (R_{int})	3698 [$R_{(\text{int})}$ = 0.0337]	6044 [$R_{(\text{int})}$ = 0.0691]	7821 [$R_{(\text{int})}$ = 0.0691]
Reflns. used in refinement, n	3698	6044	7821
LS parameters, p	251	383	392
Restraints, r	0	2	0
$R1$ (F)^a $I>2.0s(I)$	0.0279	0.0528	0.0409
$wR2$ (F^2)^a, all data	0.0693	0.1276	0.0918
$S(F^2)^a$, all data	1.232	0.982	0.994

	2.1·DBM	**2.1·DIM**	**2.1·bipm**
Radiation type:	*Mo-Kα*	*Mo-Kα*	*Cu-Kα*
Crystal habitat	Plate	Plate	Plate
Crystal colour	Yellow	Yellow	Yellow
Crystal size (mm)	0.25 x 0.20 x 0.09	0.11 x 0.10 x 0.04	0.19 x 0.11 x 0.11
Crystal system	Monoclinic	Monoclinic	Monoclinic
Space group	$P\,2_1/n$	$P\,2_1/c$	$C\,2/c$
a (Å)	9.700 (1)	9.9239 (3)	18.3821 (16)
b (Å)	10.147 (1)	10.2585 (3)	8.7924 (7)
c (Å)	33.229 (4)	38.157 (1)	22.0804 (18)
α (°)	90	90	90
β (°)	93.310 (6)	95.577 (1)	96.202 (3)
γ (°)	90	90	90
V (Å^3)	3264.9 (6)	3866.2 (2)	3547.8 (5)
Density (Mg m^{-3})	3.492	2.973	2.533
Temperature (K)	100	100	100
$\mu_{(\text{Mo-Ka})}$ (mm^{-1})	16.364	10.809	20.465
θ range (°)	2.46 to 55.04	4.112 to 55.282	11.168 to 145.498
Reflns. collected	46591	50559	18779
Independent reflns. (R_{int})	7481 [$R_{(\text{int})}$ = 0.0866]	8972 [$R_{(\text{int})}$ = 0.0634]	3467 [$R_{(\text{int})}$ = 0.0639]
Reflns. used in refinement, n	7481	8972	3467
LS parameters, p	379	406	87
Restraints, r	0	0	0
$R1$ (F)^a $I>2.0s(I)$	0.0533	0.0378	0.1747
$wR2$ (F^2)^a, all data	0.1371	0.078	0.463
$S(F^2)^a$, all data	1.019	1.017	1.258

[a] $R1(F) = \Sigma(|F_o| - |F_c|)/\Sigma|F_o|$; $wR2(F^2) = [\Sigma w(F_o^2 - F_c^2)^2/\Sigma wF_o^4]^{1/2}$; $S(F^2) = [\Sigma w(F_o^2 - F_c^2)^2/(n + r - p)]^{1/2}$

Table 2.8 (continued). *Data collection, structure solution and refinement parameters for crystal structures in chapter 2.*

	2.3	**2.4**	**2.5**
Radiation type:	*Mo-Kα*	*Mo-Kα*	*Mo-Kα*
Crystal habitat	Plate	Plate	Plate
Crystal colour	Orange	Orange	Yellow
Crystal size (mm)	0.61 x 0.10 x 0.03	0.31 x 0.07 x 0.04	0.30 x 0.04 x 0.03
Crystal system	Monoclinic	Monoclinic	Triclinic
Space group	*C* 2/c	*C* 2/c	*P* -1
a (Å)	15.0668 (5)	14.753 (2)	6.9995 (4)
b (Å)	4.2622 (1)	4.0792 (4)	8.2042 (5)
c (Å)	19.2630 (6)	19.149 (2)	8.9136 (8)
α (°)	90	90	79.680 (6)
β (°)	97.754 (2)	98.462 (5)	76.592 (6)
γ (°)	90	90	72.370 (5)
V (Å^3)	1225.71 (6)	1139.8 (2)	471.24 (6)
Density (Mg m^{-3})	3.063	2.734	2.2473
Temperature (K)	100	100	100
$\mu_{(\text{Mo-Ka})}$ (mm^{-1})	6.96	9.077	2.762
θ range (°)	4.268 to 55.42	4.302 to 54.998	4.74 to 52.76
Reflns. collected	10130	9173	3486
Independent reflns. (R_{int})	1434 [$R_{(\text{int})}$ = 0.0224]	1304 [$R_{(\text{int})}$ = 0.0330]	3236
Reflns. used in refinement, *n*	1434	1304	3236
LS parameters, *p*	74	70	109
Restraints, *r*	0	0	0
$R1$ (F)^a *I>2.0s(I)*	0.0123	0.0154	0.0467
$wR2$ (F^2)^a, all data	0.0313	0.0397	0.1243
S(F^2)^a, all data	1.068	1.051	1.043

	2.6·MeCN	**2.7**
Radiation type:	*Mo-Kα*	*Mo-Kα*
Crystal habitat	Plate	Plate
Crystal colour	Colourless	Colourless
Crystal size (mm)	0.30 x 0.30 x 0.05	0.16 x 0.15 x 0.05
Crystal system	Monoclinic	Tetragonal
Space group	*C* 2/c	*P* 4/n
a (Å)	16.4345 (9)	13.4871 (4)
b (Å)	16.1788 (9)	13.4871 (4)
c (Å)	21.410 (1)	12.5689 (5)
α (°)	90	90
β (°)	104.528 (3)	90
γ (°)	90	90
V (Å^3)	5510.7 (6)	2286.3 (1)
Density (Mg m^{-3})	2.648	3.4357
Temperature (K)	100	100
$\mu_{(\text{Mo-Ka})}$ (mm^{-1})	12.301	13.214
θ range (°)	3.59 to 55.074	3.24 to 55.1
Reflns. collected	23597	28305
Independent reflns. (R_{int})	6311 [$R_{(\text{int})}$ = 0.0479]	2649 [$R_{(\text{int})}$ = 0.0581]
Reflns. used in refinement, *n*	6311	2649
LS parameters, *p*	303	123
Restraints, *r*	0	0
$R1$ (F)^a *I>2.0s(I)*	0.031	0.0405
$wR2$ (F^2)^a, all data	0.066	0.1325
S(F^2)^a, all data	1.01	1.069

[a] $R1(F) = \Sigma(|F_o| - |F_c|)/\Sigma|F_o|$; $wR2(F^2) = [\Sigma w(F_o^2 - F_c^2)^2/\Sigma wF_o^4]^{1/2}$; $S(F^2) = [\Sigma w(F_o^2 - F_c^2)^2/(n + r - p)]^{1/2}$

2.3 Results & discussion

2.3.1 Trigonal prismatic clusters [Pd_3(4-halopyrazolate)$_6$]

The [Pd_3(4-halopyrazolate)$_6$] clusters, where the halogen is bromine or iodine, were synthesised by a method analogous to that described by Umakoshi and co-workers for the parent non-halogenated analogue.[19] It was found that, when using 4-chloropyrazole, no crystals formed (even after several weeks of slow evaporation of the solvent at room temperature).

The brominated version, [$Pd_3(Brpz)_6$]·3MeCN (compound **2.1·MeCN**), crystallises in space group *Pbcm*, and comprises discrete clusters, linked through both halogen- and hydrogen-bonding. Interaction between the clusters and solvent propagates one dimension of a 2D supramolecular network, through N···Br–C halogen bonds. The network is extended in a second dimension by C–H···Br–C hydrogen bonding (see Figure 2.9). A short-range intramolecular interaction could not be identified which connects the clusters in a third dimension.

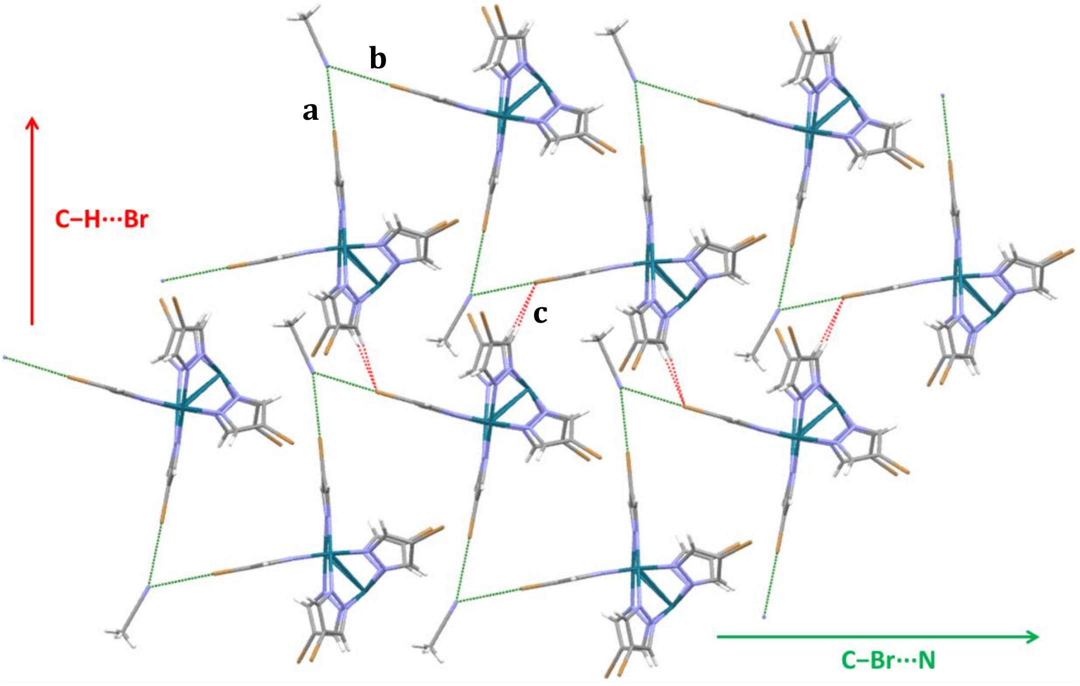

Figure 2.9. *Cluster-cluster and cluster-solvent interactions (in two dimensions) in compound* ***2.1·MeCN****. Halogen bonding shown by thick green dashed lines, hydrogen bonding shown by thin red dashed lines.*

Three crystallographically unique acetonitrile solvent molecules exist per cluster. One of these propagates the network shown in Figure 2.9. The other two equivalent acetonitrile molecules are observably disordered over two positions, and one of these acetonitrile molecules is hydrogen-bonded (C–H···N) to the cluster **2.1**. The third equivalent does not appear to participate in any observable hydrogen or halogen bonds with cluster or solvent.

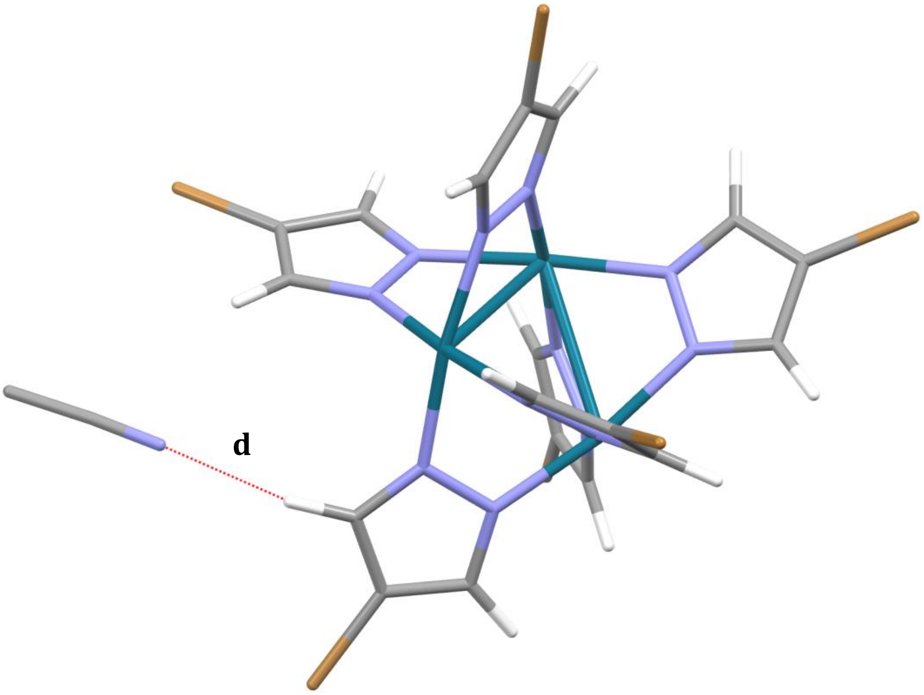

Figure 2.10. *C–H···N hydrogen bonding between clusters of **2.1** and acetonitrile. The acetonitrile molecule shown in this Figure is crystallographically unique from those shown in Figure 2.9 and does not propagate a supramolecular network through this hydrogen bond.*

Table 2.11. *Hydrogen ("H-bond"), halogen bond/halogen-halogen interactions ("X-bond"/"X···X") and other interaction geometries for compound* ***2.1·MeCN****. Interactions are listed as labelled in Figures 2.9 and 2.10.*

Interaction		X/H···A (Å)	θ(D–X/H···A) (°)	θ(R–A···X/H) (°)	$r_X + r_A$ (Å)[a]	R_{XA}[a]
a X-bond	C–Br···N	3.344 (5)	179.12 (19)	161.8 (5)	3.40	0.98
b X-bond	C–Br···N	3.379 (6)	178.69 (19)	131.4 (4)	3.40	0.99
c H-bond	C–H···Br	2.9864	168.5	119.36	3.05	0.98
d H-bond	C–H···N	2.405	142.43	169.18	2.75	0.87

[a] *$R_{XA} = d(X/H\cdots A)/(r_{X/H} + r_A)$, where $r_{X/H}$ and r_A are the van der Waals radii*[32] *of the bond donor, X/H, and the acceptor, A, respectively, following the definition of Lommerse et al.*[33] *Hydrogen bond lengths normalised to neutron diffraction values.*[34]

In this network, the aryl bromine is shown to play a versatile role, acting as both a halogen bond donor and hydrogen bond acceptor. The structure is also highly dependent upon solvent, which propagates the supramolecular network present, and contributes to three of the four noted intermolecular interactions in the structure. Assessment of the reduced interaction distances (R_{XA}) indicates that none of the interactions described by Figures 2.9 or 2.10 are particularly strong.

The iodinated congener $[Pd_3(Ipz)_6]\cdot 2MeCN$ (compound **2.2·MeCN**) also features extended halogen bonding between clusters, and interaction with solvent. However, this structure is more typical of the halogenated clusters previously reported by the Brammer group.[17,18] The packing of clusters is dominated by many C–I···π interactions, where iodine acts as a halogen bond donor. Dimers of this motif connect pairs of clusters (see Figure 2.12), and then these are further connected in all three dimensions by other C–I···π halogen bonds (see Figure 2.13).

Further halogen bonding of the type C–I···I–C is found also, connecting clusters in a one-dimensional chain (see Figure 2.14). The interaction geometry between the iodine atoms involved indicates this is a type II halogen-halogen interaction, a halogen bond (see chapter 1 section 1.1.1.3).

Although there is evidently a great deal more halogen bonding in the structure **2.2·MeCN** than in **2.1·MeCN**, hydrogen bonding to the solvent clearly also plays a role in the packing. Hydrogen bonds donated by aryl hydrogens on the cluster also interact with the acetonitrile solvate, and in turn the solvent molecule hydrogens are also hydrogen-bonded to on iodine atom on each cluster. The reduced distances (R_{XA}), where measurable, suggest attractive interactions in each case also.

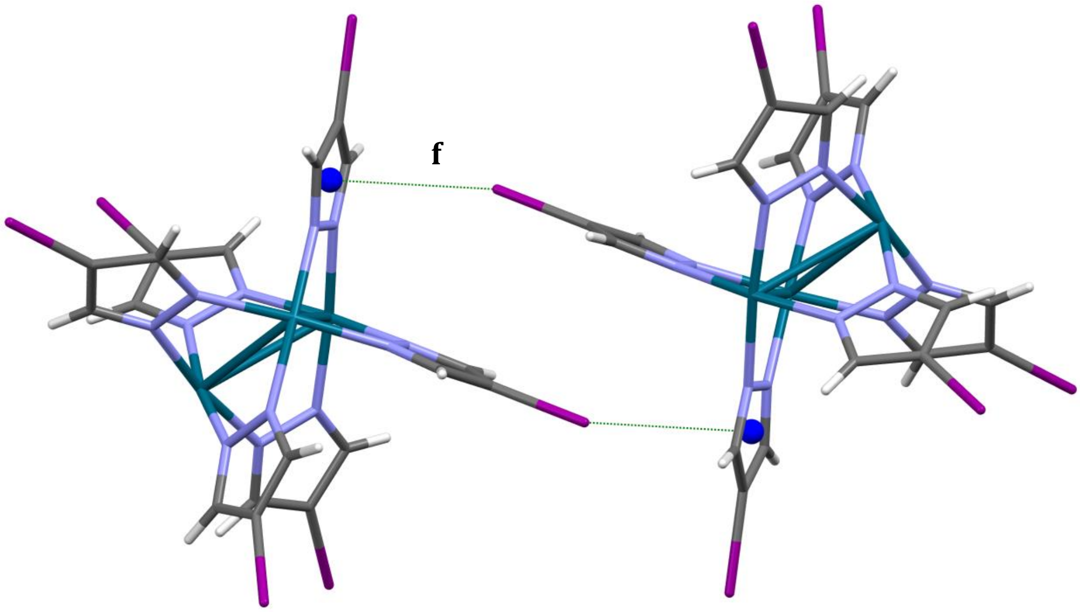

Figure 2.12. *The C–I···π dimer motif in compound* ***2.2·MeCN****. Halogen bonding shown by green dashed lines. Aryl ring centroids shown as blue spheres.*

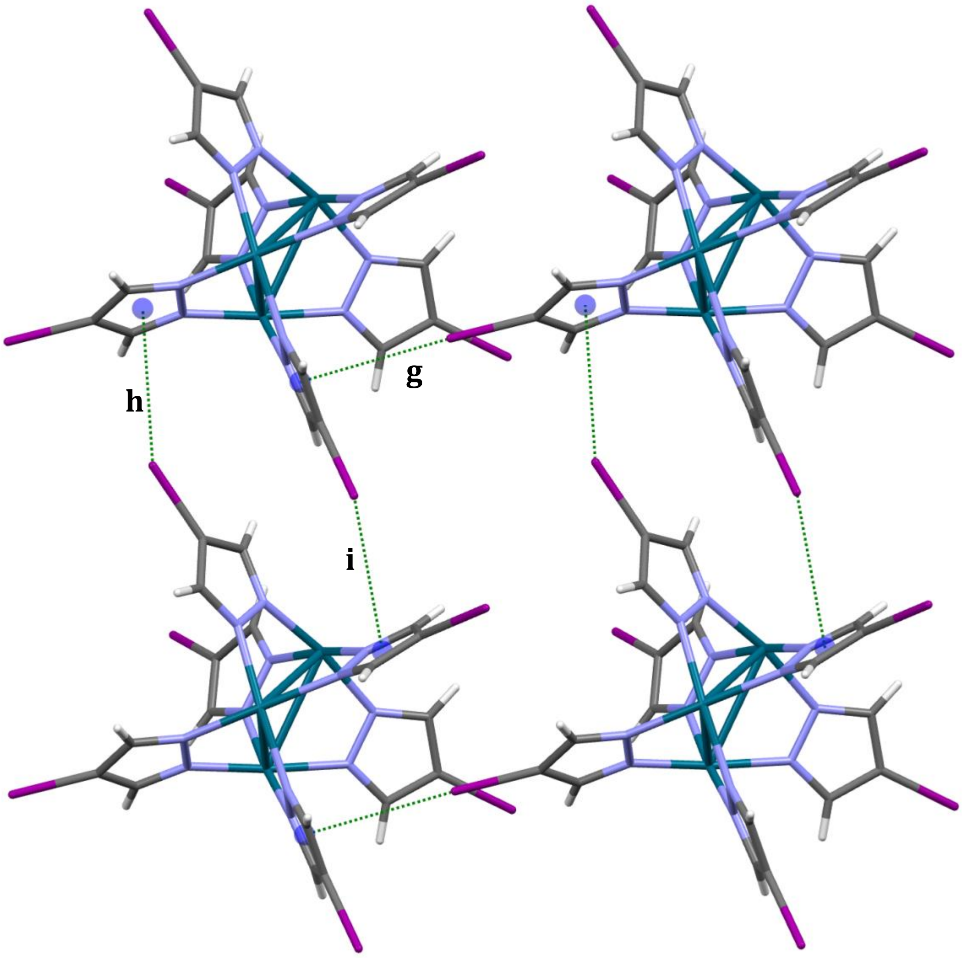

Figure 2.13. *Other C–I···π interactions in* ***2.2·MeCN****. Halogen bonding shown by green dashed lines. Aryl ring centroids shown as blue spheres.*

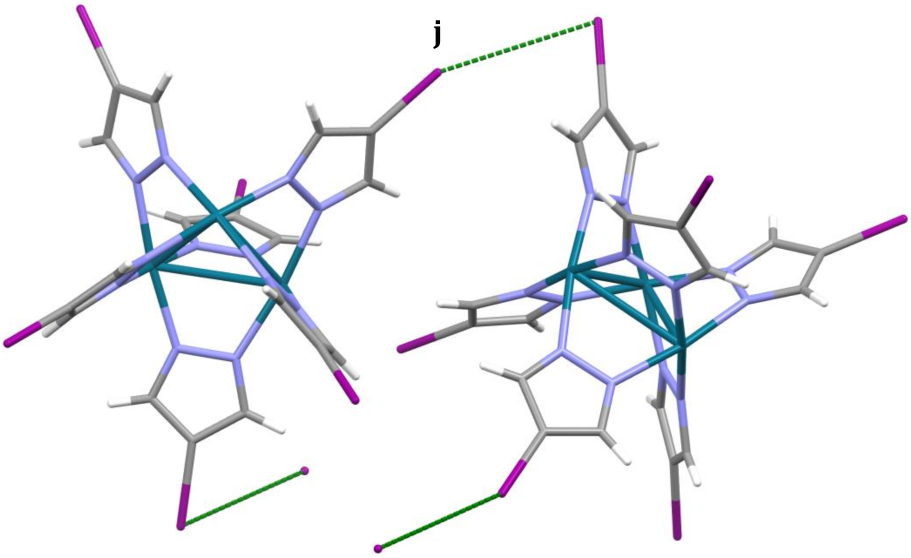

Figure 2.14. *1D chains of C–I···I–C halogen bonds in* ***2.2·MeCN****. Halogen bonding shown by green dashed lines. The chain is continued by the incomplete dashed lines at the bottom of the picture.*

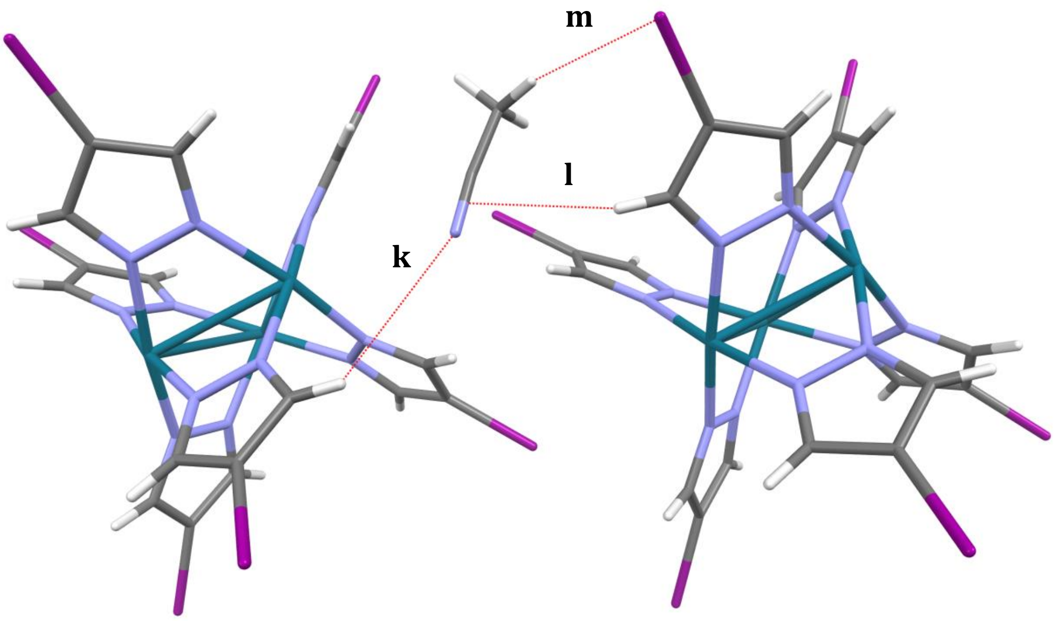

Figure 2.15. *Hydrogen bonding to solvent in* ***2.2·MeCN****. Hydrogen bonding shown by red dashed lines.*

The reduced van der Waals distance (R_{XA}) of C–I···π interactions are calculated based on the assumed van der Waals radius of the pyrazolate ring being as shown in equation 2.16. This estimation is simply based on the relative amounts of carbon and nitrogen in the ring.

$$r_{\pi-ring} = \left(\frac{2}{5} r_{nitrogen}\right) + \left(\frac{3}{5} r_{carbon}\right)$$

Equation 2.16. *Estimated van der Waals radius of pyrazolate rings discussed in this chapter.*

Table 2.17. *Hydrogen ("H-bond"), halogen bond/halogen-halogen interactions ("X-bond"/"X···X") and other interaction geometries for compound **2.2·MeCN**. Interactions are listed as labelled in Figures 2.12, 2.13, 2.14, and 2.15.*

Interaction		X/H···A (Å)	θ(D–X/H···A) (°)	θ(R–A···X/H) (°)	$r_X + r_A$ (Å)^a	R_{XA}^{a}
f X-bond	C–I···π	3.438 (5)	162.3 (3)	n/a	3.62	0.95
g X-bond	C–I···π	3.659 (5)	171.8 (3)	n/a	3.62	1.01
h X-bond	C–I···π	3.717 (4)	145.8 (3)	n/a	3.62	1.03
i X-bond	C–I···π	3.862 (4)	135.4 (3)	n/a	3.62	1.07
j X-bond	C–I···I–C	3.943 (1)	153.8 (3)	75.0 (3)	3.96	1.00
k H-bond	C–H···N	2.626	122.69	125.42	2.75	0.95
l H-bond	C–H···π	2.496	156.25	n/a	2.84	0.88
m H-bond	C–H···I	3.137	136.82	106.17	3.18	0.99

[a]See references given for Table 2.11 for definitions of 'R_{XA}'. Hydrogen bond lengths normalised to neutron diffraction values.[34]

The C–X···π dimer motif observed in **2.2·MeCN** is prevalent in previous work on halobenzoate clusters in the Brammer group,[17,18] and appears in this case to be favoured by the stronger halogen bond donor iodine (although these interactions are still weak). Weak hydrogen bonding to solvent appears to play a role in the packing of these clusters in the solid state, as evidenced by the formation of multiple hydrogen bonds to the clusters in both **2.1·MeCN** and **2.2·MeCN**. Varying the halogen- and hydrogen-bonding capabilities of the solvent will clearly affect the packing of the clusters in the solid state, indicating how strong a role the pyrazolyl halogen plays in the packing of these clusters.

2.3.1.2 Solvates of cluster 2.1 – tuning halogen- and hydrogen-bonding

The parent material **2.1·MeCN** could be recrystallised from a variety of polar solvents, to give crystals of other solvates with different packing arrangements in the solid state. This was achieved by selection of a family of dihalomethane solvents which have different halogen-bonding and hydrogen-bonding ability.

In each case, only a few crystals of these materials were formed, preventing bulk analysis.

[$Pd_3(Brpz)_6$]·1.5DCM, 2.1·DCM

In recrystallising the parent material **2.1·MeCN** from dichloromethane, crystals of **2.1·DCM** are formed. In this new material, the clusters Pd_3Brpz_6 show significantly more interaction with the solvent molecules than each other. This results in the formation of 'embraces' of clusters around DCM molecules. These 'embraces' are largely hydrogen-bond based, but also contain halogen-halogen interactions between cluster and solvent, and between clusters (see Figures 2.18 and 2.19).

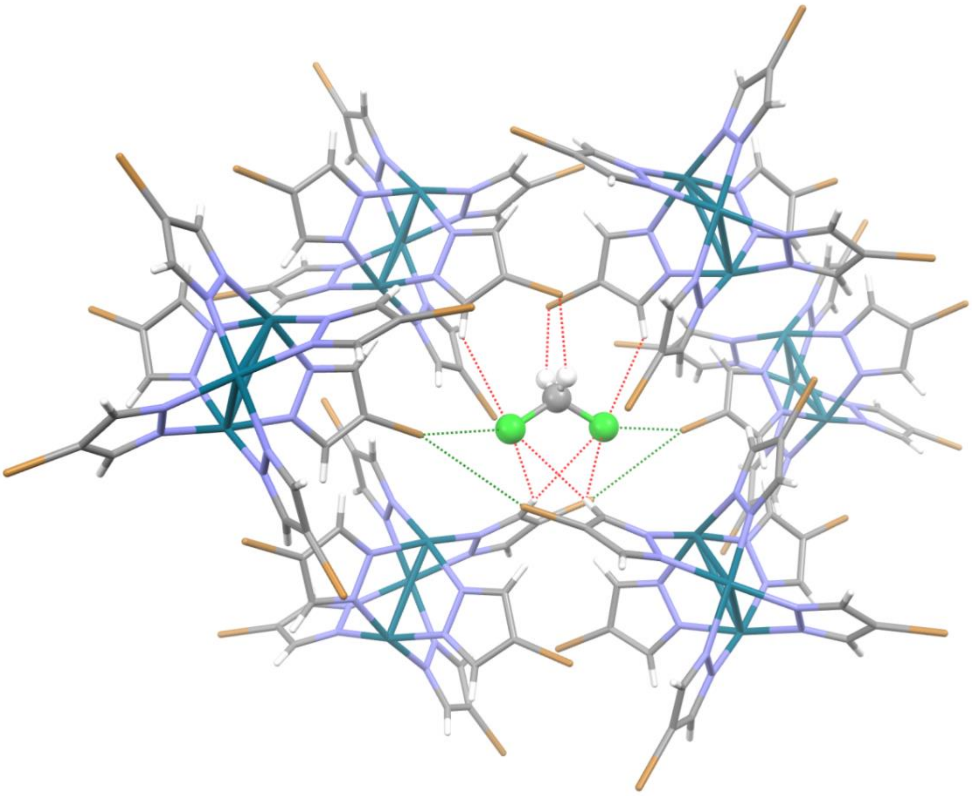

Figure 2.18. *'Embraces' of hydrogen- and halogen-halogen interactions formed by **2.1·DCM**. Halogen-halogen interactions shown by green dashed lines, hydrogen bonding shown by red dashed lines. DCM solvate shown in ball-and-stick view for clarity.*

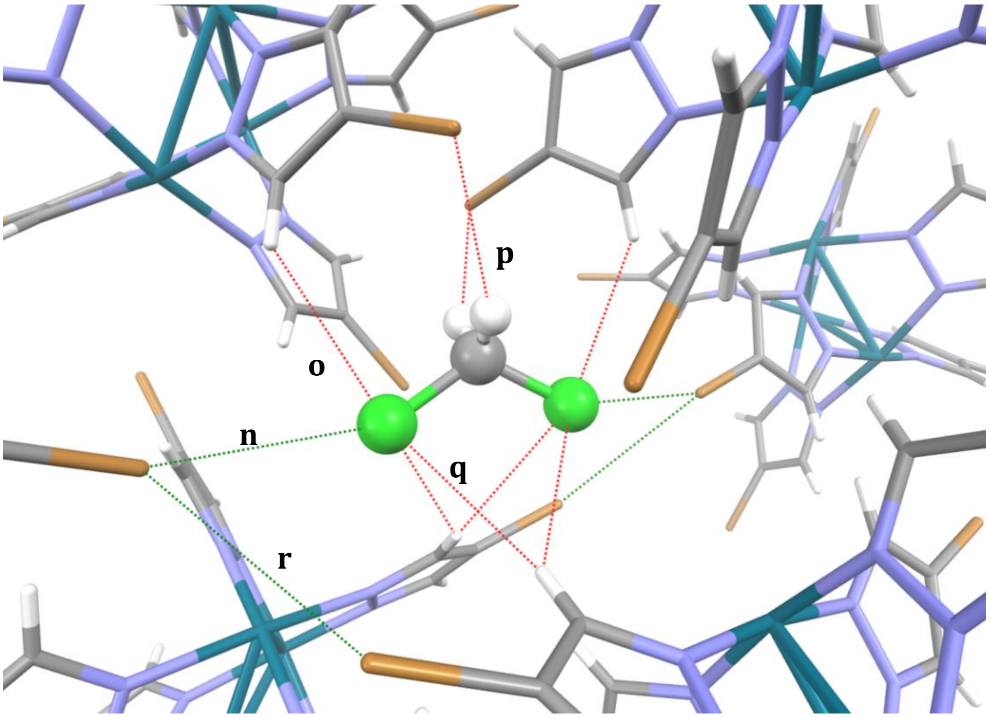

Figure 2.19. *Zoomed view of the interactions around DCM in structure* **2.1·DCM**.

Table 2.20. *Hydrogen ("H-bond"), halogen bond/halogen-halogen interactions ("X-bond"/"X···X") and other interaction geometries for compound* ***2.1·DCM****. Interactions are listed as labelled in Figures 2.18 and 2.19.*

Interaction		X/H···A (Å)	θ(D–X/H···A) (°)	θ(R–A···X/H) (°)	$r_X + r_A$ (Å)[a]	R_{XA}[a]
n X···X	C–Br···Cl–C	3.375 (2)	160.5 (2)	145.0 (3)	3.60	0.94
o H-bond	C–H···Cl–C	2.913	138.33	89.91	2.95	0.99
p H-bond	C–H···Br–C	2.660	153.31	93.23	3.05	0.87
q H-bond	C–H···Cl–C	2.916	146.06	82.69	2.95	0.99
r X···X	C–Br···Br–C	3.6153 (9)	125.6 (2)	141.0 (2)	3.70	0.98

[a] *See references given for Table 2.11 for definitions of 'R_{XA}'. Hydrogen bond lengths normalised to neutron diffraction values.*[34]

The structure is dominated by interactions between the cluster and solvent. The dichloromethane solvate offers many interaction sites, acting as a hydrogen bond donor and acceptor, and participating in halogen-halogen interactions as well. The geometries of the halogen-halogen interactions, both between solvent-and-cluster and cluster-and-cluster, suggest these are type I halogen-halogen interactions. They may be considered attractive, though they are not considered halogen bonds.

[Pd$_3$(Brpz)$_6$]·DBM, 2.1·DBM

In recrystallising the parent material **2.1·MeCN** from dibromomethane, crystals of **2.1·DBM** are formed. This enables a comparison of the packing effected by a solvent molecule of a similar shape, but different halogen- and hydrogen-bonding capability.

The structure of **2.1·DBM**, in comparison with **2.1·DCM** has a structure less centred on interaction with solvent, though hydrogen bonding still plays a clear role in the packing. The structure features a complex series of interactions, almost exclusively between clusters. The motifs of intermolecular interactions obvious at close range, involving multiple interactions between clusters, are shown below. Most notable is the presence of the C-X···π dimer motif, analogous to previous work,[17,18] which is not present in the DCM-solvated structure (see Figure 2.21). In addition, 1D chains of C–Br···Br–C halogen bonds (type II halogen-halogen interaction) also connect clusters (Figure 2.22), in a manner similar to the iodinated parent cluster, **2.2·MeCN**.

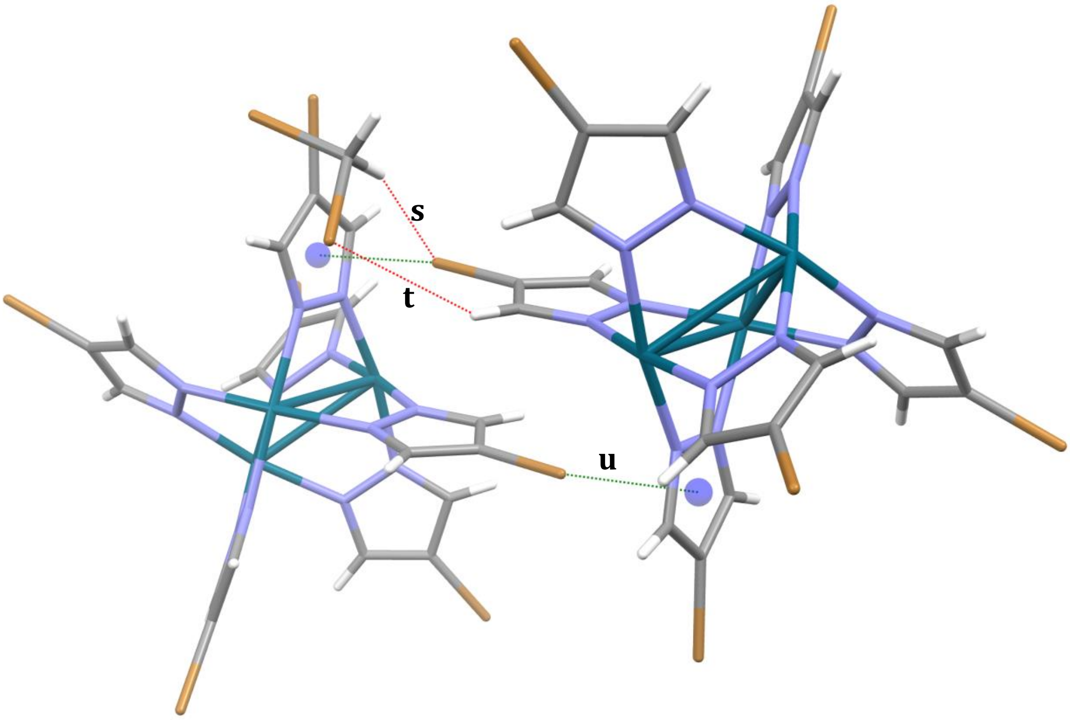

*Figure 2.21. The C-Br···π dimer motif (and hydrogen bonding to solvent) in **2.1·DBM**. Halogen bonding shown by green dashed lines, hydrogen bonding shown by red dashed lines. Aryl ring centers shown as blue spheres.*

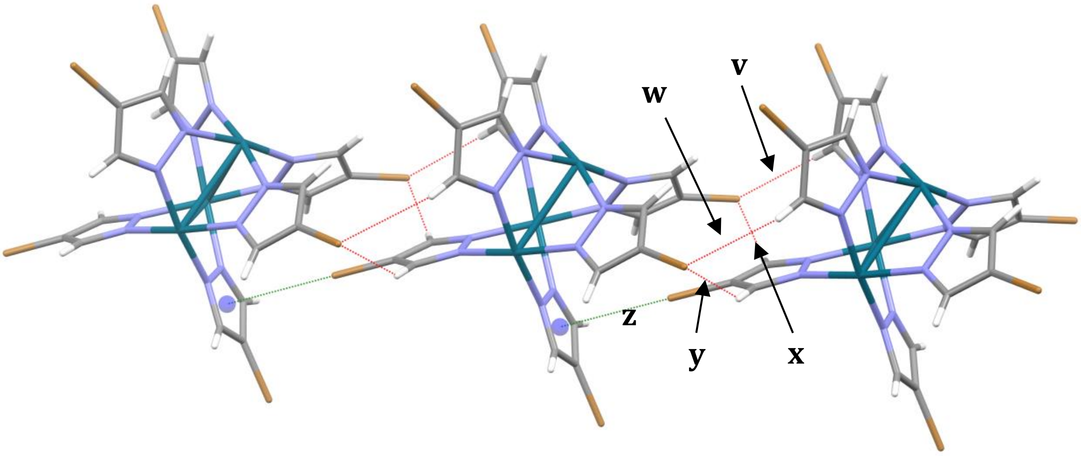

Figure 2.22. *1D chains of hydrogen bonding and halogen bonding in **2.1·DBM**. Halogen bonding shown by green dashed lines, hydrogen bonding shown by red dashed lines. Aryl ring centers shown as blue spheres.*

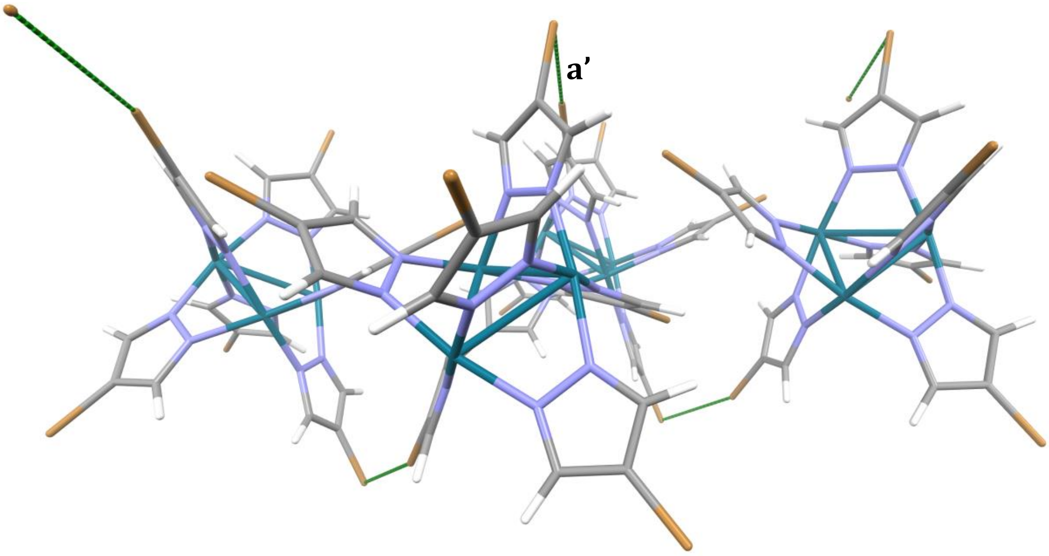

Figure 2.23. *1D chains of C–Br···Br–C halogen bonds in **2.1·DBM**. Halogen bonding shown by green dashed lines. Perspective zoom and shading used to help visually distinguish structural features projecting out from the plane of the page.*

Table 2.24. *Hydrogen ("H-bond"), halogen bond/halogen-halogen interactions ("X-bond"/"X···X") and other interaction geometries for compound* ***2.1·DBM****. Interactions are listed as labelled in Figures 2.21, 2.22 and 2.23.*

Interaction		X/H···A (Å)	θ(D–X/H···A) (°)	θ(R–A···X/H) (°)	$r_X + r_A$ (Å)[a]	R_{XA}[a]
s H-bond	C–H···Br–C	2.953	160.56	88.11	3.05	0.97
t H-bond	C–H···Br–C	2.976	146.24	89.25	3.05	0.98
u X-bond	C–Br···π	3.316 (4)	166.5 (3)	n/a	3.49	0.95
v H-bond	C–H···Br–C	2.880	164.09	109.58	3.05	0.94
w H-bond	C–H···Br–C	2.748	155.21	117.46	3.05	0.90
x H-bond	C–H···Br–C	2.679	152.78	81.78	3.05	0.88
y H-bond	C–H···Br–C	2.793	141.57	81.53	3.05	0.92
z X-bond	C–Br···π	3.335 (4)	177.6 (3)	n/a	3.49	0.96
a' X-bond	C–Br··· Br–C	3.530 (1)	154.3 (3)	78.54 (3)	3.70	0.95

[a]*See references given for Table 2.11 for definitions of 'R_{XA}'. Hydrogen bond lengths normalised to neutron diffraction values.*[34]

In replacing the dichloromethane solvent with dibromomethane, the structure has become dominated by cluster-cluster interactions, over cluster-solvent interactions. This is explained by the poorer ability of dibromomethane to donate and accept hydrogen bonds (less electron withdrawing group Br over Cl, more diffuse electron density on Br to accept hydrogen bonds). Interestingly, however, there is no observable short-range halogen bonding to the solvent, the cluster instead forming the 1D chains of halogen bonds shown in Figure 2.23.

[Pd$_3$(Brpz)$_6$]·2DIM, 2.1·DIM

In recrystallising the parent material **2.1·MeCN** from dichloromethane along with 30 molar equivalents of diiodomethane, crystals of **2.1·DIM** are formed. Diiodomethane is the only solvent found crystallographically within the structure, however, and no incorporation of DCM was observed. Similarly to the structure **2.1·DBM**, a large series of complex interactions connect the clusters and solvent molecules. Only those over shortest range are described here.

The clusters in **2.1·DIM** are linked into extended hydrogen- and halogen-bonded networks in the same fashion as in **2.1·DBM** (see Figures 2.22 and 2.23). Chains of C–

H⋯Br hydrogen bonds and C–Br⋯π halogen bonds create 1D chains (as shown in Figure 2.22), and 1D chains of type II C–Br⋯Br–C halogen-halogen interactions (halogen bonds) connect clusters in an orthogonal direction (as shown in Figure 2.23). Type I halogen-halogen interactions are also observed between pairs of clusters (see Figure 2.25).[35] This interaction connects further the chains of halogen-bonded clusters (as in Figure 2.23), to create an extended network.

One diiodomethane solvent molecule is bound to each cluster through both C–I⋯π halogen bonding, and a hydrogen bond to the bromine atom of an adjacent ligand on the cluster. The other crystallographically unique diiodomethane molecule displays interaction at short range between the iodine atom and palladium(II) ion (see Figure 2.25, right). The coordination of halocarbons to transition metals (through the halogen, R–X–M) is a known phenomenon,[36,37] in which the electron density on the halogen, orthogonal to the R–X bond forms a coordination bond to a metal centre. The interaction geometry of C–I⋯Pd ("**e'**"), shown in Figure 2.25 and quantified in Table 2.26, suggests the observed interaction in **2.1.DIM** is an attractive intermolecular interaction, possibly comparable in general nature to such coordination bonds.

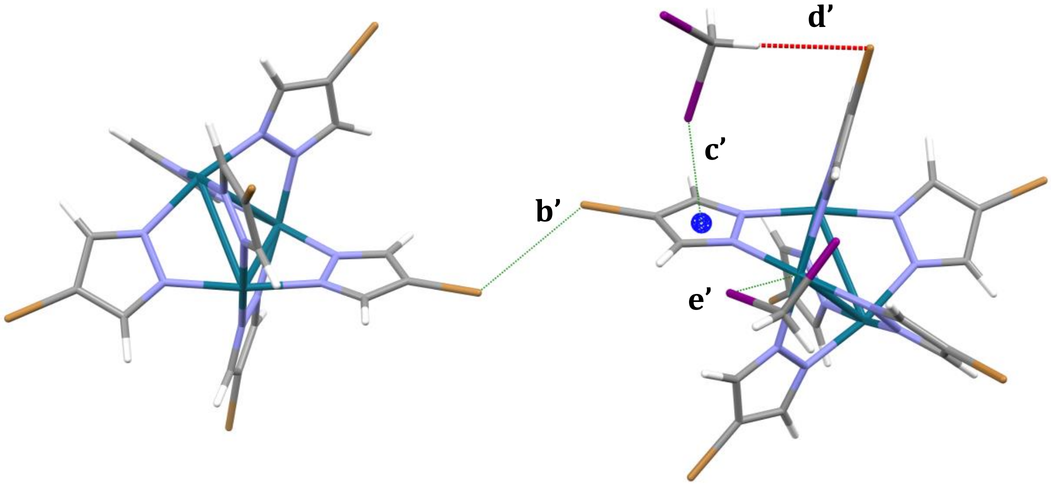

Figure 2.25. *Interaction between clusters and with solvent in structure* ***2.1·DIM****. Halogen-halogen / halogen-metal interactions shown by green dashed lines, hydrogen bonding shown by red dashed lines. Aryl ring centers shown as blue spheres.*

Table 2.26. *Hydrogen ("H-bond"), halogen bond/halogen-halogen interaction ("X-bond") and other interaction geometries for compound **2.1·DIM**. Interactions are listed as labelled in Figures 2.25, and then interaction **f'** as shown in Figure 2.23 and the interactions **g'-k'** as in Figure 2.22.*

Interaction		X/H···A (Å)	θ(D–X/H···A) (°)	θ(R–A···X/H) (°)	$r_X + r_A$ (Å)[a]	R_{XA}[a]
b' X···X	C–Br···Br–C	3.543 (2)	131.2 (2)	131.2 (2)	3.70	0.96
c' X-bond	C–I···π	3.459 (3)	154.0 (2)	n/a	3.62	0.96
d' H-bond	C–H···Br–C	2.748	162.38	79.44	3.05	0.90
e' M···X	Pd···I–C	3.5071 (8)	114.8 (3)	n/a	3.61	0.97
f' X-bond	C–Br···Br–C	3.691 (1)	153.8 (2)	77.9 (2)	3.70	1.00
g' H-bond	C–H···Br–C	2.860	151.17	122.37	3.05	0.94
h' H-bond	C–H···Br–C	2.940	155.79	116.35	3.05	0.96
I' H-bond	C–H···Br–C	2.887	139.59	84.79	3.05	0.95
j' H-bond	C–H···Br–C	2.845	148.36	85.63	3.05	0.93
k' X-bond	C–Br···π	3.465 (3)	177.3 (2)	n/a	3.49	0.99

[a]See references given for Table 2.11 for definitions of 'R_{XA}'. Hydrogen bond lengths normalised to neutron diffraction values.[34]

In changing the solvent present, the intermolecular interaction motifs clearly change. Introduction of dichloromethane (recrystallising **2.1·MeCN** to form **2.1·DCM**), gives a solvent-directed assembly of the clusters, around the better (though still weak) hydrogen bond donor and acceptor dichloromethane. In addition, more sites for possible interaction are available around dichloromethane compared to acetonitrile, and so this also explains the 'embrace' effect that is seen in **2.1·DCM**. The sheer number of interactions at short range observable between cluster and solvent in all the dihalomethane solvates demonstrates the suitability of using a solvent of high 'connectivity' with a cluster of high 'connectivity'.

Comparing the dichloromethane solvate **2.1·DCM** to the dibromomethane and diiodomethane solvates **2.1·DBM** and **2.1·DIM**, significantly fewer interactions with the solvent are found. In changing to the heavier, less electronegative halogen congeners, the hydrogen bond donor and acceptor ability of the solvent is reduced. However, hydrogen bonding to the solvent is clearly still seen in all the materials, though significantly less in number of interactions in **2.1·DBM** and **2.1·DIM**.

The halogen bonding and halogen-halogen interactions present within the structures are also altered, from **2.1·DCM** to **2.1·DBM**, to **2.1·DIM**. The presence of a 1D halogen-bonded network between clusters in both the latter structures suggests the ability of dibromomethane and diiodomethane to support halogen-bonded structures. This may be due to the lack of competition from hydrogen bond formation, which for dichloromethane is stronger (although still relatively weak). The C–X···π motif, found in the crystal structures of 4-iodobenzoate cluster compounds studied by the Brammer group (see section 2.1.2 and Figure 2.4)[38] is also found in the structures of both **2.1·DBM** and **2.1·DIM**, both between clusters and between cluster and solvent.

One complication in comparing the relative strength of these intermolecular interactions using the reduced interaction distance (R_{XA}), is these interactions with the π-system. An accurate representation of the actual centre of interaction (centre of electron density in the ring) and of the van der Waals radius of the ring in each interaction is not possible crystallographically, and can only be estimated. This was estimated to be 1.64 Å using equation 2.16. Even so, this may introduce systematic error in the interpretation of these interactions.

The observation that the cluster **2.1**, when re-crystallised from dichloromethane with just 30 mole equivalents of diiodomethane formed crystals of **2.1·DIM** may suggest a selective entrapment of the halogen-bond supporting diiodomethane. However, this observation is based upon a single crystal structure. While only very small quantities of crystals were produced, nonetheless a single-crystal structure cannot be representative of the bulk phase, and large-scale repetition would have to be conducted to establish whether or not this uptake is truly selective.

This family of solvates have demonstrated the extent to which the solid-state packing of such stellated clusters can be altered by the crystallisation partner molecules (i.e. solvent). Particularly, comparing structures resulting from crystallisation with dichloromethane (**2.1·DCM**) to those from dibromo- and diiodomethane (**2.1·DBM**, **2.1·DIM**) demonstrates the strong influence of solvent on the packing of molecules such as cluster **2.1** with a high degree of connectivity.

2.3.1.3 A co-crystal of cluster 2.1: Shape-matching the 'stellation'

The cluster **2.1** demonstrably crystallises as a solvate from many solvent systems, and never as a single component. This may be due to the 'stellated' nature of the cluster itself – an awkward shape that does not facilitate efficient packing of the cluster alone. The voids that are resultant about the cluster due to its shape are shown in Figure 2.27.

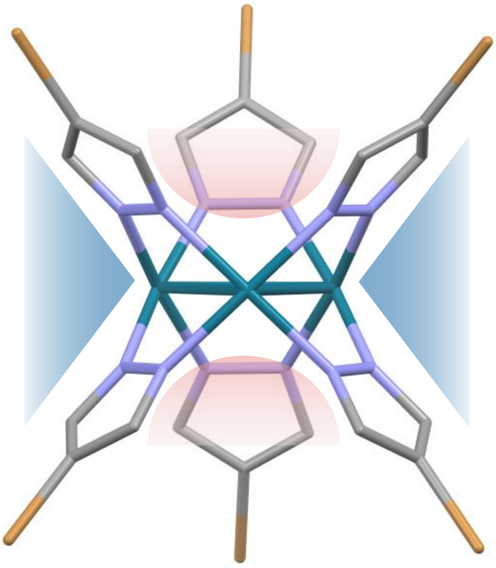

Figure 2.27. *The cluster* ***2.1****, showing the bowl-like voids between groups of three pyrazolate ligands (red) and triangular voids between pairs of pyrazolate ligands (blue). Hydrogen atoms omitted for clarity.*

These observations led to the search for a partner molecule of appropriate shape to co-crystallise with **2.1**. Creating such a co-crystal would demonstrate a truly controlled approach to crystallisation, and demonstrate well the principles of crystal engineering in creating ordered, designed solids.

2,2'-bipyrimidine was selected for this, for several reasons. First, due to the shape of the ligand edges (highlighted in blue in Figure 2.28i), which in principle could stack well in the triangular void between pairs of pyrazolates (see Figure 2.27). Secondly, the observation of bifurcated halogen bonds formed by bipyrimidine derivatives seen in the crystal engineering literature, facilitating the formation of halogen-bonded networks (see Figure 2.28ii).[39]

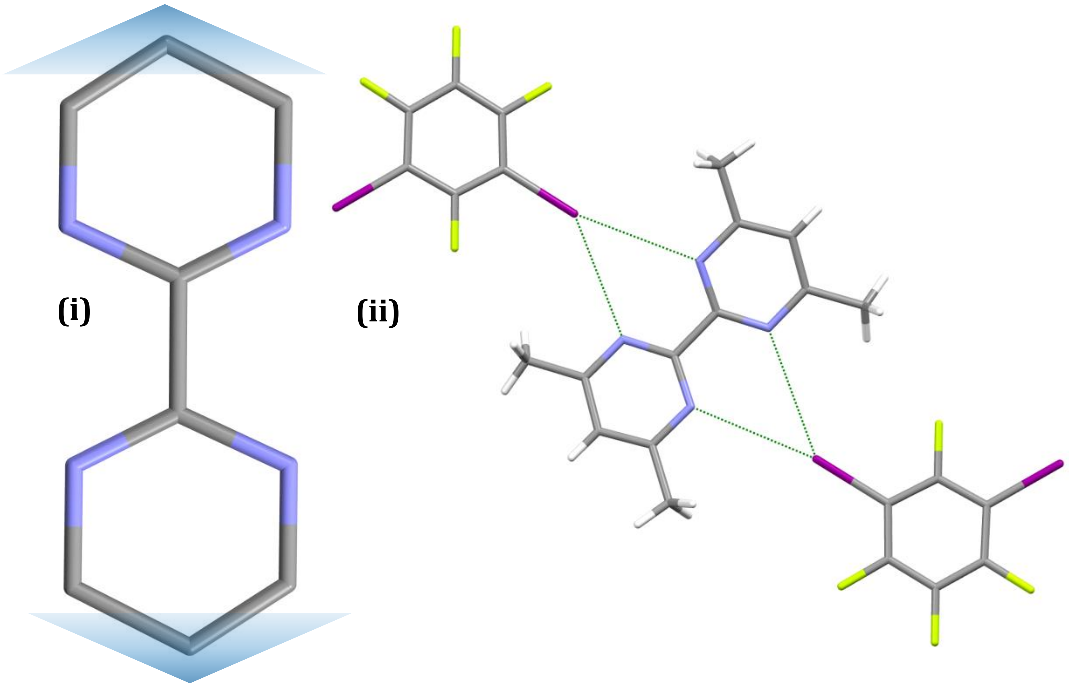

Figure 2.28. ***(i)****The triangular edge of 2,2’-bipyrimidine, highlighted in blue and* ***(ii)*** *infinite halogen-bonded networks consisting of bifurcated halogen bonds at the acceptor site in (1,3,4,5-tetrafluoro-2,5-diiodobenzene)·(3,5,3’,5’-tetramethyl-2,2’-bipyrimidine).*[39]

Recrystallisation of **2.1·MeCN** from dichloromethane in the presence of 100 mole equivalents of bipyrimidine (bipm) gave compound **2.1·bipm**, $[Pd_3(Brpz)_6]$(bipm). As with the solvates of recrystallised **2.1**, only a few crystals of the compound were obtained, preventing bulk analysis. The structure **2.1.bipm** contains columns of cluster **2.1**, between which lie bipyrimidine molecules, located within the triangular voids between pairs of pyrazolates (see Figure 2.29).

However this was not accompanied by the formation of bifurcated halogen bonds to the bipyrimidine. A distinctly singular halogen bond is found between one bipyrimidine nitrogen atom and the bromine of an adjacent cluster. These connect 1D chains of C–Br···Br–C halogen bonds (type II halogen-halogen interaction), to create a two-dimensional halogen-bonded network (see Figure 2.30).

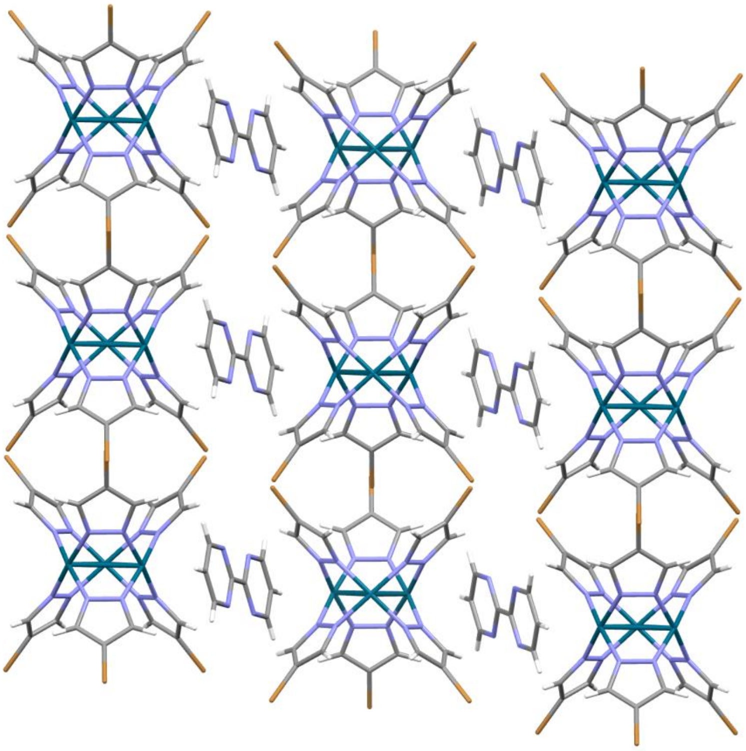

Figure 2.29. *Columns of clusters and bipyrimidine in the structure of* ***2.1.bipm*** *down the crystallographic* b*-axis, showing stacking of bipyrimidine within the angular voids of cluster* ***2.1****.*

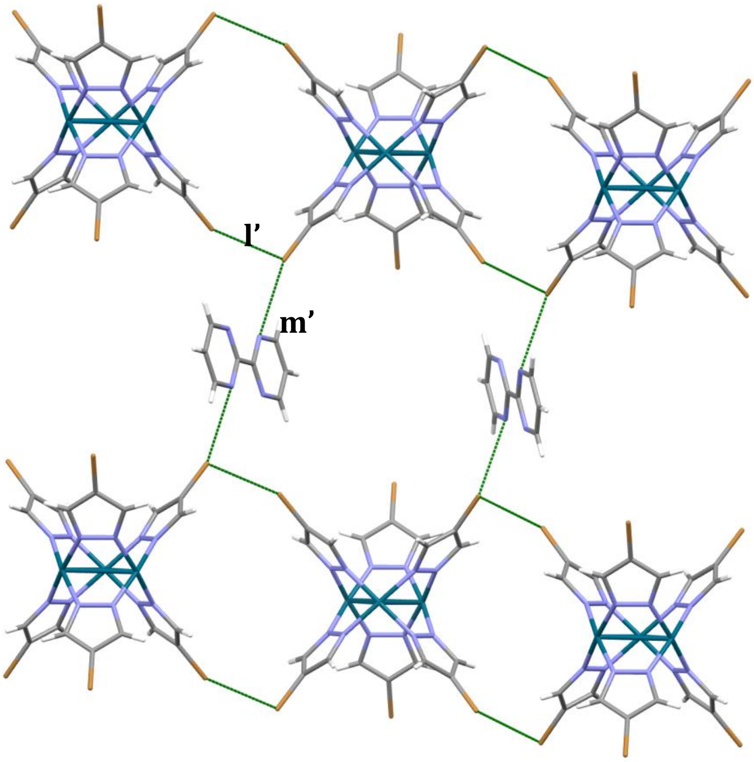

Figure 2.30. *The two-dimensional halogen-bonded supramolecular networks of* ***2.1*** *and bipyrimidine in the structure of* ***2.1·bipm****.*

These halogen-bonded networks are not interpenetrated, but are linked through hydrogen bonding both between clusters, and between clusters and bipyrimidine molecules. Two such halogen-bonded networks and their connection through hydrogen bonding are shown in Figures 2.31 and 2.32.

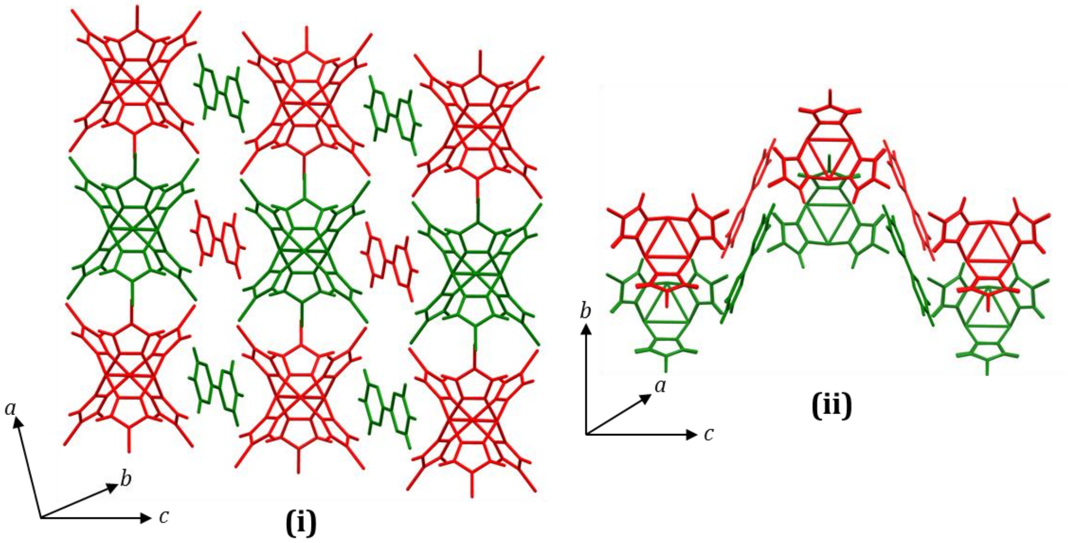

Figure 2.31. ***(i)*** *A colour-coded view of Figure 2.29 to show the two halogen-bonded networks, one in red and the other in green.* ***(ii)*** *An orthogonal view of the same colour-coded supramolecular networks, showing that the two are not interpenetrated.*

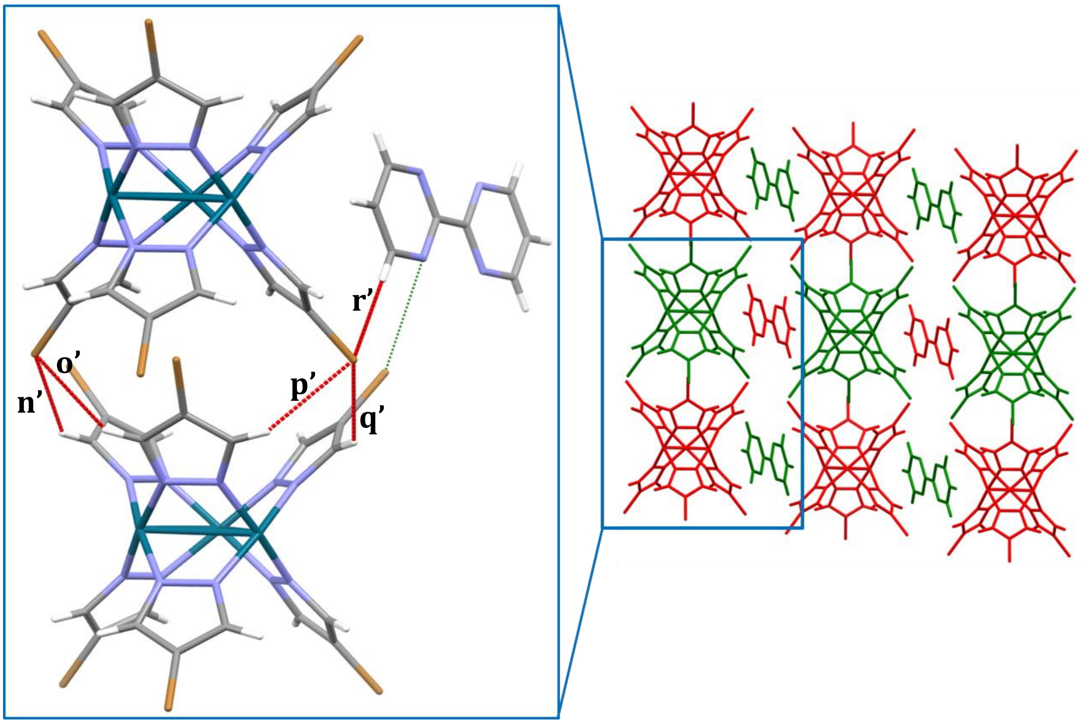

Figure 2.32. *Hydrogen bonding connecting the halogen-bonded supramolecular networks of cluster* ***2.1*** *and bipyrimidine in the structure of* ***2.1·bipm****. The colour coding for the structure on the right is the same as Figure 2.31.*

Table 2.33. *Hydrogen ("H-bond"), halogen bond/halogen-halogen interactions ("X-bond"/"X···X") and other interaction geometries for compound* ***2.1·bipm****. Interactions are listed as labelled in Figures 2.30 and 2.32.*

Interaction		X/H···A (Å)	θ(D–X/H···A) (°)	θ(R–A···X/H) (°)	$r_X + r_A$ (Å)[a]	R_{XA}[a]
l' X-bond	C–Br···Br–C	3.5549 (2)	152.2544 (16)	107.73946 (14)	3.70	0.96
m' X-bond	C–Br···N	3.3726 (3)	149.285 (3)	132.989 (4)	3.40	0.99
n' H-bond	C–H···Br	2.841	134.68	136.56	3.05	0.93
o' H-bond	C–H···Br	2.849	138.90	95.81	3.05	0.93
p' H-bond	C–H···Br	2.833	142.37	92.16	3.05	0.93
q' H-bond	C–H···Br	2.890	131.56	136.83	3.05	0.95
r' H-bond	C–H···Br	2.817	174.99	73.82	3.05	0.92

[a]*See references given for Table 2.11 for definitions of 'R_{XA}'. Hydrogen bond lengths normalised to neutron diffraction values.*[34]

The structural motifs which were intended to be included within this co-crystal structure appear to be present. The bipyrimidine molecules are stacked into the angular cavities between clusters, and a halogen-bonding supramolecular network has been created, supported by C–Br···N halogen bonds. However bifurcated halogen bonds were not formed, and hydrogen bonding still supports the structure, connecting the 2D halogen-bonded networks in the third dimension. Even so, in comparison with the family of dihalomethane solvates **2.1·DCM**, **2.1·DBM** and **2.1·DIM**, it may be argued that a greater degree of control has been exerted over the self-assembly of the **2.1·bipm** co-crystal.

2.3.2 Simple complexes of 1*H*-4-halopyrazoles with Pd^{II}

Simple complexes of the halopyrazole ligands and palladium chloride could be prepared by using the same synthetic conditions as to make **2.1·MeCN** and **2.2·MeCN**, but in the absence of base. This gave another small family of complexes with interesting comparative hydrogen- and halogen-bonding properties.

trans-[PdCl$_2$(HXpz)$_2$], 2.3 (X=Br) and 2.4 (X=I)

trans-[PdCl$_2$(HXpz)$_2$], **2.3** (X=Br) and **2.4** (X=I) are isostructural compounds, in which molecules are connected by networks of hydrogen- and halogen bonding, with some minor but notable differences in the intermolecular interactions between them.

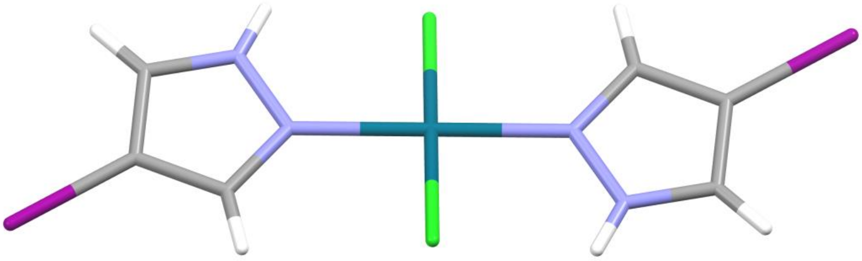

Figure 2.34. *Molecular structure of [PdCl$_2$(HIpz)$_2$]* ***2.4****.*

Type II halogen-halogen interactions (halogen bonds of the type C–X···Cl–Pd) connect complexes into a 2D network in both structures. These networks are two-fold interpenetrated, as is shown in Figure 2.35. However, upon assessing the hydrogen bonding in the structures, two different types of hydrogen bonds are apparent, occurring over different interaction distances (R_{XA}) in each structure.

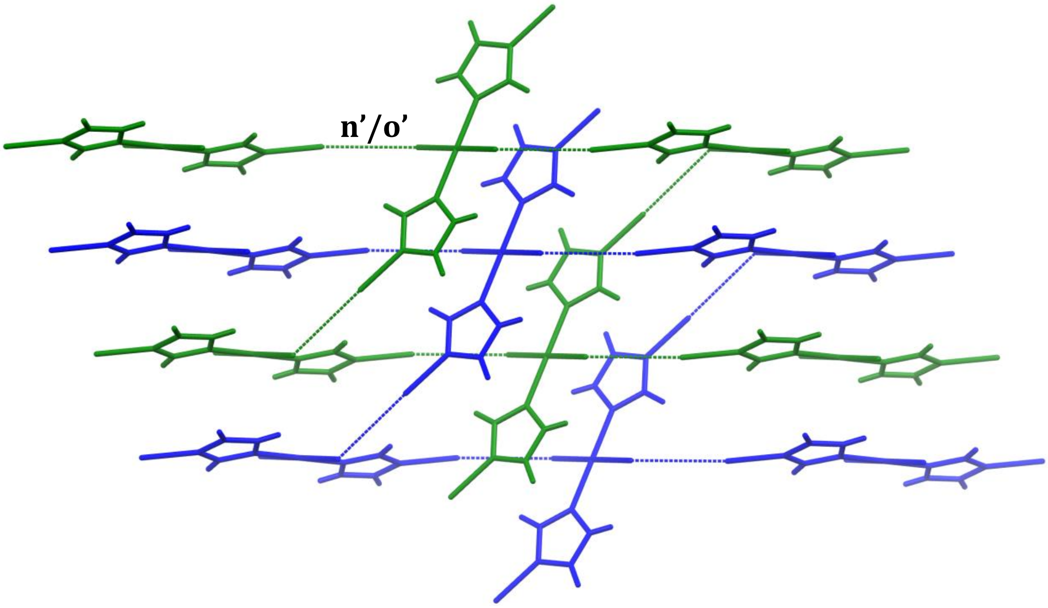

Figure 2.35. *Interpentrated halogen-bond networks in* ***2.3*** *and* ***2.4*** *(structure* ***2.4*** *in this Figure), one shown in green and the other in blue. Interaction* ***n'*** *corresponds to the structure* ***2.3****, and* ***o'*** *corresponds to the same interaction in* ***2.4****.*

Structures **2.3** and **2.4** contain N–H···Cl hydrogen bonds of between the 'inorganic' halogen Cl and the halopyrazole (see Figure 2.36). This type of hydrogen bond has been described previously in the literature (most commonly where the halogen is Cl, Br or I).[40,41] This interaction occurs, however, over a longer range in the bromo-analogue **2.3** (greater than the sum of van der Waals radii).

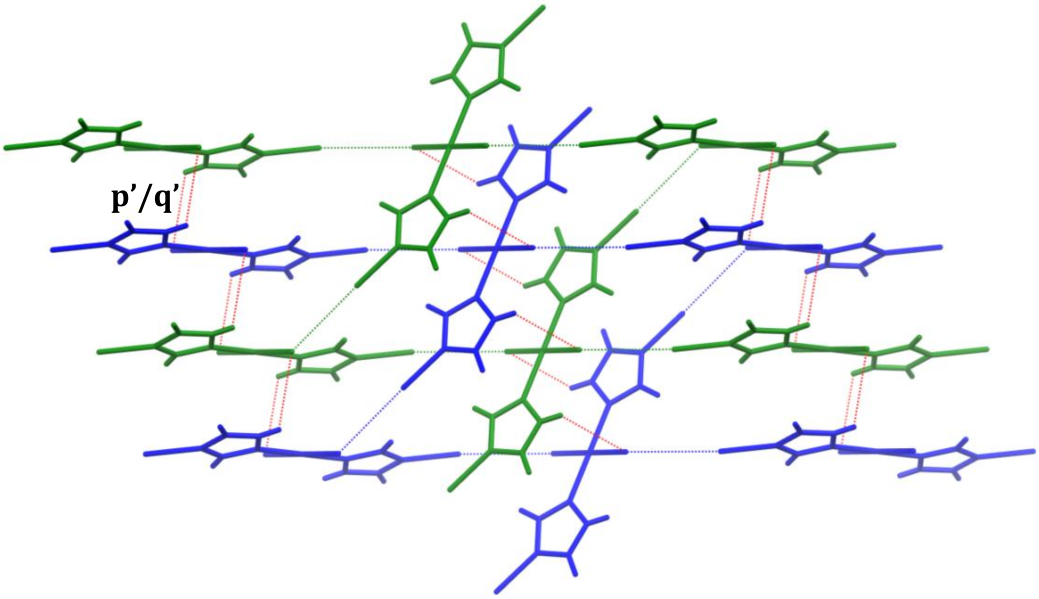

Figure 2.36. *Hydrogen bonding (shown in red) connecting halogen-bonded networks in* ***2.4*** *(and in* ***2.3*** *over a longer range). Interaction* ***p'*** *corresponds to the structure* ***2.3****, and* ***q'*** *corresponds to the same interaction in* ***2.4****.*

However, in the bromo- analogue **2.3**, the apparent short-range hydrogen bonds connecting the halogen-bonded networks are of the type N–H···Br (see Figure 2.37). This hydrogen bonding also extends the interconnected networks into a third dimension (see Figure 2.37), creating a highly connected framework of hydrogen bonding. These interaction geometries in the iodinated structure **2.4** are also calculated for comparison, and are shown in Table 2.39).

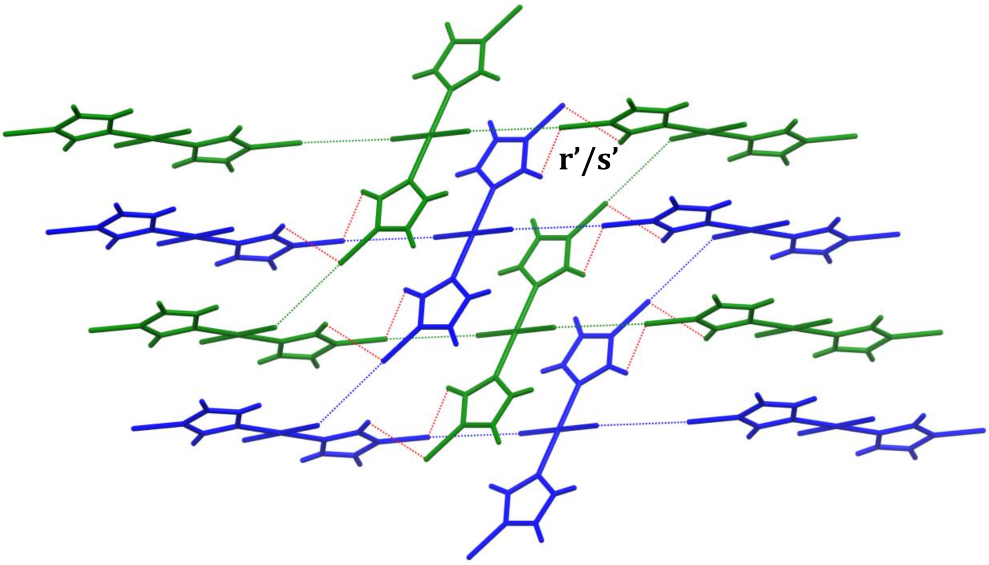

Figure 2.37. *Hydrogen bonding (shown in red) connecting the 2D interpenetrated halogen-bonded networks in **2.3**. Again, one such network is in green, and the other in blue. Interaction **r'** corresponds to the structure **2.3**, and **s'** corresponds to the same interaction in **2.4**.*

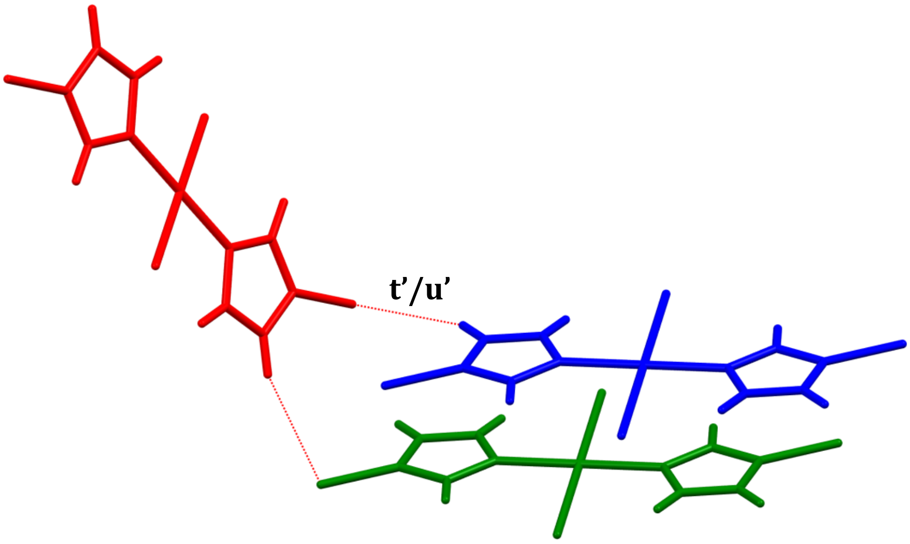

Figure 2.38. *Hydrogen bonding (shown in red) in the third dimension, connecting to the 2D halogen-bonded networks shown in Figure **2.32**. The additional complex in the third dimension is shown in red for clarity. Interaction **t'** corresponds to the structure **2.3**, and **u'** corresponds to the same interaction in **2.4**.*

Table 2.39. *Hydrogen ("H-bond"), halogen bond/halogen-halogen interactions ("X-bond"/"X···X") and other interaction geometries for compounds **2.3** and **2.4**. Interactions are listed as labelled in Figures 2.35 to 2.38. Interactions corresponding to the brominated **2.3** are above the bold line, and to the iodinated **2.4** below the bold line.*

Interaction		X/H···A (Å)	θ(D–X/H···A) (°)	θ(R–A···X/H) (°)	$r_X + r_A$ (Å)[a]	R_{XA}[a]
n' X-bond	C–Br···Cl–Pd	3.4808 (3)	173.9854 (8)	125.782 (5)	3.60	0.97
p' H-bond[b]	N–H···Cl–Pd	2.914	112.67	81.81	2.95	0.99
r' H-bond[b]	C–H···Br–C	2.955	119.39	101.12	3.05	0.97
t' H-bond[b]	C–H···Br–C	2.897	153.33	107.08	3.05	0.95
o' X-bond	C–I···Cl–Pd	3.47847 (9)	171.1550 (3)	125.270 (2)	3.73	0.93
q' H-bond[b]	N–H···Cl–Pd	2.836	113.99	82.49	2.95	0.96
s' H-bond[b]	C–H···I–C	3.151	116.15	96.92	3.18	0.99
u' H-bond[b]	C–H···I–C	3.113	150.92	108.78	3.18	0.98

[a]See references given for Table 2.11 for definitions of 'R_{XA}'. Hydrogen bond lengths normalised to neutron diffraction values.[34]

Comparing the same halogen- and hydrogen- bonding motifs in **2.3** and **2.4**, using Table 2.39 demonstrates the effect of changing the halogen on the competition between these interactions.

Clearly in both cases the halogen bond is important in the packing of the complexes, but more so in the iodinated structure **2.4**, where it occurs over a shorter reduced distance, R_{XA}. This is explained by the larger 'σ-hole' on iodine, more capable of acting as a halogen bond donor, in comparison with that on bromine.

The hydrogen bonds in both structures are quite long – close to the sum of the van der Waals radii for the atoms involved. The slightly shorter distances for the C–H···Br hydrogen bonds in **2.3** compared with the analogous C–H···I hydrogen bonds in **2.4** correspond to the better hydrogen-bond acceptor ability of bromine, compared with iodine.[41]

cis-[PdCl$_2$(4-chloro-1-amidinopyrazol-)], 2.5

Analogous synthesis using 4-chloropyrazole did not give crystals isostructural with **2.3** and **2.4**, but instead crystals of *cis*-[PdCl$_2$(4-chloro-1-amidinopyrazol-)], **2.5** were found. The chloropyrazole had reacted in solution with the acetonitrile to form a new, unexpected chelating ligand. This structure also contains novel hydrogen- and halogen-bonded motifs, as explained below.

Complexes of **2.5** are connected in 1D chains by pairs of hydrogen bonds and halogen bonds. Hydrogen bonds are between either the protonated N atom in the amidino-group (or the aryl hydrogen on pyrazole), and the 'inorganic' halogen Cl attached to the metal (N–H···Cl or C–H···Cl). The halogen bonds are between these halogens, and those on the ligand.

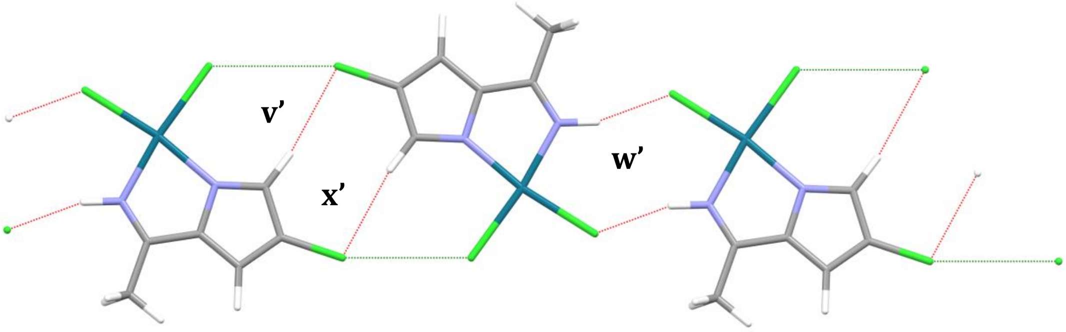

Figure 2.40. *1D hydrogen-bonded (shown in red) and halogen-bonded (shown in green) chains of complex* ***2.5****.*

These chains of complexes are connected to others in a second dimension by additional hydrogen bonds, accepted by the chloride ligand. These are donated by the other aryl hydrogen on the pyrazole ring (C–H···Cl).

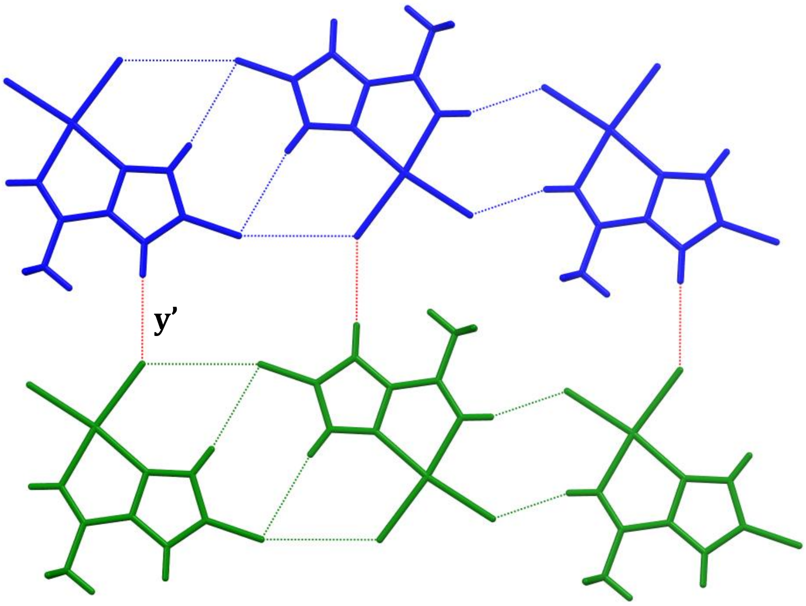

Figure 2.41. *Hydrogen bonding (shown in red) connecting the 1D halogen-bonded/hydrogen-bonded chains shown in Figure 2.40, extending into a second dimension. The previously described, separate halogen-/hydrogen-bonded chains from Figure 2.40 are shown in green and blue for clarity.*

It can be seen that the structure of **2.5** is hydrogen-bond dominated. All of the hydrogen bonds shown in Figures 2.40 and 2.41 (geometries given in Table 2.42) are less than the sum of van der Waals radii. The geometry of the halogen bond between the ‘inorganic’ halogen and the pyrazole halogen suggests it is a type I halogen-halogen interaction.

Table 2.42*. Hydrogen (“H-bond”), halogen bond/halogen-halogen interactions (“X-bond”/”X···X”) and other interaction geometries for compound* ***2.5****. Interactions are listed as labelled in Figures 2.40 and 2.41.*

Interaction		X/H···A (Å)	θ(D–X/H···A) (°)	θ(R–A···X/H) (°)	$r_X + r_A$ (Å)[a]	R_{XA}[a]
v’ X···X	C–Cl···Cl–Pd	3.4921 (15)	160.37 (17)	126.58 (5)	3.50	0.99
w’ H-bond[b]	N–H···Cl–Pd	2.315	155.94	124.12	2.95	0.87
x’ H-bond[b]	C–H···Cl–Pd	2.933	168.28	101.13	2.95	0.99
y’ H-bond[b]	C–H···Cl–Pd	2.614	176.78	143.51	2.95	0.87

[a] *See references given for Table 2.11 for definitions of ‘R_{XA}’. Hydrogen bond lengths normalised to neutron diffraction values.*[34]

The reaction of the 4-chloropyrazole ligand toward acetonitrile in the presence of M^{II} does have precedent in the literature. The first example this was shown in 1986 by McCleverty and co-workers, where that nucleophilic attack on acetonitrile under relatively mild conditions was facilitated by the coordination of acetonitrile to a metal.[42] This specific nucleophilic attack (acetonitrile and pyrazole) has been reported and this reaction mechanism confirmed less than a dozen times in the literature,[42–51] and only ever in the presence of metals.

Points of synthetic interest, such as whether or not the novel ligand can be removed from the complex, and why this reaction occurs where the nucleophile is 4-chloropyrazole, but not when it is 4-bromo- or 4-iodopyrazole were not studied further. The latter may be due to the relative stability of 4-chloropyrazolate as a free conjugate base relative to the bromo- or iodo- congeners.

Although a series of three isostructural complexes (iodo-, bromo-, chloro-) cannot be discussed, it is shown that structures **2.3** and **2.4** (based on iodo- and bromo- ligands, which act as better halogen bond donors) contain supramolecular halogen bonding networks, whereas the structure of **2.5** (based on chloro- ligands) is based on a mixed halogen- and hydrogen-bonding supramolecular network.

2.3.3 Cubic clusters [Pt_2Ag_4(4-halopyrazolate)$_8$]

The second pyrazolate cluster of interest published by Umakoshi and co-workers was the cubic cluster [$Pt_2Ag_4(pz)_8$]·(solvent).[19] The 4-halopyrazolate analogues provide an interesting point of comparison, as they may serve as halogen bonding nodes, each cluster containing eight halopyrazolates (one at each vertex of the cube), thus providing a cubic arrangement of halogen atoms.

[Pt_2Ag_4(4-bromopyrazolate)$_8$]·3MeCN, 2.6

Analogous synthetic conditions to those used to create the halogen-free cluster [$Pt_2Ag_4(pz)_8$]·(solvent),[19] were used to create the brominated cluster [$Pt_2Ag_4(Brpz)_8$]·3MeCN, **2.6·MeCN**. This cluster packs in the solid state with three equivalents of acetonitrile, and features extensive halogen- and hydrogen- bonding between clusters.

The cubic shape of the clusters facilitates the formation of a Br_4 halogen-bonded square motif (C–Br···Br–C), as shown in Figure 2.43. This is four type II halogen-halogen interactions (halogen bonds), between four bromine atoms. Each bromine atom in the motif is both an acceptor and a donor of a halogen bond, creating a square. This connects four separate clusters, and occurs at every bromine atom in the cluster, thus creating a 2D network of clusters connected by this motif.

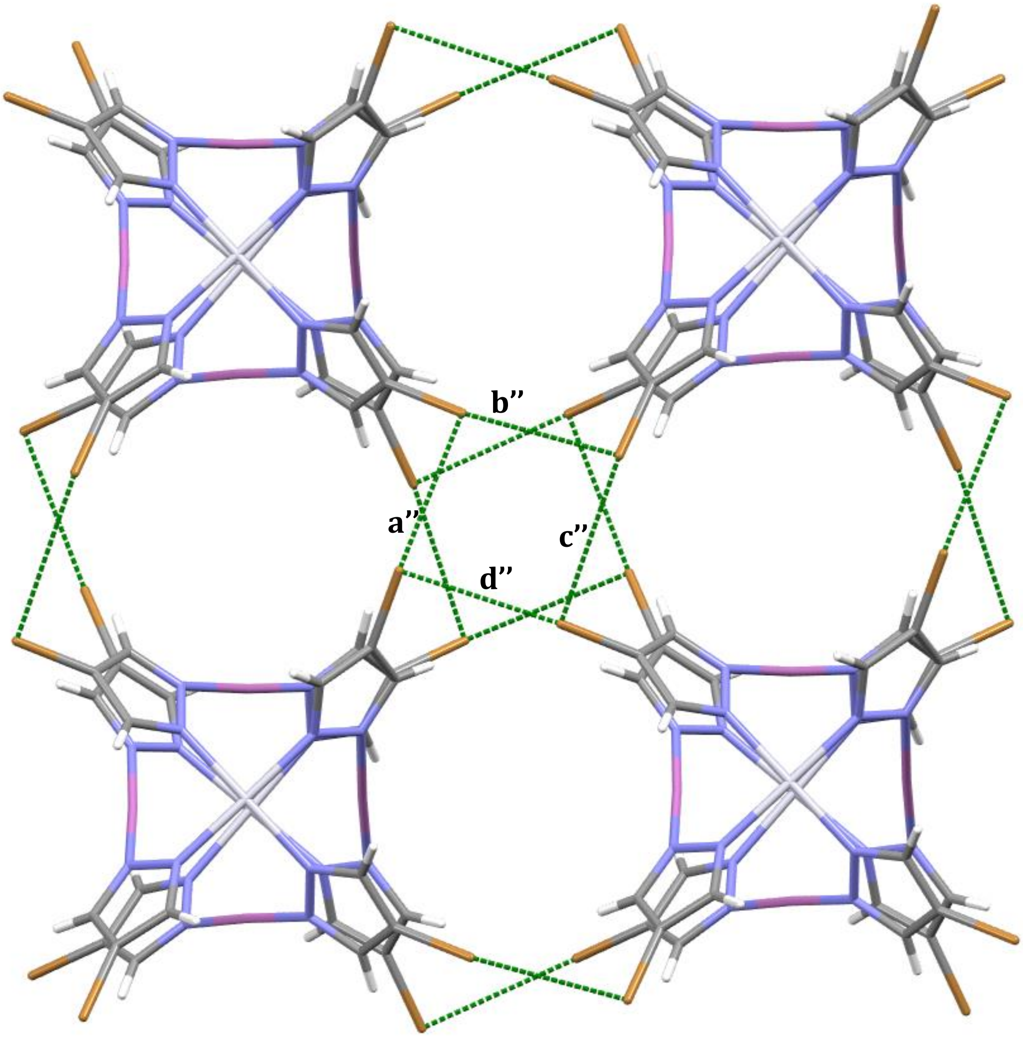

Figure 2.43. *Halogen bonds comprising the Br_4 square motif, between four clusters of* ***2.6****, in the structure* ***2.6·MeCN*** *(solvent omitted for clarity). Two full Br_4 square motifs are shown in the centre of the image, with one between the four pyrazolates pointing out of the plane of the page, and between the four pointing into the plane of the page. Halogen bonds at the edges of the image are part of adjacent Br_4 square motifs not complete in this image.*

These layers of halogen-bonded clusters are connected in the third dimension by hydrogen bonding between the aryl hydrogen atoms and the bromine atoms involved in the halogen bonded squares (C–H···Br–C). Two crystallographically unique hydrogen bonds can be found, existing as dimers of interactions between clusters (see Figure 2.44).

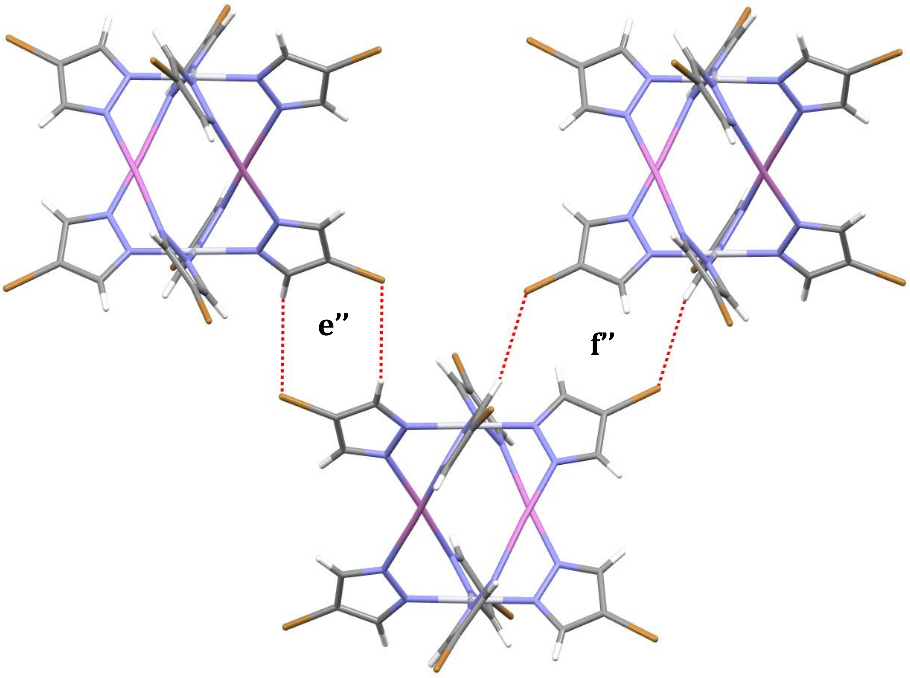

Figure 2.44. *Hydrogen bond dimers connecting layers of clusters involved in the* Br_4 *halogen bonding motif.*

The structure also contains three equivalents of acetonitrile. Two of these are found to be crystallographically disordered in two orientations. Neither of these orientations demonstrates a strongly identifiable intermolecular interaction with the cluster. This makes sense, as if there are no strong interactions holding a solvent molecule in place, it is more free to occupy alternative orientations, as is often seen in MOFs, where positional disorder of solvent molecules can become so great that the solvent is not crystallographically located (see also examples in chapter 4).

The acetonitrile molecule that could be crystallographically located in a single orientation accepts a hydrogen bond from aryl hydrogen atom, C≡N···H–C. In addition, the $-CH_3$ group on the acetonitrile appears to donate a hydrogen bond to a bromine atom on a cluster in the next 'Br_4 layer.' These interactions are shown in

Figure 2.45, with interaction **e''** for visual reference. The geometry of these hydrogen bonds are featured in Table 2.46.

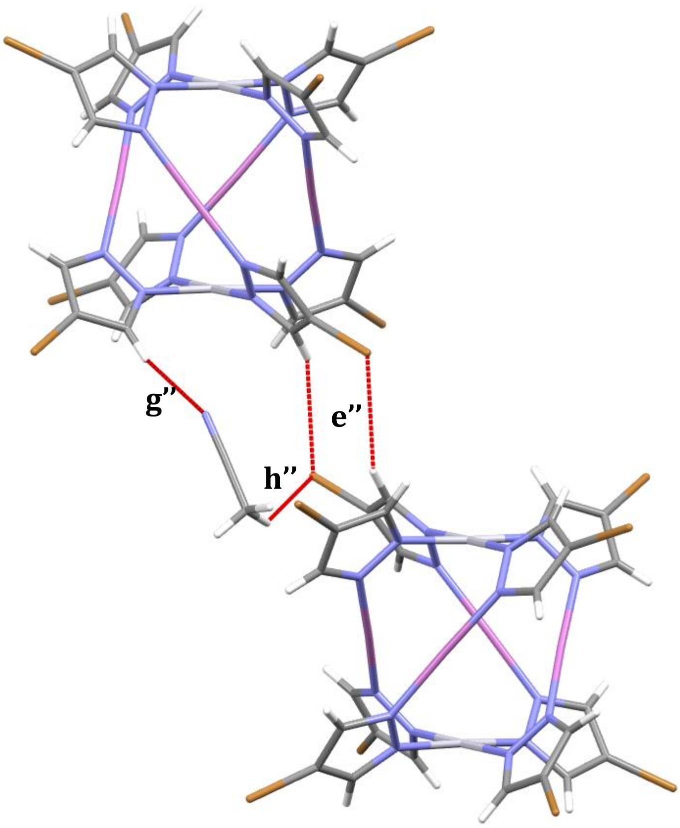

Figure 2.45. *Hydrogen bonds between crystallographically ordered solvent and adjacent clusters of* ***2.6*** *in structure* ***2.6.MeCN****. Hydrogen bond dimer* ***e''*** *from Figure 2.44 is also shown for visual reference.*

Table 2.46. *Hydrogen ("H-bond"), halogen bond/halogen-halogen interactions ("X-bond"/"X···X") and other interaction geometries for compound* ***2.6·MeCN****. Interactions are listed as labelled in Figures 2.43, 2.44 and 2.45.*

Interaction		X/H···A (Å)	θ(D–X/H···A) (°)	θ(R–A···X/H) (°)	$r_X + r_A$ (Å)[a]	R_{XA}[a]
a’’ X-bond	C–Br···Br–C	3.5968 (2)	155.900 (2)	90.825 (3)	3.70	0.97
b’’ X-bond	C–Br···Br–C	3.5207 (2)	167.2020 (9)	92.855 (3)	3.70	0.95
c’’ X-bond	C–Br···Br–C	3.8031 (2)	145.320 (3)	94.745 (3)	3.70	1.05
d’’ X-bond	C–Br···Br–C	3.6027 (2)	158.233 (2)	92.767 (3)	3.70	0.97
e’’ H-bond	C–H···Br–C	2.829	146.24	119.47	3.05	0.93
f’ H-bond	C–H···Br–C	2.897	144.91	112.51	3.05	0.95
g’’ H-bond	C–H···N≡C	2.371	155.00	146.64	2.75	0.86
h’’ H-bond	C–H···Br–C	2.945	135.39	71.28	3.05	0.97

[a] *See references given for Table 2.11 for definitions of 'R_{XA}'. Hydrogen bond lengths normalised to neutron diffraction values.*[34]

As shown in Table 2.46, hydrogen bonding between clusters and to the ordered acetonitrile solvent plays a significant role in the packing of clusters of **2.6** in the solid state. The iodo- analogue was pursued, to determine if the X$_4$ square motif would be replicated, and to find what role hydrogen bonding would play in the packing of the clusters.

[Pt$_2$Ag$_4$(Ipz)$_8$], 2.7

Crystals of cluster **2.7** were obtained by the same method as used to give **2.6·MeCN**, but using 4-iodopyrazole instead of 4-bromopyrazole. **2.7** is also a cubic cluster of the same type as **2.6**, but does not crystallise as a solvate. The X$_4$ square motif is also not present, instead 2D networks of clusters are formed via the C–I···π motif, as in structure **2.2·MeCN** and the Brammer group's previous work with iodobenzoate clusters.[17,18] Every iodopyrazolate group on the cluster is involved in this motif. A pair of clusters and the halogen bonds between them are shown in Figure 2.47, and demonstrate the similarity of this motif to the C–I···π dimer (where two such interactions exist between a pair of clusters).

In addition, each iodine which accepts a halogen bond (as described above) is also within short distance (< sum of van der Waals radii) of a silver (I) ion in the neighbouring cluster, in a manner similar to that of the diiodomethane solvent in structure **2.1·DIM**, discussed previously in section 2.3.1.2.[36,37]

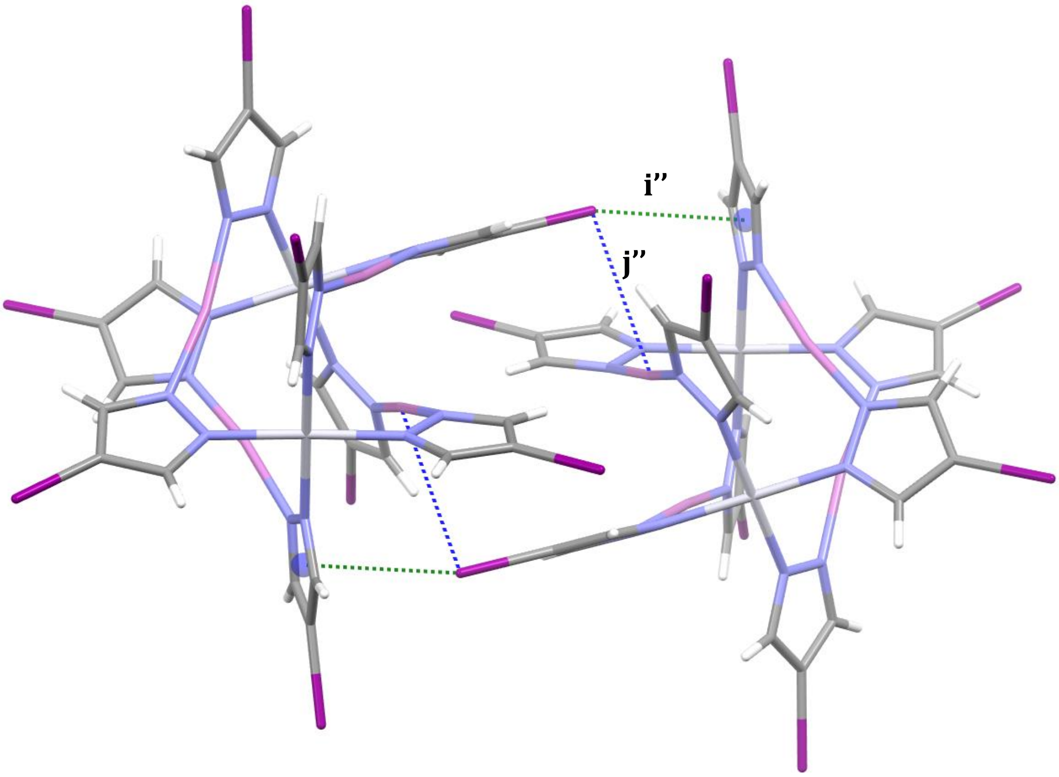

Figure 2.47. *A pair of clusters connected by the C–I···π halogen bonding motif (shown in green) in **2.7**, and interaction between silver (in pink) and iodine (interaction in blue).*

As in structure **2.6.MeCN**, these halogen-bonded layers are connected in the third dimension by hydrogen bonding between the aryl hydrogen atom and the halogen (see Figure 2.48). However in **2.7**, this occurs at distances greater than the sum of van der Waals radii, indicating that this is a weaker interaction. This again demonstrates that iodine is a poorer hydrogen bond acceptor than bromine due to its larger atomic radius, and more diffuse electron density.

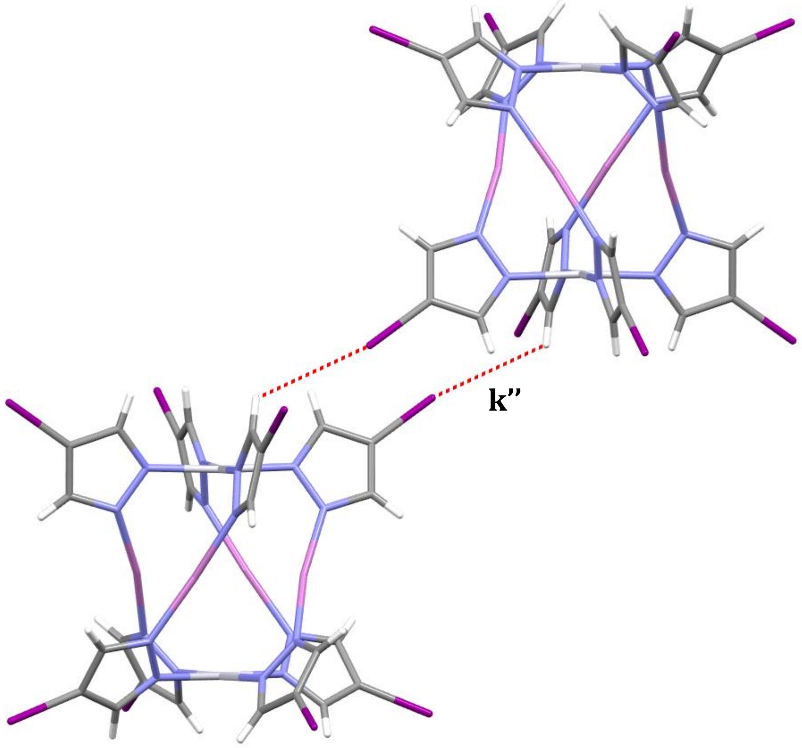

Figure 2.48. *Hydrogen bonding between clusters in different halogen-bonded 2D networks in* ***2.7****.*

Table 2.49. *Hydrogen ("H-bond"), halogen bond/halogen-halogen interactions ("X-bond"/"X···X") and other interaction geometries for compound* ***2.7****. Interactions are listed as labelled in Figures 2.47 and 2.48.*

Interaction		X/H···A (Å)	θ(D–X/H···A) (°)	θ(R–A···X/H) (°)	$r_X + r_A$ (Å)[a]	R_{XA}[a]
i'' X-bond	C–I···π	3.38313 (7)	n/a	164.2 (3)	3.62	0.93
j'' M···X	Ag···I–C	3.580 (1)	n/a	95.0 (3)	3.70	0.97
k'' H-bond	C–H···I–C	3.252	117.92	160.21	3.18	1.02

[a] *See references given for Table 2.11 for definitions of 'R_{XA}'. Hydrogen bond lengths normalised to neutron diffraction values.*[34]

The effect of changing the halogen in moving from **2.6.MeCN** to **2.7** is clear – replacing bromine with iodine favours the C–I···π motif, and the formation of weaker hydrogen bonds in comparison to bromine. This demonstrates again that although bromine is very versatile as both a donor and acceptor of intermolecular interactions in the solid state, it is difficult to predict the interactions it will form in self-assembly.

2.4 Conclusions & Future work

Stellated clusters based on halopyrazolates have demonstrated a highly versatile range of interactions with solvents capable of hydrogen- and halogen-bonding. In all but one case, the clusters crystallise as solvates, further emphasising the inefficient packing of stellated materials and their need for a crystallisation 'partner'.

Such clusters containing iodopyrazolate demonstrate a persistent preference for halogen bonding, in particular the C–I⋯π motif, due to the larger σ-hole on iodine, in comparison to bromine.

In recrystallising stellated cluster **2.1** from three dihalomethanes, the capability of highly-connective solvent molecules to order other molecules about them in the solid state was demonstrated, particularly in the case of dichloromethane. The formation of different relative amounts of hydrogen- and halogen-bonding in these structures was shown. Moving from dichloromethane (better hydrogen bond donor/acceptor) to diiodomethane (better halogen bond donor), the dominance of hydrogen- and halogen-bonds in the structure was deliberately altered.

Finally, the selection of a co-crystallising 'partner' molecule for **2.1** was made (bipyrimidine), based on the size and shape of the cavities around cluster **2.1** and the intermolecular interactions it is capable of supporting, and the crystal engineering of a co-crystal of these molecules was successfully demonstrated.

Simple complexes of 1*H*-4-X-pyrazoles (X = Cl, Br, I) were synthesised. In the case of the chlorinated ligand, a reaction with acetonitrile solvent occurred, giving a complex of an amidinopyrazole ligand **2.5**. The structure of **2.5** was shown to be dominated by hydrogen bonding. The isostructural **2.3** and **2.4** (X = Br, I respectively) gave structures based on both halogen bonds and weak hydrogen bonds. A comparison of the halogen bond distances in the two structures indicated that the C–X⋯Cl halogen bonding was stronger in the structure of the iodine-containing complex.

Cubic clusters **2.6·MeCN** and **2.7** [Pt_2Ag_4(4-X-pyrazolate)$_8$] (X = Br, I respectively) were synthesised and their structures shown to be dominated by halogen bonding between the clusters. The brominated **2.6** contained a 2D supramolecular network propagated solely by the Br_4 square halogen-bonding motif, and the iodinated **2.7** contained the C–I⋯π motif, persistent in the Brammer group's previous work with iodobenzoate clusters.

Future work on the crystal engineering of these clusters could look at other small molecules that form co-crystals with cluster **2.1** or **2.2**. This could include the design of novel motifs such as crown-ether like molecules that may halogen bond to all halogens on a single face of the cluster in a "king-and-crown" manner (see Figure 2.50).

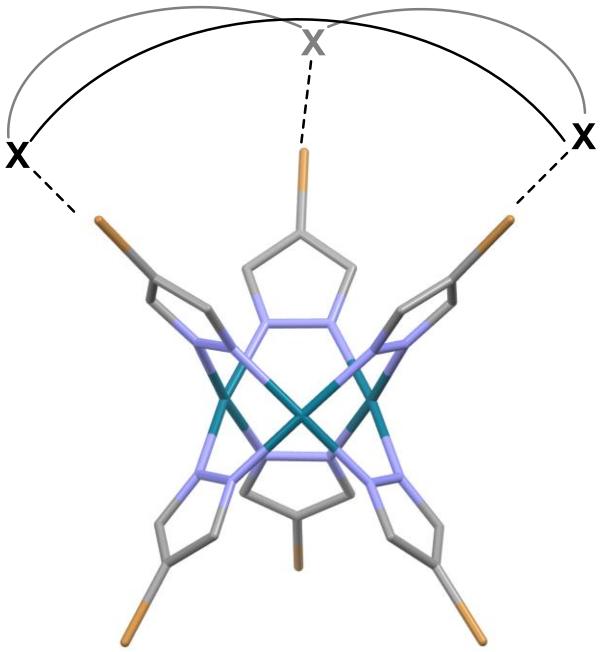

Figure 2.50. *A suggested synthetic target "king-and-crown" motif using cluster* ***2.1*** *and an appropriate crown ether. Here "X" represents some heteroatom capable of receiving halogen bonds (i.e. O, N, S).*

2.5 References

1 G. R. Desiraju, *Angew. Chem. Int. Ed. Engl.*, 1995, **34**, 2311–2327.

2 T. Steiner, *Angew. Chem. Int. Ed. Engl.*, 2002, **41**, 48–76.

3 G. R. Desiraju, *J. Chem. Sci.*, 2010, **122**, 667–675.

4 G. R. Desiraju, *J. Am. Chem. Soc.*, 2013, **135**, 9952–9967.

5 T. Clark, M. Hennemann, J. S. Murray and P. Politzer, *J. Mol. Model.*, 2007, **13**, 291–296.

6 E. Corradi, S. V. Meille, M. T. Messina, P. Metrangolo and G. Resnati, *Angew. Chem. Int. Ed. Engl.*, 2000, **39**, 1782–1786.

7 P. Metrangolo and G. Resnati, *Chem. Eur. J.*, 2001, **7**, 2511–2519.

8 P. Metrangolo, H. Neukirch, T. Pilati and G. Resnati, *Acc. Chem. Res.*, 2005, **38**, 386–395.

9 H. Takezawa, T. Murase, G. Resnati, P. Metrangolo and M. Fujita, *J. Am. Chem. Soc.*, 2013, **136**, 1786–1788.

10 P. Metrangolo and G. Resnati, *IUCrJ*, 2014, 5–7.

11 H. Takezawa, T. Murase, G. Resnati, P. Metrangolo and M. Fujita, *Angew. Chem. Int. Ed. Engl.*, 2015, **54**, 8411–8414.

12 L. Brammer, G. Mínguez Espallargas and S. Libri, *CrystEngComm*, 2008, **10**, 1712–1727.

13 D. A. Smith, L. Brammer, C. A. Hunter and R. N. Perutz, *J. Am. Chem. Soc.*, 2013, **136**, 1288–1291.

14 F. M. Amombo Noa, S. A. Bourne and L. R. Nassimbeni, *Cryst. Growth Des.*, 2015, **15**, 3271–3279.

15 M. J. Langton, S. W. Robinson, I. Marques, V. Felix and P. D. Beer, *Nature Chem.*, 2014, **6**, 1039–1043.

16 L. Brammer, P. Smart and G. Minguez Espallargas, *CrystEngComm*, 2008, **10**, 1335–1344.

17 P. Smart, *Design and synthesis of metal-organic frameworks and their characterisation by single crystal and powder diffraction (PhD Thesis, University of Sheffield)*, 2012.

18 P. Smart, Á. Bejarano-Villafuerte, R. M. Hendry and L. Brammer, *CrystEngComm*, 2013, **15**, 3160–3167.

19 K. Umakoshi, Y. Yamauchi, K. Nakamiya, T. Kojima, M. Yamasaki, H. Kawano and M. Onishi, *Inorg. Chem.*, 2003, **42**, 3907–3916.

20 A. Vlachos, V. Psycharis, C. P. Raptopoulou, N. Lalioti, Y. Sanakis, G. Diamantopoulos, M. Fardis, M. Karayanni, G. Papavassiliou and A. Terzis, *Inorg. Chim. Acta*, 2004, **357**, 3162–3172.

21 A. Figuerola, V. Tangoulis, J. Ribas, H. Hartl, I. Brüdgam, M. Maestro and C. Diaz, *Inorg. Chem.*, 2007, **46**, 11017–11024.

22 C. Serre, F. Millange, C. Thouvenot, M. Noguès, G. Marsolier, D. Louër and G. Férey, *J. Am. Chem. Soc.*, 2002, **124**, 13519–13526.

23 T. Loiseau, C. Serre, C. Huguenard, G. Fink, F. Taulelle, M. Henry, T. Bataille and G. Férey, *Chem. Eur. J.*, 2004, **10**, 1373–1382.

24 F. Salles, G. Maurin, C. Serre, P. L. Llewellyn, C. Knöfel, H. J. Choi, Y. Filinchuk, L. Oliviero, A. Vimont, J. R. Long and G. Férey, *J. Am. Chem. Soc.*, 2010, **132**, 13782–13788.

25 C.-P. Li and M. Du, *Chem. Commun.*, 2011, **47**, 5958–5972.

26 P. F. H. Schwab, F. Fleischer and J. Michl, *J. Org. Chem.*, 2002, **67**, 443–449.

27 R. H. Blessing, *Acta Crystallogr. Sect. B*, 1995, **51**, 33–38.

28 G. M. Sheldrick, *SADABS: Empirical absorption correction program (based on the method of Blessing), 1996*.

29 G. M. Sheldrick, *Acta Crystallogr. Sect. A*, 2008, **64**, 112–122.

30 G. M. Sheldrick, *Acta Crystallogr. Sect. C*, 2015, **71**, 3–8.

31 O. V. Dolomanov, L. J. Bourhis, R. J. Gildea, J. A. K. Howard and H. Puschmann, *J. Appl. Crystallogr.*, 2009, **42**, 339–341.

32 J. P. M. Lommerse, A. J. Stone, R. Taylor and F. H. Allen, *J. Am. Chem. Soc.*, 1996, **118**, 3108–3116.

33 A. Bondi, *J. Phys. Chem.*, 1964, **3**, 441–451.

34 F. H. Allen, *Acta Crystallogr. Sect. B*, 1986, **42**, 515–522.

35 L. C. Gilday, S. W. Robinson, T. A. Barendt, M. J. Langton, B. R. Mullaney and P. D. Beer, *Chem. Rev.*, 2015, **115**, 7118–7195.

36 N. Ramasubbu, R. Parthasarathy and P. Murray-Rust, *J. Am. Chem. Soc.*, 1986, **108**, 4308–4314.

37 R. J. Kulawiec and R. H. Crabtree, *Coord. Chem. Rev.*, 1990, **99**, 89–115.

38 L. Brammer, P. Smart, G. Minguez Espallargas, G. M. Espallargas and L. Brammer, *CrystEngComm*, 2008, **10**, 1335–1344.

39 B. Ji, W. Wang, D. Deng and Y. Zhang, *Cryst. Growth Des.*, 2011, **11**, 3622–3628.

40 G. Aullón, D. Bellamy, G. Orpen, L. Brammer and E. A. Bruton, *Chem. Commun.*, 1998, 653–654.

41 L. Brammer, E. A. Bruton and P. Sherwood, *Cryst. Growth Des.*, 2001, **1**, 277–290.

42 C. J. Jones, J. A. McCleverty and A. S. Rothin, *Dalt. Trans.*, 1986, 109–111.

43 M. R. Kolliparaa, P. Sarkhelb, S. Chakrabortya and R. Lalrempuiaa, *J. Coord. Chem.*, 2003, **56**, 1085–1091.

44 P. Govindaswamy, Y. A. Mozharivskyj and M. R. Kollipara, *J. Organomet. Chem.*, 2004, **689**, 3265–3274.

45 E. Reisner, V. B. Arion, A. Rufi, I. Chiorescu, F. Schmid and B. K. Keppler, *Dalt. Trans.*, 2005, 2355–2364.

46 M. Arroyo, Á. López-Sanvicente, D. Miguel and F. Villafañe, *Eur. J. Inorg. Chem.*, 2005, **2005**, 4430–4437.

47 M. Arroyo, D. Miguel, F. Villafañe, S. Nieto, J. Pérez and L. Riera, *Inorg. Chem.*, 2006, **45**, 7018–7026.

48 B. Cebrián-Losantos, E. Reisner, C. R. Kowol, A. Roller, S. Shova, V. B. Arion and B. K. Keppler, *Inorg. Chem.*, 2008, **47**, 6513–6523.

49 C. C. Hsieh, C. J. Lee and Y. C. Horng, *Organometallics*, 2009, **28**, 4923–4928.

50 X. Liu and W. Chen, *Dalt. Trans.*, 2012, **41**, 599–608.

51 Q. Liang, Y.-L. Wang, Y. Zhao and G.-J. Cao, *Acta Crystallogr. Sect. C*, 2014, **70**, 182–184.

Stellated halogenated cluster compounds:

Towards porous molecular materials for selective gas sorption

3

Chapter Three

3.1 Introduction

The work described in this chapter continues from that in chapter 2, in which the crystal engineering aspects of stellated clusters were explored. Here, their functionality as potentially porous molecular crystals is investigated.

3.1.1 Porous molecular crystals

Molecular materials have been shown to act as hosts for gaseous guests,[1–10] particularly so where cavities exist intrinsic to the molecule (such as porous organic cages – see Figure 3.1).[4,6–8,10] Porous organic cages are organic molecules which are designed to adopt a conformation in the solid state that creates a cavity within the molecule. The high degree of control over the packing of cages (i.e. to recrystallise and re-arrange the discrete molecules, or to co-crystallise them with different cages)[7,10] has been shown to affect their solid-state properties, such as their gas uptake properties is one aspect that has made them attractive to study, in comparison with MOFs.

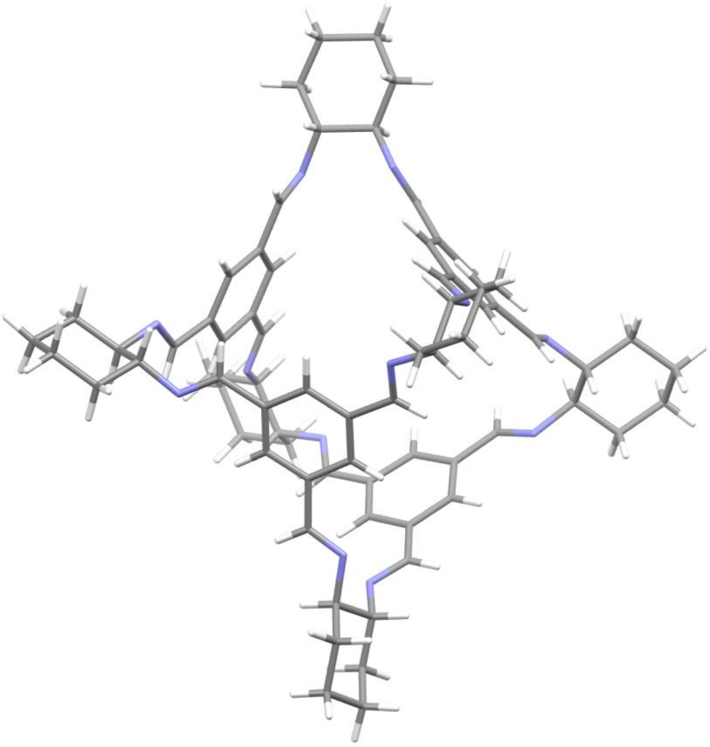

Figure 3.1. *A porous organic cage containing intrinsic, designed voids, which are capable of taking up gas.*[8]

Molecular crystals with extrinsic porosity have also been explored. The work of Barbour and Atwood on calixarene-based systems has demonstrated the inefficient packing of these bowl-shaped molecules with long alkyl substituents can template the formation of extrinsic voids which are capable of capturing gas (see Figure 3.2).[1,2,11,12]

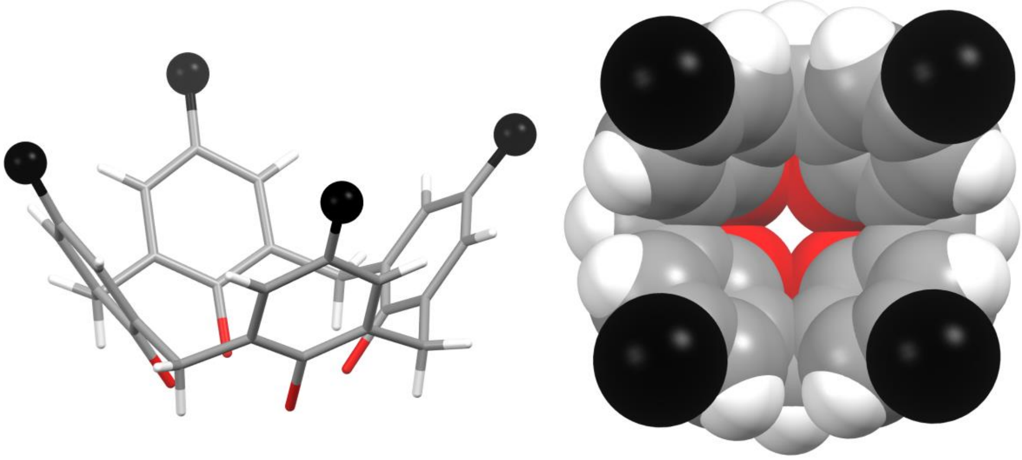

Figure 3.2. Left: *A calixarene of the type used by Barbour and Atwood to create molecular crystals capable of taking up gas. The black sphere represents some alkyl group.* ***Right:*** *A top-down view of the bowl-shaped cavity effected by the calixarene.*

As well as exploration of angular molecules such as calixarenes as noted above, the pre-organisation of pores within molecular crystals has been explored by using specific intermolecular interactions. One particularly noteworthy case is the exploitation of π···π stacking of ligands. This study used a ruthenium cluster with mixed fluorinated and non-fluorinated biphenyl carboxylate ligands, and the designed complementarity of these electron-rich and –poor rings enabled a π-stacking templated pore formation (see Figure 3.3).[9]

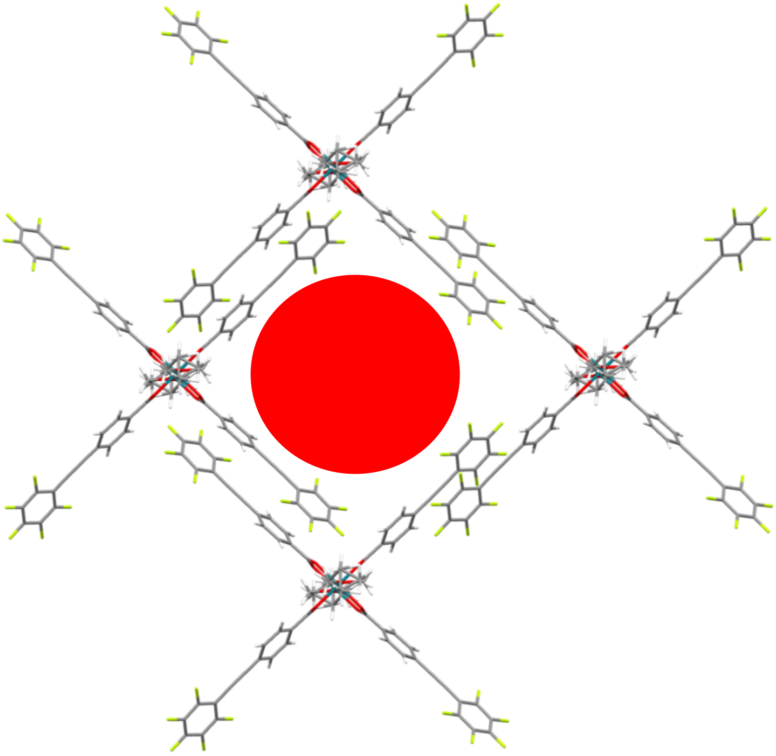

Figure 3.3. *Formation of pores in [Ru_2(4-perfluorophenylethynylbenzoate)$_4$(THF)$_2$], due to π-stacking of molecular clusters.*[9] *The pore is represented here by a red circle.*

This porous molecular material resembles most MOFs in that it possesses regular pores which are present in the as-synthesised material already, and do not change upon desolvation or gas uptake. The porous character of crystals of the cluster in Figure 3.3, and of most MOFs is referred to as 'second-generation' porosity by Kitagawa, and it is noted that 'soft porous' or 'third-generation' materials (those which lose their porosity on desolvation, and re-inflate upon introduction of gas) may prove more interesting targets (see introduction section 1.3.1.2).[13]

3.1.2 Chapter aims

The strong solvent-dependence of the crystal structure of **2.1·MeCN**, [Pd_3(4-bromopyrazolate)$_6$]·3MeCN (and the other solvates of **2.1** outlined in chapter 2), as well as the angular cavities effected by its stellated shape, led to its investigation as a potentially porous molecular material. The aim for creating porosity in **2.1** was to desolvate the material, potentially creating pores extrinsic to the clusters, which would pack inefficiently due to their stellated shape (as for the calixarenes as noted above). This would leave voids capable of adsorbing new guests.

3.2 Experimental

3.2.1 Synthesis

Compound **2.1·MeCN** was synthesised and characterised as described in chapter 2.

3.2.2 Powder X-ray diffraction

The crystalline **2.1·MeCN** was ground in a pestle and mortar and packed into capillaries (of the types specified below) before data collection. In all cases (except where specified), data were collected at ambient temperature.

X-ray diffraction data for the air-dried sample of **2.1·MeCN** were recorded on a Cu $K\alpha_2$ Bruker D8 ADVANCE X-Ray powder diffractometer operating in capillary mode. The sample was packed in a 0.5 mm borosilicate capillary. The instrument was fitted with a focusing Göbel mirror optic and a high-resolution energy-dispersive Lynxeye XE detector. Scans were collected between 5-40° 2θ using a step size of 0.15° and step time of 5 sec, giving a total exposure time of 190 mins. The sample capillary was spun about its axis at a rate of 30 rev min^{-1}.

X-ray diffraction data for the *in-situ* desolvation and subsequent gas uptake studies were collected at beamline I11 at Diamond Light Source (λ = 0.825821 Å for CO_2 study, λ = 0.826210 (5) Å for N_2 study),[14,15] equipped with a wide angle (90°) PSD detector comprising 18 Mythen-2 modules, and a multi analyser crystal (MAC) detector, comprising five MAC modules, each containing 9 MAC channels.

In the case of Mythen-2 data (where specified below), a pair of scans was conducted, related by a 0.25 ° detector offset to account for gaps between detector modules. Four such scan pairs were collected at six seconds exposure per scan, whilst the sample capillary was rotated about its axis over an 80° range, to average beam exposure. The resulting patterns were summed to give the final pattern for structural analysis (total beam exposure time 48 seconds).

In the N_2 uptake study, data using the Mythen-2 detector was too badly affected by the wavelength of X-rays used being close to the absorption edge for Bromine, resulting in fluorescence of the sample; therefore data were collected using the MAC detector. This collection required continuous sample beam exposure of the sample for 900 seconds (15 mins) during collection.

The data were compared to the calculated X-ray powder diffraction patterns from the single crystal structure of **2.1·MeCN**. The patterns were indexed using the TOPAS Academic programme.[16] TOPAS was also used for the Pawley and Rietveld fitting of data, as specified.[17,18]

3.2.2.1 Sample of 2.1·MeCN, exposed to air for 15 hours.

Visual inspection indicated the presence of a significant quantity of a new phase, although the peaks were insufficient in quantity and definition to index successfully.

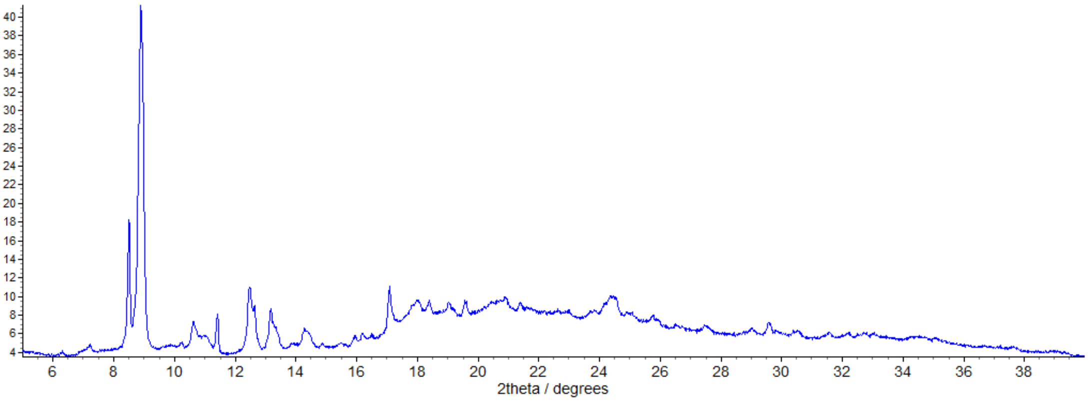

Figure 3.4. *Observed X-ray powder diffraction pattern for **2.1·MeCN**, exposed to air at room temperature for 15 hours.*

3.2.2.2 *In situ* study, desolvation of 2.1·MeCN and CO_2 uptake

The microcrystalline **2.1.MeCN** was loaded into a 0.5 mm quartz capillary, and placed in a gas cell mounted on a standard goniometer head. The cell was sealed with Araldite two-part glue to prevent gas leaks. After allowing the glue to dry for 20 minutes, the cell was evacuated with a vacuum pump at 10^{-5} mbar, and this pumping was continued throughout the desolvation study, during which patterns were measured at 15 minute time intervals.

Sample at 298 K, 10^{-5} mbar.

The initial pattern measured on the material at 298 K under vacuum was indexed using the TOPAS programme,[16] and a unit cell similar to that of **2.1·MeCN** from single-crystal X-ray diffraction was used as the starting point for a Pawley refinement,[17] employing 1427 parameters (8 background, 1 zero error, 5 profile, 3 cell, 1410 reflections), resulting in final indices of fit R_{wp} = 2.736, $R_{wp'}$ = 29.88.

[**2.1·MeCN**: a = 15.4207 (3) Å, b = 15.7124 (3) Å, c = 15.4076 (3) Å, V = 3733.2 (1) Å^3].

Poor powder averaging, in addition to bromine absorption/fluorescence issues affected this data collection and resulted in peak intensities which were abnormally high (for example the peaks at 2θ 5.95° and 6.1°).

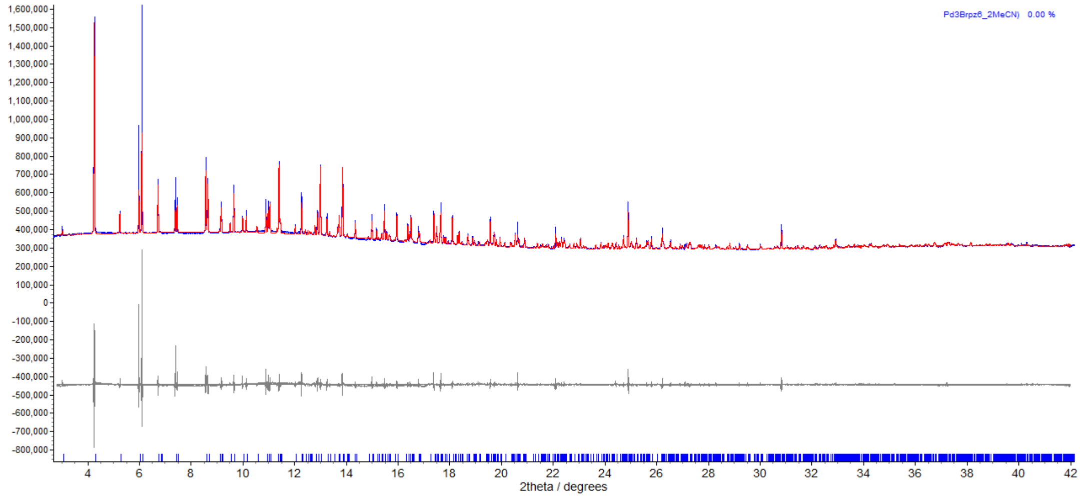

Figure 3.5. *Observed (blue) and calculated (red) profiles and difference plot [*I_{obs}*-*I_{calc}*] (grey) of the Pawley refinement. (*2θ *range 2.8 - 40 °,* d_{min} *= 1.15 Å).*

Sample after 15 mins at 348 K, 10^{-5} mbar.

The sample was heated at 348 K for 15 minutes under vacuum, and the pattern was recorded again. The unit cell of **2.1·MeCN** from the previous refinement was used as the starting point for a Pawley refinement,[17] employing 791 parameters (8 background, 1 zero error, 5 profile, 3 cell, 774 reflections), resulting in final indices of fit R_{wp} = 2.830, $R_{wp'}$ = 35.46.

[**2.1·MeCN**: a = 15.4698 (2) Å, b = 15.7289 (4) Å, c = 15.4502 (3) Å, V = 3759.4 (1) Å^3].

Additional peaks at 2θ 4.53° and 6.97° that could not be attributed to the known **2.1·MeCN** were observed, and suggested the growth of a new crystalline phase. They were, however, insufficient in number to be indexed to a unit cell.

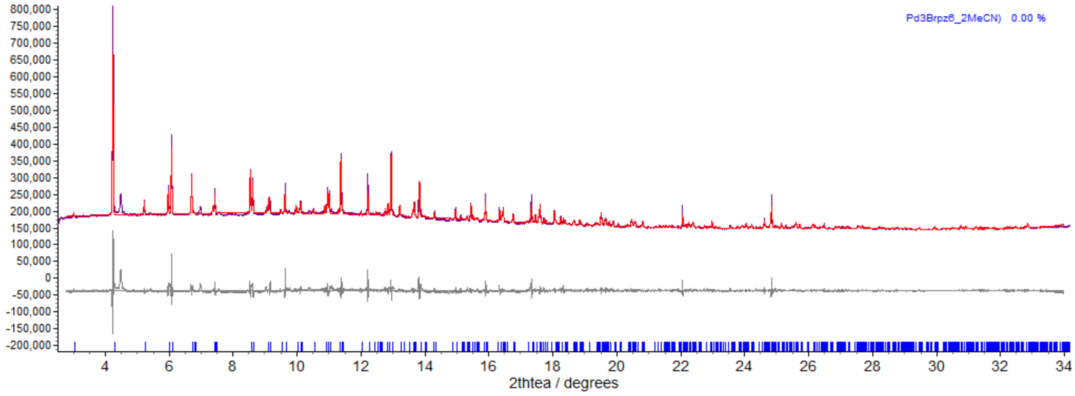

Figure 3.6. *Observed (purple) and calculated (red) profiles and difference plot [I_{obs}-I_{calc}] (grey) of the Pawley refinement. (2θ range 2.8 - 34 °, d_{min} = 1.42 Å).*

Sample after 30 mins at 348 K, 10^{-5} mbar.

The sample was heated at 348 K for a further 15 minutes under vacuum, and the pattern was recorded again. A sufficient number of peaks corresponding to the new desolvated phase **2.1** were observed, and as such were indexed successfully. The unit cells of **2.1·MeCN** from the previous refinement, and the newly indexed **2.1** were used as the starting point for a mixed-phase Pawley refinement,[17] employing 3434 parameters (7 background, 1 zero error, 9 profile, 6 cell, 3411 reflections), resulting in final indices of fit R_{wp} = 1.615, $R_{wp'}$ = 8.368.

[**2.1·MeCN**: a = 15.4824 (3) Å, b = 15.7004 (4) Å, c = 15.4519 (3) Å, V = 3756.1 (1) Å^3; **2.1**: a = 15.5670 (7) Å, b = 15.5304 (6) Å, c = 28.0061 (11) Å, V = 6770.8 (5) Å^3].

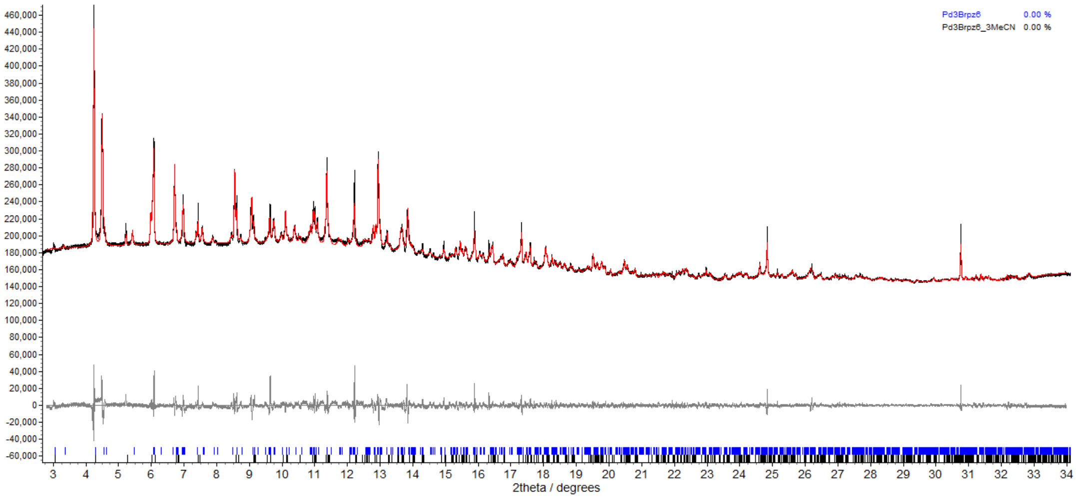

Figure 3.7. *Observed (black) and calculated (red) profiles and difference plot [I_{obs}-I_{calc}] (grey) of the mixed-phase Pawley refinement. (2θ range 2.8 - 34 °, d_{min} = 1.42 Å).*

Sample after 45 mins at 348 K, 10^{-5} mbar.

The sample was heated at 348 K for a further 15 minutes under vacuum, and the pattern was recorded again. The unit cells of **2.1·MeCN** and **2.1** from the previous refinement were used as the starting point for a mixed-phase Pawley refinement,[17] employing 1512 parameters (7 background, 1 zero error, 9 profile, 6 cell, 1489 reflections), resulting in final indices of fit R_{wp} = 1.114, $R_{wp'}$ = 11.94.

[**2.1·MeCN**: a = 15.4851 (4) Å, b = 15.6976 (7) Å, c = 15.4506 (4) Å, V = 3755.7 (2) Å^3; **2.1**: a = 15.5495 (3) Å, b = 15.5368 (3) Å, c = 28.0010 (5) Å, V = 6764.7 (2) Å^3].

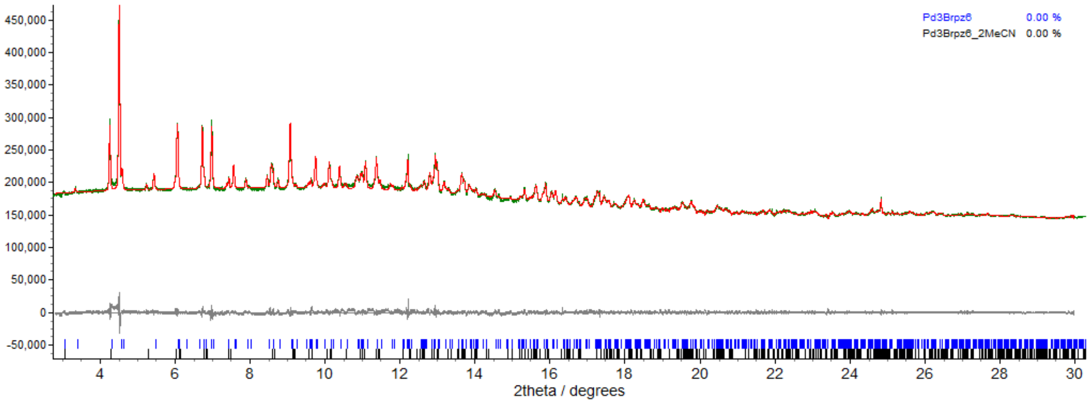

Figure 3.8. *Observed (green) and calculated (red) profiles and difference plot [I_{obs}-I_{calc}] (grey) of the mixed-phase Pawley refinement. (2θ range 2.8 - 30 °, d_{min} = 1.59 Å).*

Sample after 60 mins at 348 K, 10^{-5} mbar.

The sample was heated at 348 K for a further 15 minutes under vacuum, and the pattern was recorded again. The unit cells of **2.1·MeCN** and **2.1** from the previous refinement were used as the starting point for a mixed-phase Pawley refinement,[17] employing 1751 parameters (6 background, 1 zero error, 9 profile, 6 cell, 1729 reflections), resulting in final indices of fit R_{wp} = 1.153, $R_{wp'}$ = 11.87.

[**2.1·MeCN**: a = 15.5211 (9) Å, b = 15.6856 (1) Å, c = 15.475 (1) Å, V = 3767.5 (5) Å^3; **2.1**: a = 15.555 (1) Å, b = 15.534 (1) Å, c = 27.996 (1) Å, V = 6764.7 (7) Å^3].

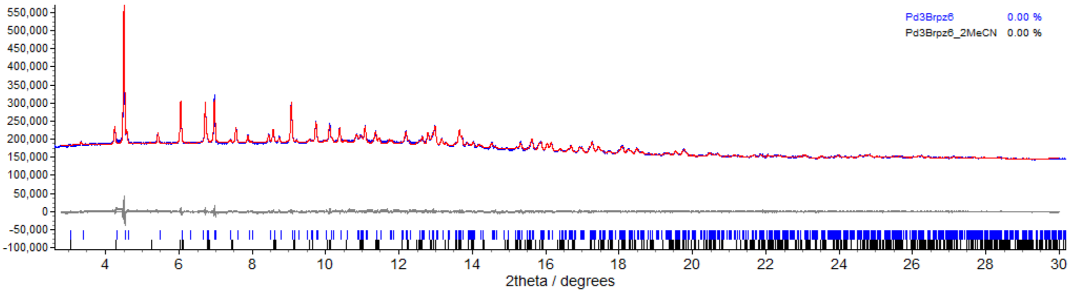

Figure 3.9. *Observed (blue) and calculated (red) profiles and difference plot [I_{obs}-I_{calc}] (grey) of the mixed-phase Pawley refinement. (2θ range 2.8 - 30 °, d_{min} = 1.59 Å).*

Sample after 75 mins at 348 K, 10^{-5} mbar.

The sample was heated at 348 K for a further 15 minutes under vacuum, and the pattern was recorded again. The unit cells of **2.1·MeCN** and **2.1** from the previous refinement were used as the starting point for a mixed-phase Pawley refinement,[17] employing 1512 parameters (6 background, 1 zero error, 9 profile, 6 cell, 1490 reflections), resulting in final indices of fit R_{wp} = 1.220, $R_{wp'}$ = 14.86.

[**2.1·MeCN**: *a* = 15.5317 (6) Å, *b* = 15.6762 (7) Å, *c* = 15.4955 (8) Å, *V* = 3772.8 (3) Å^3; **2.1**: *a* = 15.5567 (5) Å, *b* = 15.5332 (5) Å, *c* = 27.9881 (7) Å, *V* = 6763.2 (3) Å^3].

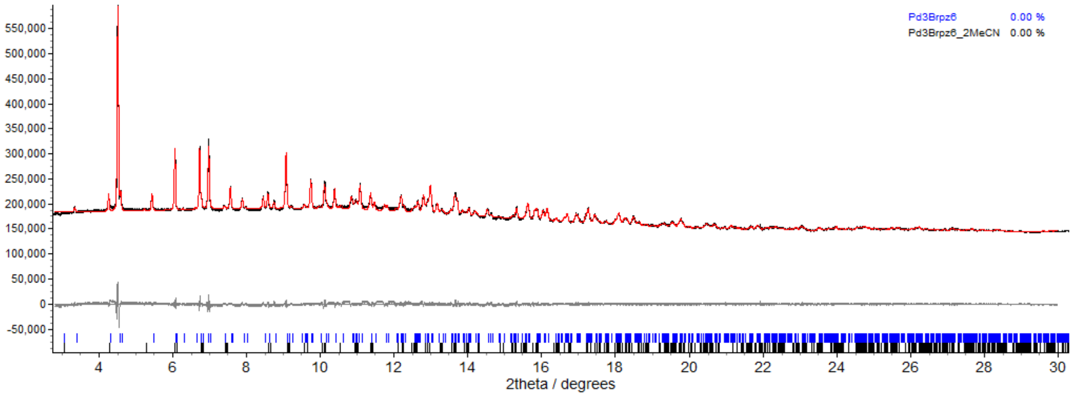

Figure 3.10. *Observed (black) and calculated (red) profiles and difference plot [I_{obs}-I_{calc}] (grey) of the mixed-phase Pawley refinement. (2θ range 2.8 - 30 °, d_{min} = 1.59 Å).*

Sample after 90 mins at 348 K, 10^{-5} mbar.

The sample was heated at 348 K for a further 15 minutes under vacuum, and the pattern was recorded again. The unit cells of **2.1·MeCN** and **2.1** from the previous refinement were used as the starting point for a mixed-phase Pawley refinement,[17] employing 1512 parameters (6 background, 1 zero error, 9 profile, 6 cell, 1490 reflections), resulting in final indices of fit R_{wp} = 1.248, $R_{wp'}$ = 15.55.

[**2.1·MeCN**: *a* = 15.5400 (9) Å, *b* = 15.666 (1) Å, *c* = 15.503179 (1) Å, *V* = 3774.3 (4) Å^3; **2.1**: *a* = 15.5479 (4) Å, *b* = 15.5288 (5) Å, *c* = 27.9809 (7) Å, *V* = 6760.0 (3) Å^3].

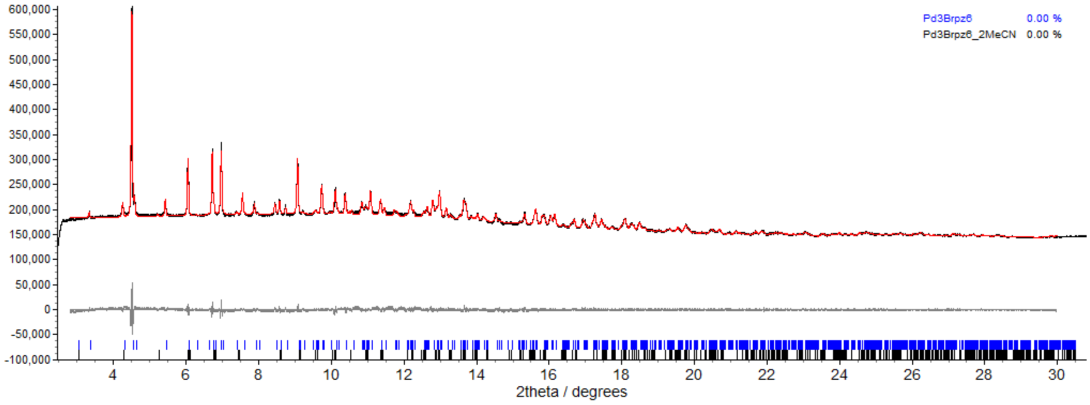

Figure 3.11. *Observed (black) and calculated (red) profiles and difference plot [I_{obs}-I_{calc}] (grey) of the mixed-phase Pawley refinement. (2θ range 2.8 - 30 °, d_{min} = 1.59 Å).*

Sample after 105 mins at 348 K, 10^{-5} mbar.

The sample was heated at 348 K for a further 15 minutes under vacuum, and the pattern was recorded again. The unit cells of **2.1·MeCN** and **2.1** from the previous refinement were used as the starting point for a mixed-phase Pawley refinement,[17] employing 1036 parameters (6 background, 1 zero error, 9 profile, 6 cell, 1014 reflections), resulting in final indices of fit R_{wp} = 1.328, $R_{wp'}$ = 15.39.

[**2.1·MeCN**: *a* = 15.5524 (8) Å, *b* = 15.6585 (9) Å, *c* = 15.5051 (6) Å, *V* = 3775.9 (3) Å^3; **2.1**: *a* = 15.5614 (4) Å, *b* = 15.5239 (5) Å, *c* = 27.9857 (7) Å, *V* = 6760.6 (3) Å^3].

The pattern remained essentially unchanged from the previous measurement. The sample was therefore cooled to 298 K, despite the apparent presence of some small amount of **2.1·MeCN**, to preserve the crystallinity and prevent overexposure to the beam before the subsequent CO_2 uptake study.

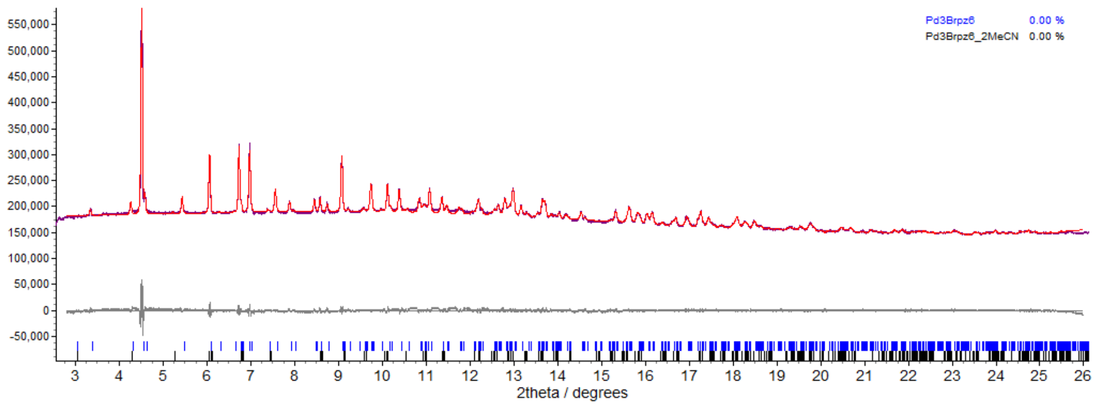

Figure 3.12. *Observed (purple) and calculated (red) profiles and difference plot [I_{obs}-I_{calc}] (grey) of the mixed-phase Pawley refinement. (2θ range 2.8 - 26 °, d_{min} = 1.84 Å).*

Sample upon returning to 298 K, 10^{-5} mbar.

The sample was allowed to cool to 298 K over a period of 30 minutes, before collecting another powder diffraction pattern. The unit cell of **2.1** from the previous refinement were used as the starting point for a Pawley refinement,[17] employing 654 parameters (7 background, 1 zero error, 5 profile, 3 cell, 631 reflections), resulting in final indices of fit R_{wp} = 1.241, $R_{wp'}$ = 14.71.

[**2.1**: a = 15.4701 (2) Å, b = 15.4356 (3) Å, c = 27.9282 (5) Å, V = 6669.0 (2) Å^3].

It appeared that over this cooling period, visible traces of the original **2.1·MeCN** material have disappeared, and converted fully to the desolvated **2.1** phase. As such, **2.1·MeCN** was not included in this refinement. A small peak at 2θ 4.74° which did not correspond to the known **2.1** was observed, but no other such peaks could be found. As such it could not be analysed any further.

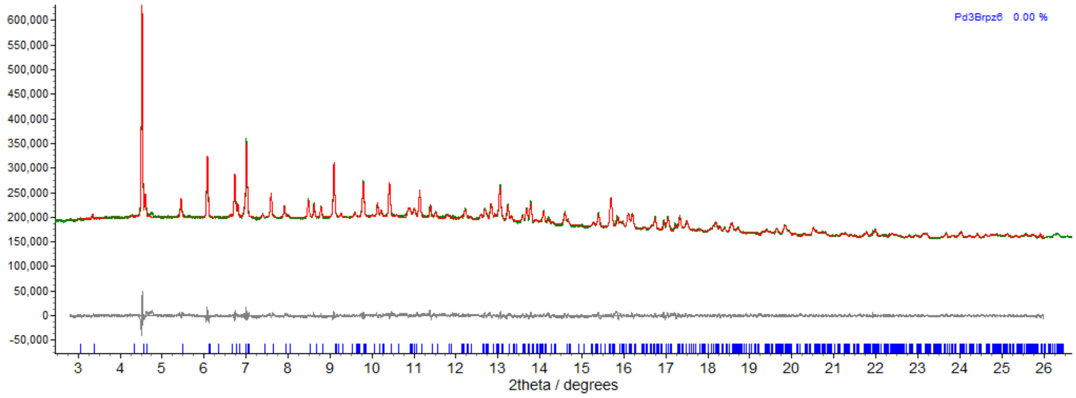

Figure 3.13. *Observed (green) and calculated (red) profiles and difference plot [I_{obs}-I_{calc}] (grey) of the Pawley refinement. (2θ range 2.8 - 26 °, d_{min} = 1.84 Å).*

Determination of crystal structure of 2.1 at 298 K, 10^{-5} mbar.

The pattern shown in Figure 3.13 was used for refinement to determine the structure of the desolvated **2.1**. A simulated annealing approach was taken, in which the cluster **2.1** was used as a rigid body group. The structure of cluster **2.1** was taken from a room-temperature single crystal X-ray structure determination of **2.1·MeCN**. The translation and rotation of each crystallographically unique cluster about its centre were allowed to refine, but not the individual atoms and bonds within the cluster. The resultant structure is introduced in section 3.3.1.3. The starting unit cell for the simulated annealing and Rietveld refinement,[18] was that used in the Pawley refinement above. Refinement employed 34 parameters (9 background, 1 zero error, 5 profile, 3 cell, 1 scale, 6 rotation – three for each of the two crystallographically unique clusters, 6 translation – three for each cluster, 3 thermal parameters – for Pd, Br and C/H/N atoms). Rietveld refinement converged to R_{wp} = 2.040, $R_{wp'}$ = 28.44. [**2.1:** a = 15.4612 (6) Å, b = 15.4609 (6) Å, c = 27.9478 (8) Å, V = 6680.8 (4) Å^3].

The crystallographic information file for the structure **2.1** is provided in the digital appendix.

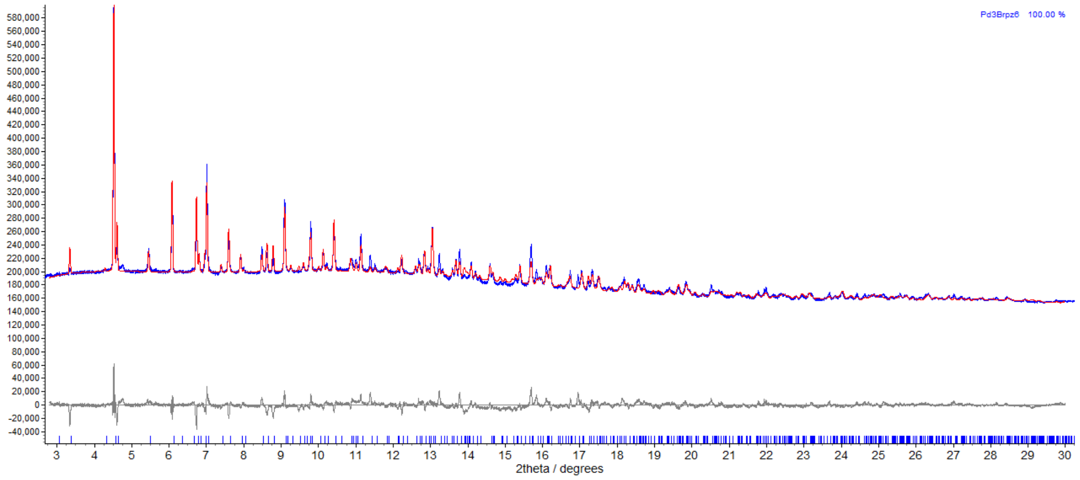

Figure 3.14. *Observed (blue) and calculated (red) profiles and difference plot [I_{obs}-I_{calc}] (grey) of the Rietveld refinement. (2θ range 2.8 - 30 °, d_{min} = 1.59 Å).*

Sample dosed with 1 bar CO_2.

Now holding temperature at 298 K, the gas cell containing the sample was dosed to 1.06 bar CO_2, and the system was allowed to equilibrate for 30 minutes, before collecting another powder diffraction pattern. Given there was no visible change in the pattern (apart from the extra peak at 2θ 4.74°), the unit cell of **2.1** from the previous refinement were used as the starting point for a Pawley refinement,[17] employing 792 parameters (6 background, 1 zero error, 5 profile, 3 cell, 770 reflections), resulting in final indices of fit R_{wp} = 1.380, $R_{wp'}$ = 16.60.

[**2.1**: *a* = 15.4673 (3) Å, *b* = 15.4388 (4) Å, *c* = 27.9385 (5) Å, *V* = 6671.6 (2) Å^3].

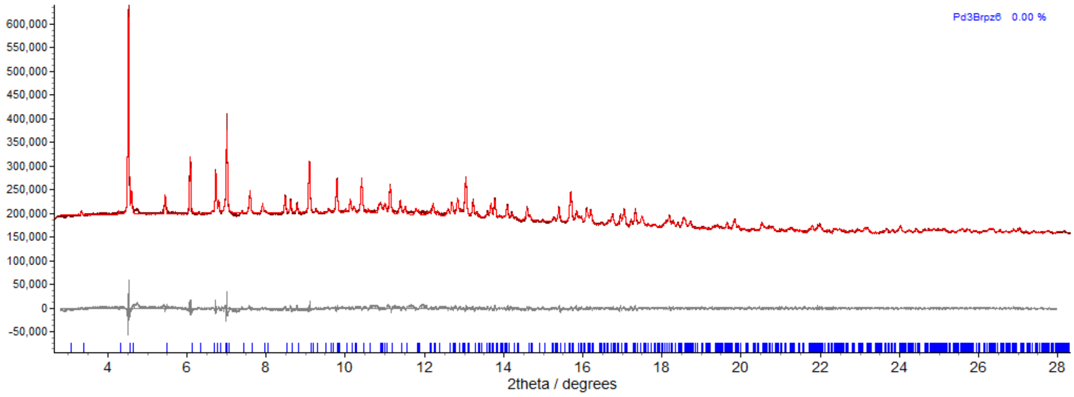

Figure 3.15. *Observed (brown) and calculated (red) profiles and difference plot [I_{obs}-I_{calc}] (grey) of the Pawley refinement. (2θ range 2.8 - 28 °, d_{min} = 1.71 Å).*

Sample dosed with 5 bar CO_2.

The gas cell containing the sample was dosed to 5.39 bar CO_2, and the system was allowed to equilibrate for 30 minutes, before collecting another powder diffraction pattern. Given there was no visible change in the pattern (apart from the extra peak at 2θ 4.74°), the unit cell of **2.1** from the previous refinement were used as the starting point for a Pawley refinement,[17] employing 792 parameters (6 background, 1 zero error, 5 profile, 3 cell, 770 reflections), resulting in final indices of fit R_{wp} = 1.311, $R_{wp'}$ = 15.25.

[**2.1**: *a* = 15.5307 (4) Å, *b* = 15.4357 (3) Å, *c* = 27.9346 (6) Å, *V* = 6696.7 (2) Å^3].

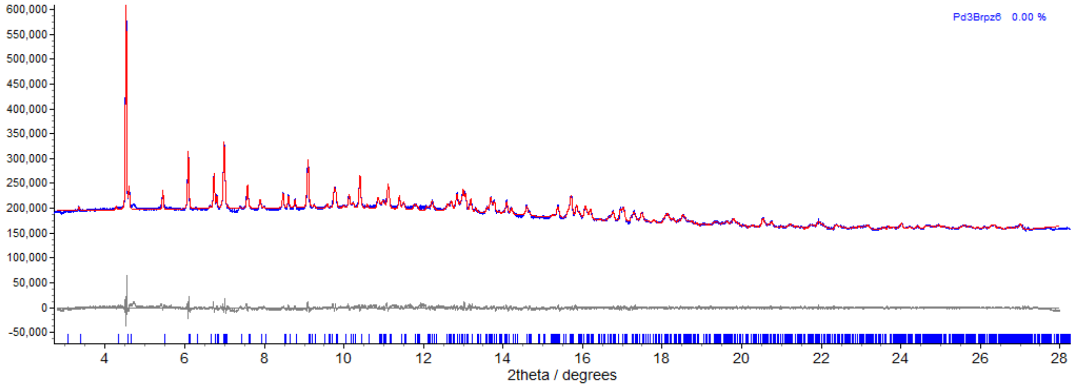

Figure 3.16. *Observed (blue) and calculated (red) profiles and difference plot [I_{obs}-I_{calc}] (grey) of the Pawley refinement. (2θ range 2.8 - 28 °, d_{min} = 1.71 Å).*

Sample dosed with 10 bar CO_2.

The gas cell containing the sample was dosed to 10.11 bar CO_2, and the system was allowed to equilibrate for 30 minutes, before collecting another powder diffraction pattern. Given there was no visible change in the pattern (apart from the extra peak at 2θ 4.74°), the unit cell of **2.1** from the previous refinement were used as the starting point for a Pawley refinement,[17] employing 799 parameters (6 background, 1 zero error, 5 profile, 3 cell, 777 reflections), resulting in final indices of fit R_{wp} = 1.354, $R_{wp'}$ = 17.13.

[**2.1**: a = 15.5673 (5) Å, b = 15.4351 (3) Å, c = 27.9412 (6) Å, V = 6713.8 (3) Å^3].

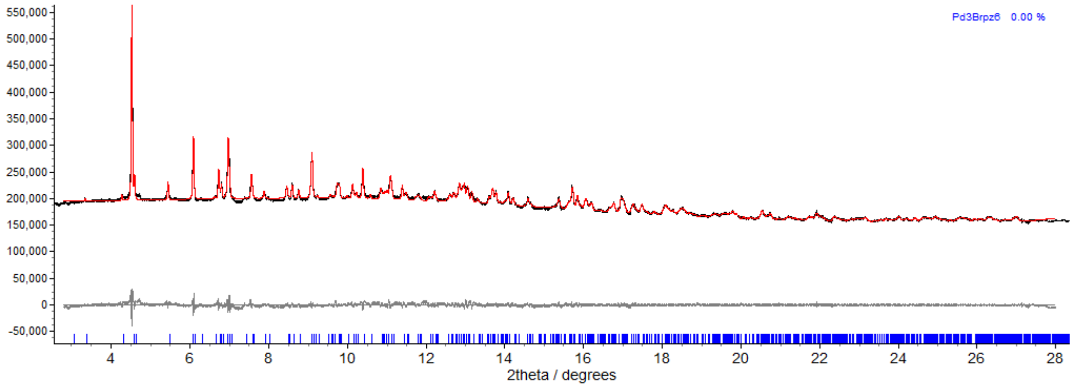

Figure 3.17. *Observed (black) and calculated (red) profiles and difference plot [I_{obs}-I_{calc}] (grey) of the Pawley refinement. (2θ range 2.8 - 28 °, d_{min} = 1.71 Å).*

Sample dosed with 20 bar CO_2.

The gas cell containing the sample was dosed to 19.92 bar CO_2, and the system was allowed to equilibrate for 30 minutes, before collecting another powder diffraction pattern. The appearance of a significant number of peaks not attributed to **2.1** was observed, and they were successfully indexed to a new unit cell. This phase was called **"2.1·nCO$_2$"** for the purposes of the refinement. This new unit cell **"2.1·nCO$_2$"**, and that of **2.1** from the previous refinement were used as the basis of a mixed-phase Pawley refinement,[17] employing 2707 parameters (8 background, 1 zero error, 10 profile, 7 cell, 2681 reflections), resulting in final indices of fit R_{wp} = 0.907, $R_{wp'}$ = 5.266.

[**2.1**: a = 15.5658 (7) Å, b = 15.4354 (7) Å, c = 27.944 (1) Å, V = 6713.9 (6) Å^3; **"2.1·nCO$_2$"**: a = 28.8714 (8) Å, b = 17.8882 (5) Å, c = 30.1754 (8) Å, β = 97.117 (1)°, V = 15454.2 (7) Å^3].

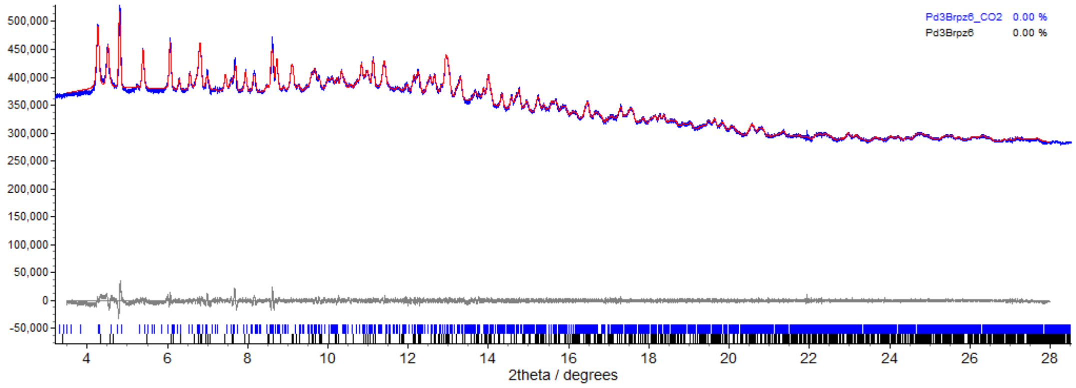

Figure 3.18. *Observed (blue) and calculated (red) profiles and difference plot [I_{obs}-I_{calc}] (grey) of the Pawley refinement. (2θ range 2.8 - 28 °, d_{min} = 1.71 Å).*

Sample dosed with 40 bar CO_2.

The gas cell containing the sample was dosed to 39.92 bar CO_2, and the system was allowed to equilibrate for 30 minutes, before collecting another powder diffraction pattern. Visual inspection now clearly indicated that **"2.1·nCO₂"** was the only phase present, and its unit cell from the previous refinement was used as the basis for a new Pawley refinement,[17] employing 1849 parameters (7 background, 1 zero error, 5 profile, 4 cell, 1832 reflections), resulting in final indices of fit R_{wp} = 1.113, $R_{wp'}$ = 11.06.

[**"2.1·nCO₂"**: a = 28.8728 (6) Å, b = 17.8876 (4) Å, c = 30.1764 (6) Å, β = 97.112 (1)°, V = 15465.1 (6) Å^3].

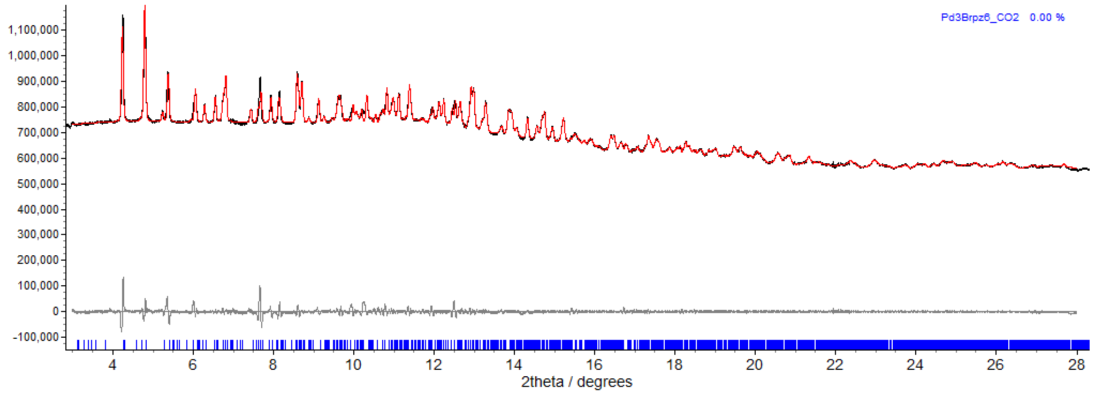

Figure 3.19. *Observed (black) and calculated (red) profiles and difference plot [I_{obs}-I_{calc}] (grey) of the Pawley refinement. (2θ range 2.8 - 28 °, d_{min} = 1.71 Å).*

Sample pressure reduced to 20 bar CO_2.

The gas cell containing the sample was exhausted to return the pressure of CO_2 to 20.50 bar (at this point the sample had been dosed with 39.92 bar CO_2 two hours ago, and a slight pressure leak had taken place, lowering the pressure to 39.70 bar CO_2), and the system was allowed to equilibrate for 30 minutes, before collecting another powder diffraction pattern. Visual inspection indicated that **“2.1·nCO$_2$”** was still the only phase present, and its unit cell from the previous refinement was used as the basis for a new Pawley refinement,[17] employing 1849 parameters (7 background, 1 zero error, 5 profile, 4 cell, 1832 reflections), resulting in final indices of fit R_{wp} = 0.938, $R_{wp'}$ = 9.835.

[**“2.1·nCO$_2$”**: a = 28.8726 (6) Å, b = 17.8922 (5) Å, c = 30.1836 (6) Å, β = 97.114 (2)°, V = 15472.6 (6) Å^3].

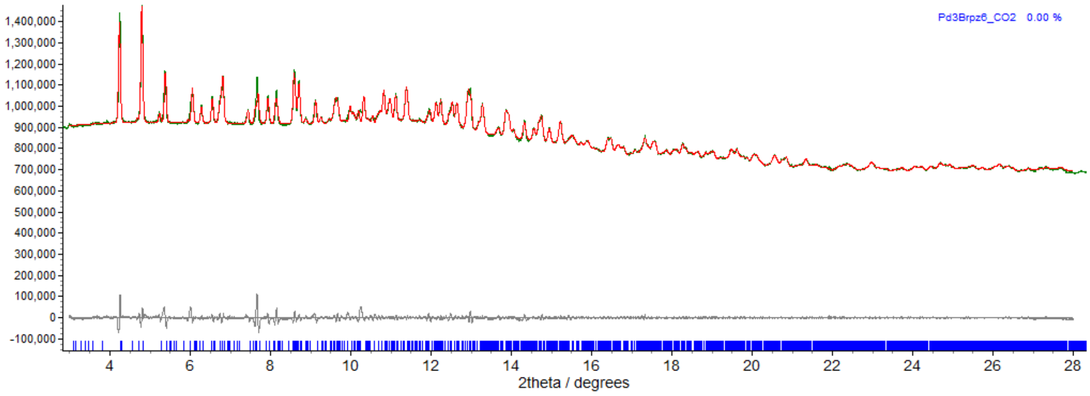

Figure 3.20. *Observed (green) and calculated (red) profiles and difference plot [I_{obs}-I_{calc}] (grey) of the Pawley refinement. (2θ range 2.8 - 28 °, d_{min} = 1.71 Å).*

Sample pressure reduced to 10 bar CO_2.

The gas cell containing the sample was exhausted to return the pressure of CO_2 to 10.18 bar and the system was allowed to equilibrate for 30 minutes, before collecting another powder diffraction pattern. Visual inspection indicated that **“2.1·nCO$_2$”** was still the only phase present, and its unit cell from the previous refinement was used as the basis for a new Pawley refinement,[17] employing 1850 parameters (7 background, 1 zero error, 5 profile, 4 cell, 1833 reflections), resulting in final indices of fit R_{wp} = 0.910, $R_{wp'}$ = 6.380.

[**“2.1·nCO$_2$”**: a = 28.8578 (5) Å, b = 17.8904 (4) Å, c = 30.1554 (5) Å, β = 97.127 (2)°, V = 15448.2 (6) Å^3].

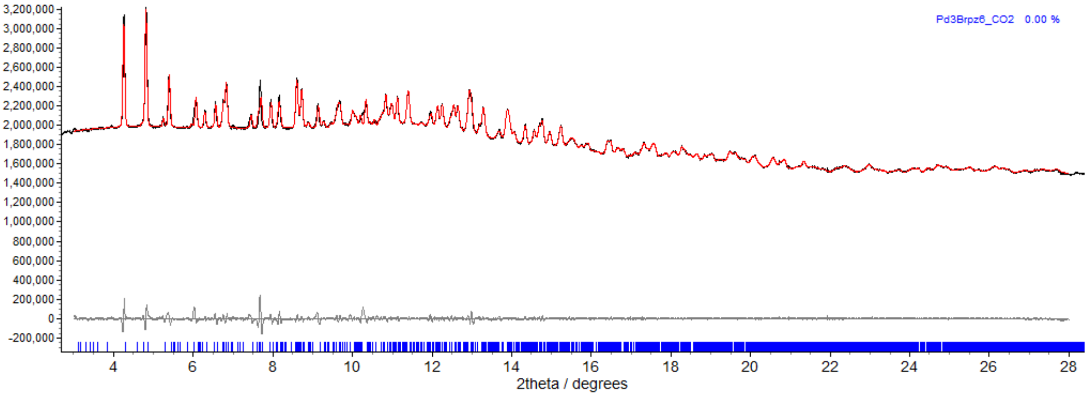

Figure 3.21. *Observed (black) and calculated (red) profiles and difference plot [I_{obs}-I_{calc}] (grey) of the Pawley refinement. (2θ range 2.8 - 28 °, d_{min} = 1.71 Å).*

Sample pressure reduced to 5 bar CO_2.

The gas cell containing the sample was exhausted to return the pressure of CO_2 to 4.97 bar and the system was allowed to equilibrate for 30 minutes, before collecting another powder diffraction pattern. Visual inspection indicated that **"2.1·nCO$_2$"** was still the only phase present, and its unit cell from the previous refinement was used as the basis for a new Pawley refinement,[17] employing 1847 parameters (7 background, 1 zero error, 5 profile, 4 cell, 1830 reflections), resulting in final indices of fit R_{wp} = 1.026, $R_{wp'}$ = 9.824.

[**"2.1·nCO$_2$"**: a = 28.8275 (9) Å, b = 17.8855 (6) Å, c = 30.1235 (8) Å, β = 97.127 (2)°, V = 15411.5 (8) Å^3].

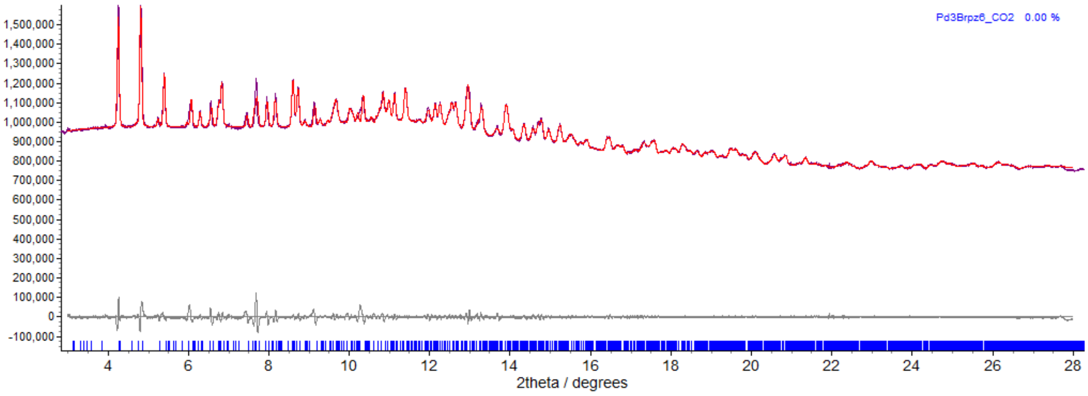

Figure 3.22. *Observed (purple) and calculated (red) profiles and difference plot [I_{obs}-I_{calc}] (grey) of the Pawley refinement. (2θ range 2.8 - 28 °, d_{min} = 1.71 Å).*

Sample pressure reduced to 1 bar CO_2.

The gas cell containing the sample was exhausted to return the pressure of CO_2 to 1.05 bar and the system was allowed to equilibrate for 30 minutes, before collecting another powder diffraction pattern. Visual inspection indicated that **“2.1·nCO_2”** was still the only phase present, and its unit cell from the previous refinement was used as the basis for a new Pawley refinement,[17] employing 1847 parameters (7 background, 1 zero error, 5 profile, 4 cell, 1830 reflections), resulting in final indices of fit R_{wp} = 1.140, $R_{wp'}$ = 12.56.

[**“2.1·nCO_2”**: a = 28.821 (1) Å, b = 17.8869 (7) Å, c = 30.113 (1) Å, β = 97.118 (3)°, V = 15404 (1) Å^3].

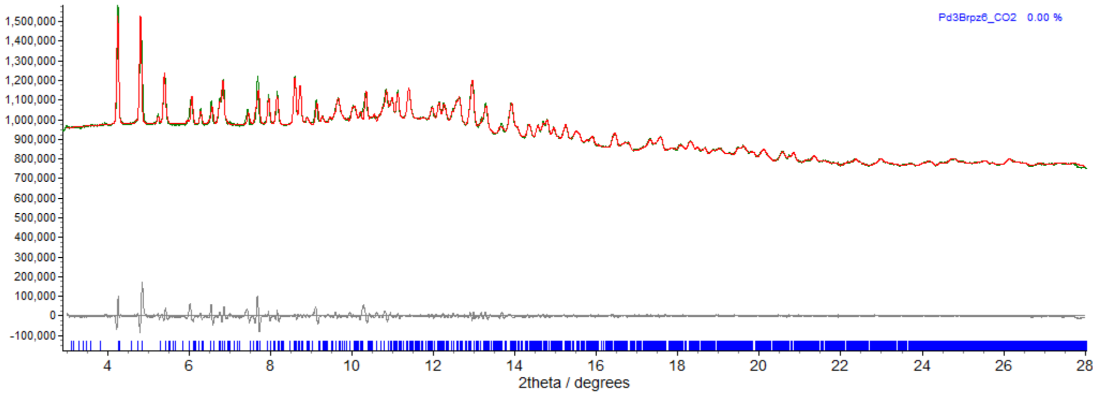

Figure 3.23. *Observed (green) and calculated (red) profiles and difference plot [I_{obs}-I_{calc}] (grey) of the Pawley refinement. (2θ range 2.8 - 28 °, d_{min} = 1.71 Å).*

Sample pressure reduced to 10^{-4} mbar.

The gas cell containing the sample was evacuated with the vacuum pump to a pressure of 10^{-4} mbar and the system was allowed to equilibrate for 30 minutes, before collecting another powder diffraction pattern. Visual inspection indicated that **“2.1·nCO_2”** was still the only phase present, and its unit cell from the previous refinement was used as the basis for a new Pawley refinement,[17] employing 1847 parameters (7 background, 1 zero error, 5 profile, 4 cell, 1830 reflections), resulting in final indices of fit R_{wp} = 1.241, $R_{wp'}$ = 16.12.

[**“2.1·nCO_2”**: a = 28.770 (2) Å, b = 17.8852 (8) Å, c = 30.093 (3) Å, β = 97.052 (3)°, V = 15367 (1) Å^3].

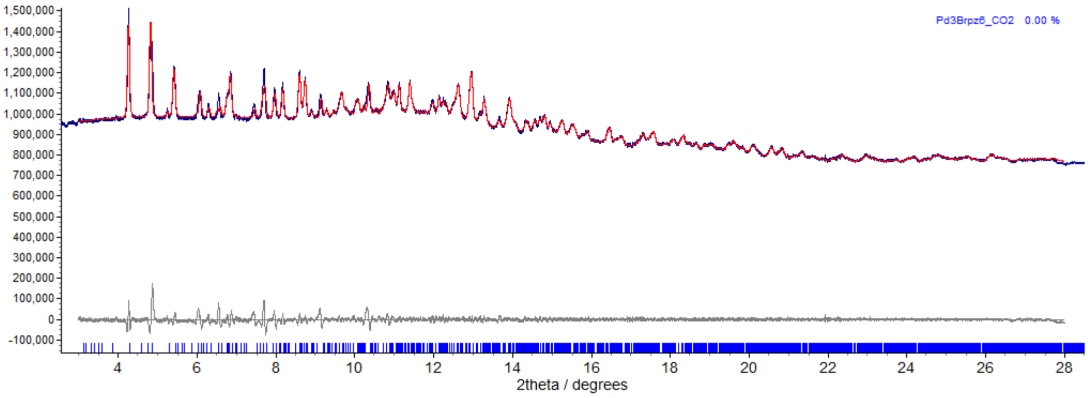

Figure 3.24. *Observed (blue) and calculated (red) profiles and difference plot* $[I_{obs}-I_{calc}]$ *(grey) of the Pawley refinement. (*2θ *range 2.8 - 28 °,* d_{min} *= 1.71 Å).*

3.2.2.3 *In situ* study, desolvation of 2.1·MeCN and N_2 uptake

A fresh sample of microcrystalline **2.1.MeCN** was loaded into a 0.5 mm quartz capillary, and placed in a gas cell mounted on a standard goniometer. The cell was sealed with Araldite two-part glue to prevent gas leaks. After allowing the glue to dry for 20 minutes, the cell was evacuated with a vacuum pump at 10^{-5} mbar, and this pumping was continued throughout the desolvation study.

In this instance, data collected using the Mythen-2 detector were too badly affected by bromine absorption/fluorescence to be fitted quantitatively, but visual inspection could identify the phases present, based on the patterns shown in section 3.2.1.2. The desolvation of **2.1·MeCN** to **2.1** was followed using the Mythen-2 detector, which allows fast data collections, and the exposure of the sample to nitrogen was followed using the slower MAC detector, which required 15 minutes exposure for each collection. Mythen-2 data for the desolvation study are also shown in Figure 3.26.

Sample at 298 K, 10^{-5} mbar.

The sample was heated at 348 K for 15 minutes under vacuum, and the pattern was recorded again. In addition to peaks for **2.1·MeCN**, a significant number of peaks for reflections corresponding to the desolvated phase **2.1**, enabled indexing. The unit cells of **2.1·MeCN** and **2.1** were used as the starting point for a mixed-phase Pawley refinement,[17] employing 1237 parameters (8 background, 1 zero error, 9 profile, 6 cell, 1213 reflections), resulting in final indices of fit R_{wp} = 13.68, $R_{wp'}$ = 26.42.

[**2.1·MeCN**: *a* = 15.4272 (2) Å, *b* = 15.7165 (3) Å, *c* = 15.4120 (3) Å, *V* = 3736.8 (1) Å^3; **2.1**: *a* = 15.478 (2) Å, *b* = 15.437 (2) Å, *c* = 27.931 (3) Å, *V* = 6674 (2) Å^3].

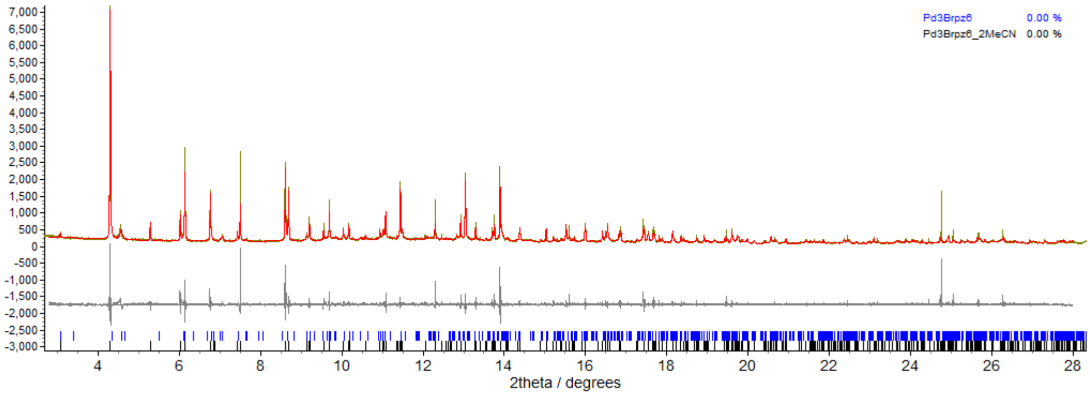

Figure 3.25. *Observed (green) and calculated (red) profiles and difference plot [I_{obs}-I_{calc}] (grey) of the Rietveld refinement. (2θ range 2.8 - 28 °, d_{min} = 1.71 Å).*

Sample during desolvation at 348 K, 10^{-5} mbar

The sample was heated at 348 K for 90 minutes under vacuum, and was monitored by a series of patterns collected using the Mythen-2 detector (as shown in Figure 3.26). Although quantitative fitting of the data was not possible, a visual assessment of the phase(s) present could be made.

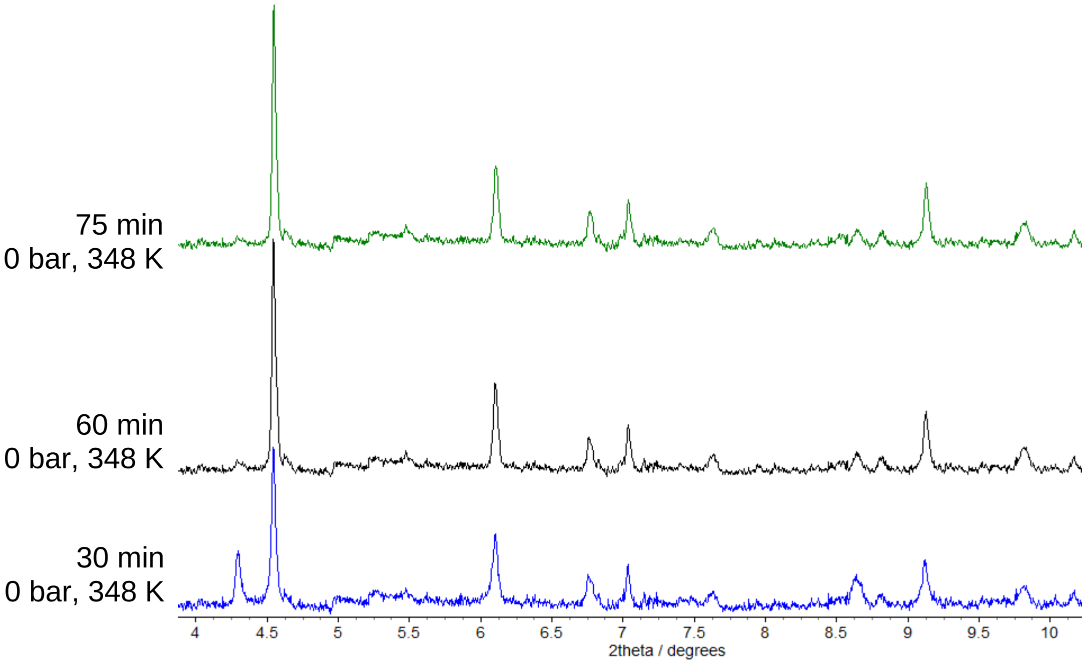

Figure 3.26. *X-ray powder diffraction pattern progression for the desolvation of* ***2.1.MeCN*** *to* ***2.1*** *using Mythen-2 detector data. The time intervals are noted next to each pattern.*

Sample returned to 298 K, 10^{-5} mbar after desolvation.

The sample was brought back to 298 K, and the pattern was recorded again using the MAC detector. The unit cell of **2.1**, the only phase visibly present (other than the previously identified, but hitherto unassigned peak at 2θ 4.74°), was used as the starting point for a Pawley refinement,[17] employing 647 parameters (7 background, 1 zero error, 5 profile, 3 cell, 631 reflections), resulting in final indices of fit R_{wp} = 12.16, $R_{wp'}$ = 34.70.

[**2.1**: a = 15.4961 (9) Å, b = 15.477 (1) Å, c = 27.975 (1) Å, V = 6709.4 (7) Å^3].

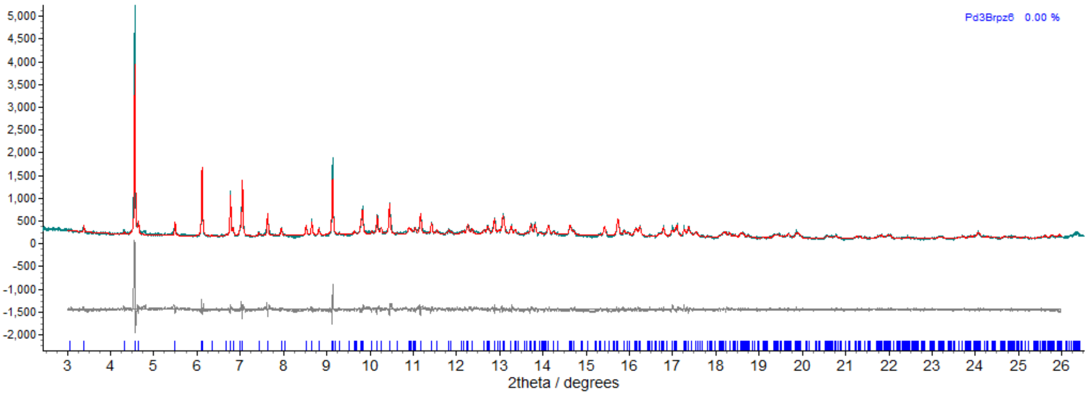

Figure 3.27. *Observed (blue) and calculated (red) profiles and difference plot [I_{obs}-I_{calc}] (grey) of the Rietveld refinement. (2θ range 2.8 - 28 °, d_{min} = 1.71 Å).*

Sample dosed with 10 bar N_2.

Now holding temperature at 298 K, the gas cell containing the sample was dosed to 10.23 bar N_2, and the system was allowed to equilibrate for 30 minutes, before collecting another powder diffraction pattern (over 15 minutes of exposure). Given there was no visible change in the pattern, the unit cell of **2.1** from the previous refinement were used as the starting point for a Pawley refinement,[17] employing 786 parameters (7 background, 1 zero error, 5 profile, 3 cell, 770 reflections), resulting in final indices of fit R_{wp} = 11.36, $R_{wp'}$ = 29.42.

[**2.1**: a = 15.4927 (6) Å, b = 15.4810 (5) Å, c = 27.9775 (9) Å, V = 6710.2 (4) Å^3].

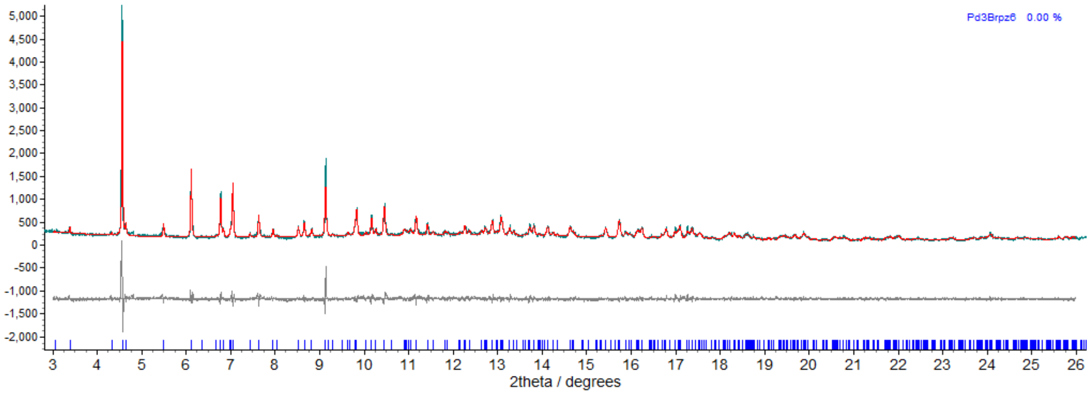

Figure 3.28. *Observed (blue) and calculated (red) profiles and difference plot [I_{obs}-I_{calc}] (grey) of the Rietveld refinement. (2θ range 2.8 - 26 °, d_{min} = 1.83 Å).*

Sample dosed with 20 bar N_2.

Now holding temperature at 298 K, the gas cell containing the sample was dosed to 20.03 bar N_2, and the system was allowed to equilibrate for 30 minutes, before collecting another powder diffraction pattern (over 15 minutes of exposure). Given there was no visible change in the pattern, the unit cell of **2.1** from the previous refinement were used as the starting point for a Pawley refinement,[17] employing 646 parameters (6 background, 1 zero error, 5 profile, 3 cell, 631 reflections), resulting in final indices of fit R_{wp} = 10.00, $R_{wp'}$ = 22.64.

[**2.1**: a = 15.5108 (6) Å, b = 15.4810 (5) Å, c = 27.9775 (9) Å, V = 6710.2 (4) $Å^3$].

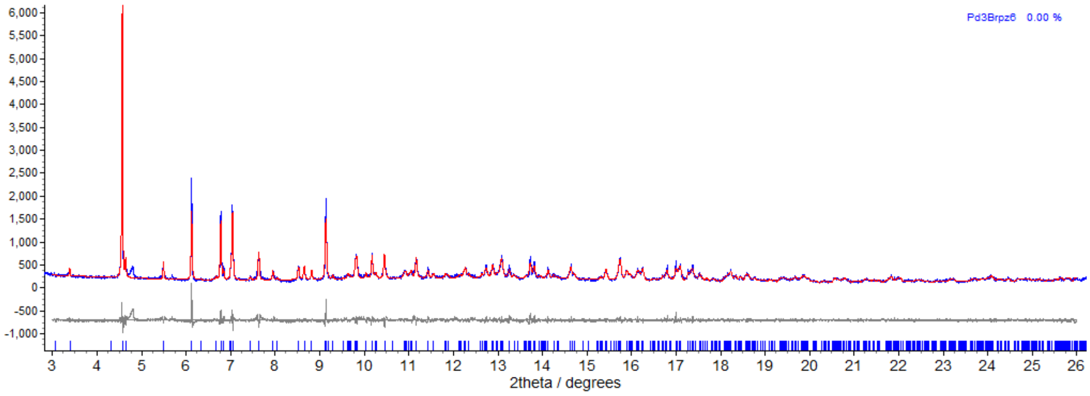

Figure 3.29. *Observed (blue) and calculated (red) profiles and difference plot [I_{obs}-I_{calc}] (grey) of the Rietveld refinement. (2θ range 2.8 - 26 °, d_{min} = 1.83 Å).*

Sample dosed with 40 bar N_2.

Now holding temperature at 298 K, the gas cell containing the sample was dosed to 40.00 bar N_2, and the system was allowed to equilibrate for 30 minutes, before collecting another powder diffraction pattern (over 15 minutes of exposure). Given there was no visible change in the pattern, the unit cell of **2.1** from the previous refinement were used as the starting point for a Pawley refinement,[17] employing 647 parameters (7 background, 1 zero error, 5 profile, 3 cell, 631 reflections), resulting in final indices of fit R_{wp} = 11.10, $R_{wp'}$ = 23.48.

[**2.1**: a = 15.4847 (6) Å, b = 15.4664 (4) Å, c = 27.9582 (7) Å, V = 6695.8 (3) Å^3].

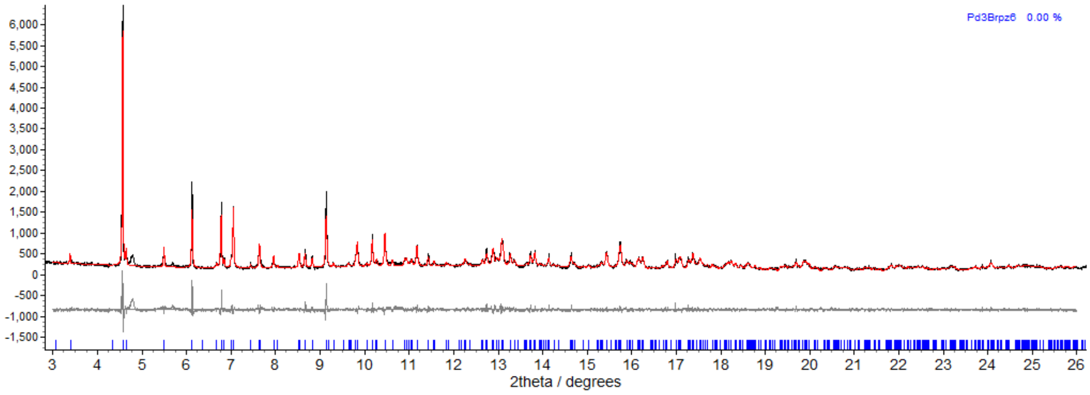

Figure 3.30. *Observed (black) and calculated (red) profiles and difference plot* $[I_{obs}$-$I_{calc}]$ *(grey) of the Rietveld refinement. (2θ range 2.8 - 26 °,* d_{min} *= 1.83 Å).*

3.2.3 Thermogravimetric analysis

The crystalline **2.1·MeCN** was filtered from the mother liquor at the pump, and allowed to dry in air for exactly ten minutes to remove surface solvent on the crystals. Thermogravimetric analysis data were then conducted using a Perkin–Elmer Pyris1 TGA model thermogravimetric analyser. The sample was held at 25°C for a period of 5 minutes, before ramping at a rate of 5°C min^{-1} to 85°C, and then held at that temperature for 120 minutes, under a flow of dry N_2 gas. The annotated TGA trace is shown in the main text in section 3.3.1.1.

3.3 Results & discussion

3.3.1 Desolvation of 2.1.MeCN to give 2.1

3.3.1.1 Initial evidence for desolvation of 2.1·MeCN

An isothermal thermogravimetric analysis (TGA) trace for the solvated parent compound **2.1·MeCN** was recorded, to investigate the possibility of removing the acetonitrile solvent at a constant temperature. By holding at 85°C for a period of two hours it was possible to desolvate the material, with a mass loss consistent with the formation of the solvent-free material **2.1** (expected loss for 3 MeCN = 9.3%, observed loss = 9.1%). The TGA trace (shown in Figure 3.31) also demonstrates that the cluster material appears to be stable at 85°C for a sustained period, showing no further loss of mass beyond that of the acetonitrile.

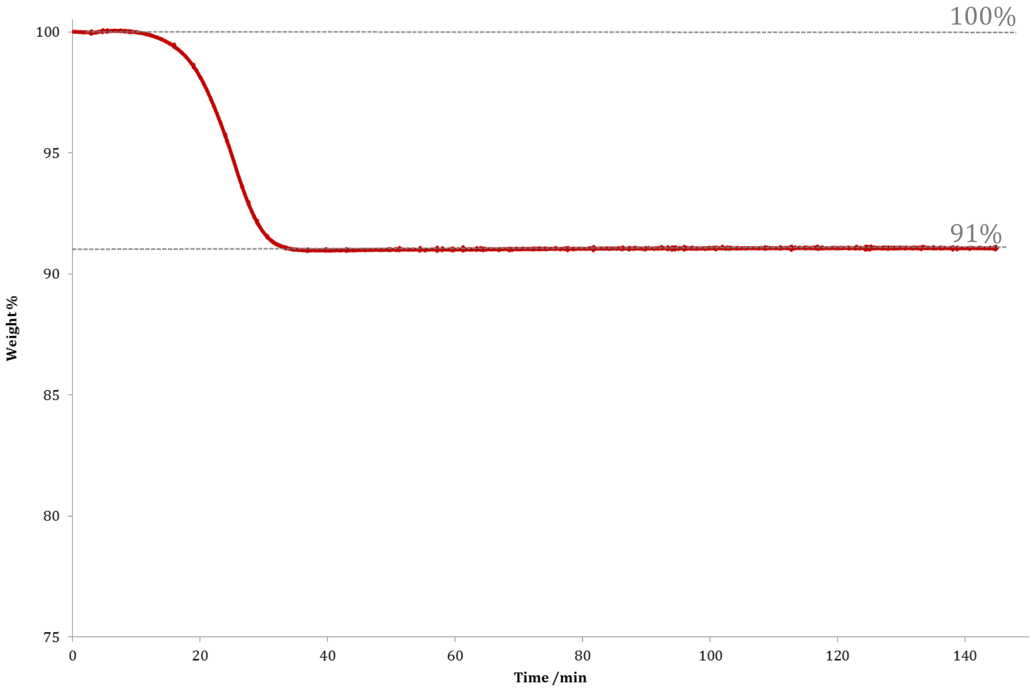

Figure 3.31. *Thermogravimetric analysis trace for* ***2.1·MeCN****, holding the temperature at 85°C for two hours under a flow of nitrogen. The mass loss onset at 10 mins of 9% indicates loss of all three MeCN equivalents.*

This loss was then followed crystallographically (both by single-crystal and powder X-ray diffraction). Rapid *in situ* single crystal X-ray diffraction monitoring of the desolvation process was conducted by periodically recording sufficient frames to index the diffraction pattern and determine the unit cell parameters, with heating. A crystal of **2.1·MeCN** was mounted and heated *in situ* to 85°C over a period of one hour. The diffraction data collected suggested a rapid drop in crystallinity upon heating to 85°C, indicated by the disappearance of high-angle reflections corresponding to **2.1·MeCN**. This was accompanied by the appearance of smear-like reflections at low diffraction angle (see Figure 3.32).

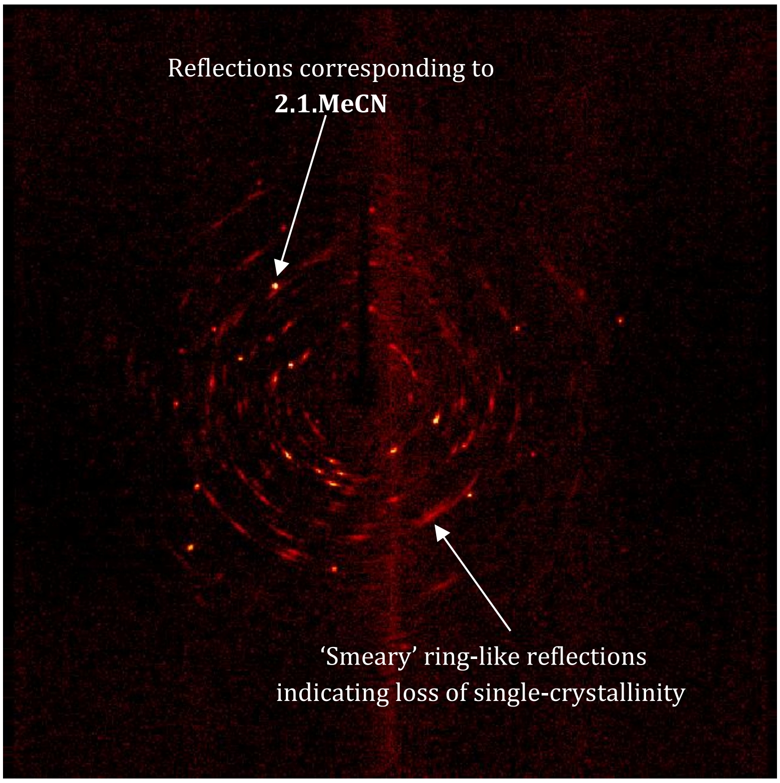

Figure 3.32. *Single-crystal X-ray diffraction image collected on a crystal of* ***2.1·MeCN*** *after heating to 85 °C. Smeary, low-angle reflections corresponding to a new phase have grown in, but some reflections consistent with* ***2.1·MeCN*** *remain.*

These new reflections suggested the formation of a new crystalline phase as the solvent left the material. However, the great number of reflections and lack of intensity or observable order indicated that this corresponded to a microcrystalline material (powder), and that the phase change was not lithotropic (single-crystal-to-single-crystal, SCSC). This is logically consistent with the removal of acetonitrile from the structure of **2.1·MeCN**, as it is shown to be integral to the supramolecular network of clusters (as shown in chapter 2, see also Figure 3.33). Departure of acetonitrile from the crystal structure would therefore likely cause a significant structural change, fracturing of the crystals.

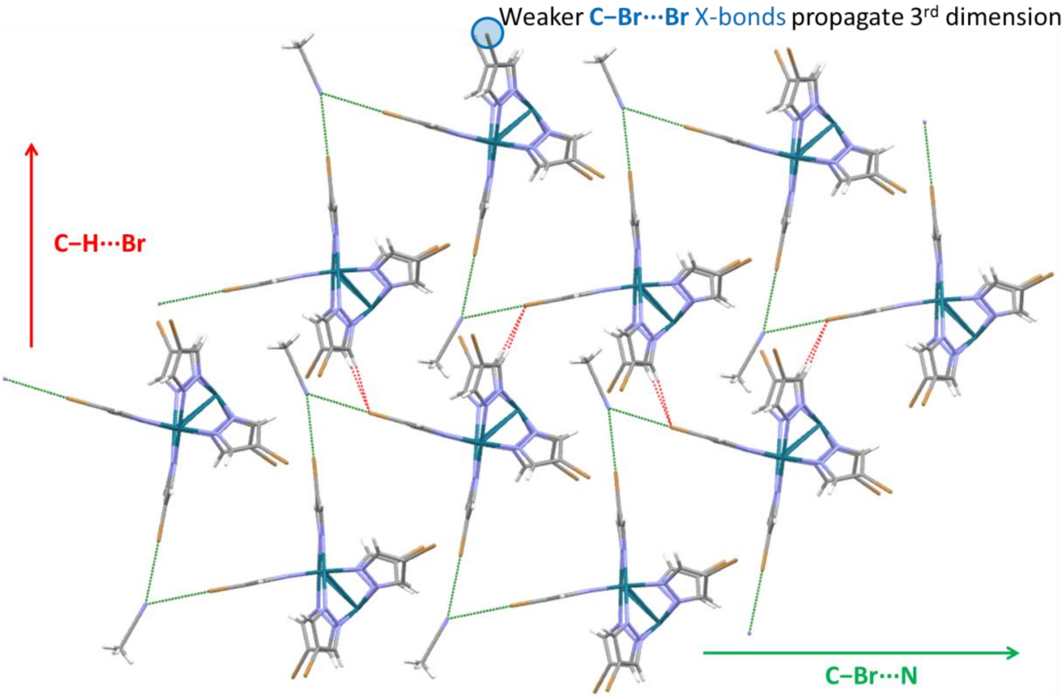

Figure 3.33. *Two-dimensional view of the supramolecular network of interactions holding clusters together in the structure of* ***2.1·MeCN****. Halogen bonds are shown in green and hydrogen bonds in red.*

This loss of solvent was easily followed by X-ray powder diffraction. Indeed, leaving dry, ground **2.1·MeCN** open to air for 15 hours resulted in a partial transformation to a new phase (*ex situ* desolvation). This is evidenced by the appearance of significant new peaks in the powder diffraction pattern (see Figure 3.34).

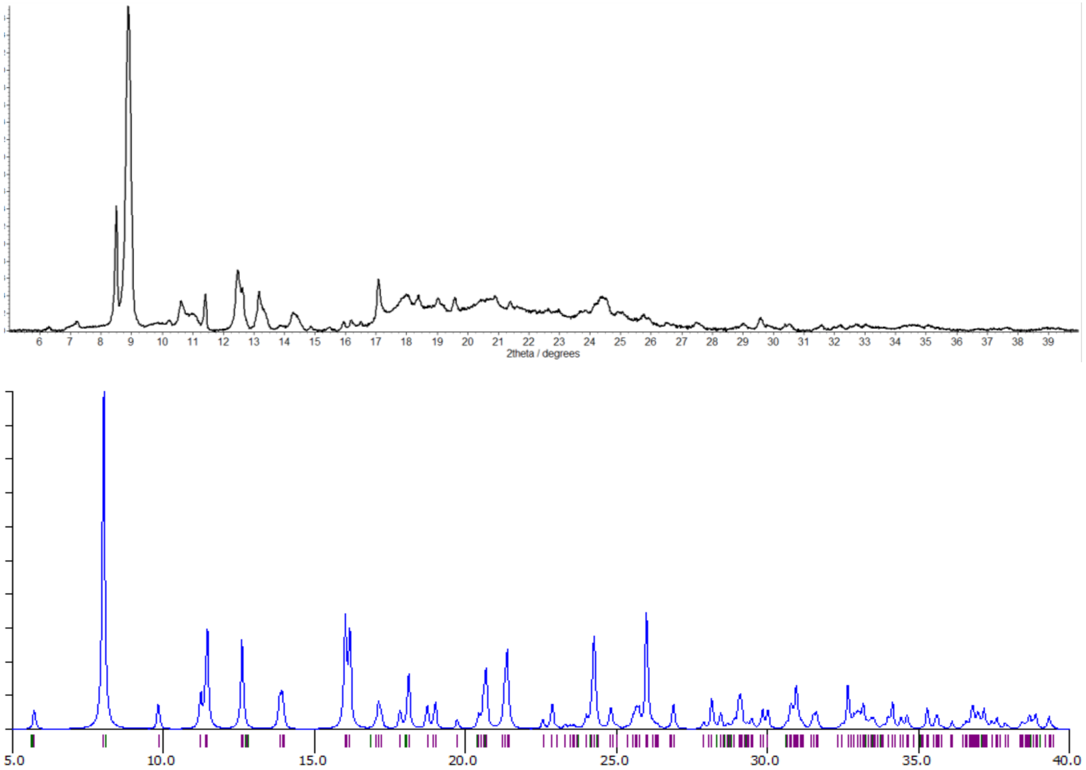

Figure 3.34. *X-ray powder diffraction pattern for the partially desolvated **2.1/2.1·MeCN** mixture after ex situ desolvation under ambient conditions (top) and the calculated pattern from single-crystal data on the solvated **2.1·MeCN** (bottom).*

3.3.1.2 A detailed *in situ* crystallographic study

The desolvation was then studied *in situ* at Diamond Light Source (beamline I11) by X-ray powder diffraction. Over 90 minutes at 75 °C under vacuum of 10^{-5} mbar, the material changed phase completely and there was no further change in the powder pattern was observed. The powder pattern progression for this phase change can be found in Figure 3.35**.** The experimental details of the *in situ* experiment can be found in the experimental section.

It should be noted that although these data were obtained from synchrotron radiation, the data quality appears poor. This is due to two factors – the wavelength of radiation used (λ = 0.825821 Å), and the nature of powder averaging within the X-ray beam. The wavelength used at Diamond beamline I11 is very close to the X-ray absorption edge of bromine, and as a highly brominated sample, **2.1.MeCN** gives observably poor diffraction patterns when collected using the fast Mythen2 detector. The goniometer and cell in which the powder sample is mounted rotates over a range of 80° about an axis perpendicular to the incident X-ray beam, to average sample exposure. This was not perfectly aligned with the collection strategy, causing uneven X-ray exposure and so unusual peak profiles.

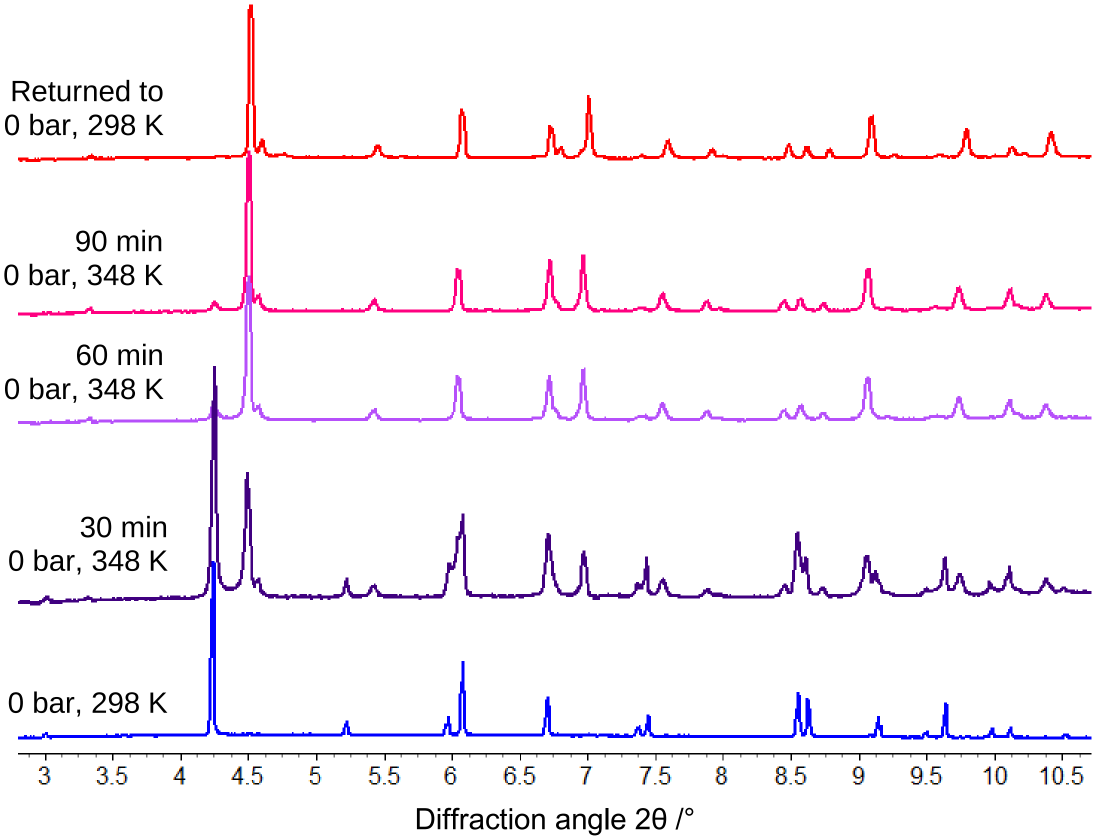

Figure 3.35. *X-ray powder diffraction pattern progression for desolvation of* ***2.1·MeCN*** *under heat and vacuum.*

The different relative conditions required to desolvate **2.1·MeCN** *ex situ* (as in Figure 3.33) and *in situ* (as in Figure 3.35) can be explained by considering the experimental set-up. In desolvating *ex situ*, the powder is exposed to air and is not in an enclosed environment. However in the *in situ* desolvation experiment, the powder was packed tightly into a narrow (0.5 mm) capillary, open at only one end. The desolvation conditions in TGA more closely match those of the *ex situ* experiment, and so the loss of acetonitrile has an onset temperature of 75 °C without the need for high-vacuum.

The powder pattern of the new phase at 25 °C can be indexed (and Pawley fit) to a single unit cell, with parameters a = 15.5307 (4) Å, b = 15.4357 (3) Å, c = 27.9346 (6) Å, V = 6696.7 (2) Å^3 (Orthorhombic $Pca2_1$). A comparison of this new unit cell and that of the parent compound **2.1·MeCN** (at 25 °C) suggests an approximate doubling of the unit cell (and therefore the Z value), as shown in Figure 3.36.

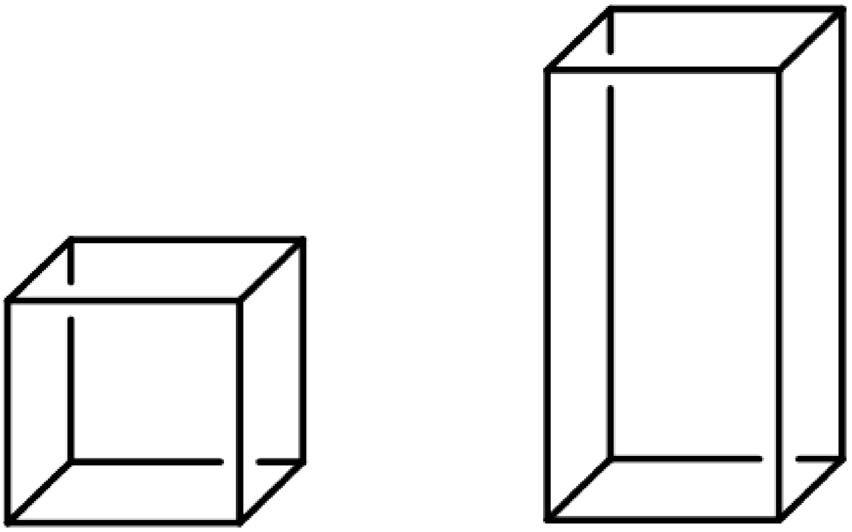

2.1·MeCN
Orthorhombic *Pbcm*
a = 15.4207 (3) Å
b = 15.7124 (3) Å
c = 15.4076 (3) Å
V = 3733.2 (1) $Å^3$
Z = 4

2.1
Orthorhombic $Pca2_1$
a = 15.4701 (2) Å
b = 15.4356 (3) Å
c = 27.9282 (5) Å
V = 6669.0 (2) $Å^3$
Z = 8

Figure 3.36. *Unit cell shape and volume comparison for compounds **2.1.MeCN** and the desolvated analogue **2.1**.*

Comparing the unit cells, the transformation appears to correspond to a near-doubling of one cell axis in **2.1**, while two axes remain relatively unchanged from the orthorhombic (near-cubic) starting material. However, the new, longer *c*-axis is not quite double any of the axes in **2.1.MeCN**. Dividing the cell volumes by the number of formula units per unit cell (*Z*), this means there is an 11.4% contraction in the volume per cluster molecule. This would be consistent with a loss of molecules from the material, resulting in a closer packing of the cluster molecules.

3.3.1.3 Structure of the desolvated cluster 2.1

Although the data quality was relatively poor (due to the issues with bromine absorption noted previously), the structure of **2.1** was successfully determined from powder diffraction data, using a simulated annealing approach followed by Rietveld refinement (see experimental section 3.2.1.2). The structure contains only the cluster **2.1**. The clusters stack such that their stellated shapes complement each other as far as possible – the angular cavities between pyrazolate ligands lie orthogonal to one another (see Figure 3.37).

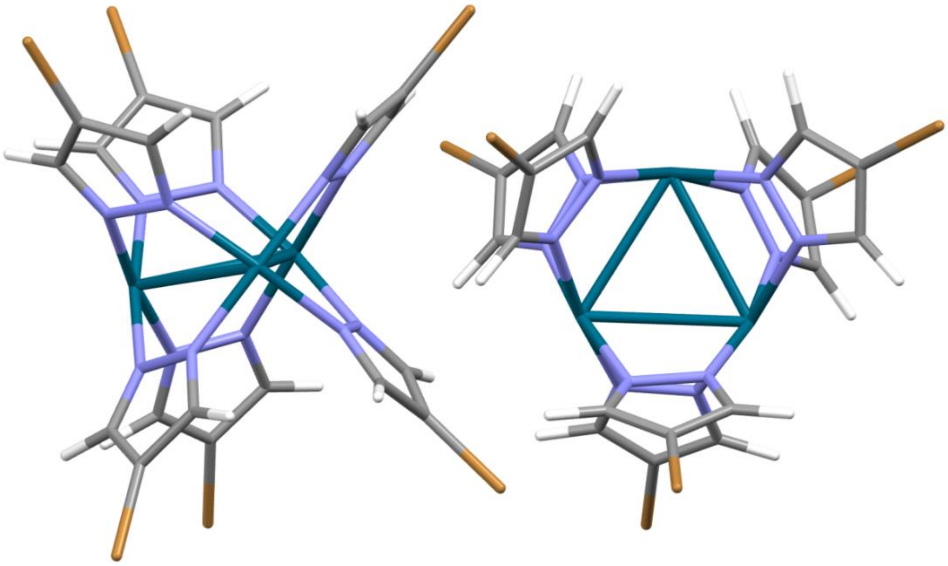

Figure 3.37. *The two crystallographically unique clusters in the structure of* ***2.1****, showing how they stack closely to each other after desolvation.*

A type I halogen-halogen interaction between clusters is also observed, although the relative strength of this and other interactions within the structure of **2.1** cannot accurately be assessed. This is because the individual atom positions in the structure have not been refined.

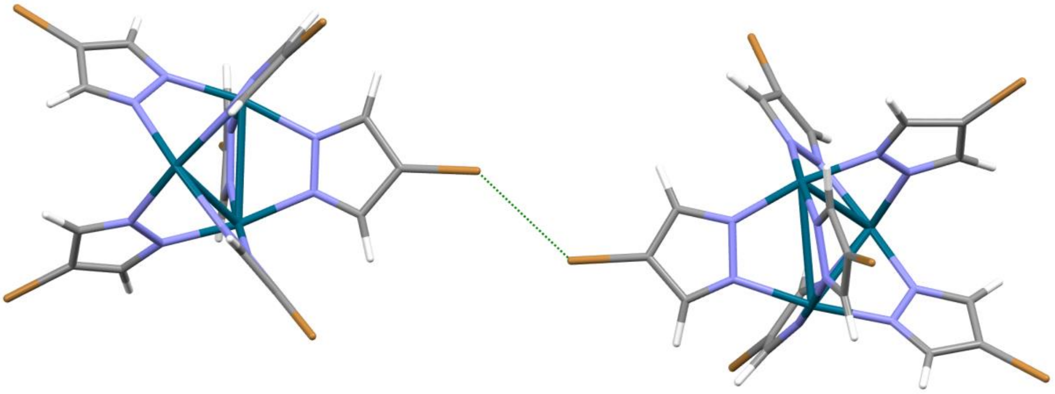

Figure 3.38. *Type I halogen-halogen interaction (Br···Br) in the structure of desolvated* ***2.1****, with an estimated* R_{BrBr} *of 0.87.*

The inefficient packing of the clusters creates a structure which contains voids that make up 8.9% of the unit cell volume. These voids are shown in pink in Figure 3.39. The largest of these voids, highlighted on the right of Figure 3.39 sits within the bowl-like cavity of the cluster **2.1**, in a manner resembling the cavities of porous molecular calixarenes introduced in section 3.1.1.[1,11]

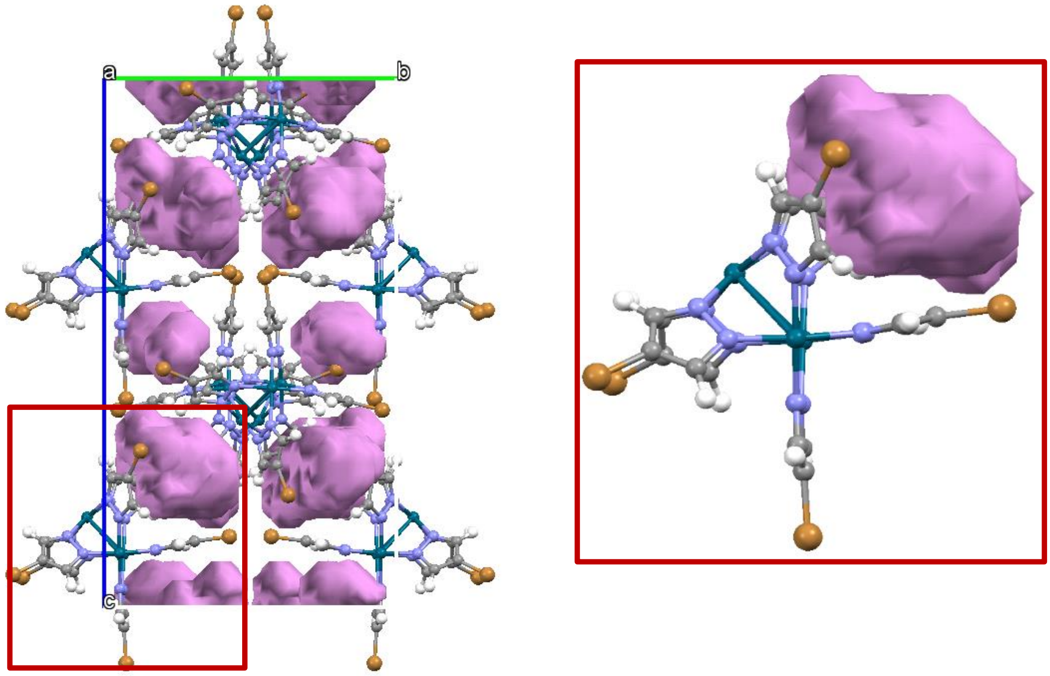

***Figure 3.39. Left:** Voids within one unit cell in the structure of the desolvated **2.1**, represented by pink surfaces. Unit cell axes are also shown for clarity. **Right, inset:** Expansion of the region highlighted in red on the left, demonstrating the main void position and shape within the bowl-shaped cavity of **2.1**.*

3.3.2 CO$_2$ uptake by cluster 2.1: *in situ* crystallographic study

The same sample described in the previous section, studied for its desolvation behaviour (study shown in Figure 3.35) was used for an *in situ* crystallographic study of CO$_2$ uptake. The sample in the cell was dosed with successive pressures of CO$_2$, and the sample was allowed to equilibrate for half an hour at each pressure before recording the X-ray diffraction pattern. Successive powder patterns for the ascending pressures (1 bar, 5 bar, 10 bar, 20 bar, 40 bar CO$_2$) are shown in Figure 3.40. Pawley fits of these patterns can be found in the experimental section 3.2.1.2.

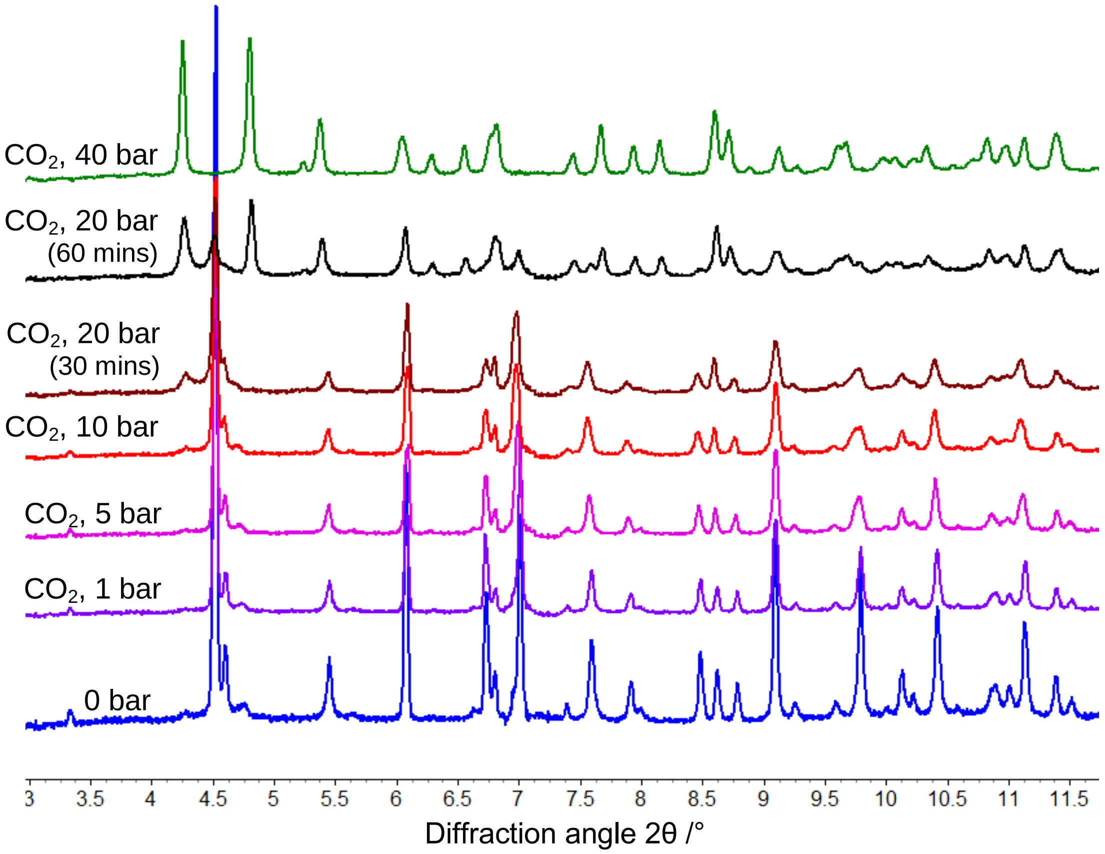

Figure 3.40. *X-ray powder pattern progression with increasing successive pressures (bottom to top) of* CO_2 *acting on* ***2.1****.*

No visible change occurred in the pattern until the sample reached 20 bar CO_2. At this point, the pattern contained peaks corresponding to the original **2.1** and a significant number of peaks corresponding to a new phase. Upon increasing the pressure to 40 bar CO_2, the material had changed phase completely to the new phase. This indicated either a pressure-induced phase change, or an uptake of CO_2, possibly involving a rearrangement of the clusters.

To provide further information, the pressure was dropped through 20 bar CO_2, to 10 bar, 1 bar and then returned to vacuum at 10^{-5} mbar. Surprisingly, the material remained in this new phase, despite allowing half an hour for equilibration at each descending pressure (shown in Figure 3.41).

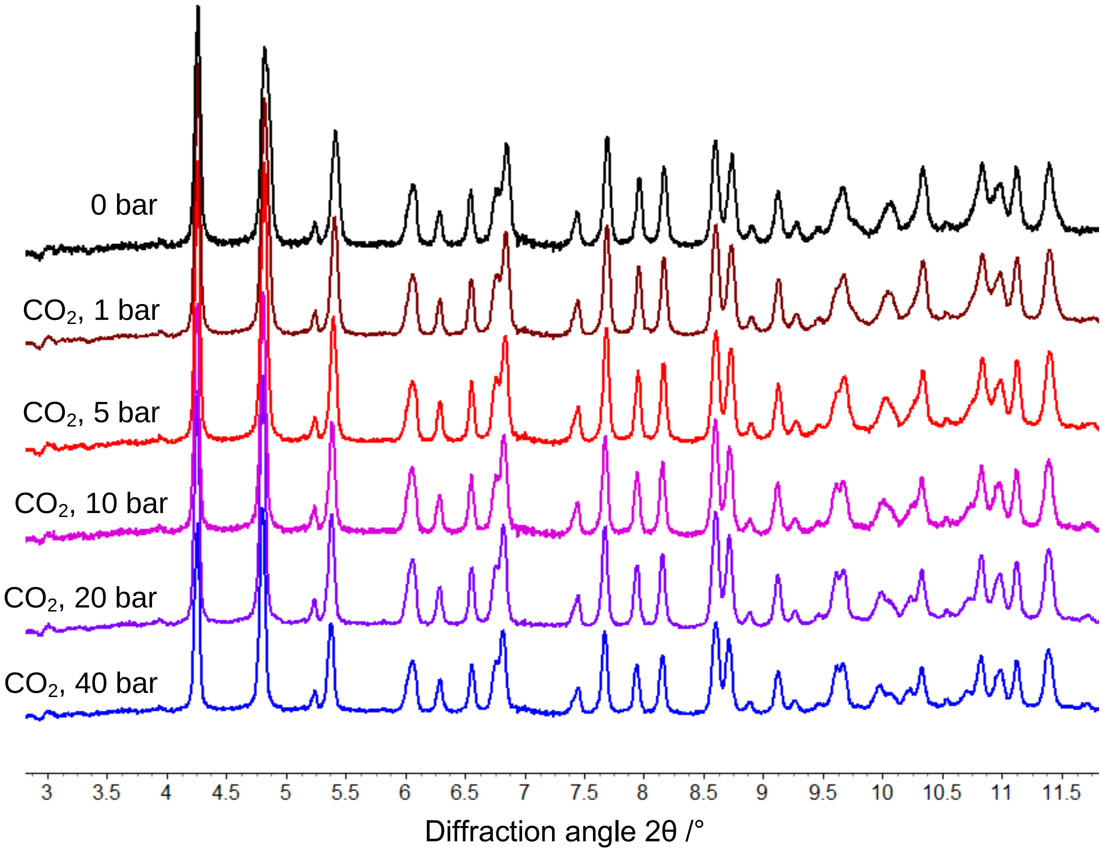

Figure 3.41. *X-ray powder pattern progression with decreasing successive pressures (bottom to top) of CO_2 (and then vacuum) acting on the new phase.*

It was possible that the compression of the material to a more stable structure could be taking place. The stability of the solvent-free phase **2.1** had not been tested under higher-than ambient pressure, and as highlighted in chapter 2, the stellated material has never been crystallised other than as a solvate. Indexing and Pawley fitting the new diffraction patterns suggested new cell parameters of a = 28.8728 (6) Å, b = 17.8876 (4) Å, c = 30.1764 (6) Å, β = 97.112 (1)°, V = 15465.1 (6) Å^3 (Monoclinic $C2$). The suggested unit cell for the new material is compared to those of **2.1·MeCN** and **2.1** in Figure 3.42.

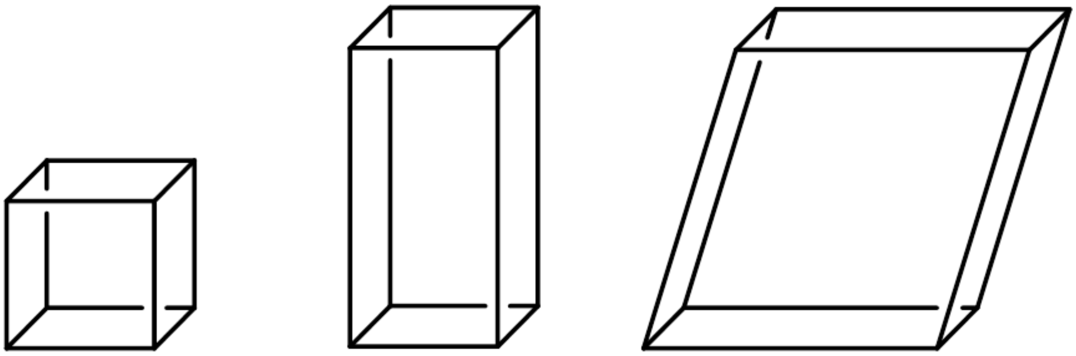

2.1·MeCN	**2.1**	**“2.1·nCO$_2$”**
Orthorhombic *Pbcm*	Orthorhombic $Pca2_1$	Monoclinic *C*2
a = 15.4445 (6) Å	a = 15.5307 (4) Å	a = 28.8728 (6) Å
b = 15.745 (1) Å	b = 15.4357 (3) Å	b = 17.8876 (4) Å
c = 15.5403 (7) Å	c = 27.9346 (6) Å	c = 30.1764 (6) Å
		β = 97.112 (1)°
V = 3779 Å^3	V = 6697 Å^3	V = 15464.1 (6) Å^3
Z = 4	Z = 8	Z = 16

Figure 3.42. *Unit cell shape and volume comparison for compounds **2.1·MeCN**, **2.1** and the ‘new phase’ created under 40 bar CO$_2$.*

Again considering the increased number of clusters per unit cell (as shown in Figure 3.42), this represents a 15.5% volume increase in the material (per cluster) compared with the desolvated **2.1**, and even a 1.02% expansion in the material, compared with the solvated material **2.1·MeCN**. An increase in the relative volume of the material compared with **2.1·MeCN** and **2.1** at low pressure would not be consistent with a pressure-induced phase change to a more closely-packed phase. This would indicate an uptake of CO$_2$ into the crystal, thus facilitating an expansion. A comparison of the relative expansion and contraction of the material from unit cell data is shown in Table 3.43.

Table 3.43. *A tabulation of the unit cell data for **2.1·MeCN**, **2.1** and **“2.1·nCO$_2$”**, with Z values and calculated volume expansions and contractions, per cluster, relative to the parent compound **2.1·MeCN**.*

Compound	Volume /Å^3	Z	Volume ÷ Z	% net volume increase, per cluster
2.1·MeCN	3779	4	944.8	n/a
2.1	6697	8	837.1	-11.40
“2.1·nCO$_2$”	15465	16	966.6	+1.02

The fact that the material did not change phase again or revert to the solvent-free phase **2.1** upon reducing the pressure suggests that either the material has retained CO_2, or at least the arrangement of the clusters in the structure is retained upon the removal of CO_2. Retention of CO_2 would indicate an impressive hysteresis in the gas sorption, which requires further study by gravimetric means to be confirmed. All attempts to determine the structure of the new **"2.1·nCO$_2$"** phase by simulated annealing were unsuccessful.

In the absence of crystal structure data for the proposed **"2.1·nCO$_2$"** phase, this assumes that the cluster compound has not been destroyed by the pressures involved in the experiment. However, the observation that these clusters are not destroyed even when heated for a sustained period as a solid, or even in solution (i.e. recrystallisation of **2.1·MeCN** from boiling dibromomethane) gives confidence to their stability at 40 bar of external pressure. In addition, high pressure crystallography shown in the literature for molecular species such as amino acids,[19–21] metal complexes[22] (including palladium-containing complexes)[23] indicate that even geological pressures of gigapascals are accommodated by bond distortions rather than their cleavage.

3.3.3 N_2 uptake by cluster 2.1: *in situ* crystallographic study

A comparable X-ray diffraction study to investigate potential nitrogen gas uptake was conducted on a fresh sample of **2.1·MeCN** at Diamond Light Source. The aims of this study were to determine if the behaviour of **2.1** towards CO_2 was selective, and possibly give further support to the conclusion that study 3.3.2 (above) demonstrates an uptake of gas rather than a pressure-induced phase change.

An *in situ* powder diffraction study in which compound **2.1·MeCN** was also desolvated to **2.1** was conducted, followed by adding successive pressures of N_2. The powder pattern progression for this study is shown in Figure 3.44.

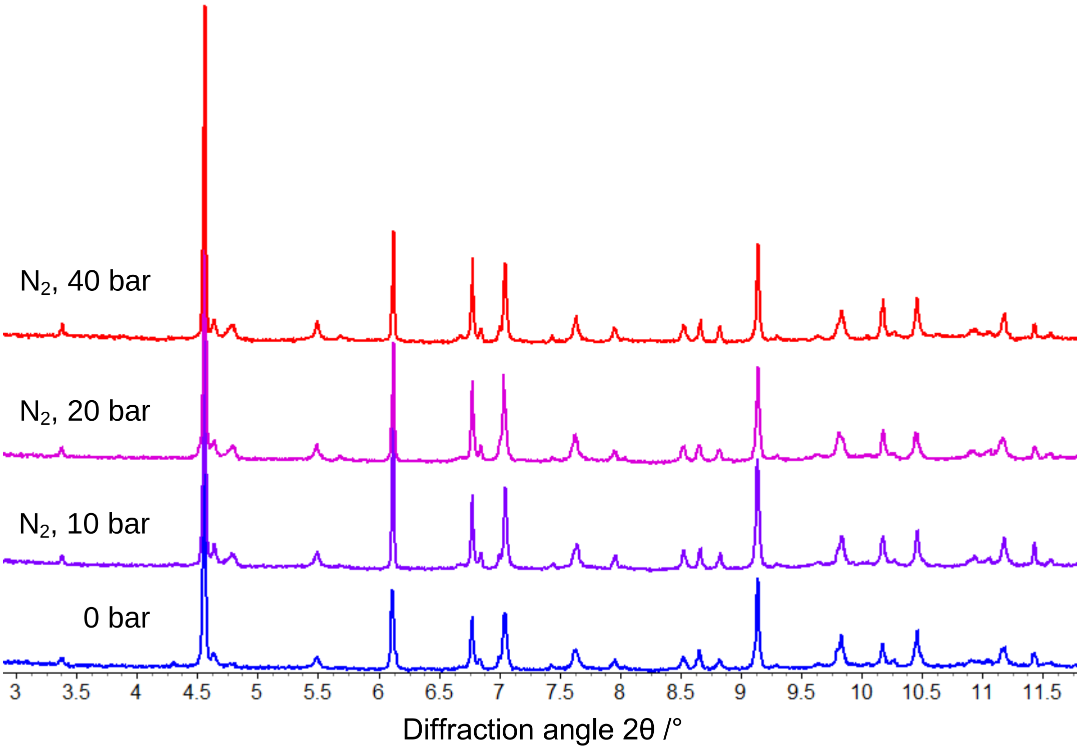

Figure 3.44. *X-ray powder pattern progression with increasing successive pressures of N_2 acting on* ***2.1****.*

The data clearly show that, allowing for the same half-hour equilibrations at each successive pressure, the material has not changed phase even at 40 bar N_2. In fact, this experiment allowed an additional 15 minute period of equilibration during collection due to use of the MAC detector for this study, rather than the rapid Mythen2 detector. This indicates that cluster **2.1** does not take up N_2 (on the timescale of this experiment).

The appearance of a small reflection at 4.75° 2θ is noted, as well as that of an even smaller reflection at 5.7° 2θ, but these could not be indexed to the known unit cell of **“2.1·CO_2”** identified previously. This could indicate that there is some response to nitrogen on a slow timescale. Whether this is an uptake of nitrogen, or is a pressure-induced phase change is not clear without gravimetric sorption data to support these diffraction data.

3.3.4 Rationale for potential selectivity for CO_2 over N_2

Considering the reasons behind guest selectivity within hosts, two factors are perhaps most important: the size of the guest molecules and their ability to interact with the host. Dinitrogen is a small, linear, non-polar molecule that is incredibly inert. It does not form strong hydrogen- or halogen-bonds, and is not strongly coordinating. Considering carbon dioxide, it too is small and linear, but is capable of forming a variety of interactions, including accepting weak hydrogen bonds, accepting halogen bonds, and acting as a Lewis base at open metal sites (which is noted as the origin of CO_2 selectivity in several MOF materials).[24–27]

In chapter 2, the ability of cluster **2.1** to form hydrogen- and halogen-bonds as both acceptor and donor is demonstrated extensively, as well as the potential ability of the palladium metal to act as an intermolecular interaction site, as in **2.1·DIM**. An ideal guest for the host **2.1** should be capable of participating in these interactions, and these factors may be the source of the apparent selectivity of **2.1** for CO_2 over N_2.

3.4 Conclusions & Future work

It was demonstrated that **2.1·MeCN** could be successfully desolvated, leaving behind the solvent-free stellated cluster material **2.1**. This results in the conversion of larger crystals into a microcrystalline solid, and does not appear to be a lithotropic (single-crystal-to-single-crystal / SCSC) transformation.

The desolvated material **2.1**, when exposed to pressures of CO_2 above 20 bar at 298 K, changes phase to the tentatively named **"2.1·nCO_2"**, possibly a new carbon-dioxide containing material based on powder X-ray diffraction data. When the external pressure of CO_2 was removed, the material retained the same crystal structure, suggesting a possible hysteresis. This surprising behaviour of a classically non-porous material further exemplifies the importance of the study of such compounds as an alternative to metal-organic frameworks (MOFs) and other porous materials.

When exposed to nitrogen gas, even at 40 bar at 298 K, **2.1** did not respond by taking in gas, or changing phase. This indicates selectivity for CO_2 over N_2, on the timescale of these crystallographic experiments.

Future work with these materials should aim to investigate the causes of this apparent selectivity for CO_2 over N_2, and the extent of the hysteretic sorption capabilities of **2.1**. This could be achieved by using mixed-gas streams of CO_2 and N_2 in gravimetric sorption measurements, including measuring the output gas. Other gases of interest that might help explain this selectivity could include carbon monoxide, sulphur dioxide and methane.

The material **2.7**, $[Pt_2Ag_4(Ipz)_8]$ (introduced in chapter 2) is a stellated cluster that was crystallised without solvent present, and showed the absence of strong intermolecular interactions in at least one dimension within the crystal. This would be an interesting candidate for gas uptake study for these reasons, as it may have the simplicity and flexibility required to take up guests, but it could not be synthesised in a sufficient quantity for such studies.

3.5 References

1 J. L. Atwood, L. J. Barbour and A. Jerga, *Science*, 2002, **296**, 2367–2369.

2 J. L. Atwood, L. J. Barbour and A. Jerga, *Angew. Chem. Int. Ed. Engl.*, 2004, **43**, 2948–2950.

3 P. Sozzani, S. Bracco, a. Comotti, L. Ferretti and R. Simonutti, *Angew. Chem. Int. Ed. Engl.*, 2005, **44**, 1816–1820.

4 L. Dobrzańska, G. O. Lloyd, H. G. Raubenheimer and L. J. Barbour, *J. Am. Chem. Soc.*, 2005, **127**, 13134–13135.

5 L. Dobrzańska, G. O. Lloyd, H. G. Raubenheimer and L. J. Barbour, *J. Am. Chem. Soc.*, 2006, **128**, 698–9.

6 Y. Jin, B. A. Voss, A. Jin, H. Long, R. D. Noble and W. Zhang, *J. Am. Chem. Soc.*, 2011, **133**, 6650–66588.

7 M. J. Bojdys, M. E. Briggs, J. T. A. Jones, D. J. Adams, S. Y. Chong, M. Schmidtmann and A. I. Cooper, *J. Am. Chem. Soc.*, 2011, **133**, 16566–71.

8 T. Hasell, J. A. Armstrong, K. E. Jelfs, F. H. Tay, K. M. Thomas, S. G. Kazarian and A. I. Cooper, *Chem. Commun.*, 2013, **49**, 9410–9412.

9 T. Itoh, M. Kondo, H. Sakamoto, K. Wakabayashi, M. Kanaike, K. Itami and S. Masaoka, *Dalt. Trans.*, 2015, **44**, 15334–15342.

10 R. Manurung, D. Holden, M. Miklitz, L. Chen, T. Hasell, S. Y. Chong, M. Haranczyk, A. I. Cooper and K. E. Jelfs, *J. Phys. Chem. C*, 2015, **119**, 22577–22586.

11 J. L. Atwood, L. J. Barbour, A. Jerga and B. L. Schottel, *Science*, 2002, **298**, 1000–1002.

12 S. J. Dalgarno, P. K. Thallapally, L. J. Barbour and J. L. Atwood, *Chem. Soc. Rev.*, 2007, **36**, 236–245.

13 S. Kitagawa and K. Uemura, *Chem. Soc. Rev.*, 2005, **34**, 109–119.

14 S. P. Thompson, J. E. Parker, J. Potter, T. P. Hill, A. Birt, T. M. Cobb, F. Yuan and C. C. Tang, *Rev. Sci. Intrum.*, 2009, **80**, 075107.

15 S. P. Thompson, J. E. Parker, J. Marchal, J. Potter, A. Birt, F. Yuan, R. D. Fearn, A. R. Lennie, S. R. Street and C. C. Tang, *J. Synchrotron Rad.*, 2011, **18**, 637–648.

16 A. A. Coelho, *TOPAS Academic, version 4.1 (2007), see http://www.topas-academic.net*, .

17 G. S. Pawley, *J. Appl. Crystallogr.*, 1981, **14**, 357–361.

18 H. M. Rietveld, *J. Appl. Crystallogr.*, 1969, **2**, 65–71.

19 F. P. A. Fabbiani, D. R. Allan, W. I. F. David, S. A. Moggach, S. Parsons and C. R. Pulham, *CrystEngComm*, 2004, **6**, 504–511.

20 S. A. Moggach, D. R. Allan, C. A. Morrison, S. Parsons and L. Sawyer, *Acta Crystallogr. Sect. B*, 2005, **61**, 58–68.

21 A. Dawson, D. R. Allan, S. A. Belmonte, J. Clark, Stewart, W. I. F. David, P. A. McGregor, S. Parsons, C. R. Pulham and L. Sawyer, *Cryst. Growth Des.*, 2005, **5**, 1415–1427.

22 J. P. Tidey, H. L. S. Wong, M. Schröder and A. J. Blake, *Coord. Chem. Rev.*, 2014, **277-278**, 187–207.

23 D. R. Allan, D. Bailey, N. Bird, A. J. Blake, N. R. Champness, D. Huang, C. P. Keane, J. McMaster, T. J. Prior, J. P. Tidey and M. Schröder, *Acta Crystallogr. Sect. B*, 2014, **70**, 469–486.

24 J. Liu, P. K. Thallapally, B. P. McGrail, D. R. Brown and J. Liu, *Chem. Soc. Rev.*, 2012, **41**, 2308–2322.

25 W.-Y. Gao, W. Yan, R. Cai, K. Williams, A. Salas, L. Wojtas, X. Shi and S. Ma, *Chem. Commun.*, 2012, **48**, 8898–8890.

26 A. Hazra, S. Bonakala, S. K. Reddy, S. Balasubramanian and T. K. Maji, *Inorg. Chem.*, 2013, **52**, 11385–11397.

27 B. Supronowicz, A. Mavrandonakis and T. Heine, *J. Phys. Chem. C*, 2013, **117**, 14570–14578.

A chiral/racemic pair of triazole-based MOFs:

Investigating gas uptake and chiral guest selectivity

Chapter Four

4.1 Introduction

4.1.1 Chiral MOFs and enantioselective separation

As well as being highly promising storage and separation materials for simple gases (as noted in chapter 1), the great degree of customisation achievable for metal-organic frameworks also provides the possibility for storage and separation of more complex guests. One such area which is being explored is the entrapment and reaction of chiral guests, using MOFs as enantioselective hosts.

Two key approaches to these enantioselective hosts have been studied by crystal engineers.[1–3] These involve either the use of chiral ligands to direct the self-assembly of a chiral coordination network, or the spontaneous resolution of achiral components into a chiral framework upon assembly[4–12] (including the post-synthetic introduction of 'chiral resolution agents').[9,12] The use of enantiomerically pure ligands has included both the utilisation of natural products and/or their derivatives as ligands,[13–17] and the synthesis of entirely new chiral multi-topic ligands.[18–23]

Several of these chiral MOF systems have been applied to enantio- or diastereospecific catalysis within their pores.[15,19,20,23] In particular, impressive results were obtained by Lin and co-workers in exploiting the tune-ability of MOFs to create a related family of materials for a variety of enantioselective organic transformations.[19] This was achieved by using structurally related carboxylate ligands with chiral functionality (see Figure 4.1), to construct a series of iso-reticular MOFs.

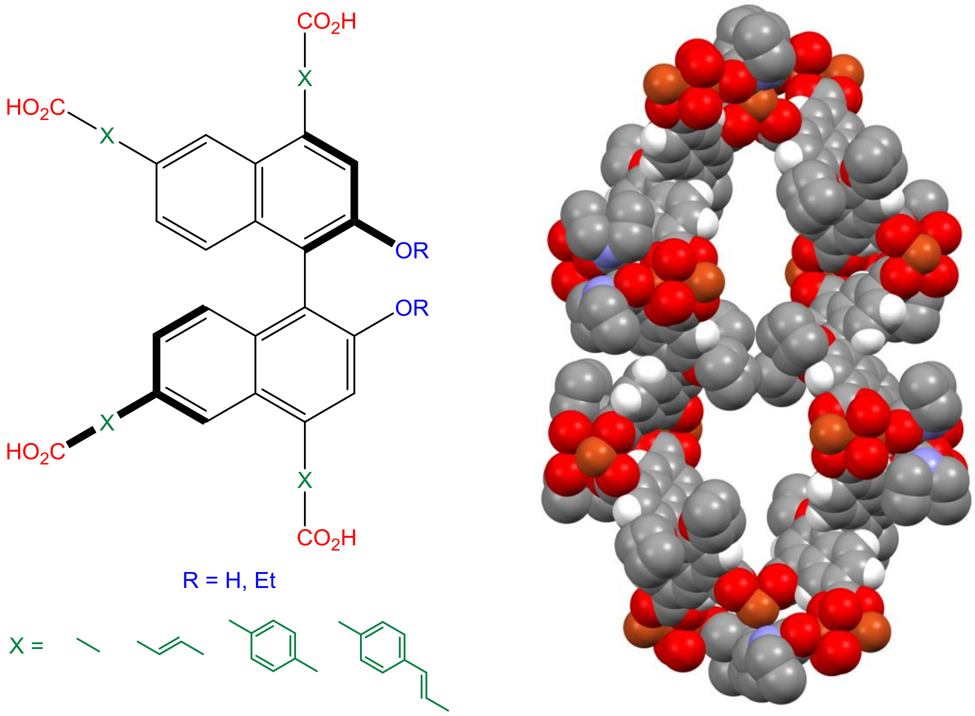

Figure 4.1. Left: *The general ligand type used by Lin et. al. to create a series of* Cu^{II}*-based MOFs effecting a structure with pores* (***right***) *capable of facilitating enantioselective catalysis.*[19]

A recent review by Duerinck and Denayer cites ten noteworthy examples of the application of chiral MOFs to separation guests in the liquid phase as of 2014,[24] with enantioselectivities for chiral guests as high as 98.2% ee (enantiomeric excess) recorded.[13] In the case of the host affording 98.2% ee, a coordination polymer based upon a modified quinine ligand connecting Cd^{II} centres, demonstrates well the crystal engineering approach to functional materials. The authors lay out their reason for the choice of this ligand – it forms a neutral, diamondoid network with M^{2+}, and has a mixture of hydrophobic and hydrophilic surface area that facilitates the inclusion of different guests. The resultant homochiral network, shown in Figure 4.2, was capable of selectively trapping *S*-butan-2-ol (with 98.2% ee, as noted above) so successfully that the only guest identifiable in the pore by single-crystal X-ray diffraction was the *S*-enantiomer.

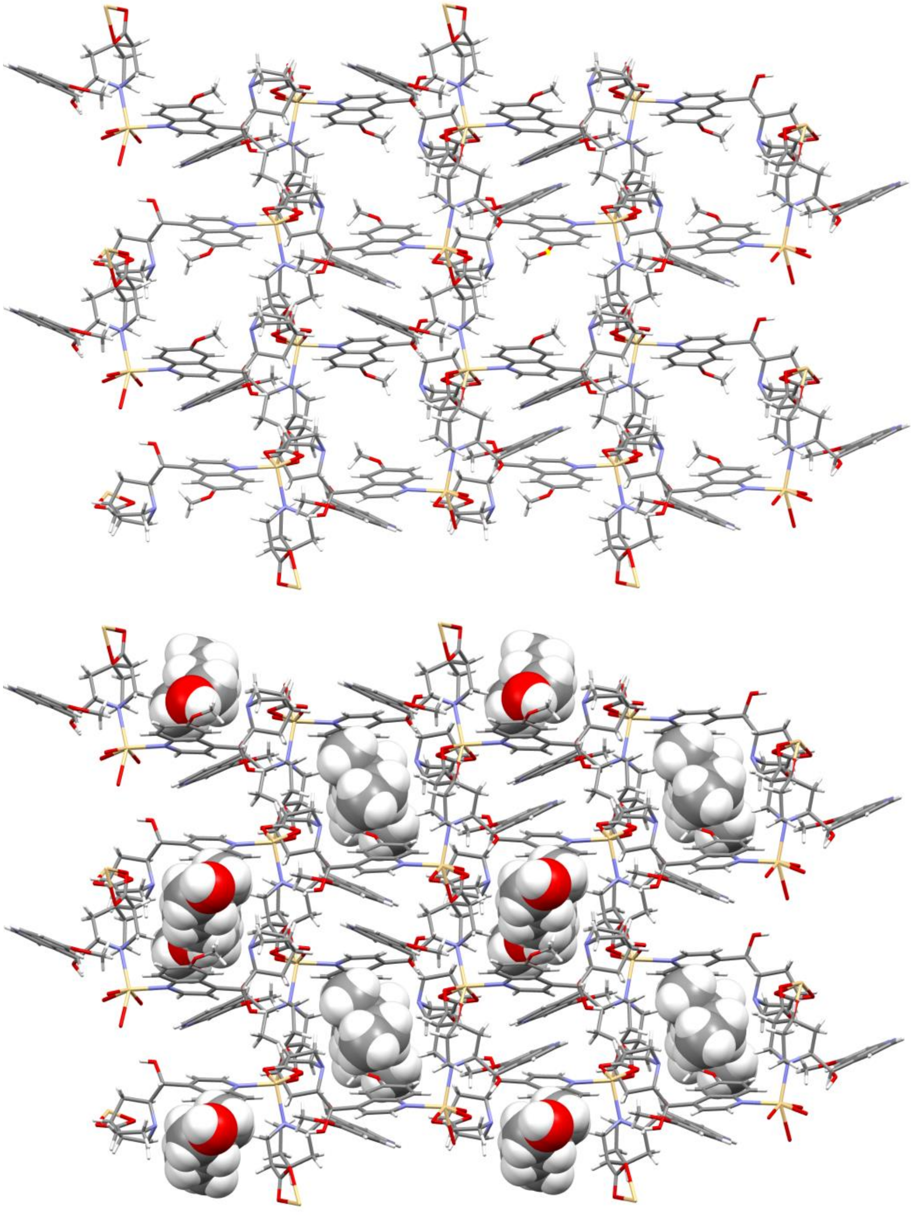

Figure 4.2. Top: *The structure of the empty framework material [Cd(quinine-carboxylate)$_2$].* ***Bottom:*** *The same host structure containing the crystallographically-located S-butan-2-ol.*[13]

Fewer examples of uptake of chiral guests in the gas/vapour phase exist.[25–30] The work cited has largely focussed on the study of chiral separation afforded by using these MOFs as stationary phases in chiral gas chromatography. Particularly notable is the use of camphorate as a bridging ligand in these materials (four of the six examples noted in the review by Duerinck and Denayer use it). In one particularly interesting and unique case, a camphorate-containing MOF was applied as a functional surface material (SURMOF) onto a quartz crystal microbalance (QCM).[26] The chiral selectivity of the functionalised surface was probed by monitoring mass loading of different enantiomerically pure chiral vapours into the SURMOF (see QCM profiles in Figure 4.3). This work marks the first time gravimetric measurements have been used to probe chiral vapour uptake in MOFs.

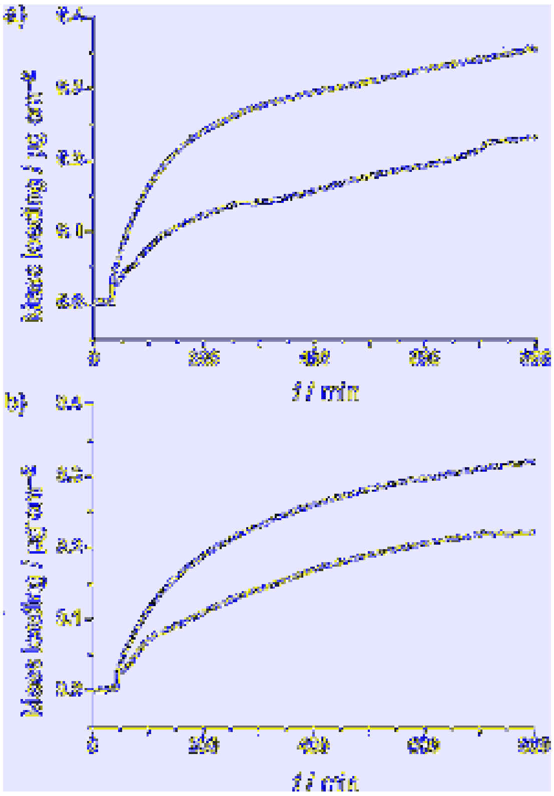

Figure 4.3. *QCM profiles for the uptake of pure S-hexane-2,5-diol vapour (red) or R-hexane-2,5-diol vapour (black) in the surface MOF coatings of [Zn*$_2$*((+)-camphorate)*$_2$*(dabco)] (top graph) or [Zn*$_2$*((-)-camphorate)*$_2$*(dabco)] (bottom graph), demonstrating the selectivity of uptake. Figure reproduced from reference 26.*

These studies highlight the usefulness of camphorate as a directing ligand in creating familiar, carboxylate-based chiral metal-organic frameworks, as well as the potential power of chiral MOFs as selective host materials for chiral guests. The use of gravimetry to quantify chiral guest uptake within a MOF, without destroying the material as in analysis by solution-phase methods is also a promising, but underexplored avenue of investigation.

Camphorate-based MOFs have also been explored by the Brammer group as functional materials. As well as being rare examples of MOFs which undergo multi-step transformations from 2D polymeric materials to 3D polymeric materials (see chapter 1, section 1.3.1.2),[31] their chiral nature was also probed.

It was found that the 2-dimensional MOF [Zn_2(*(+)*-camphorate)$_2$(pyridine)$_2$] was able to uptake liquid 1,2-propanediol, and appeared selectively entrap the *R*-enantiomer (see Figure 4.4).[32] However, the difficulty of separating enantiomers of propanediol by chiral gas chromatography meant the result was not completely clear, although a 20% ee for *R*-propanediol was suggested.

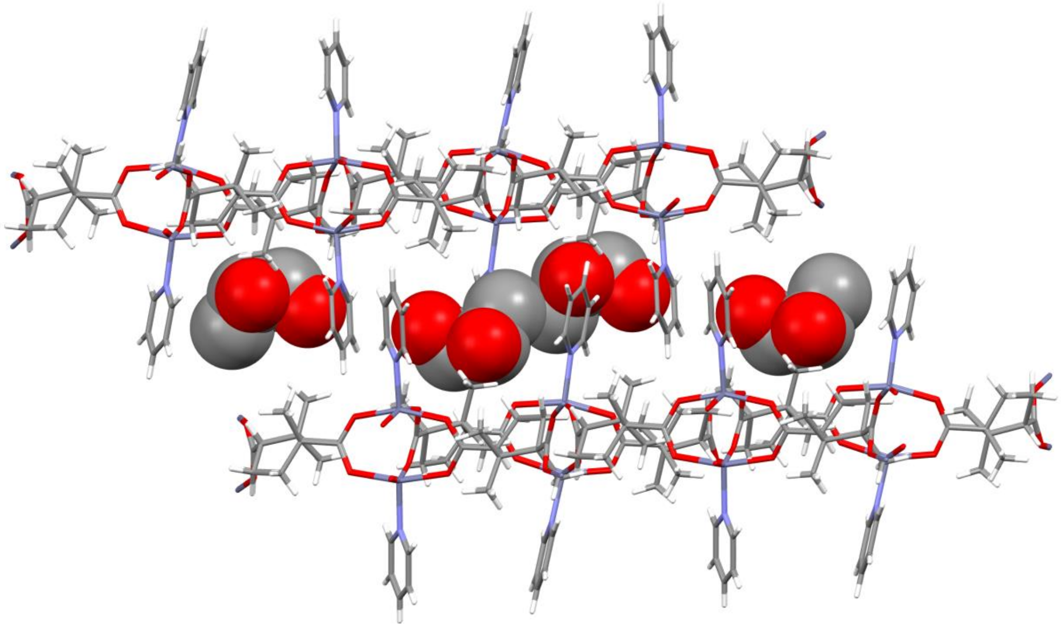

Figure 4.4. *Crystal structure of [Zn_2((+)-camphorate)$_2$(pyridine)$_2$](1,2-propanediol)$_2$, as the result of soaking crystals of [Zn_2((+)-camphorate)$_2$(pyridine)$_2$] in propranediol for seven weeks.*[32]

4.1.2 Project aims

The work outlined in this chapter aimed to use an enantiomerically pure ligand in the synthesis of a homochiral MOF. In line with this project's focus on azole-based materials, an azole-type chiral ligand was sought to direct the formation of chiral MOFs.

An N-heterocyclic carbene derivative of 1,2,4-triazole used as a ligand in an enantiospecifically catalytic complex was identified.[33] Ruthenium complexes containing the ligand (shown in Figure 4.5) were found to catalyse enantiospecific hydrogenation reactions with up to 61% ee. The synthetic route toward the carbene ligand indicated that a simple, one-pot reaction (as in step one/two, below) would yield a neutral triazole ligand suitable for use in MOF synthesis.

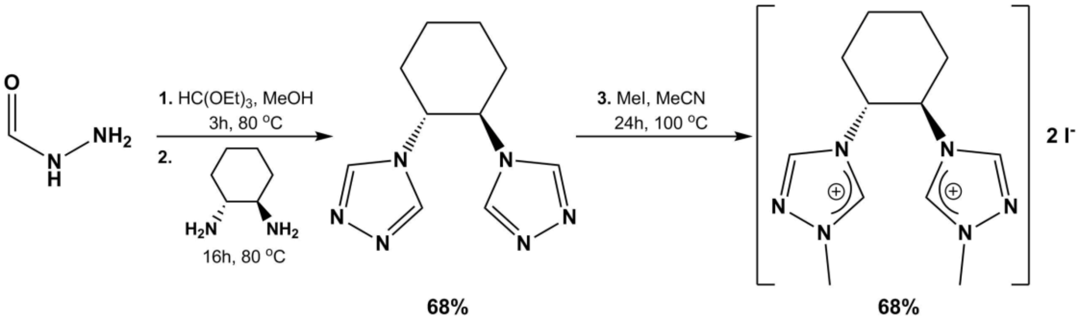

Figure 4.5. *Synthetic pathway reported in the literature, leading to a chiral NHC.*[33] *Step one/two yields a viable, isolable triazole ligand of interest to this project.*

The work described in this chapter aimed to synthesise and characterise new chiral MOF materials constructed using the triazole ligand shown in Figure 4.5. The porosity of the new MOFs was to be determined crystallographically and by their exposure to CO_2, and their ability to uptake chiral guests to be determined. The ability of the resultant MOFs to selectively entrap chiral guests from a racemic mixture was also to be tested.

4.2 Experimental

4.2.1 Synthesis

All reactants were purchased from Fluorochem, Aldrich or Fisher Scientific and used as received without further purification. Methanol was dried over calcium hydride and distilled, then degassed by bubbling argon through the solvent for no less than 30 minutes before use. As formic hydrazide is an incredibly hygroscopic solid, it was stored under argon in a desiccator jar. NMR spectra and mass spectra for ligands can be found in appendix A.

***(+,-)*-trans-cyclohexane-1,2-bis-4'(1,2,4-triazole); *RR,SS*cbt**

This synthesis largely follows the synthetic procedure outline for the *R,R*- isomer in the literature.[33]

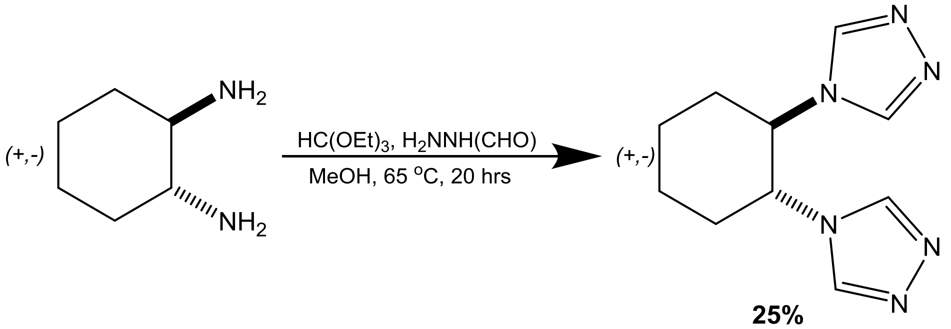

Triethylorthoformate (2.9 mL, 9 mmol) and dry methanol (10 mL) were added to formic hydrazide (0.53 g, 4.5 mmol) under argon with stirring, effecting dissolution. The solution was refluxed under argon for six hours, before adding 1,2-*trans*-cyclohexanediamine (0.33 mL, 4.5 mmol) dropwise, followed by a further 2 mL of dry methanol. The solution was refluxed for a further 20 hours, before cooling to room temperature. The solvent was removed *in vacuo* and the clear waxy residue was washed with ethanol (absolute, c. 5 mL), effecting the precipitation of the title compound as a fine, white solid, which was isolated by filtering at the pump, and used without any further purification (252 mg, 1.14 mmol, 25% yield). ^{1}H-NMR (250 MHz, DMSO-d^6): δ 1.47 (m, 2H, $^{\text{c-hex}}CH_2$), 1.70-2.22 (m, 4H, $^{\text{c-hex}}CH_2$), 4.60 (m, 2H, $^{\text{c-hex}}$CH), 8.40 (s, 4H, $^{\text{triazole}}$CH). MS (ES+): *m/z* = 219.1 [MH+].

(-,-)-trans-cyclohexane-1,2-bis-4'(1,2,4-triazole); *RR*cbt

This synthesis largely follows the literature procedure for the title compound.[33]

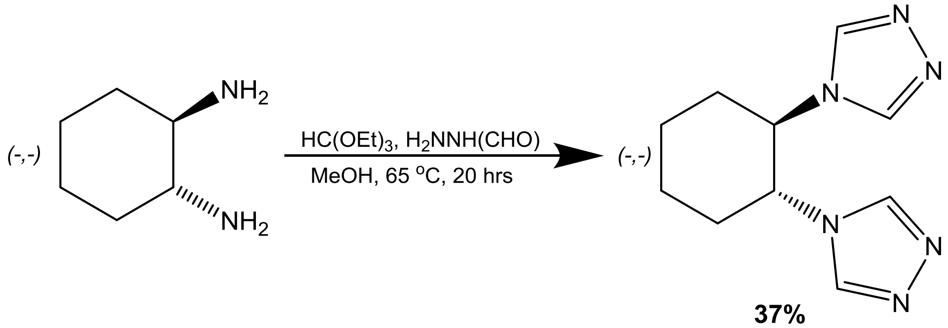

Triethylorthoformate (2.9 mL, 9 mmol) and dry methanol (10 mL) were added to formic hydrazide (0.53 g, 4.5 mmol) under argon with stirring, effecting dissolution. The solution was refluxed under argon for six hours, before adding 1,2-*trans*-cyclohexanediamine (0.33 mL, 4.5 mmol) dropwise, followed by a further 2 mL of dry methanol. The solution was refluxed for a further 20 hours, before cooling to room temperature. Some off-white precipitate had formed, and the remaining solvent was removed *in vacuo* and the residue was washed with ethanol (absolute, c. 5 mL), effecting further precipitation of the title compound as a fine, off-white solid, which was isolated by filtering at the pump, and used without any further purification (290 mg, 1.66 mmol, 37% yield). $[\alpha]_{(589\text{ nm } 19\,^{\circ}\text{C})}$ -45.0 ± 1.30 $dm^{-1}\,g^{-1}\,cm^3$ (c = $2\text{x}10^{-3}$ g mL^{-1} in DMSO). ^{1}H-NMR (250 MHz, DMSO-d^6): δ 1.47 (m, 2H, $^{\text{c-hex}}CH_2$), 1.86 (m, 2H, $^{\text{c-hex}}CH_2$), 1.96 (m, 2H, $^{\text{c-hex}}CH_2$), 2.10 (m, 2H, $^{\text{c-hex}}CH_2$), 4.65 (m, 2H, $^{\text{c-hex}}CH$), 8.40 (s, 4H, $^{\text{triazole}}CH$). MS (ES+): *m/z* = 219.1 [MH+].

[Zn(bdc)(*RR,SS*cbt)]·xH_2O·yDMF, 4.1·xH_2O·yDMF

Zinc nitrate hexahydrate (30 mg, 0.10 mmol), terephthalic acid (17 mg, 0.10 mmol) and ***RR,SS*cbt** (24 mg, 0.10 mmol) were dissolved in 8 mL DMF, and the clear solution placed in a 24 mL-capacity screwcap glass vial. The solution was heated in an oven to 100 °C at a rate of 10 °C min^{-1}, held at 100 °C for a period of 12 hours and then cooled to 25 °C at a rate of 0.1 °C min^{-1}. This yielded white, needle-like crystals of the title compound, which were washed with a small volume of ice-cold fresh DMF and stored under fresh DMF until analysis (34 mg, 0.062 mmol, 62% yield). CHN expected: C 45.66%, H 5.16%, N 17.75%; anal. found: C 45.32%, H 4.95%, N 17.72%.

(Molar mass and expected CHN content based on composition of **4.1·1.8H_2O·0.9DMF**, which gives best fit to the elemental analysis data).

[Zn(bdc)(*RR*cbt)]·xH_2O·yDMF, 4.2·xH_2O·yDMF

Zinc nitrate hexahydrate (30 mg, 0.10 mmol), terephthalic acid (17 mg, 0.10 mmol) and ***RR*cbt** (24 mg, 0.10 mmol) were dissolved in 8 mL DMF, and the clear solution placed in a 24 mL-capacity screwcap glass vial. The solution was heated in an oven to 100 °C at a rate of 10 °C min^{-1}, held at 100 °C for a period of 12 hours and then cooled to 25 °C at a rate of 0.1 °C min^{-1}. This effected white, needle-like crystals of the title compound, which were washed with a small volume of ice-cold fresh DMF and stored under fresh DMF until analysis (36 mg, 0.065 mmol, 65% yield). CHN expected: C 45.86%, H 5.20%, N 17.83%; anal. found: C 45.80%, H 5.39%, N 17.82%.
(Molar mass and expected CHN content based on composition of **4.2·1.7H_2O·1.0DMF**, which gives best fit to the elemental analysis data).

4.2.2 Guest soaking experiments

4.2.2.1 Chloroform soaking

Crystals of either **4.1·xH_2O·yDMF** or **4.2·xH_2O·yDMF** were isolated from DMF by filtering at the pump, before placing in a fresh 24 mL-capacity glass vial and adding chloroform (dried by the Grubbs method),[34] in sufficient amount to cover the crystals completely. The vial was then sealed. The solvent was exchanged at least three times for fresh, dry chloroform, and the samples were allowed to soak for one week before further use. X-ray powder diffraction measurements showed changes in the intensities of key peaks (see section 4.2.5), indicating successful exchange of solvent. The formulae were, as such, considered then to be **4.1·$nCHCl_3$** or **4.2·$nCHCl_3$**.

4.2.2.2 1-Phenylethanol soaking

25 mg of crystals of **4.1·$nCHCl_3$** or **4.2·$nCHCl_3$**, as prepared above were isolated by filtering at the pump, and allowed to air-dry for a period of 3 days in a sealed vessel. The crystals were then heated in open vials in an oven at 80 °C for 90 minutes. Upon cooling to just above room temperature (to avoid as much water uptake as possible), the crystals were immediately submerged in 2 mL 1-phenylethanol (98%, racemic), and the vials sealed.

After a period of 12 weeks, half of the resultant crystals of **4.1·$aPhCH_2(OH)Me$** or **4.2·$aPhCH_2(OH)Me$** were isolated from the mother liquor by filtering at the pump, and were allowed to dry under air for ten minutes exactly. The crystals were dissolved/digested for analysis by adding 0.5 mL DMSO, and then adding trifluoroacetic acid (99%) dropwise with agitation, until dissolution was achieved. The solution was neutralised by dropwise addition of triethylamine. The other half of the sample, undigested, was used for further analysis.

4.2.3 Gravimetric gas sorption measurements

Gravimetric sorption measurements were recorded using an Intelligent Gravimetric Analyser (IGA) model 003 supplied by Hiden Isochema Ltd. The balance and pressure control system of the instrument are fully thermostatted to 0.1 K, and the microbalance has a weighing resolution of 0.2 μg. Prior to the measurements, the sample was outgassed using conditions specific to each run (as specified in subsequent sections). During measurements, the pressure of gas was gradually increased over roughly 15 seconds, avoiding disruption to the microbalance. Pressure control used two pressure transducers, with ranges 0-0.1 and 0-2 MPa, each with an accuracy of 0.02% in the specified range. The pressure was maintained at the set point by active computer control. The mass uptake was measured as a function of time and the approach to equilibrium monitored in real time with a computer algorithm. The maximum time for equilibration of any one pressure point was 6 hours. After equilibration was established, the pressure of gas was increased to the next set value. The sample temperature was constantly monitored and maintained throughout the experiment using a thermo-stirrer.

4.2.3.1 CO_2 uptake in 4.1 at 298 K

The sample was outgassed at 393 K for a period of 12 hours, resulting in a mass loss of 13.68% before equilibration. The sample was dosed as noted above to 19.5 bar CO_2 at 298 K. The resultant isotherm (both adsorption and desorption profiles) is shown in section 4.3.5.

4.2.3.2 CO_2 uptake in 4.2 at 298 K

The sample was outgassed at 393 K for a period of 12 hours, resulting in a mass loss of 15.06% before equilibration. The sample was dosed as noted above to 19.5 bar CO_2 at 298 K. The resultant isotherm (both adsorption and desorption profiles) is shown in section 4.3.5.

4.2.3.3 1,2-propanediol uptake in 4.1 at 298 K

The sample was outgassed at 393 K for a period of 12 hours, resulting in a mass loss of 20.01% before equilibration. The pressure of the sample chamber was increased to 1 bar of pure N_2 gas, to obtain the initial mass of MOF after adsorption of N_2 (to remove the effect of N_2 on the measurement). A flow of N_2 gas was saturated with racemic 1,2-propanediol, and diluted using a second stream of pure N_2 gas to obtain a series of data points, corresponding to 0.05 increases in relative pressure of 1,2-propanediol. All data points were measured at 1 bar of N_2, and the temperature was maintained at 323 K, giving a vapour pressure of 1.4 mbar of 1,2-propanediol. The resultant adsorption isotherm is shown in section 4.3.6.

4.2.4 Single crystal X-ray diffraction

Single crystal X-ray diffraction data were collected for compound **4.1·xH_2O·yDMF** on a Bruker *APEX-2*, using Mo-Kα radiation, and for **4.1·aPhCH_2(OH)Me** and **4.2·aPhCH_2(OH)Me** on a Bruker D8 *VENTURE* diffractometer, equipped with a PHOTON 100 CMOS detector, using Cu-Kα radiation. Data for **4.2·xH_2O·yDMF** were collected on a Newport CCD diffractometer equipped with a PILATUS detector at Diamond Light Source beamline I19 (λ =0.6889 (3) Å). Data at I19 were collected as a series of eight sequences of frames, covering approximately one hemisphere of reciprocal space. Each frame was collected as a 0.2 second exposure, with the beam attenuated to 54% of full power, via the insertion of a 1 mm sheet of aluminium foil in the beam path.

All data were corrected for absorption using empirical methods (*SADABS*), based on symmetry-equivalent reflections combined with measurements at different azimuthal angles.[35,36] Crystal structures were solved and refined against all F^2 values, using *Olex2*.[37] Non-hydrogen atoms were refined anisotropically (except atoms which were part of the disordered terephthalate ligand, which were refined isotropically), and hydrogen atoms placed in calculated positions refined using idealised geometries (riding model) and assigned fixed isotropic displacement parameters.

Solvent contained within frameworks **4.1** and **4.2** could not be located crystallographically. Once structure solution and satisfactory refinement of the framework was achieved, PLATON SQUEEZE was applied.[38,39] The output of the

SQUEEZE routine and its implications for the pore solvent content and pore/void volumes are discussed in sections 4.3.1 and 4.3.6.2.

Data collection and refinement parameters for all collections are provided in Table 4.6. Crystallographic information files for all structures in Table 4.6 are provided in the digital appendix.

Table 4.6. *Data collection, structure solution and refinement parameters for crystal structures in chapter 4.*

	4.1·xH_2O·yDMF	**4.2·xH_2O·yDMF**
	Mo-Kα raditaion	*Synchrotron radiation*
Crystal habitat	Plate	Plate
Crystal colour	Colourless	Colourless
Crystal size (mm)	0.45 x 0.28 x 0.06	0.15 x 0.11 x 0.10
Crystal system	Monoclinic	Monoclinic
Space group	*C* 2/c	*C* 2
a (Å)	14.6071 (8)	14.5193 (5)
b (Å)	32.918 (2)	32.973 (1)
c (Å)	11.4298 (6)	11.7099 (5)
α (°)	90	90
β (°)	101.936 (4)	101.066 (4)
γ (°)	90	90
V ($Å^3$)	5377.0 (5)	5501.8 (4)
Density (Mg m^{-3})	1.106	0.876
Temperature (K)	100	266
μ (mm^{-1})	0.941	0.455
θ range (°)	3.106 to 41.752	3.018 to 62.642
Reflns. collected	13196	56037
Independent reflns. (R_{int})	2838 [$R_{(int)}$ = 0.0874]	16554 [$R_{(int)}$ = 0.1237]
Reflns. used in refinement, *n*	2838	16554
LS parameters, *p*	249	475
Restraints, *r*	0	17
$R1$ (F)[a] *I>2.0s(I)*	0.0654	0.0872
$wR2$ (F^2)[a], all data	0.189	0.2486
$S(F^2)$[a], all data	1.008	0.917

	4.1·aPhCH_2(OH)Me	**4.2·aPhCH_2(OH)Me**
	Cu-Kα raditaion	*Cu-Kα raditaion*
Crystal habitat	Plate	Plate
Crystal colour	Colourless	Colourless
Crystal size (mm)	0.25 x 0.05 x 0.04	0.12 x 0.09 x 0.05
Crystal system	Monoclinic	Monoclinic
Space group	*C* 2/c	*C* 2
a (Å)	14.7280 (7)	14.5372 (4)
b (Å)	33.0013 (16)	32.7538 (8)
c (Å)	11.4766 (6)	11.6363 (3)
α (°)	90	90
β (°)	101.949 (3)	100.4364 (14)
γ (°)	90	90
V ($Å^3$)	5457.3 (5)	5488.9 (3)
Density (Mg m^{-3})	1.0899	1.0928
Temperature (K)	100	100
μ (mm^{-1})	1.492	1.494
θ range (°)	6.7 to 118.06	5.4 to 101.06
Reflns. collected	17037	5692
Independent reflns. (R_{int})	3915 [R(int) = 0.0684]	2929 [R(int) = 0.0338]
Reflns. used in refinement, *n*	3915	2929
LS parameters, *p*	253	510
Restraints, *r*	0	0
$R1$ (F)[a] *I>2.0s(I)*	0.0853	0.0296
$wR2$ (F^2)[a], all data	0.2104	0.0764
$S(F^2)$[a], all data	1.031	1.089

[a] $R1(F) = \Sigma(|F_o| - |F_c|)/\Sigma|F_o|$; $wR2(F^2) = [\Sigma w(F_o^2 - F_c^2)^2/\Sigma wF_o^4]^{1/2}$; $S(F^2) = [\Sigma w(F_o^2 - F_c^2)^2/(n + r - p)]^{1/2}$

4.2.5 Powder X-ray diffraction

The crystalline products were all ground in a pestle and mortar and packed in to 0.7 mm capillaries before data collection (except as noted below). In all cases data were collected at ambient temperature. The location of data collection, wavelength and 2θ range over which data were collected are noted beneath each pattern subheading below.

X-ray diffraction data for the phase purity check on **4.1·xH$_2$O·yDMF**, and the desolvation and CO$_2$ uptake study on **4.1** were collected at station ID31 (now ID22) at the European Synchrotron Radiation Facility (ESRF) (λ = 0.35421 (1) Å).[40] The data were collected using a nine-channel multi-analyser crystal (MAC) detector. 8 scans (range specified for each scan below) were collected at a speed of 4° min^{-1}, and were assessed individually for beam damage before summing them together for analysis. The capillary was rotated about its axis to average beam exposure during collection.

X-ray diffraction data for the phase-purity check on **4.2·xH$_2$O·yDMF** were collected on a Stöe Stadi P diffractometer using Cu *Kα* radiation (λ = 1.5406 Å) in the Department of Materials Science and Engineering, University of Sheffield (with the sample packed in a 0.5 mm borosilicate capillary). Data were collected using a PSD detector with a single scan at a rate of 0.067° min^{-1}, using a rotating capillary.

X-ray diffraction data for the phase-purity checks on the chloroform-soaked **4.1·nCHCl$_3$** and **4.2·nCHCl$_3$** were collected on a Panalytical X'Pert powder diffractometer using Cu *Kα* radiation (λ = 1.5406 Å) in the Department of Chemistry, University of Manchester. Data were collected on a rotating flat-plate stage (sample loaded and packed evenly onto a 14 mm diameter silicon wafer plate) operating in reflection mode. Data were collected at a scan rate of 2.35° min^{-1}, and the stage was rotated at a rate of 60 rev min^{-1} to even sample exposure.

X-ray diffraction data for the *in situ* CO$_2$ uptake study on **4.2** were collected at beamline I11 at Diamond Light Source (λ = 0.826633 Å for CO$_2$ study),[41,42] equipped with a wide angle (90°) PSD detector comprising 18 Mythen-2 modules. A pair of scans was conducted, each related by a 0.25 ° detector offset to account for gaps between detector modules. Four such scan pairs were collected at five seconds exposure per scan, whilst the sample capillary was rotated about its axis over an 80°

range, to average beam exposure. The resulting patterns were summed to give the final pattern for structural analysis (total beam exposure time 40 seconds).

The data were compared (where relevant) to the calculated X-ray powder diffraction patterns from the single crystal structures they correspond to. The patterns were indexed using the TOPAS Academic programme.[43] TOPAS was also used for the Pawley and Rietveld fitting of data, as specified.[44,45]

4.2.5.1 Phase purity check, 4.1·xH$_2$O·yDMF

ID31, $\lambda = 0.35421\ (1)$ Å, ($0 \leq 2\theta \leq 20°$).

The dry, ground sample was packed in to a 0.7 mm borosilicate capillary and sealed at both ends with beeswax. The capillary was spun about its axis during collection to average beam exposure. The pattern was indexed using the TOPAS programme,[43] and a unit cell similar to that of **4.1·xH$_2$O·yDMF** from single crystal X-ray diffraction was found. This cell was used as a starting point for a Pawley refinement,[44] employing 1191 parameters (13 background, 1 zero error, 5 profile, 4 cell, 1168 reflections), resulting in final indices of fit $R_{wp} = 9.237$, $R_{wp'} = 20.00$.

[**4.1·xH$_2$O·yDMF**: a = 14.3315 (2) Å, b = 32.2148 (3) Å, c = 11.27956 (9) Å, β = 101.500 (1)°, V = 5103.07 (8) Å^3].

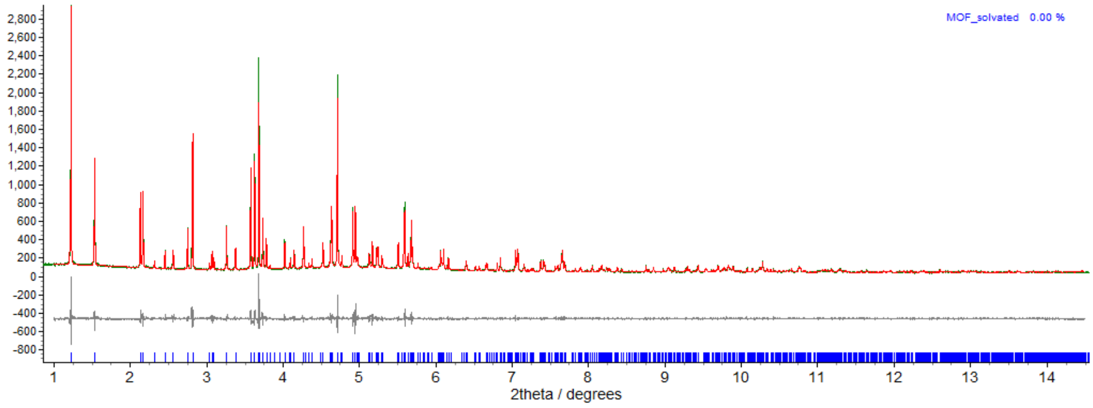

Figure 4.7. *Observed (green) and calculated (red) profiles and difference plot [I_{obs}-I_{calc}] (grey) of the Pawley refinement. (2θ range 1.00 – 14.5 °, d_{min} = 1.37 Å).*

The starting model used for an attempted structure solution of the solvated MOF, using the simulated annealing approach was also conducted using TOPAS, was the single-crystal structure of **4.1·xH$_2$O·yDMF** (framework only) collected at 100 K. Based on the estimation of solvent content by elemental analysis (see section 4.3.1), three solvent molecules were added to the model – one molecule of DMF as a rigid body (with occupancy 0.9) and two oxygen atoms (occupancy 0.9) representing water. The positions of the solvent molecules (and in the case of DMF, rotation of the molecule) were allowed to freely refine. This was followed by Rietveld refinement,[45] employing 24 parameters (13 background, 1 zero error, 5 profile, 4 cell, 1 scale). Rietveld refinement converged to R_{wp} = 20.26, $R_{wp'}$ = 42.48.

[**4.1·xH$_2$O·yDMF**: a = 14.3346 (4) Å, b = 32.2212 (7) Å, c = 11.2812 (3) Å, β = 101.498 (4)°, V = 5106.0 (3) Å^3].

Due to the high number of possible variables in accurately describing the solvent within the pores crystallographically (occupancy, number of disordered positions) and the poor resolution of the data, no further attempts were made to describe the pore contents by powder X-ray diffraction.

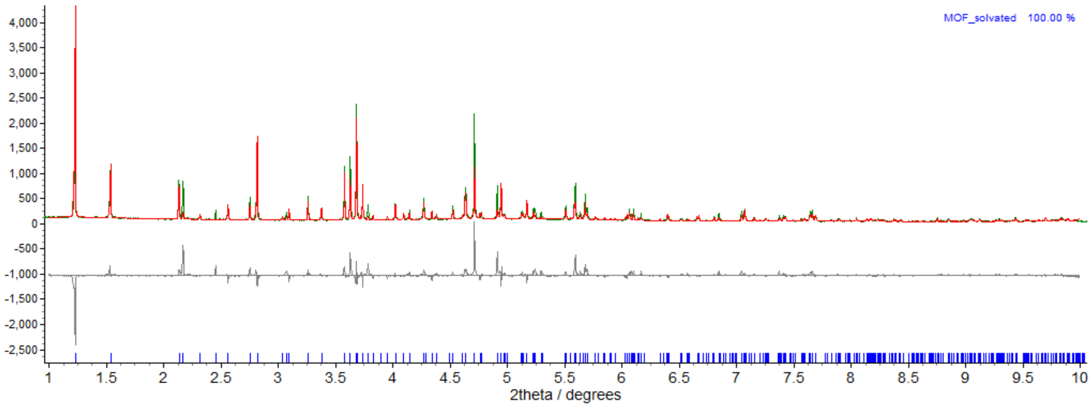

Figure 4.8. *Observed (green) and calculated (red) profiles and difference plot [I_{obs}-I_{calc}] (grey) of the Rietveld refinement. (2θ range 1.00 – 10.0 °, d_{min} = 1.98 Å).*

4.2.5.2 Phase purity check, 4.2·xH$_2$O·yDMF

University of Sheffield Stöe Stadi P (Cu-Kα source), λ = 1.5406 Å, (3 ≤ 2θ ≤ 50°).

The pattern was indexed using the TOPAS programme,[43] and a unit cell similar to that of **4.2·xH$_2$O·yDMF** from single crystal X-ray diffraction was found. This cell was used as a starting point for a Pawley refinement,[44] employing 528 parameters (10 background, 1 zero error, 5 profile, 4 cell, 508 reflections), resulting in final indices of fit R_{wp} = 5.522, $R_{wp'}$ = 26.39.

[**4.2·xH$_2$O·yDMF**: a = 14.585 (1) Å, b = 32.742 (2) Å, c = 11.5892 (9) Å, β = 101.613 (8)°, V = 5421 (1) Å^3].

The data quality was too low to facilitate structure fitting as indicated in section 4.2.3.1 above, considering the difficulties involved with solvent modelling described in that section.

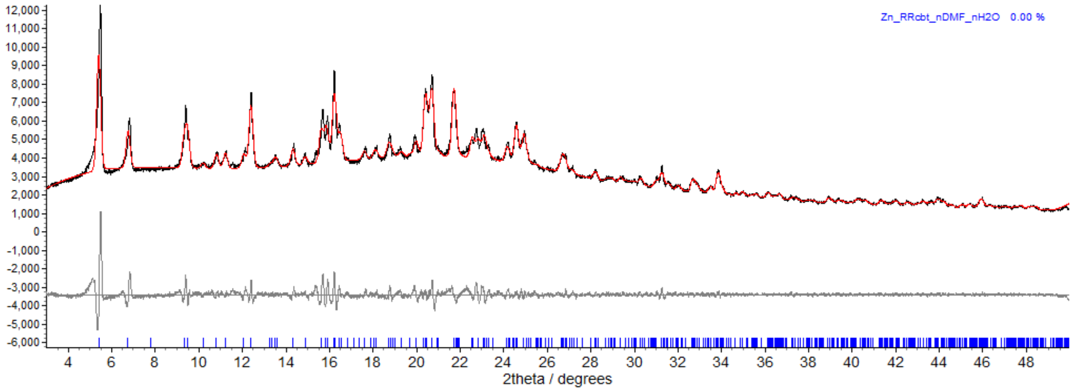

Figure 4.9. *Observed (black) and calculated (red) profiles and difference plot [I_{obs}-I_{calc}] (grey) of the Pawley refinement. (2θ range 3.0 – 50 °, d_{min} = 1.82 Å).*

4.2.5.3 Phase purity check, 4.1·nCHCl$_3$

University of Manchester Panalytical X'Pert (Cu-Kα source), λ = 1.5406 Å, (3 ≤ 2θ ≤ 50°).

The sample was ground gently (still a little moist with chloroform) and packed evenly onto a 14 mm diameter silicon wafer flat-plate stage. The stage was spun about its axis (perpendicular to the normal) at a speed of 60 rot min^{-1} to even sample exposure.

The pattern was indexed using the TOPAS programme,[43] and a unit cell similar to that of **4.1·xH$_2$O·yDMF** from single crystal X-ray diffraction was found. This cell was used as a starting point for a Pawley refinement,[44] employing 824 parameters (8 background, 1 zero error, 5 profile, 4 cell, 806 reflections), resulting in final indices of fit R_{wp} = 4.057, $R_{wp'}$ = 10.38.

[**4.1·nCHCl$_3$**: a = 14.7335 (4) Å, b = 33.1095 (8) Å, c = 11.5816 (5) Å, β = 101.710 (4)°, V = 5532.1 (3) Å^3].

The data quality was too low to facilitate structure fitting as indicated in section 4.2.3.1 above, considering the difficulties involved with solvent modelling described in that section. The intensity of the initial reflection may also be affected by the scan range limitations.

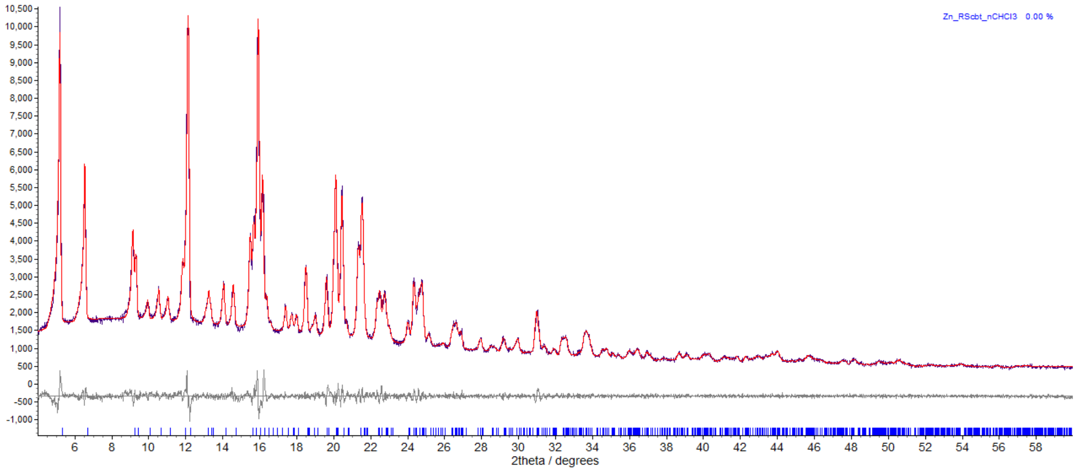

Figure 4.9. *Observed (purple) and calculated (red) profiles and difference plot [I_{obs}-I_{calc}] (grey) of the Pawley refinement. (2θ range 4.0 – 60 °, d_{min} = 1.54 Å).*

4.2.5.4 Phase purity check, 4.2·nCHCl$_3$

University of Manchester Panalytical X'Pert (Cu-Kα source), λ = 1.5406 Å, (3 ≤ 2θ ≤ 50°).

The sample was ground gently (still a little moist with chloroform) and packed evenly onto a 14 mm diameter silicon wafer flat-plate stage. The stage was spun about its axis (perpendicular to the normal) at a speed of 60 rot min^{-1} to even sample exposure. The pattern was indexed using the TOPAS programme,[43] and a unit cell similar to that of **4.2·xH$_2$O·yDMF** from single crystal X-ray diffraction was found. This cell was used as a starting point for a Pawley refinement,[44] employing 395 parameters (15 background, 1 zero error, 5 profile, 4 cell, 370 reflections), resulting in final indices of fit R_{wp} = 4.118, $R_{wp'}$ = 13.37.

[**4.2·nCHCl$_3$**: a = 14.812 (1) Å, b = 33.161 (2) Å, c = 11.651 (1) Å, β = 102.10 (1)°, V = 5595.8 (7) Å^3].

The data quality was too low to facilitate structure fitting as indicated in section 4.2.3.1 above, considering the difficulties involved with solvent modelling described in that section. The intensity of the initial reflection may also be affected by the scan range limitations.

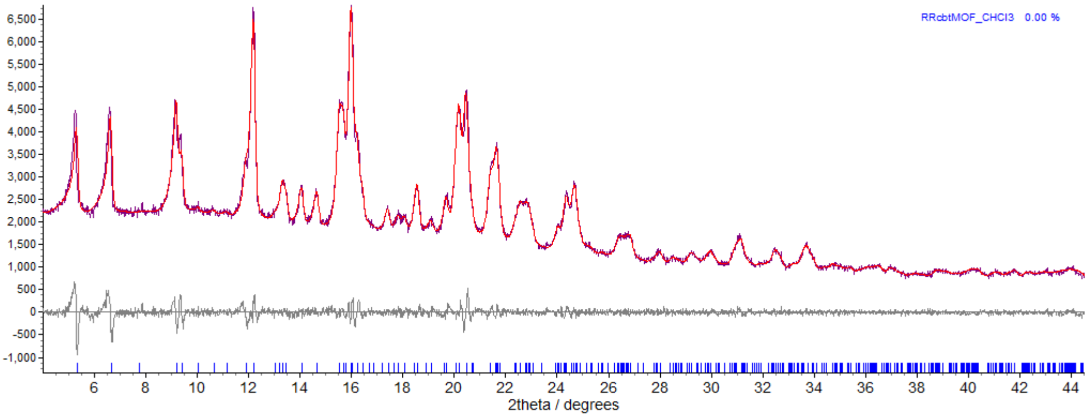

Figure 4.11. *Observed (purple) and calculated (red) profiles and difference plot [I_{obs}-I_{calc}] (grey) of the Pawley refinement. (2θ range 4.0 – 60 °, d_{min} = 1.54 Å).*

4.2.5.5 *In-situ* study, desolvation of 4.1·xH$_2$O·yDMF and CO$_2$ uptake

ID31, λ = 0.35421 (1) Å, (-2.0 ≤ 2θ ≤ 14°).

A dry, ground sample of the parent material **4.1·xH$_2$O·yDMF** was packed in to a 0.7 mm quartz capillary and placed in a gas cell mounted on a standard goniometer. The cell was sealed with Araldite two-part glue to prevent gas leaks. Several hours were allowed for the glue to dry before connecting the cell to the vacuum line and evacuating the cell with a pressure of around 10^{-5} mbar, and this pumping was continued for a period of 10 hours to attempt desolvation before analysis.

Sample at 10^{-5} mbar

Initial inspection of the pattern indicated that the pumping had caused a loss of crystallinity, and that the data now offered a resolution of no more than 2.5 Å. The pattern was indexed using the TOPAS programme,[43] and a unit cell similar to that of **4.1·xH$_2$O·yDMF** from single crystal X-ray diffraction was found. This cell was used as a starting point for a Pawley refinement,[44] employing 231 parameters (10 background, 1 zero error, 5 profile, 4 cell, 211 reflections), resulting in final indices of fit R_{wp} = 5.699, $R_{wp'}$ = 34.30.

[**4.1·xH$_2$O·yDMF**: a = 14.6562 (6) Å, b = 32.9219 (9) Å, c = 11.4997 (4) Å, β = 102.038 (5)°, V = 5426.7 (3) Å^3].

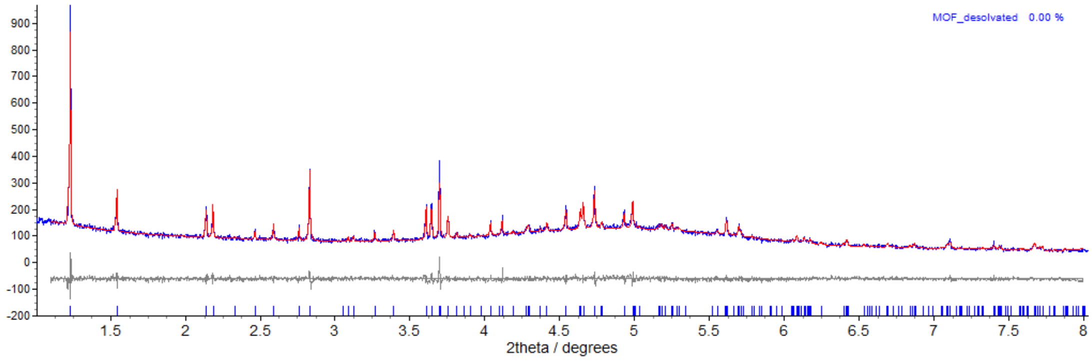

Figure 4.12. *Observed (blue) and calculated (red) profiles and difference plot [I_{obs}-I_{calc}] (grey) of the Pawley refinement. (2θ range 1.1 – 8.0 °, d_{min} = 2.50 Å).*

The starting model used for an attempted Rietveld refinement,[45] also conducted using TOPAS, was the single-crystal structure of **4.1·xH₂O·yDMF** (squeezed) collected at 100 K. Refinement employed 22 parameters (10 background, 1 zero error, 5 profile, 4 cell, 1 scale, 1 global thermal scale parameter). Rietveld refinement converged to R_{wp} = 11.73, $R_{wp'}$ = 70.57.

[**4.1·xH$_2$O·yDMF**: a = 14.657 (3) Å, b = 32.914 (3) Å, c = 11.500 (3) Å, β = 102.04 (2)°, V = 5426 (2) Å^3].

No solvent was modelled inside the pore, to assess whether or not solvent had been completely removed by the pumping. Despite refining the scale factor and a global thermal scaling parameter for the structure, the model for the empty framework alone was not sufficient to describe the observed pattern. As such, from this point onward only Pawley refinements were used to fit the data.

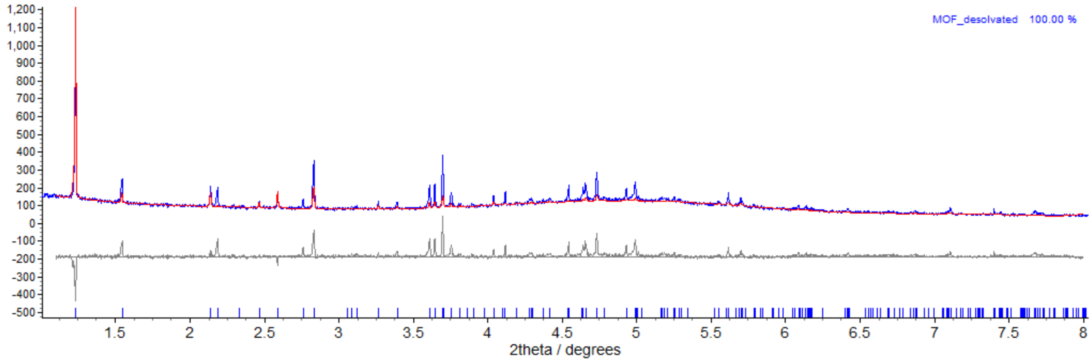

Figure 4.13. *Observed (blue) and calculated (red) profiles and difference plot [I_{obs}-I_{calc}] (grey) of the Rietveld refinement. (2θ range 1.1 – 8.0 °, d_{min} = 2.50 Å).*

Sample at 5 bar CO_2

The sample was dosed with 5 bar CO_2 and the pattern was recorded again after just three minutes, due to experimental time constraints. The sample was scanned in a different position along the capillary, and crystallinity appeared to be improved there. The pattern was indexed using the TOPAS programme,[43] and a unit cell similar to that of **4.1·xH$_2$O·yDMF** from single crystal X-ray diffraction was found. This cell was used as a starting point for a Pawley refinement,[44] employing 866 parameters (10 background, 1 zero error, 5 profile, 4 cell, 846 reflections), resulting in final indices of fit R_{wp} = 9.570, $R_{wp'}$ = 28.63.

[**4.1·xH$_2$O·yDMF·zCO$_2$**: a = 14.6980 (2) Å, b = 33.0346 (4) Å, c = 11.5562 (2) Å, β = 101.227 (2)°, V = 5503.7 (1) Å^3].

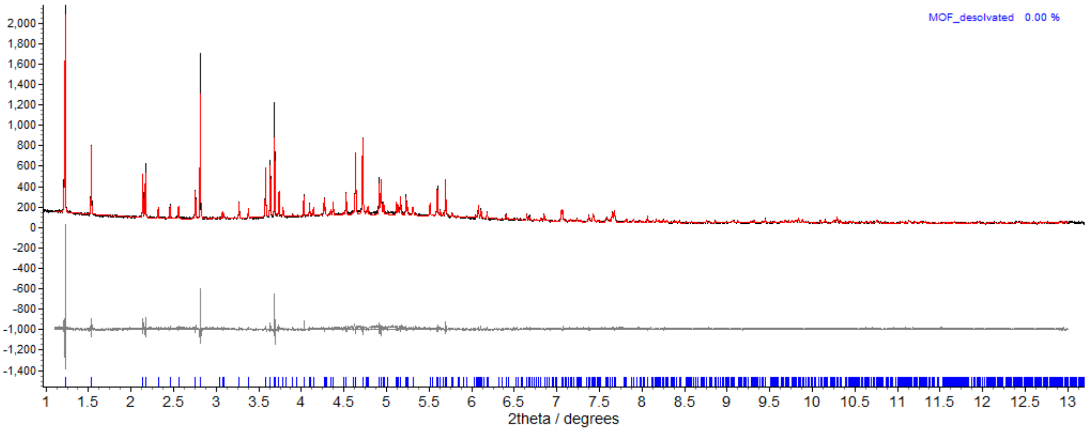

Figure 4.14. *Observed (black) and calculated (red) profiles and difference plot [I_{obs}-I_{calc}] (grey) of the Pawley refinement. (2θ range 1.10 – 13.0 °, d_{min} = 1.56 Å).*

Sample at 20 bar CO_2

The sample was dosed with 20 bar CO_2 and the pattern was recorded again after allowing the system to equilibrate for 45 minutes. The pattern was indexed using the TOPAS programme,[43] and a unit cell similar to that of **4.1·xH$_2$O·yDMF** from single crystal X-ray diffraction was found. This cell was used as a starting point for a Pawley refinement,[44] employing 872 parameters (10 background, 1 zero error, 5 profile, 4 cell, 852 reflections), resulting in final indices of fit R_{wp} = 9.238, $R_{wp'}$ = 28.01.

[**4.1·xH$_2$O·yDMF·zCO$_2$**: a = 14.7214 (2) Å, b = 33.0878 (4) Å, c = 11.5932 (2) Å, β = 100.849 (2)°, V = 5546.1 (1) Å^3].

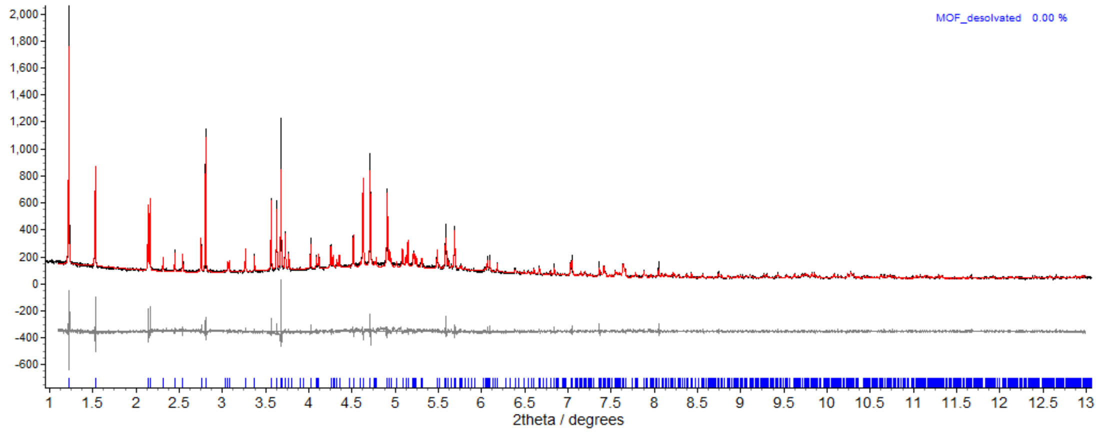

Figure 4.15. *Observed (black) and calculated (red) profiles and difference plot [I_{obs}-I_{calc}] (grey) of the Pawley refinement. (2θ range 1.10 – 13.0 °, d_{min} = 1.56 Å).*

Sample at 50 bar CO_2

The sample was dosed with 50 bar CO_2 and the pattern was recorded again after allowing the system to equilibrate for 30 minutes. The pattern was indexed using the TOPAS programme,[43] and a unit cell similar to that of **4.1·xH_2O·yDMF** from single crystal X-ray diffraction was found. This cell was used as a starting point for a Pawley refinement,[44] employing 876 parameters (10 background, 1 zero error, 5 profile, 4 cell, 856 reflections), resulting in final indices of fit R_{wp} = 8.996, $R_{wp'}$ = 28.83.
[**4.1·xH_2O·yDMF·zCO_2**: a = 14.7328 (2) Å, b = 33.1149 (4) Å, c = 11.6163 (2) Å, β = 100.705 (2)°, V = 5568.7 (1) Å^3].

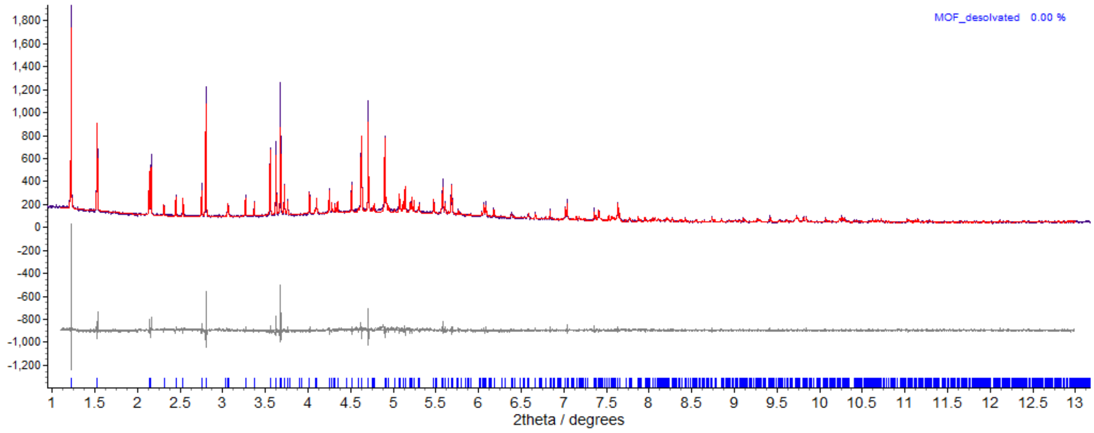

Figure 4.16. *Observed (purple) and calculated (red) profiles and difference plot [I_{obs}-I_{calc}] (grey) of the Pawley refinement. (2θ range 1.10 – 13.0 °, d_{min} = 1.56 Å).*

Sample returned to 10^{-5} mbar

The sample was evacuated with the vacuum pump and the pressure reduced to around 10^{-5} mbar. The pattern was recorded again after allowing the system to equilibrate for 15 minutes. The crystallinity of the sample was notably decreased upon removal of the CO_2, giving a minimum resolution of no more than 2.26 Å. The pattern was indexed using the TOPAS programme,[43] and a unit cell similar to that of **4.1·xH$_2$O·yDMF** from single crystal X-ray diffraction was found. This cell was used as a starting point for a Pawley refinement,[44] employing 315 parameters (10 background, 1 zero error, 5 profile, 4 cell, 295 reflections), resulting in final indices of fit R_{wp} = 8.312, $R_{wp'}$ = 33.24.

[**4.1·xH$_2$O·yDMF**: a = 14.6372 (4) Å, b = 32.9094 (6) Å, c = 11.4974 (3) Å, β = 102.045 (3)°, V = 5416.4 (2) Å^3].

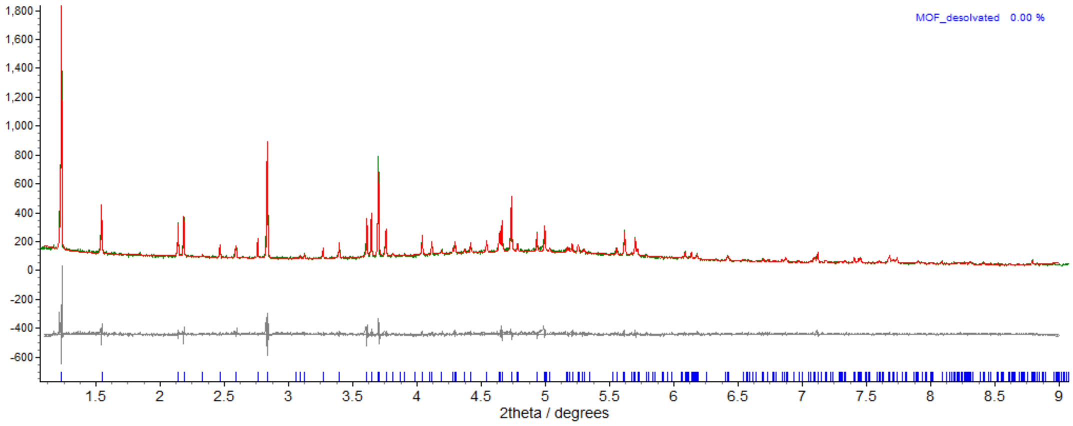

Figure 4.17. *Observed (green) and calculated (red) profiles and difference plot [I_{obs}-I_{calc}] (grey) of the Pawley refinement. (2θ range 1.1 – 9.0 °, d_{min} = 2.26 Å).*

4.2.5.6 *In-situ* study, desolvation of 4.2·nCHCl$_3$ and CO$_2$ uptake

Diamond I11, λ = 0.826633 Å, (2.0 ≤ 2θ ≤ 92°).

A dry, ground sample of the chloroform-soaked material **4.2·nCHCl$_3$** was packed in to a 0.7 mm quartz capillary and placed in a gas cell mounted on a standard goniometer. The cell was sealed with Araldite two-part glue to prevent gas leaks. Several hours were allowed for the glue to dry before connecting the cell to the vacuum line and evacuating the cell with a pressure of around 10^{-5} mbar, and this pumping was continued for a period of 19 hours to attempt desolvation before analysis.

Sample at 10^{-5} mbar

Initial inspection of the pattern indicated that the pumping had caused a loss of some crystallinity, and that the pattern appeared to have an abnormally high background.

This affected the shape and intensity of the strongest (020) reflection. As such, no Rietveld fitting was attempted.

The pattern was indexed using the TOPAS programme,[43] and a unit cell similar to that of **4.2·xH$_2$O·yDMF** from single crystal X-ray diffraction was found. This cell was used as a starting point for a Pawley refinement,[44] employing 831 parameters (12 background, 1 zero error, 5 profile, 4 cell, 809 reflections), resulting in final indices of fit R_{wp} = 1.656, $R_{wp'}$ = 16.57.

[**4.2·nCHCl$_3$**: a = 14.4711 (7) Å, b = 32.968 (1) Å, c = 11.6494 (5) Å, β = 100.632 (6)°, V = 5462.3 (4) Å^3].

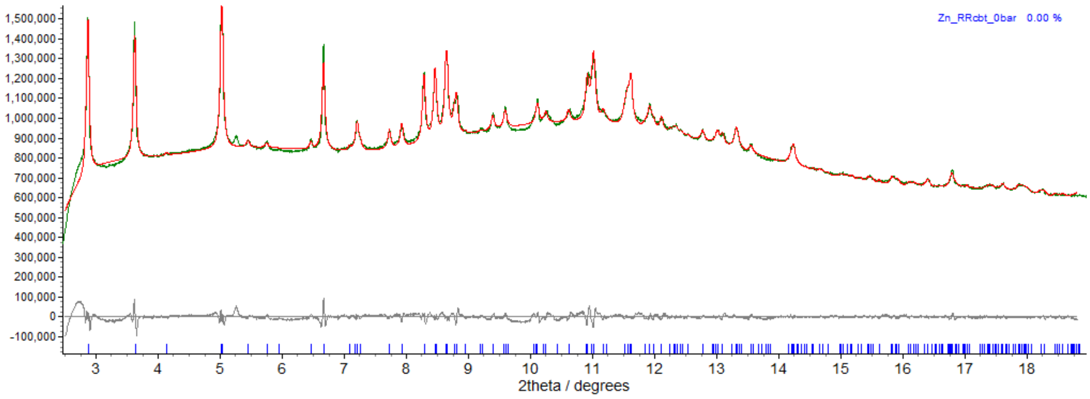

Figure 4.18. *Observed (green) and calculated (red) profiles and difference plot [I_{obs}-I_{calc}] (grey) of the Pawley refinement. (2θ range 2.5 – 18.8 °, d_{min} = 2.53 Å).*

A small reflection at 2θ = 5.25° (d = 9.0 Å) did not match any expected reflections for this cell setting, and could not be fitted (see Figure 4.19).

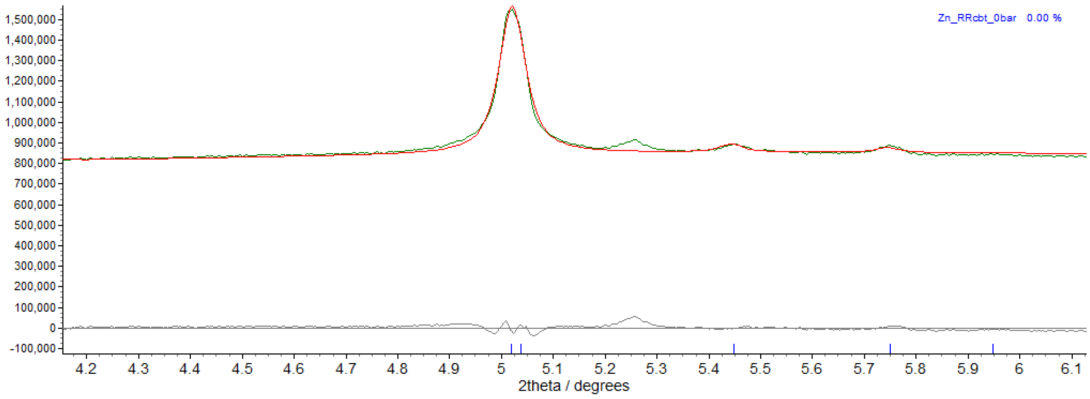

Figure 4.19. *Observed (green) and calculated (red) profiles and difference plot [I_{obs}-I_{calc}] (grey) of the Pawley refinement shown in Figure 4.17, showing the reflection which could not be fit.*

Sample at 5 bar CO$_2$

The sample was dosed with 4.93 bar CO$_2$ and the pattern was recorded again after thirty minutes, to allow for equilibration. The unit cell from the previous refinement on the material at vacuum was used as a starting point for a Pawley refinement,[44] employing 225 parameters (12 background, 1 zero error, 5 profile, 4 cell, 203 reflections), resulting in final indices of fit R_{wp} = 1.258, $R_{wp'}$ = 15.83. The small reflection at d = 9.0 Å again could not be fitted (as shown for the sample under vacuum in Figure 4.19).

[**4.2·nCHCl$_3$·zCO$_2$**: a = 14.5041 (5) Å, b = 32.962 (1) Å, c = 11.6982 (4) Å, β = 100.727 (5)°, V = 5495.0 (3) Å^3].

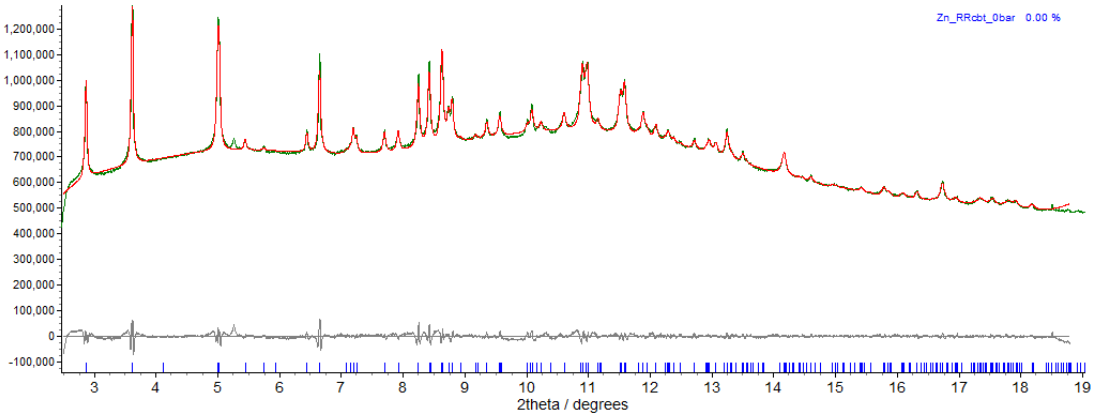

Figure 4.20. *Observed (green) and calculated (red) profiles and difference plot [I_{obs}-I_{calc}] (grey) of the Pawley refinement. (2θ range 1.10 – 13.0 °, d_{min} = 1.56 Å).*

Sample at 10 bar CO$_2$

The sample was dosed with 9.46 bar CO$_2$ and the pattern was recorded again after thirty minutes, to allow for equilibration. The unit cell from the previous refinement on the material at 5 bar CO$_2$ was used as a starting point for a Pawley refinement,[44] employing 225 parameters (11 background, 1 zero error, 5 profile, 4 cell, 204 reflections), resulting in final indices of fit R_{wp} = 1.210, $R_{wp'}$ = 15.25. The small reflection at d = 9.0 Å again could not be fitted (as shown for the sample under vacuum in Figure 4.19).).

[**4.2·nCHCl$_3$·zCO$_2$**: a = 14.5252 (5) Å, b = 32.9940 (9) Å, c = 11.7175 (3) Å, β = 100.698 (4)°, V = 5518.0 (3) Å^3].

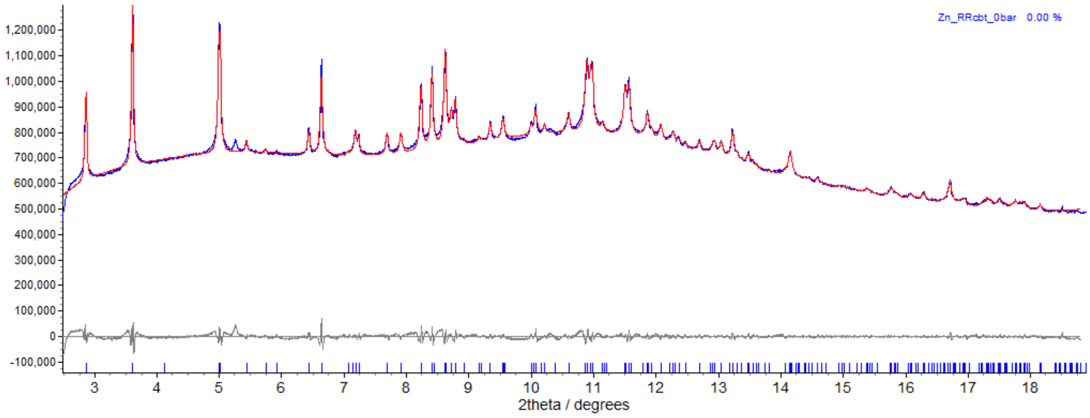

Figure 4.21. *Observed (blue) and calculated (red) profiles and difference plot [I_{obs}-I_{calc}] (grey) of the Pawley refinement. (2θ range 1.10 – 13.0 °, d_{min} = 1.56 Å).*

Sample at 20 bar CO_2

The sample was dosed with 20.00 bar CO_2 and the pattern was recorded again after thirty minutes, to allow for equilibration. The unit cell from the previous refinement on the material at 10 bar CO_2 was used as a starting point for a Pawley refinement,[44] employing 224 parameters (9 background, 1 zero error, 5 profile, 4 cell, 205 reflections), resulting in final indices of fit R_{wp} = 0.928, $R_{wp'}$ = 12.14. The small reflection at d = 9.0 Å again could not be fitted (as shown for the sample under vacuum in Figure 4.19).).

[**$4.2 \cdot nCHCl_3 \cdot zCO_2$**: a = 14.5485 (4) Å, b = 33.0378 (8) Å, c = 11.7400 (3) Å, β = 100.596 (3)°, V = 5546.6 (2) Å^3].

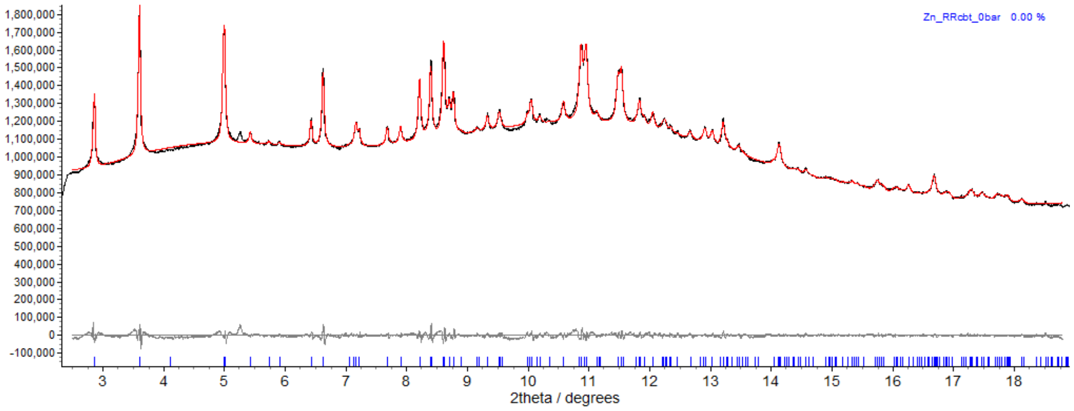

Figure 4.22. *Observed (black) and calculated (red) profiles and difference plot [I_{obs}-I_{calc}] (grey) of the Rietveld refinement. (2θ range 1.10 – 13.0 °, d_{min} = 1.56 Å).*

4.2.6 Thermogravimetric analysis

The crystalline solids filtered from the mother liquor at the pump, and allowed to dry in air for exactly ten minutes to remove surface solvent on the crystals. Thermogravimetric analyses were then conducted using a Perkin–Elmer Pyris1 TGA model thermogravimetric analyser. Samples were heated over the ranges specified in each case below, ramping at a rate of 5°C min^{-1}, under a flow of dry N_2 gas. Attempts to characterise chloroform-containing MOF materials gave inconsistent data due to the volatility of the guest.

4.2.6.1 As-synthesised 4.1·xH_2O·yDMF

The sample was heated from 25°C to 800°C, holding for 1 min at the start and end of the experiment. The initial mass loss of 17.1% corresponds to solvent loss. The rapid decrease in mass at 25 °C corresponds to loss of surface solvent on the crystals.

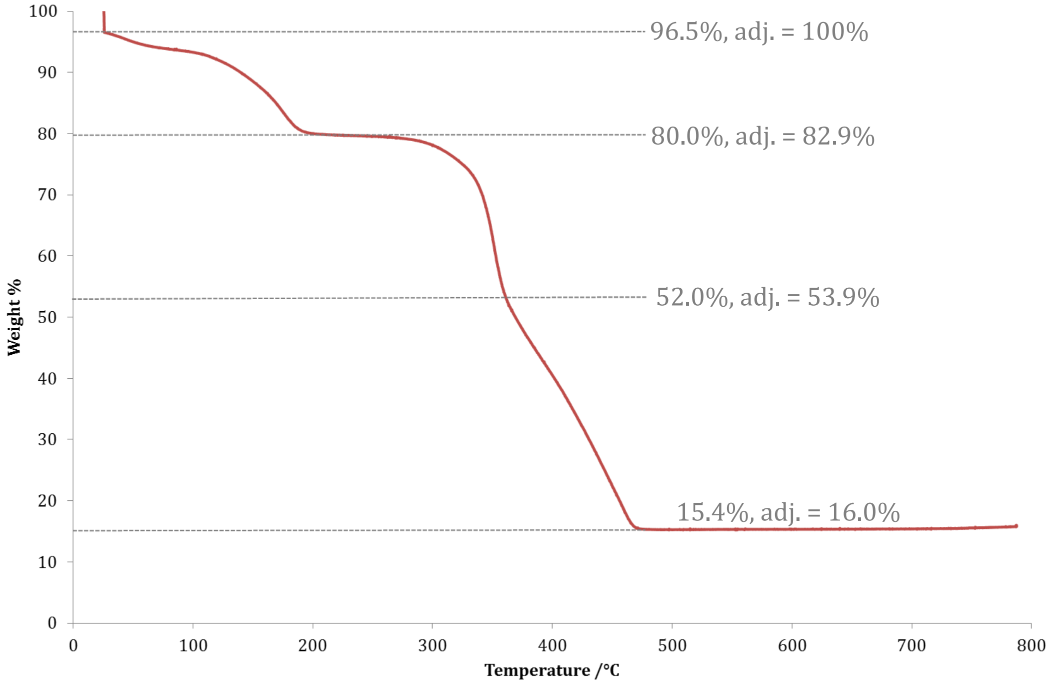

Figure 4.23. *Annotated thermogravimetric trace, for heating of the as-synthesised **4.1·xH_2O·yDMF**. "Adj." denotes mass % values adjusted for the initial loss of surface solvent on the crystals.*

4.2.6.2 As-synthesised **4.2·xH$_2$O·yDMF**

Sample was heated from 25°C to 800°C, holding for 1 min at the start and end of the experiment. The initial mass loss of 21.5% corresponds to solvent loss.

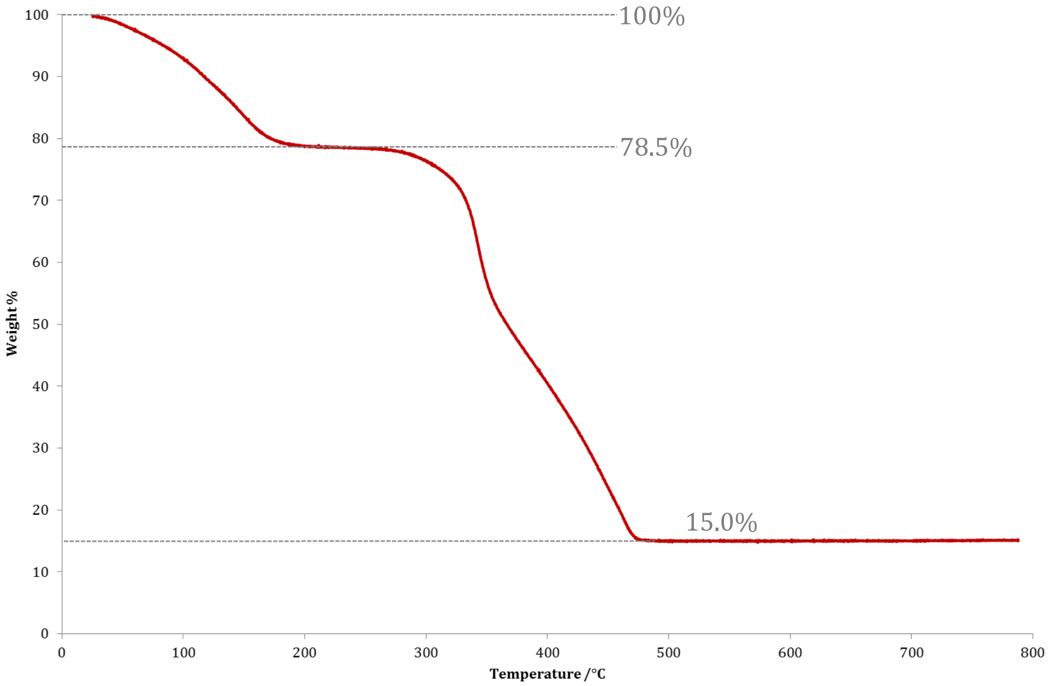

Figure 4.24. *Thermogravimetric trace, for heating of the as-synthesised* ***4.2·xH$_2$O·yDMF****.*

4.2.7 Chiral gas chromatography

Samples of **4.1·aPhCH$_2$(OH)Me** or **4.2·aPhCH$_2$(OH)Me** were analysed using a Perkin-Elmer Autosystem Chiral GC with a Supelco β-Dex 120 capillary column (L x I.D. 30 m x 0.25 mm x df 0.25 μm), heating from 60 to 160 °C at 2 °C min^{-1}. Expected retention times for 1-phenylethan-1-ol were around 31 minutes based on testing with samples of purely 1-phenylethan-1-ol (diluted with methanol). Relative content of guests was determined by direct comparison of chromatograph peak areas. The annotated chromatograms are provided in appendix A.

4.3 Results & discussion

4.3.1 Rational design of a chiral/racemic pair of MOFs

The reaction of (±)cyclohexane-1,2-diamine with the azine-forming reagents successfully yielded the ligand ***RR,SS*cbt**, which exists as a racemic mixture of *R,R*-cyclohexanebis-1,2-(1’,2’,4’-triazole) and *S,S*-cyclohexanebis-1,2-(1’,2’,4’-triazole). The reaction of the chiral counterpart (-,-)cyclohexane-1,2-diamine also successfully gave the target ligand, ***RR*cbt** (*R,R*-cyclohexanebis-1,2-(1’,2’,4’-triazole)). This was followed by their incorporation into MOFs as co-ligands to terephthalate. This enabled the synthesis of a pair of neutral zinc-based MOFs with comparable structures, **4.1·xH_2O·yDMF** (from ***RR,SS*cbt**) and **4.2·xH_2O·yDMF** (from ***RR*cbt**).

In each of the structures, Zn(II) ions are bound to two terephthalate ligands, and two of the **cbt** ligands, in a tetrahedral geometry. All ligands act as bridging ligands. The **cbt** ligands, due to the proximity of the triazole groups to each other within the molecule, create a loop-like dimer of zinc ions, shown in the centre of Figure 4.25. This dimer is further stabilised by the formation of hydrogen bonds within the framework, from the carbonyl oxygen atoms of neighbouring terephthalate ligands (see Figure 4.25).

These dimers are constructed from two **cbt** ligands of the same chirality (either both the *R,R*- form or the *S,S*- form). Therefore in the framework **4.1** (from ***RR,SS*cbt**), there are dimers of the *R,R*- ligands and of the *S,S*- ligands, whereas in framework **4.2** there are only dimers of the *R,R*- ligands. A representative section of the framework **4.1** (showing the *R,R*- dimer) is shown in Figure 4.25.

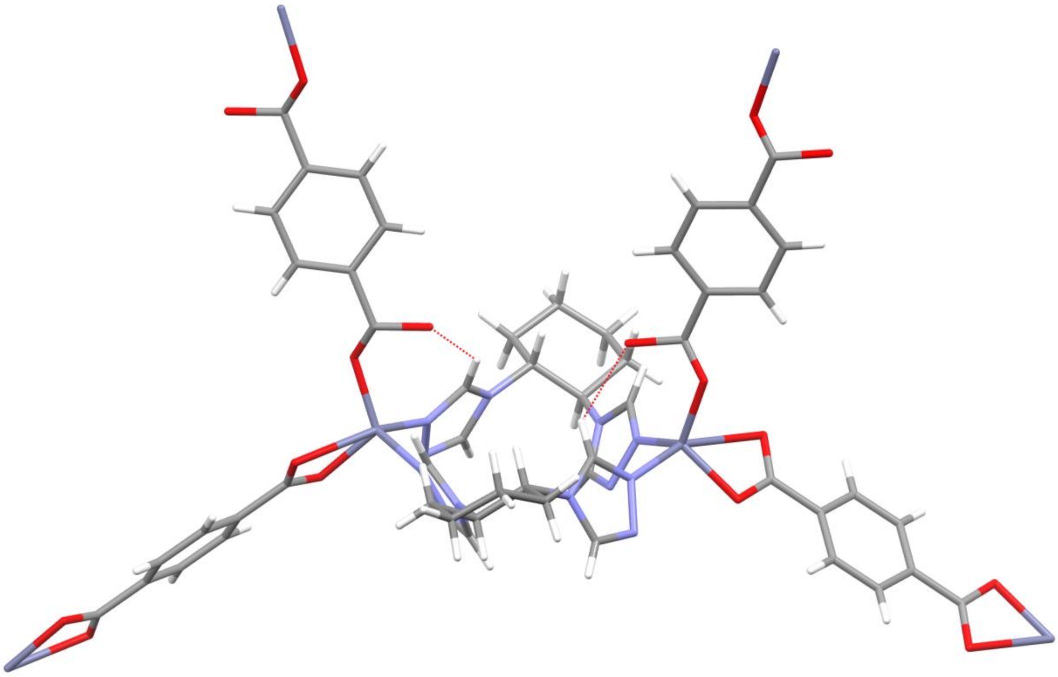

Figure 4.25. *The SBU (secondary building unit) of the framework in* ***4.1·xH₂O·yDMF****. In this picture, a pair of the R,R-* ***cbt*** *ligands is shown. Dashed red lines represent C–H···O hydrogen bonds.*

The MOF materials crystallise with very similar monoclinic unit cells (**4.1·xH_2O·yDMF** in space group *C*2/*c*, **4.2·xH_2O·yDMF** in *C*2), and are porous structures, with channels running along two dimensions. Smaller channels run parallel to the *c*-axis, and the main, larger channel is parallel with the (101) plane (perpendicular to the *b*-axis). In both cases, the walls of these channels are lined with the terephthalate ligands, as shown in figures 4.26 and 4.27.

The terephthalate ligands lining the walls of these channels are rotationally disordered over two positions in both **4.1** and **4.2**, and were successfully modelled in the crystal structure as 50% occupied in both orientations. For the sake of clarity, only one such orientation is shown in figures 4.26 and 4.27.

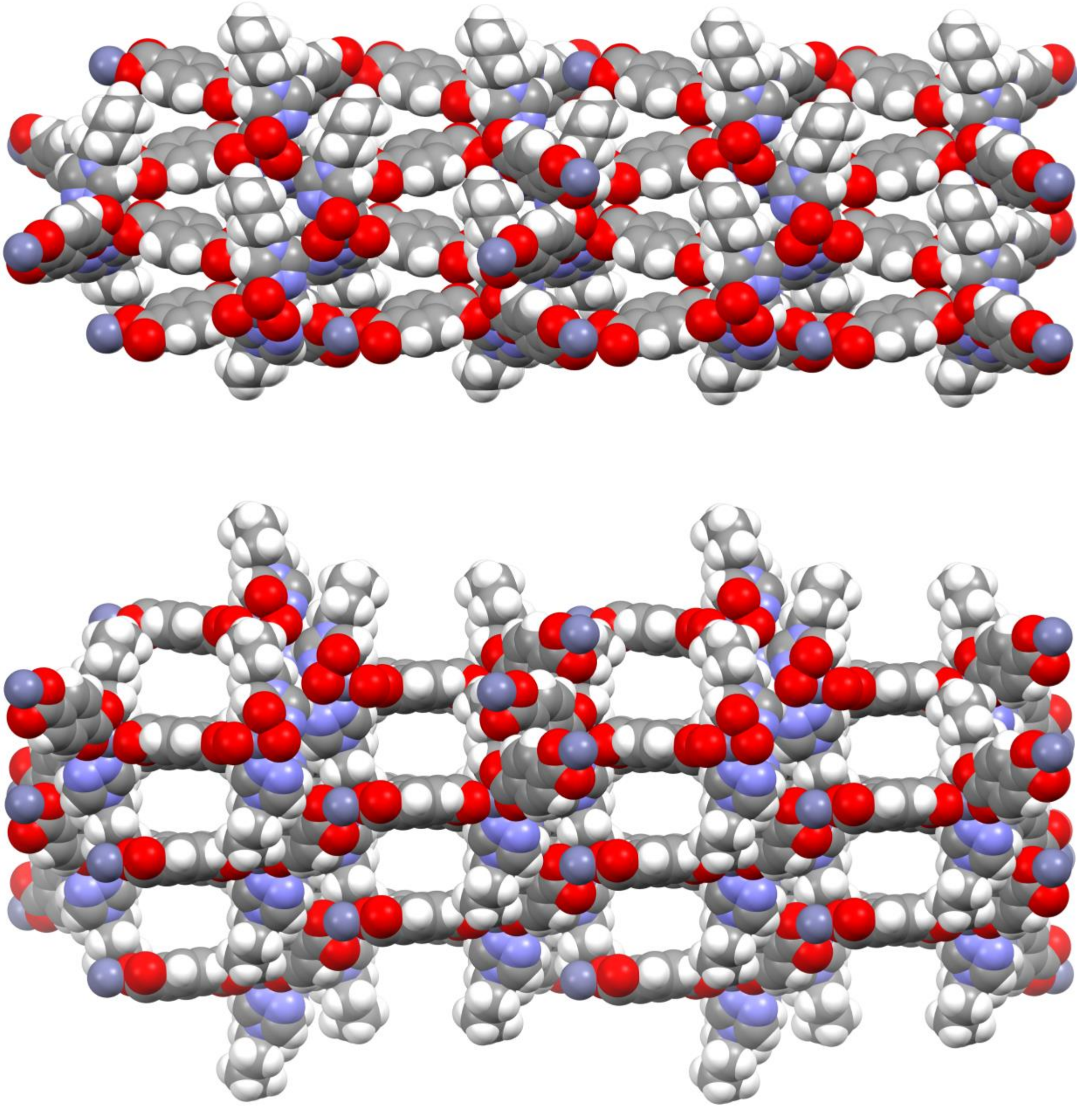

Figure 4.26. *Channels running along the crystallographic* c*-axis (top) and running parallel to the (101) plane and perpendicular to the b-axis (bottom) in* ***4.1·xH$_2$O·yDMF****.*

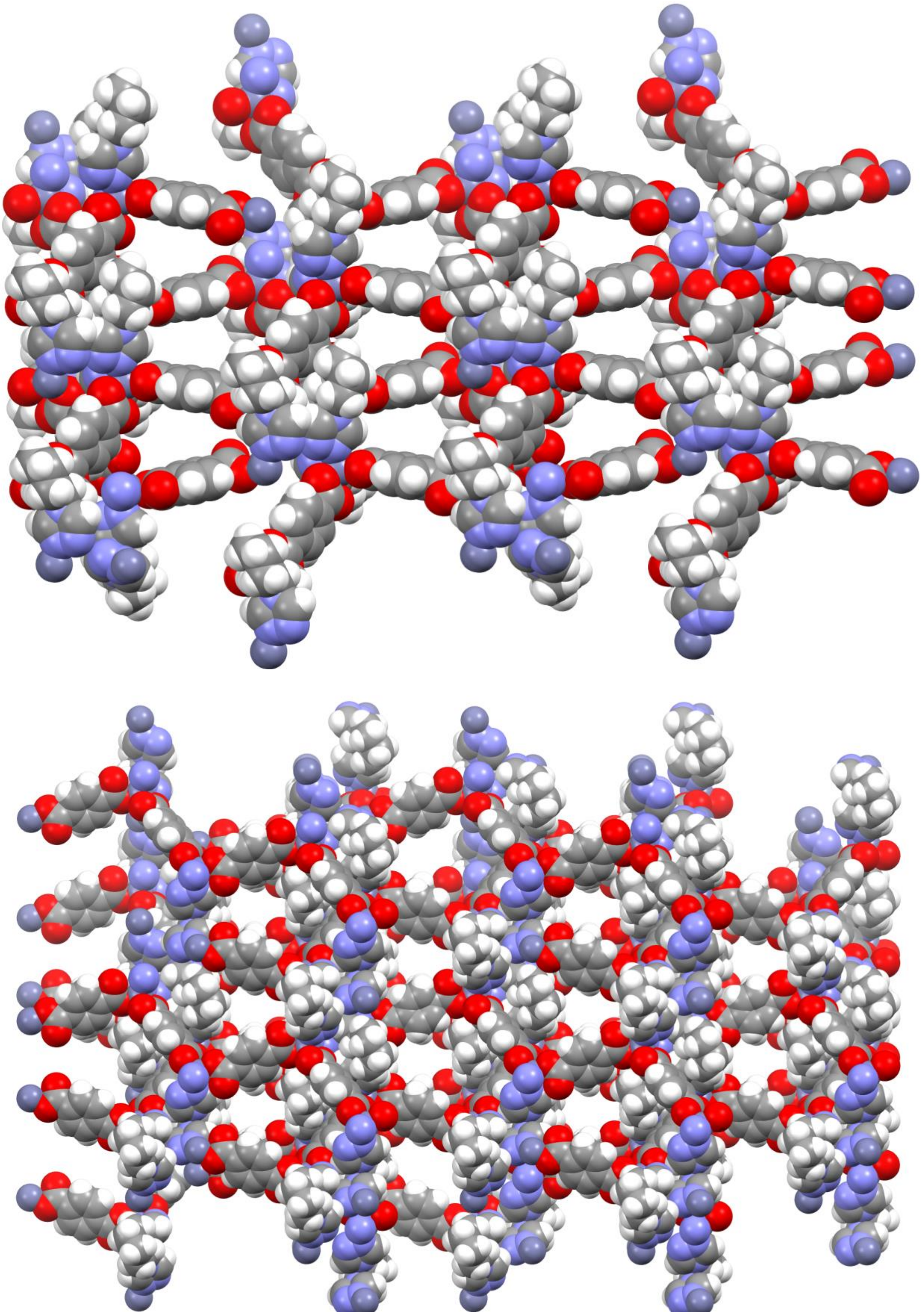

Figure 4.27. *Channels running along the crystallographic* c*-axis (top) and running parallel to the (101) plane and perpendicular to the b-axis (bottom) in* ***4.2·xH_2O·yDMF****.*

The pore shapes are visibly very different between **4.1** and **4.2**, due to the different orientation of the terephthalate ligands, brought about by the presence of either one or both enantiomers of the **cbt** ligand. In the framework **4.1**, the channels running parallel to the *c*-axis are quite small and difficult to visualise, even when not considering the disorder of the terephthalate ligands. However those parallel to the (101) plane (and perpendicular to the *b*-axis) are much larger and rectangular in shape. In the case of **4.2**, the channels are more similar to each other in size, and are not rectangular in shape.

However, PLATON SQUEEZE analysis on both frameworks indicated that the overall porosity of both materials is similar. The analysis indicated that framework **4.1** possessed a total void space of 33.8% (1816.7 Å^3 in a unit cell of 5377.04 Å^3), whereas framework **4.2** possessed a total void space of 34.5% (1899.3 Å^3 in a unit cell of 5501.77 Å^3). In the as-synthesised materials, these voids are filled with a mixture of water and DMF.

The solvent molecules occupying the pores of the as-synthesised **4.1·xH$_2$O·yDMF** and **4.2·xH$_2$O·yDMF** could not be located crystallographically, and as such were inferred from elemental analysis and thermogravimetric analysis (TGA). Elemental analysis suggests that the formulae of the materials submitted for analysis were **4.1·1.8H$_2$O·0.9DMF** and **4.2·1.7H$_2$O·1.0DMF**. A comparison of elemental analysis, TGA data and PLATON SQUEEZE calculation for the compounds can be found in Table 4.28.

Table 4.28. *Comparison of elemental analysis and thermogravimetric analysis data, suggesting the solvent content of the as-synthesised MOF materials **4.1·xH$_2$O·yDMF** and **4.2·xH$_2$O·yDMF**.*

	4.1·xH$_2$O·yDMF	4.2·xH$_2$O·yDMF
Least-squares formula fit, **elemental analysis**	1.8H$_2$O, 0.9DMF	1.7H$_2$O, 1.0DMF
% solvent mass content, **elemental analysis**	18.04%	18.86%
% solvent mass content, **TGA**	17.90%	21.50%
Solvent electrons per formula unit, **PLATON SQUEEZE**	24.25	32.50

The elemental analysis and TGA data are in a reasonable agreement, considering that samples for elemental analysis must sit dry for an unknown period before analysis, facilitating the evaporation of some pore solvent. However, the results of PLATON SQUEEZE do not agree, as DMF contains 44 electrons and water ten electrons. It may be that the void space and electrons existing close to the framework itself could not be accurately modelled due to disorder of the ligand, and so as such these results should be treated with caution.

Attempts to locate the solvent within the pores of **4.1** crystallographically were also made using synchrotron X-ray powder diffraction data (see section 4.2.3.1), by the simulated annealing approach with Rietveld refinement. However, this was not possible due to a great number of unknown variables (number of crystallographically unique solvent molecules and their occupancies) being present despite having the information in Table 4.28.

4.3.2 Desolvation and CO_2 uptake in racemic framework 4.1

To activate the material (i.e. empty its pores ready to receive new guests), the solvent needed to be removed. This could be achieved thermally, as is indicated by the thermogravimetric analyses shown in section 4.2.6. However, previous experience indicates that this can lead to a loss of crystallinity, hindering crystallographic study of gas uptake in the materials. As such, the MOF was activated for crystallographic study at the synchrotron by subjecting a sample of **4.1·x**$\mathbf{H_2O}$**·yDMF** to high vacuum (10^{-5} mbar) for a period of ten hours at ambient temperature. The resultant powder X-ray diffraction pattern was compared with those for the as-synthesised material and the calculated pattern for the MOF crystal structure with solvent not modelled, from single-crystal X-ray diffraction.

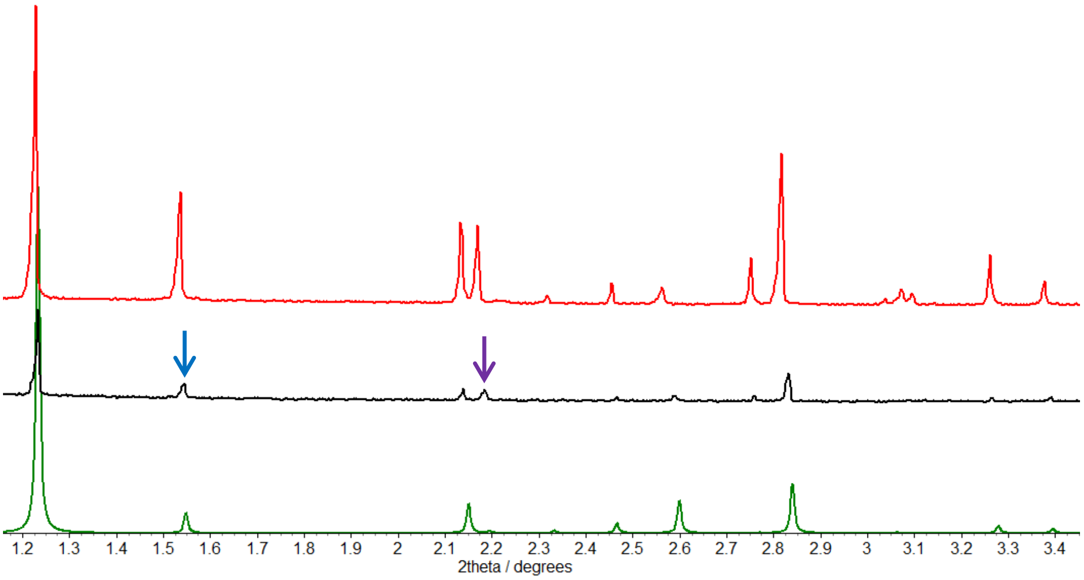

Figure 4.29. *Comparison of low-angle powder X-ray diffraction patterns of (top, red) the as-synthesised* ***4.1·xH₂O·yDMF****; (middle, black) the same material after desolvation for 10 hours at* 10^{-5} *mbar and (bottom, green) the calculated pattern for the framework only (not solvent) model of* ***4.1*** *from single-crystal X-ray diffraction at 100 K. Key reflections are highlighted with arrows for further discussion.*

Initial comparison of the pattern after desolvation with the pattern before desolvation shows that the relative intensity of some peaks (the 110 reflection is highlighted in blue at 2θ 1.55°, the 021 is highlighted in purple at 2θ 2.18°) have changed. The reduced intensity of the 110 reflection, relative to the most intense reflection (020, at 2θ 1.23°)is consistent with what is seen in the calculated pattern for the framework without solvent. However, considering other reflections (particularly the 021 reflection, highlighted in purple) are not reduced in intensity compared to that calculated for the solvent-free framework, suggests that complete transformation to the desolvated phase has not taken place.

The empty framework structure of **4.1·xH₂O·yDMF**, obtained from single-crystal X-ray diffraction was used as a starting point for Rietveld (structural) refinement against the observed data for the material after desolvation (pattern in black in figures 4.29 and overleaf in figure 4.30). Even when allowing the scale parameter and the thermal parameters of the empty framework to refine, it was clear that the model of the framework alone was insufficient to describe the electron density observed (see Figure 4.30). As expected, this fit resulted in under-description of the 110 and 021 reflections (among others), and suggests that solvent remains in the pores.

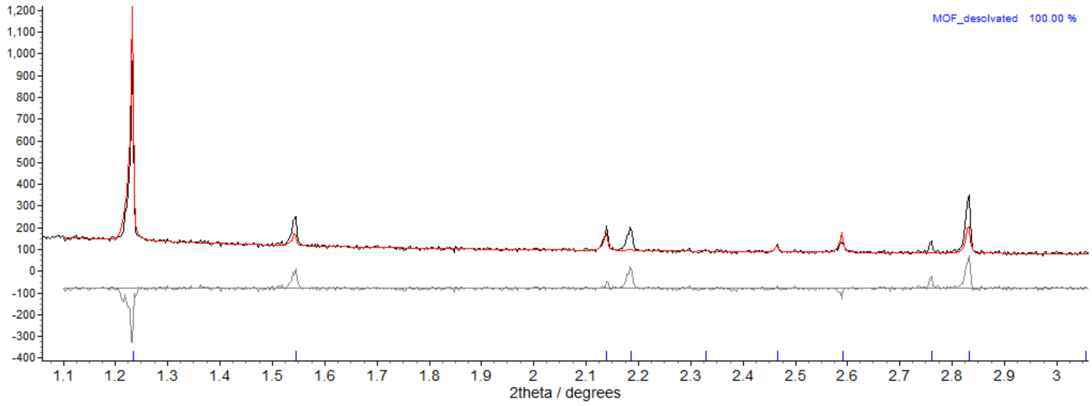

Figure 4.30. *The result of the Rietveld fit (red) of just the empty framework structure to the observed pattern (black) for* ***4.1·xH_2O·yDMF*** *after desolvation for 10 hours at 10^{-5} mbar. Difference path shown in grey.*

As the crystallographic location of solvent molecules within the pores of the as-synthesised **4.1·xH_2O·yDMF** was not possible, it was also not possible for the partially desolvated material. The resolution of the data had also been reduced by the desolvation process.

Nevertheless, as a partial desolvation was evident, the *in-situ* study was continued and CO_2 was added to the partially desolvated framework. Successive additions of 5, 20 and 50 bar CO_2 were made, and the resultant powder X-ray diffraction patterns are shown in Figure 4.31.

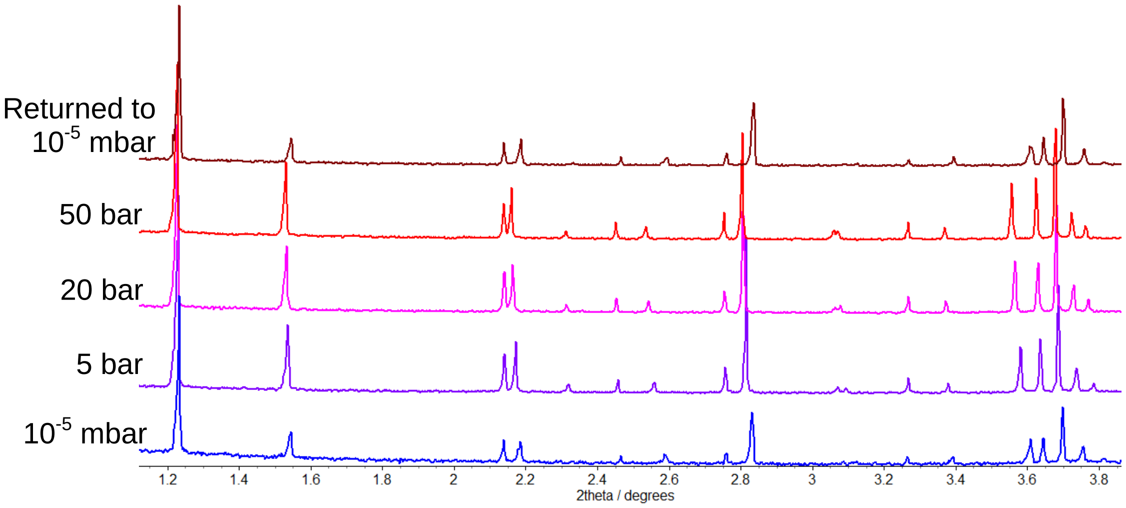

Figure 4.31. *X-ray powder diffraction pattern progression for successive dosing of the partially desolvated MOF* ***4.1·xH₂O·yDMF*** *with CO_2. Pawley fit information is presented in experimental section 4.2.3.3.*

Careful visual inspection of the patterns shows a shift of the diffraction pattern to lower diffraction angle. This indicates, according to Bragg's law (see equation 4.32) an increase in unit cell volume. This shift in the pattern was quantified by Pawley fitting (see experimental section 4.2.3.3), and the resulting unit cells of the phases represented in Figure 4.31, above are tabulated in Table 4.33, below.

$$\frac{\lambda}{\boldsymbol{d}} = 2\sin\boldsymbol{\theta}$$

Equation 4.32. *Bragg's law, rearranged to demonstrate that the diffraction angle (2θ) of any given reflection is inversely related to the d-spacing between the lattice planes represented by that reflection.*

Table 4.33. *Unit cell parameters for* ***4.1·xH_2O·yDMF*** *or* ***4.1·xH_2O·yDMF·zCO_2*** *derived from Pawley fitting of the data obtained at vacuum and under successive pressures of CO_2.*

	a /Å	*b* /Å	*c* /Å	*β* /°	V /Å^3	Net volume change
10^{-5} mbar	14.6562 (6)	32.9219 (9)	11.4997 (4)	102.038 (5)	5426.7 (3)	
5 bar CO_2	14.6980 (2)	33.0346 (4)	11.5562 (2)	101.227 (2)	5503.7 (1)	+ 1.42%
20 bar CO_2	14.7214 (2)	33.0878 (4)	11.5932 (2)	100.849 (2)	5546.1 (1)	+ 2.20%
50 bar CO_2	14.7328 (2)	33.1149 (4)	11.6163 (2)	100.705 (2)	5568.7 (1)	+ 2.62%
10^{-5} mbar	14.6372 (4)	32.9094 (6)	11.4974 (3)	102.045 (3)	5416.4 (2)	- 0.20%

'Net volume change' refers to the overall increase/decrease in unit cell volume, compared to the initial pattern for the partially desolvated ***4.1·xH_2O·yDMF*** *under vacuum.*

At 50 bar CO_2, the MOF had increased by 2.62% in volume, which suggests successful uptake of CO_2 into the framework pores. This increase in volume is facilitated by an expansion in all three crystallographic dimensions, and a contraction of the *β* angle. As the pores of the MOF are in two crystallographic faces (see Figure 4.27), this increase in all dimensions is consistent with an 'opening' of all these pores.

Gravimetric CO_2 adsorption data were collected at 298 K for the fully desolvated MOF **4.1**, and may be found in section 4.3.5.

4.3.3 Alternative desolvation mechanism – chloroform soaking

Given that an extended period of desolvation by vacuum was insufficient to remove all of the DMF and water from the as-synthesised **4.1·xH_2O·yDMF**, an attempt was made to exchange the DMF and water within the pores of **4.1** and **4.2** with chloroform. In previous MOF literature,[46,47] replacing high-boiling solvents like DMF with more volatile ones such as chloroform or methanol facilitates an easier desolvation due to the volatility of chloroform. In using a lower temperature (or even ambient temperature) for the desolvation, crystallinity is often better maintained.

Crystals of both the as-synthesised **4.1·xH$_2$O·yDMF** and **4.2·xH$_2$O·yDMF** were collected by filtration at the pump and placed into clean, dry glass vials and soaked in dry chloroform, which was changed frequently to attempt to exchange the solvent within the pores. After one week, the samples were analysed by X-ray powder diffraction to check that the phase-purity of the materials had been maintained. The X-ray powder diffraction patterns of **4.2·xH$_2$O·yDMF** before chloroform exchange and of the corresponding **4.2·nCHCl$_3$** material after exchange are compared in Figure 4.34.

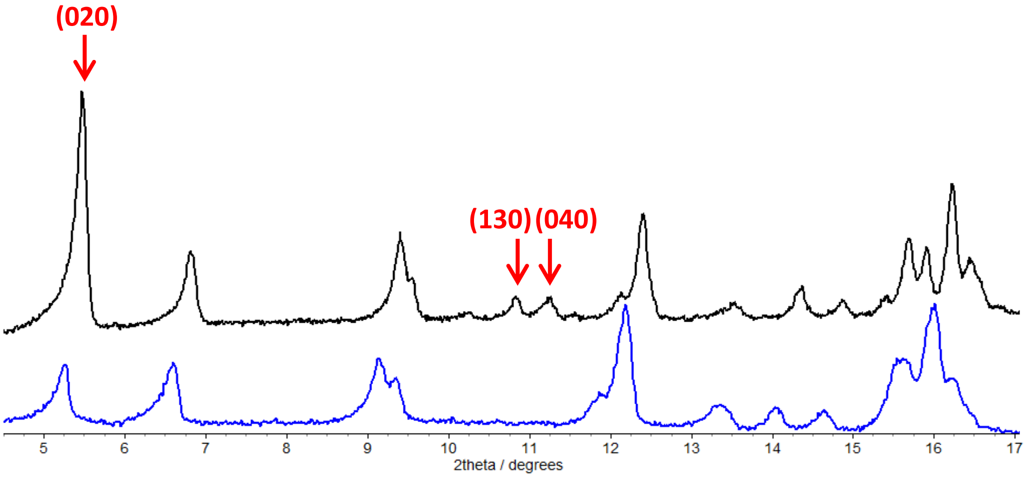

Figure 4.34. *Comparison of observed X-ray powder diffraction patterns for the as-synthesised **4.2·xH$_2$O·yDMF** before chloroform exchange (top, black), and of the chloroform-exchanged **4.2·nCHCl$_3$** (bottom, blue). Pawley fitting for these patterns are presented in experimental sections 4.2.5.2 and 4.2.5.4.*

Inspection of the powder pattern suggests that preferred orientation issues may have affected the intensities of reflections with a large (0k0) component (as labelled in Figure 4.34), which is consistent with diffraction data bring collected in reflection geometry. Otherwise, the observed powder pattern for **4.2·nCHCl$_3$** closely matches that of the as-synthesised MOF, and indexes to a similar (slightly contracted) unit cell. This suggests that the framework structure is still present. Therefore, the chloroform-exchanged material **4.2·nCHCl$_3$** was used as the starting point for an *in situ* crystallographic CO$_2$ uptake study.

4.3.4 Desolvation and CO$_2$ uptake in chiral framework 4.2

Using the chloroform-exchanged **4.2·nCHCl$_3$**, an analogous *in situ* powder X-ray diffraction study to that on **4.1·xH$_2$O·yDMF** (as described in section 4.3.2) was conducted. The sample was, as previously, evacuated under vacuum (10^{-5} mbar) for a sustained period (19 hours) before dosing with successive pressures of CO_2.

It was immediately obvious that the sample had lost a large degree of crystallinity during the desolvation, but was still sufficiently crystalline to facilitate Pawley fitting (unit cell determination). In addition, the intensity and peak-shape of the most intense (020, lowest 2θ) reflection appeared to have been reduced, either as a result of the loss of crystallinity or preferred orientation. As such, a quantitative judgement of the extent of desolvation by Rietveld refinement (as in section 4.3.2 for the racemic MOF **4.1**) could not be conducted. However, the relatively similar intensities of the first two reflections (020 and 110) indicate that, when compared with the fits discussed above, the material may still be partially solvated. The powder patterns for the material partially desolvated, and at successive pressures of CO_2 (considered to be **4.2·nCHCl$_3$·zCO$_2$**) are shown in Figure 4.35.

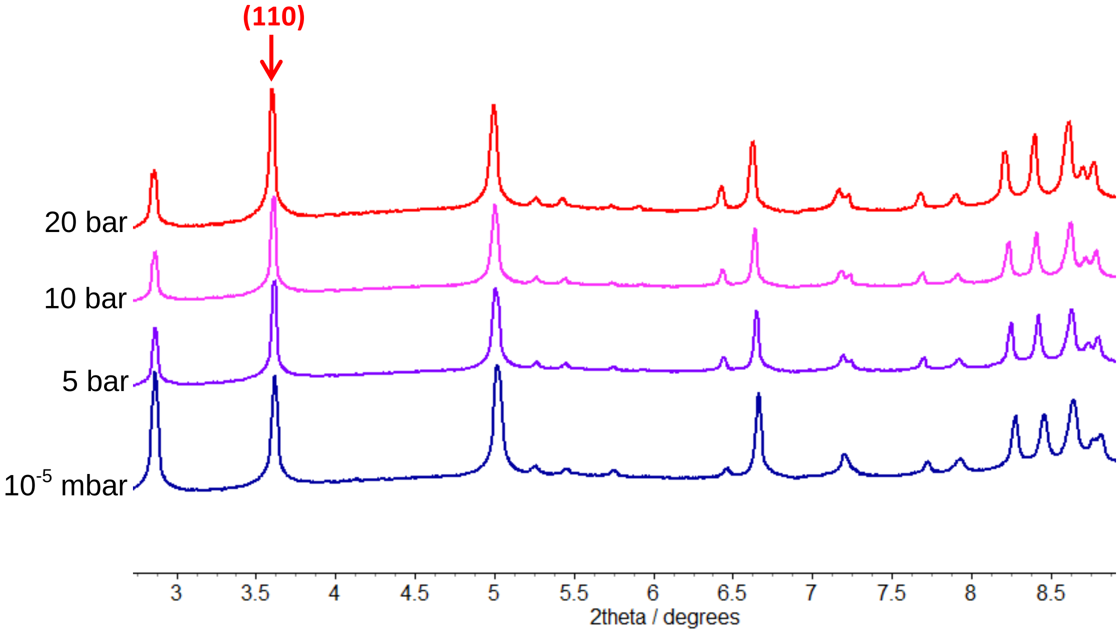

Figure 4.35. *X-ray powder diffraction pattern progression for successive dosing of the partially desolvated MOF **4.2·nCHCl$_3$** with CO_2. Pawley fit information is presented in experimental section 4.2.3.4.*

Visually, the most pronounced change is an increase in the relative intensity of the (110) reflection (labelled in Figure 4.35), which agrees qualitatively with the observed changes upon loading the racemic framework **4.1** with CO_2. A shift of the whole pattern again to lower diffraction angle is also observed, but to a lesser extent than observed for framework **4.1** (as shown in Figure 4.31). The unit cell data from refinements on the patterns shown in Figure 4.35 are shown in Table 4.36.

Table 4.36. *Unit cell parameters for* ***4.2·nCHCl₃*** *or* ***4.2·nCHCl₃·zCO₂*** *derived from Pawley fitting of the data obtained at vacuum and under successive pressures of* CO_2.

	a /Å	*b* /Å	*c* /Å	*β* /°	V /Å³	Net volume change
10^{-5} mbar	14.4711 (7)	32.968 (1)	11.6494 (5)	100.632 (6)	5462.3 (4)	
5 bar CO_2	14.5041 (5)	32.962 (1)	11.6982 (4)	100.727 (5)	5495.0 (3)	+ 0.60%
10 bar CO_2	14.5252 (5)	32.9940 (9)	11.7175 (3)	100.698 (4)	5518.0 (3)	+ 1.02%
20 bar CO_2	14.5485 (4)	33.0378 (8)	11.7400 (3)	100.596 (3)	5546.6 (2)	+ 1.54%

'Net volume change' refers to the overall increase/decrease in unit cell volume, compared to the initial pattern for the partially desolvated ***4.2·nCHCl₃*** *under vacuum.*

When the sample was dosed with 50 bar CO_2 it became apparent that the gas cell containing the sample was leaking, therefore the experiment was stopped. This means there is no direct comparison of the volume changes experienced by materials **4.1** and **4.2** at 50 bar CO_2, although the data in Table 4.36 show that the material does expand in response to CO_2 pressure, consistent with an uptake of CO_2.

4.3.5 Gravimetric CO_2 sorption in frameworks 4.1 and 4.2

Samples of the as-synthesised **4.1·xH₂O·yDMF** and **4.2·xH₂O·yDMF** were used for gravimetric CO_2 sorption study at the University of Strathclyde Chemical Engineering Department. The samples were desolvated fully with heat and reduced pressure *in situ* (as the crystallinity of the material was not integral to this study), as described in experimental section 4.2.3 and at 298 K, the samples were exposed to successive pressures of CO_2 (up to 20 bar, the operational maximum at 298 K). The resulting adsorption/desorption isotherm is shown in figures 4.37 and 4.38.

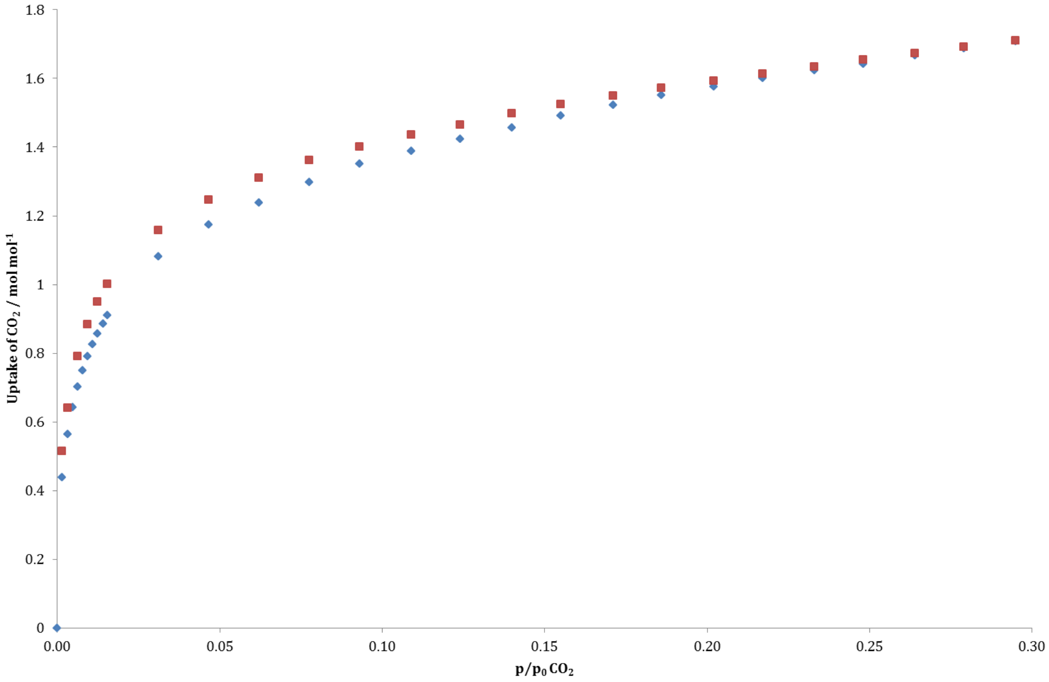

Figure 4.37. *Gravimetric CO_2 sorption isotherm for the desolvated framework* ***4.1*** *at 298 K. Blue diamonds represent the adsorption curve, and red squares represent the following desorption.*

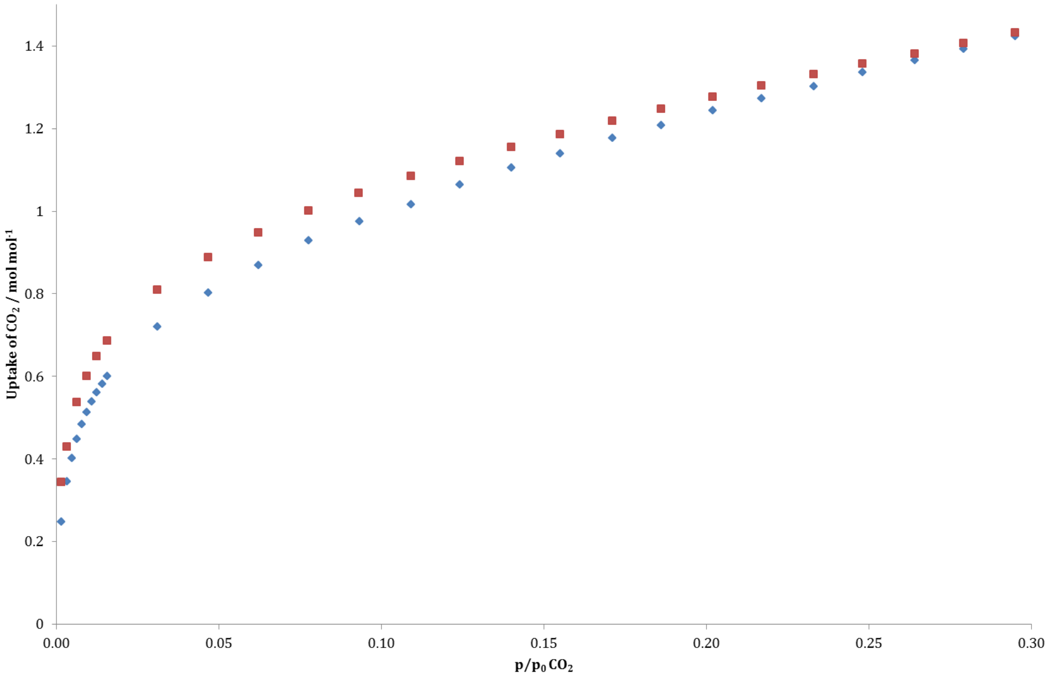

Figure 4.38. *Gravimetric CO_2 sorption isotherm for the desolvated framework* ***4.2*** *at 298 K. Blue diamonds represent the adsorption curve, and red squares represent the following desorption.*

The concentration of CO_2 within the pores of **4.1** at 20 bar was found to be 1.72 mol mol^{-1}, giving a formulation of **4.1·1.72CO$_2$**. Using a molecular volume of 38.54 Å^3 for CO_2 (calculated in SPARTAN06),[48] this means that just 66.29 Å^3 of the total 227 Å^3 void space (per formula unit of MOF) would be occupied under these conditions. For the chiral MOF **4.2**, the concentration of CO_2 within the pores at 20 bar was found to be 1.44 mol mol^{-1}, giving a formulation of **4.2·1.44CO$_2$**. This means that 55.50 Å^3 of the total 237 Å^3 void space (per formula unit of MOF) would be occupied.

Considering these figures, the uptake of CO_2 by the MOFs **4.1** and **4.2** is low. However, this measurement is only a $p/p_0(CO_2)$ of 0.30, and as such does not reflect the maximum possible uptake by the MOFs at 298 K.

4.3.6 Vapour uptake experiments

To establish the selectivity of the chiral framework **4.2** for chiral guests, two approaches were used – solution-phase and vapour-phase. In both cases, the racemic framework **4.1** was used as a control experiment.

In a novel approach to chiral guest uptake in MOFs with only one related example in the literature (as discussed in section 4.1.1),[26] the uptake of racemic 1,2-propanediol in framework **4.1** was probed gravimetrically. Propanediol was selected as it has a sufficiently high vapour pressure at modest temperatures, making it suitable for a vapour sorption experiment. The adsorption experiment was achieved by first dosing the desolvated sample with dry nitrogen (1 bar, 323 K), then using an intermix chamber to mix the dry nitrogen and nitrogen saturated with propanediol vapour. The inter-mix chamber was used to vary the saturation of a stream of nitrogen passing over the sample, and therefore the partial pressure of propanediol. The change in mass of the sample was monitored, leading to the resulting adsorption isotherm shown in Figure 4.39.

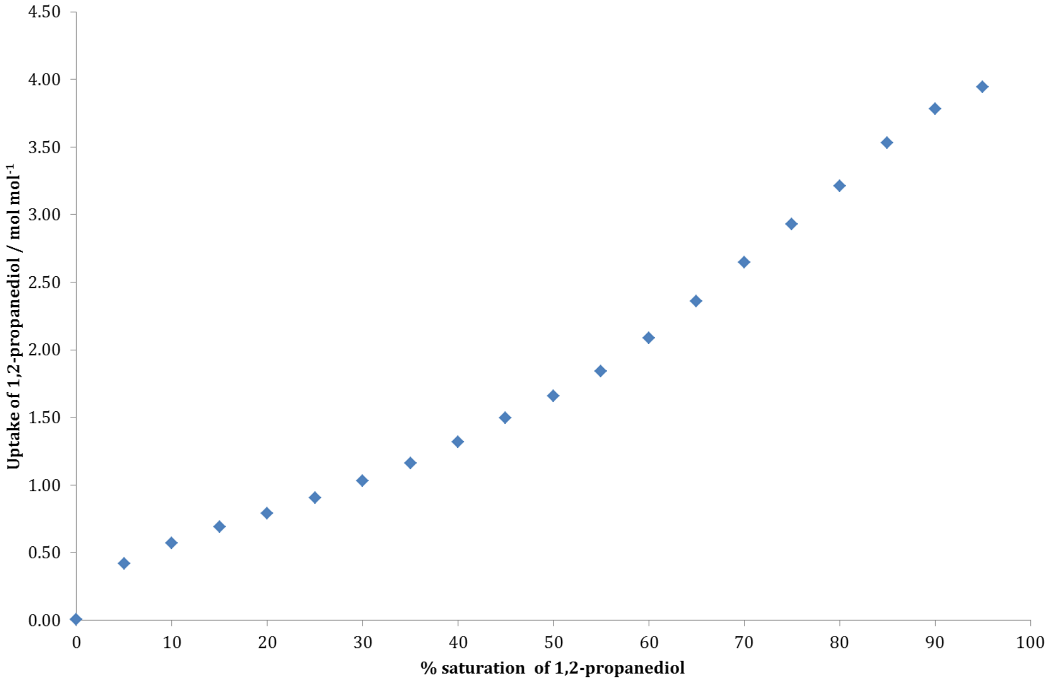

Figure 4.39. *Gravimetric racemic 1,2-propanediol/N_2 adsorption isotherm for the desolvated framework **4.1** at 323 K.*

The kinetics of adsorption using this method appeared to be very slow. This meant that at each step, the system had not reached full equilibration before the saturation level was increased. An uptake was, however, observed, but the slow equilibration rate was extrapolated to suggest that 24 hours or more equilibration time would be required at each measurement step. As such, neither the isotherm profile nor the suggested propanediol uptake of 3.94 mol mol^{-1} may be considered accurate and true reflections of the uptake behaviour of **4.1** for the guest. As such, further experiments using vapour uptake were not made.

4.3.7 Liquid enantioselectivity in framework 4.2

In a more conventional experiment, crystals of the empty framework MOFs were to be soaked in a liquid guest for a long period, and the presence of guests within the channels probed by digesting (destroying) the framework and analysing the resultant mixture.

An appropriate guest for these experiments needed to meet the following criteria: to be liquid at room temperature; give good baseline separation between enantiomers when analysed by chiral gas chromatography; and to be of the correct size and shape to complement the pores of **4.1** and **4.2**. 1-phenylethan-1-ol is a liquid at room temperature and easily separable on cyclodextrin-based chiral GC columns. Its suitability to the third criterion above was assessed by measuring the dimensions of the largest accessible pore of the MOFs and comparing this with the volume of a hypothetical box, occupied by the two possible guests. These measurements are outlined in Figure 4.40.

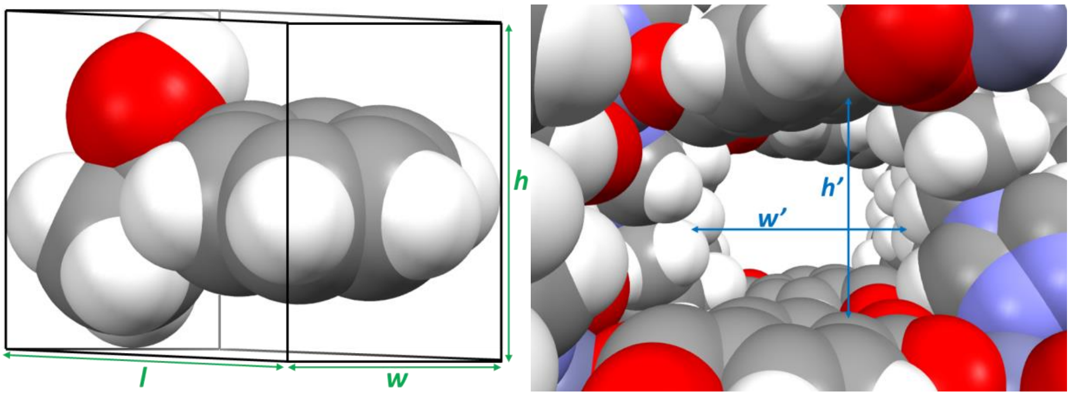

	1-phenylethan-1-ol
h	5.050 Å
w	6.159 Å
l	8.346 Å
area (h · w)	42.15 Å^2

	4.1	**4.2**
h'	6.191 Å	7.296 Å
w'	7.330 Å	6.382 Å
area	45.38 Å^2	46.56 Å^2

Figure 4.40. *Estimations of the volume and largest cross-section area of the 1-phenylethan-1-ol guest (R- enantiomer depicted above) using a simple cuboid; and of the cross-sectional area of the large channel pore of the MOFs **4.1** and **4.2** (**4.1** depicted above). The values for each guest and MOF are tabulated, taking into consideration the van der Waals radii for the atoms at the edges of the cuboid/pore.*[49] *Geometries of phenylethanol molecules taken from CSD entry BISDAK.*[50]

4.3.7.1 Chiral GC

The resultant chiral GC data for the racemic framework **4.1** suggest a small enantiomeric excess of the *R*-phenylethanol present in the pores (see Figure 4.41 and Table 4.43). This is unexpected, given that this MOF is racemic. The slight enantiomeric excess could be within a margin of systematic error, introduced either by the column (poor peakshapes or incomplete baseline separation in chromatograms) or from the sample, though this systematic error could not be quantified. The chiral gas chromatogram of the same batch of racemic phenylethanol used for this experiment did not suggest that there was an excess of either enantiomer in the bulk liquid.

The relative peak areas for the two phenylethanol enantiomeric guests in **4.2** however suggest a 3:1 ratio of guests present in the pore, in favour of the *R*-enantiomer (see Figure 4.42 and Table 4.43).

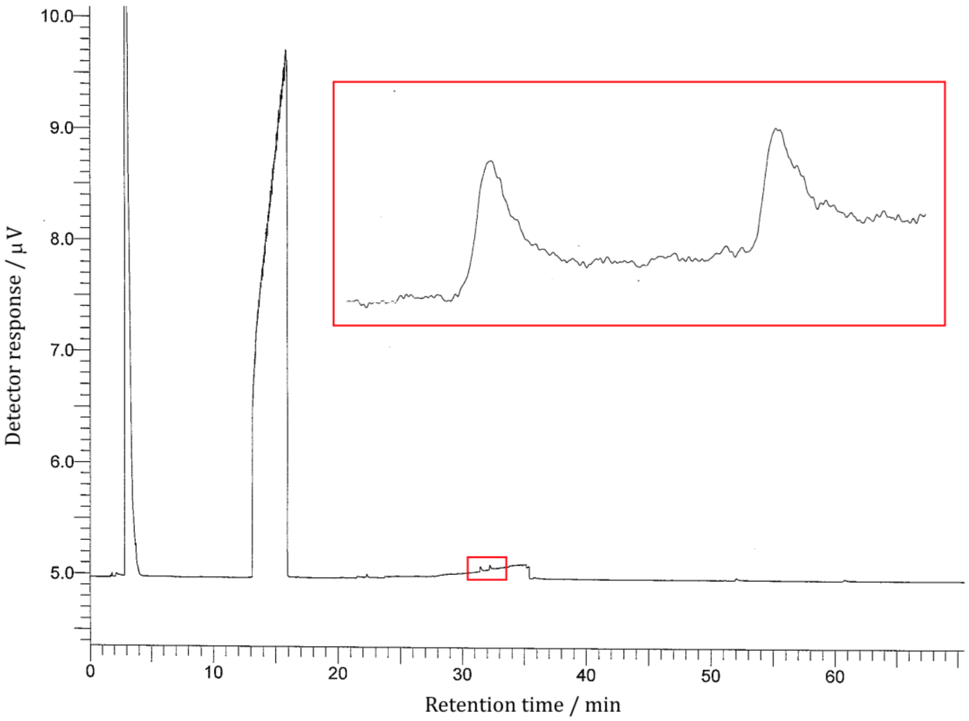

Figure 4.41. *Chiral gas chromatogram (zoomed in to show the relevant peaks) of the 1-phenylethan-1-ol soaked racemic MOF* ***4.1·aPhCH$_2$(OH)Me****, indicating an equal proportion of the R- and S-phenylethan-1-ol are present.*

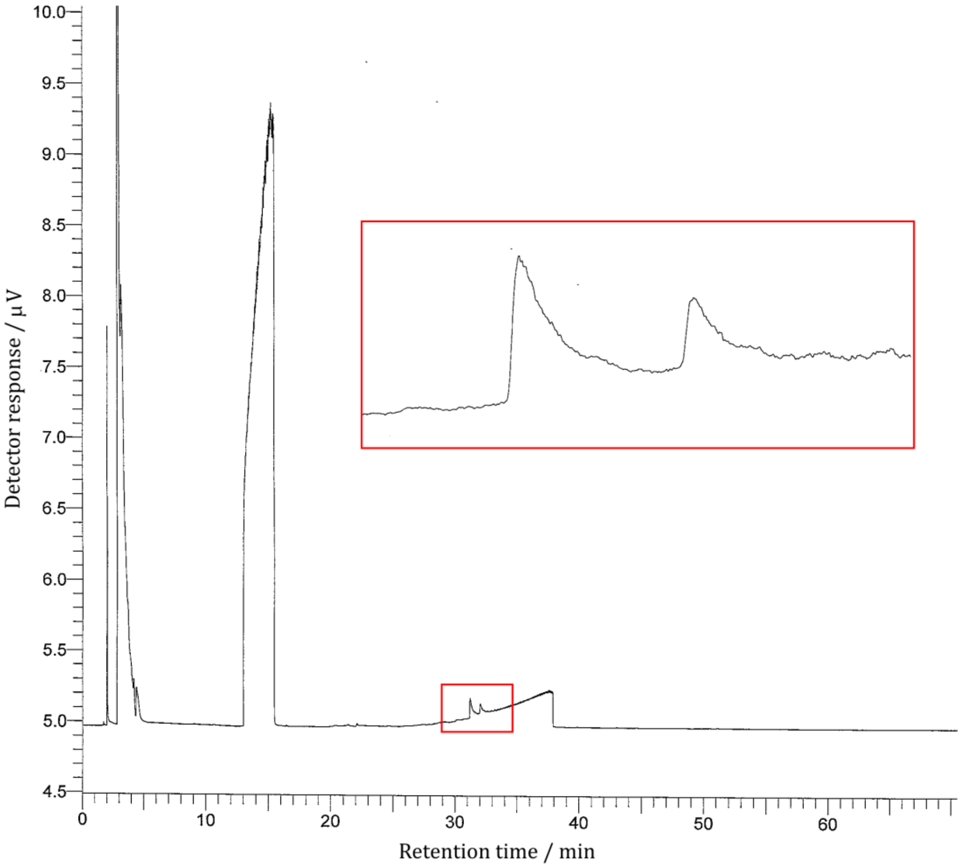

Figure 4.42. *Chiral gas chromatogram (zoomed in to show the relevant peaks) of the 1-phenylethan-1-ol soaked racemic MOF* ***4.2·aPhCH$_2$(OH)Me****, indicating a greater quantity of the R-phenylethan-1-ol is present.*

Table 4.43. *Relative guest proportions, enantiomeric excesses and selectivity constants $K_{R:S}$ of the two MOFs* ***4.1*** *and* ***4.2*** *for R-phenylethan-1-ol over S-phenylethan-1-ol. The equation for calculation of selectivity constant $K_{R:S}$ is also shown, where $K_{R:S}$ is the selectivity constant for the R-enantiomer over the S-enantiomer; Y_R is the mole fraction of the R-enantiomer in the product and X_R is the mole fraction of the R-enantiomer in the starting mixture.*

	4.1·aPhCH$_2$(OH)Me	**4.2·aPhCH$_2$(OH)Me**
% content *R*-phenylethanol	52.19	72.42%
% content *S*-phenylethanol	47.81	25.58%
% ee	4%	48%
$K_{R:S}$	1.092	2.910

$$K_{R:S} = (K_{S:R})^{-1} = \left(\frac{Y_R}{Y_S}\right) \cdot \left(\frac{X_S}{X_R}\right)$$

The chiral MOF **4.2** shows a preference for the *R*-phenylethanol guest, and traps the guest from the mixture in a 48% enantiomeric excess. This is not as high as some previously reported examples involving MOFs, where evacuated crystals of chiral MOFs have been soaked in racemic phenylethanol.[21] However, the pores of **4.2** do not contain any functional groups (other than the carboxylates) capable of forming strong intermolecular interactions like hydrogen bonds. Such interactions, like those utilised in the example in section 4.1 (Figure 4.1) have been shown to help direct guest entrapment.[19]

4.3.7.2 Single-crystal structure determination

Analysing the MOF crystals soaked in racemic phenylethanol by X-ray diffraction facilitated the comparison of the crystal structures of **4.1·aPhCH$_2$(OH)Me** and **4.2·aPhCH$_2$(OH)Me** with the parent (as-synthesised) materials.

The framework structures of **4.1** and **4.2** were unchanged, although disorder of the terephthalate ligand was not observed in **4.2·aPhCH$_2$(OH)Me**, which is present in the parent (DMF/water solvated) structures.

The phenylethanol guests in both **4.1·aPhCH$_2$(OH)Me** and **4.2·aPhCH$_2$(OH)Me** were disordered such that they could not be located crystallographically. However, inspecting the electron density difference peaks in the structure before applying PLATON SQUEEZE suggested a binding location for guests within **4.2·aPhCH$_2$(OH)Me** (see Figure 4.44).

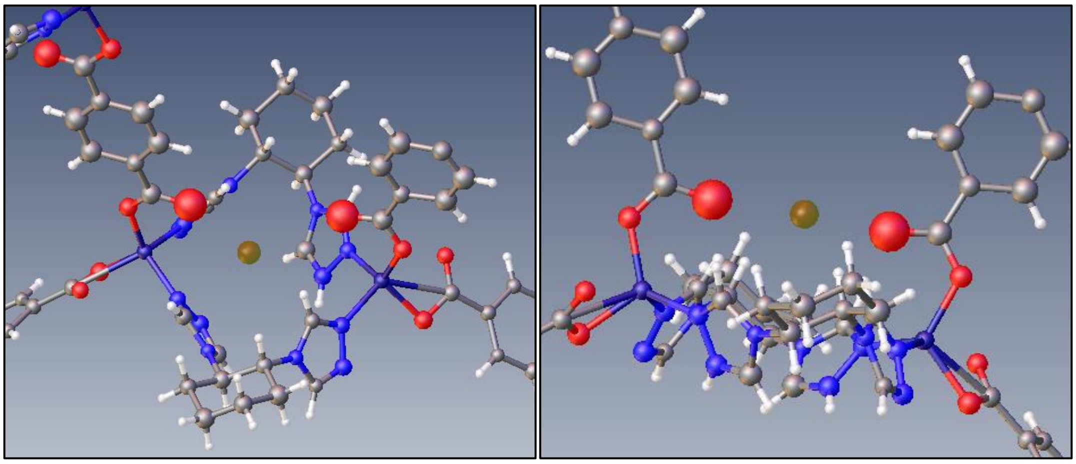

Figure 4.44. *Two views of the largest electron density difference peak within* ***4.2·aPhCH$_2$(OH)Me****, suggesting the location of either bound phenylethanol or water within the pore.*

This peak corresponded to 3 e Å^{-3}, situated 2.730 (17) Å from one carbonyl oxygen (and 3.425 (18) Å from the other shown in Figure 4.44) on the framework **4.2** may be an oxygen atom. This could be from the phenylethanol alcohol group (or from water which could also be present in the liquid), with a partial crystallographic occupancy. Other electron density difference peaks could be found near to the peak shown in Figure 4.44, however they were insufficient in magnitude to give a meaningful refinement. As such, PLATON SQUEEZE was applied to account for the residual electron density, and the guests were not crystallographically modelled.

4.4 Conclusions & Future work

4.4.1 Crystal engineering of a chiral/racemic pair of MOFs

A successful, designed approach to a pair of structurally-related chiral and racemic MOFs has been shown. The two MOFs have comparable pore volume, but different pore shape and distribution. The strategy of using a chiral co-ligand (in this case cyclohexane-bis-triazole) has been shown to be capable of templating chirality in a supramolecular material.

4.4.2 Gaseous guest uptake in 4.1 and 4.2

In-situ X-ray powder diffraction experiments on the partially-desolvated MOFs **4.1** and **4.2** demonstrate the difficulty of activating pores of these MOFs under mild conditions. Despite only achieving partial desolvation, the MOF materials **$4.1\cdot xH_2O\cdot yDMF$** and **$4.2\cdot nCHCl_3$** have been shown to take in CO_2 at room temperature. This is indicated by both the expansion of their crystallographic unit cell dimensions upon introduction of CO_2, and by gravimetric gas sorption data showing an increase in sample mass upon CO_2 introduction. The uptake of CO_2 by the fully desolvated **4.1** and **4.2** at p/p_0 0.30 was shown to be just 1.72 mol mol^{-1} and 1.44 mol mol^{-1} respectively, representing only a partial occupancy of the pores by CO_2, suggesting that there may be additional capacity for gas uptake at higher relative pressures.

Further work on these materials in this context should aim to characterise the gas uptake properties of **4.1** and **4.2** close to $p/p_0 = 1$ gravimetrically; as well as finding a way to fully desolvate the materials gently, so as to preserve crystallinity for X-ray diffraction studies. Supercritical CO_2 may be an appropriate choice for this, whereby the MOF crystals are placed into a pressure vessel and exposed to CO_2, and then the pressure is released, leaving the pores empty upon release of CO_2. This technique has been exploited before for MOF materials successfully.[51–53]

4.4.3 Chiral guest inclusion and selectivity in 4.1 and 4.2

Chiral MOF **4.2** has been shown to selectively trap *R*-1-phenylethan-1-ol over the *S*-enantiomer from a racemic mixture with a 48% enantiomeric excess ($K_{R:S}$ = 2.910).

Although selectivity for the *R*- enantiomer was observed in **4.2**, this is not as high as for some other MOFs in the literature.[13,21]

Preliminary attempts to characterise the uptake of 1,2-propanediol vapour gravimetrically indicated that the kinetics of adsorption were too slow to make measurement of a full adsorption isotherm practical, but did indeed show that racemic 1,2-propanediol was adsorbed by desolvated crystals of the racemic **4.1**. Further attempts at characterising the uptake of vapours could be made more practicable by aiming to study just one loading of chiral vapour in the racemic/chiral MOFs, rather than a series of relative humidities.

Further work on chiral separation could be conducted with other guests, but given that the pores of **4.1** and **4.2** do not contain strongly interacting functional groups, chiral selectivity is unlikely to be vastly improved. Decorating the pores with such functional groups could lead to better selectivity. This could be achieved by use of functionalised carboxylic acid co-ligands, however attempts to synthesise such materials using functionalised terephthalic acids and isophthalic acids under the same conditions so far have been unsuccessful.

4.5 References

1 Y. Liu, W. Xuan and Y. Cui, *Adv. Mater.*, 2010, **22**, 4112–4135.

2 X.-L. Yang and C.-D. Wu, *CrystEngComm*, 2014, **16**, 4907–4918.

3 K. K. Bisht, B. Parmar, Y. Rachuri, A. C. Kathalikattil and E. Suresh, *CrystEngComm*, 2015, **17**, 5341–5356.

4 C. Sporer, K. Wurst, D. B. Amabilino, D. Ruiz-Molina, H. Kopacka, P. Jaitner and J. Veciana, *Chem. Commun.*, 2002, 2342–2343.

5 U. Siemeling, I. Scheppelmann, B. Neumann, A. Stammler, H.-G. Stammler and J. Frelek, *Chem. Commun.*, 2003, **4**, 2236–2237.

6 X.-D. Chen, M. Du and T. C. W. Mak, *Chem. Commun.*, 2005, 4417–4419.

7 Z. Lin, A. M. Z. Slawin and R. E. Morris, *J. Am. Chem. Soc.*, 2007, **129**, 4880–4881.

8 Y. Yue, J. Liang, E. Gao, C. Fang, Z. Yan and C. Yan, *Inorg. Chem.*, 2008, **47**, 6115–6117.

9 Y. Wen, T. Sheng, S. Hu, X. Ma, C. Tan, Y. Wang, Z. Sun, Z. Xue and X. Wu, *Chem. Commun.*, 2013, **49**, 10644–10646.

10 G. Durá, M. C. Carrión, F. A. Jalón, A. M. Rodríguez and B. R. Manzano, *Cryst. Growth Des.*, 2013, **13**, 3275–3282.

11 K. K. Bisht and E. Suresh, *J. Am. Chem. Soc.*, 2013, **135**, 15690–15693.

12 Y. Wen, T. Sheng, Z. Sun, Z. Xue, Y. Wang, Y. Wang, S. Hu, X. Ma and X. Wu, *Chem. Commun.*, 2014, **50**, 8320–8323.

13 R. G. Xiong, X. Z. You, B. F. Abrahams, Z. Xue and C. M. Che, *Angew. Chem. Int. Ed. Engl.*, 2001, **40**, 4422–4425.

14 A. Mantion, L. Massüger, P. Rabu, C. Palivan, L. B. McCusker and A. Taubert, *J. Am. Chem. Soc.*, 2008, **130**, 2517–2526.

15 D. J. Lun, G. I. N. Waterhouse and S. G. Telfer, *J. Am. Chem. Soc.*, 2011, **133**, 5806–5809.

16 M.-S. M. Chen, M.-S. M. Chen, T. Okamura, M.-F. Lv, W.-Y. Sun and N. Ueyama, *CrystEngComm*, 2011, **13**, 3801–3810.

17 C. Martí-Gastaldo, J. E. Warren, K. C. Stylianou, N. L. O. Flack and M. J. Rosseinsky, *Angew. Chem. Int. Ed. Engl.*, 2012, **51**, 11044–11048.

18 O. R. Evans, H. L. Ngo and W. Lin, *J. Am. Chem. Soc.*, 2001, **123**, 10395–10396.

19 L. Ma, J. M. Falkowski, C. Abney and W. Lin, *Nature Chem.*, 2010, **2**, 838–846.

20 L. Ma, C. De Wu, M. M. Wanderley and W. Lin, *Angew. Chem. Int. Ed. Engl.*, 2010, **49**, 8244–8248.

21 M. C. Das, Q. Guo, Y. He, J. Kim, C. G. Zhao, K. Hong, S. Xiang, Z. Zhang, K. M. Thomas, R. Krishna and B. Chen, *J. Am. Chem. Soc.*, 2012, **134**, 8703–8710.

22 Y. Peng, T. Gong and Y. Cui, *Chem. Commun.*, 2013, **49**, 8253–8255.

23 T. Sawano, P. Ji, A. R. McIsaac, Z. Lin, C. W. Abney and W. Lin, *Chem. Sci.*, 2015, **6**, 7163–7168.

24 T. Duerinck and J. F. M. Denayer, *Chem. Eng. Sci.*, 2015, **124**, 179–187.

25 D. Bradshaw, T. J. Prior, E. J. Cussen, J. B. Claridge and M. J. Rosseinsky, *J. Am. Chem. Soc.*, 2004, **126**, 6106–6114.

26 B. Liu, O. Shekhah, H. K. Arslan, J. Liu, C. Wöll and R. A. Fischer, *Angew. Chem. Int. Ed. Engl.*, 2012, **51**, 807–810.

27 X. H. Zhang, S. M. Xie, A. H. Duan, B. J. Wang and L. M. Yuan, *Chromatographia*, 2013, **76**, 831–836.

28 S. M. Xie, X. H. Zhang, Z. J. Zhang and L. M. Yang, *Anal. Lett.*, 2013, **46**, 753–763.

29 S. M. Xie, X. H. Zhang, Z. J. Zhang, M. Zhang, J. Jia and L. M. Yang, *Anal. Bioanal. Chem.*, 2013, **405**, 3407–3412.

30 S. Xie, B. Wang, X. Zhang, J. Zhang, M. Zhang and L. Yuan, *Chirality*, 2014, **26**, 27–32.

31 P. Smart, C. A. Mason, J. R. Loader, A. J. H. M. Meijer, A. J. Florence, K. Shankland, A. J. Fletcher, S. P. Thompson, M. Brunelli, A. H. Hill and L. Brammer, *Chem. Eur. J.*, 2013, **19**, 3552–3557.

32 C. A. Mason, *The design and synthesis of homochiral coordination polymers (PhD Thesis, University of Sheffield)*, 2010.

33 S. K. U. Riederer, B. Bechlars, W. A. Herrmann and F. E. Kühn, *Dalton Trans.*, 2011, **40**, 41–43.

34 A. B. Pangborn, M. A. Giardello, R. H. Grubbs, R. K. Rosen and F. J. Timmers, *Organometallics*, 1996, **15**, 1518–1520.

35 R. H. Blessing, *Acta Crystallogr. Sect. B*, 1995, **51**, 33–38.

36 G. M. Sheldrick, *SADABS: Empirical absorption correction program (based on the method of Blessing), 1996*, 1996.

37 O. V. Dolomanov, L. J. Bourhis, R. J. Gildea, J. A. K. Howard and H. Puschmann, *J. Appl. Crystallogr.*, 2009, **42**, 339–341.

38 P. van der Sluis and A. L. Spek, *Acta Crystallogr. Sect. A*, 1990, **46**, 194–201.

39 A. L. Spek, *Acta Crystallogr. Sect. C*, 2015, **71**, 9–18.

40 A. N. Fitch, *Res. Natl. Inst. Stand. Technol.*, 2004, **109**, 133–142.

41 S. P. Thompson, J. E. Parker, J. Potter, T. P. Hill, A. Birt, T. M. Cobb, F. Yuan and C. C. Tang, *Rev. Sci. Intrum.*, 2009, **80**, 075107.

42 S. P. Thompson, J. E. Parker, J. Marchal, J. Potter, A. Birt, F. Yuan, R. D. Fearn, A. R. Lennie, S. R. Street and C. C. Tang, *J. Synchrotron Rad.*, 2011, **18**, 637–648.

43 A. A. Coelho, *TOPAS Academic, version 4.1 (2007), see http://www.topas-academic.net*, .

44 G. S. Pawley, *J. Appl. Crystallogr.*, 1981, **14**, 357–361.

45 H. M. Rietveld, *J. Appl. Crystallogr.*, 1969, **2**, 65–71.

46 B. Yuan, D. Ma, X. Wang, Z. Li, Y. Li, H. Liu and D. He, *Chem. Commun.*, 2012, **48**, 1135–1137.

47 Y.-L. Huang, Y.-N. Gong, L. Jiang and T.-B. Lu, *Chem. Commun.*, 2013, **49**, 1753–1755.

48 SPARTAN06, *Wavefunction Inc.*, 2006.

49 A. Bondi, *J. Phys. Chem.*, 1964, **3**, 441–451.

50 Z.-J. Li, J. Yao, Q. Tao, L. Jiang and T.-B. Lu, *Inorg. Chem.*, 2013, **52**, 11694–11696.

51 2011, US Patent US2011144367–A1.

52 H. J. Park, D.-W. Lim, W. S. Yang, T.-R. Oh and M. P. Suh, *Chem. Eur. J.*, 2011, **17**, 7251–7260.

53 J. Kim, D. O. Kim, D. W. Kim and K. Sagong, *J. Solid State Chem.*, 2013, **197**, 261–265.

Halogenated zeolitic imidazolate frameworks:

Investigating dihalomethane uptake and thermal degradation

5

Chapter Five

5.1 Introduction

In host-guest chemistry, specific intermolecular interactions (in particular hydrogen bonds) play a significant role in the recognition of guests. Perhaps the ultimate example of this is in enzymes, in which specific arrangements of functional groups capable of participating in intermolecular interactions recognise guests (e.g. hormones, drugs) with great specificity.

The host-guest chemistry of MOFs (such as the sensing or entrapment of guests, or catalytic activity) is greatly affected by the intermolecular interactions the MOF pores are capable of supporting. This aspect of MOF design and functionality is one of the aspects that make MOFs so desirable in comparison to zeolite materials. Several examples exist where the effect of specific hydrogen-bonding interactions within pores have been studied (and/or designed into the material), and have been shown to improve aspects of the MOF's functionality.

The incorporation of the hydrogen-bond donating group urea (or more recently a squaramide)[1] into the pores of MOFs has led to their successful use as electrophile-activating catalysts.[2–5] The presence of these strongly hydrogen-bond donating moieties in the pores has been shown to activate potentially electrophilic guests towards nucleophilic attack by other guests.

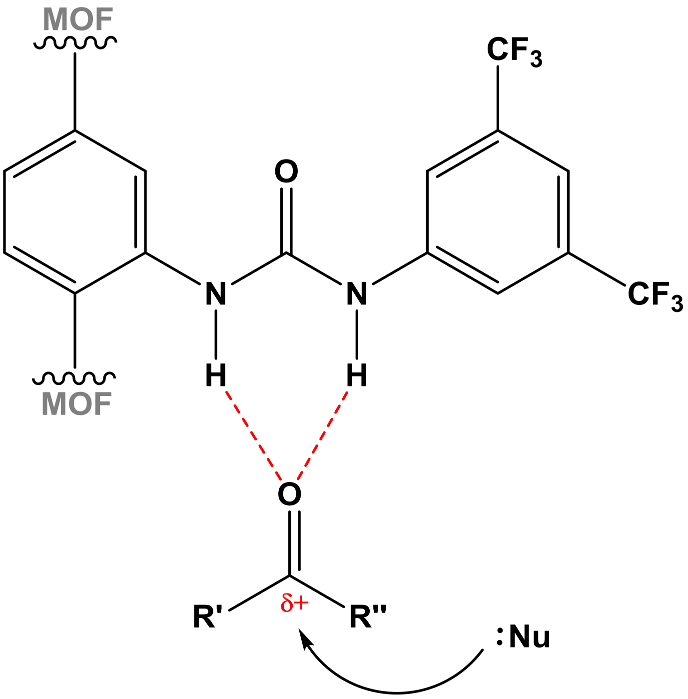

Figure 5.1. *Electrophile-activating behaviour by pendant hydrogen-bond donating groups within a MOF, activating the hydrogen bond acceptor to nucleophilic attack.*

Although many MOF systems have been shown to respond to the presence of guests within the pores through luminescence (see section 1.3.5) or to take up guests selectively (particularly in the case of gases, see section 1.3.2), specific intermolecular interactions responsible for these phenomena were not necessarily identified. However in some cases, the role of specific hydrogen bonding interactions in both the luminescent sensing of guests,[6–8] and the selective entrapment of guest molecules has been elucidated.[9–12] One particular example of the latter, is the inclusion of non-coordinated carboxylic acid ligand functional groups within the pores of a MOF by the group of Banglin Chen.[11] This acid-decorated MOF demonstrated the ability to remove methylene blue (a medical dye, shown in Figure 5.2) from water, by its adsorption into the MOF. This was achieved by hydrogen bonding between the carboxylic acid functional groups and the methylene blue.

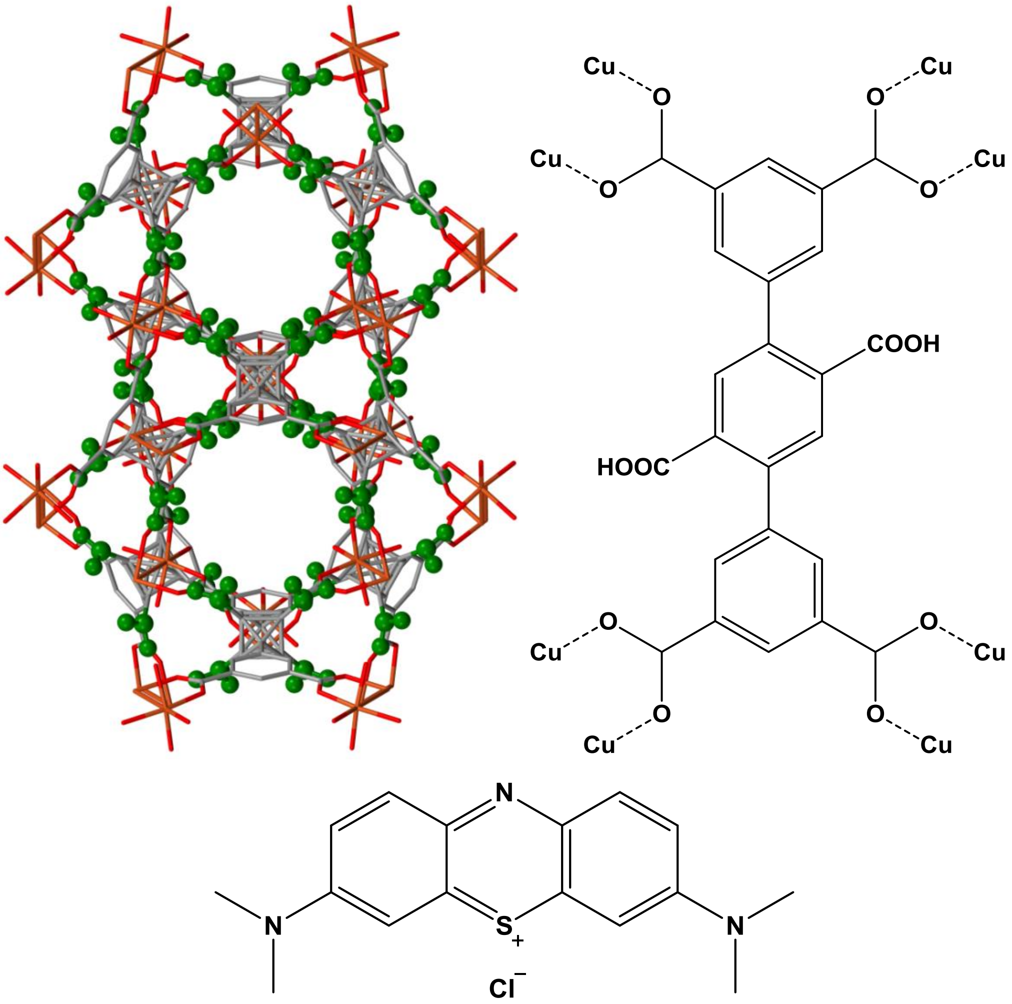

Figure 5.2. Left, top: *Carboxylic acid/carboxylate functional groups lining the pores of the MOF "ZJU-24", [$Cu_2(L)_4$] (where "L" is also shown in the picture above). The carboxylic acid/carboxylate functional groups are shown in green for emphasis.*[11] ***Right, top:*** *The structure of the hydrogen-bonding ligand used, with pendant carboxylic acid functionalities.* ***Bottom:*** *The structure of the medical dye methylene blue.*

Although MOFs (and ZIFs) containing halogen substituents exist, the role of halogen bonding in processes within MOF pores has not so far been probed. Given the examples noted above highlighting the usefulness of hydrogen bond motifs within MOFs, halogen bonding motifs should also be explored.

5.1.1 Chapter aims

The ZIF-69 family of materials of composition [M(NO_2im)(R-bim)] (M = Co, Zn; NO_2im = 2-nitroimidazolate; R-bim = R-substituted benzimidazolate) reported by Yaghi et. al.[13] and Banerjee et. al.[14] is a family of isostructural ZIFs with different pore-lining substituent groups. This family of ZIFs appeared suitable for comparison of substituent effects on guest uptake behaviour, due to their similar pore environments. Use of different R-groups as a substituent at the 5-position (6-membered ring) of the benzimidazolate ligand (R = H, Me, Cl and Br) has been shown to lead to isostructural ZIFs.

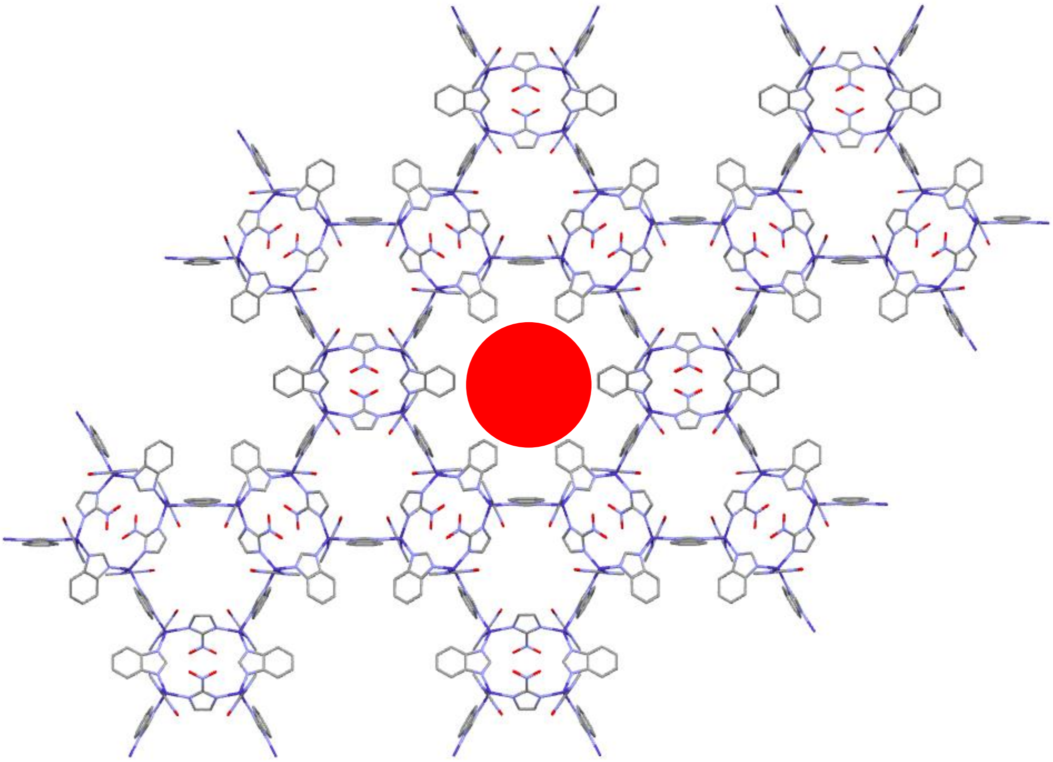

Figure 5.3. *Pore space environment in [Zn(NO_2im)(bim)]·(solvent), highlighted in red. Crystal structure as obtained by Banerjee et. al.*[14]

In the studies described by this chapter, the uptake ability (and potentially selectivity) of the ZIF materials towards halogen-containing guests was to be investigated, in particular focussing on comparing the methyl-substituted ZIF with the bromo- and iodo- functionalised ZIFs, as the pore spaces were expected to be relatively similar in size. The possibility for selective entrapment of guests more capable of forming halogen-halogen interactions, by the halogenated ZIFs over the methylated ZIF was to be explored. The possibility of determining the presence of guests within the ZIF hosts spectroscopically was to be explored, using solid-state NMR.

5.2 Experimental

5.2.1 Synthesis

All reagents and solvents were purchased from Fluorochem, Aldrich or Fisher Scientific and used as received without further purification.

[Zn(NO$_2$im)(bim)]·xH$_2$O·yDMF, 5.1·xH$_2$O·yDMF

Zinc nitrate hexahydrate (136 mg, 0.46 mmol), 2-nitroimidazole (80 mg, 0.70 mmol) and benzimidazole (54 mg, 0.46 mmol) were dissolved in 9 mL DMF, and the solution placed in a 24 mL-capacity screwcap glass vial. The solution was heated in an oven to 120 °C at a rate of 1.66 °C min^{-1}, held at 100 °C for a period of 24 hours and then cooled to 25 °C at a rate of 0.05 °C min^{-1}. This yielded fine, cream-coloured crystals of the title compound (73 mg, 0.12 mmol, 26% yield). CHN expected: C 44.94%, H 6.05%, N 21.43%; anal. found: C 45.57%, H 4.16%, N 19.65%.
(Yield and expected CHNX proportions based on a formula of **5.1·0.1H$_2$O·4.0DMF**, which gives best fit to the elemental analysis data, to the nearest tenth of an integer.)

[Zn(NO$_2$im)(Mebim)]·xH$_2$O·yDMF, 5.2·xH$_2$O·yDMF

Zinc nitrate hexahydrate (136 mg, 0.46 mmol), 2-nitroimidazole (80 mg, 0.70 mmol) and 5-methylbenzimidazole (54 mg, 0.46 mmol) were dissolved in 9 mL DMF, and the solution placed in a 24 mL-capacity screwcap glass vial. The solution was heated in an oven to 120 °C at a rate of 1.66 °C min^{-1}, held at 100 °C for a period of 24 hours and then cooled to 25 °C at a rate of 0.05 °C min^{-1}. This yielded fine, cream-coloured crystals of the title compound (102 mg, 0.20 mmol, 43% yield). CHN expected: C 42.88%, H 5.67%, N 20.36%; anal. found: C 43.27%, H 4.71%, N 19.27%.
(Yield and expected CHN proportions based on a formula of **5.2·1.5H$_2$O·2.4DMF**, which gives best fit to the elemental analysis data, to the nearest tenth of an integer.)

[Zn(NO$_2$im)(Brbim)]·xH$_2$O·yDMF, 5.3·xH$_2$O·yDMF

Zinc nitrate hexahydrate (136 mg, 0.46 mmol), 2-nitroimidazole (80 mg, 0.70 mmol) and 5-bromobenzimidazole (54 mg, 0.46 mmol) were dissolved in 9 mL DMF, and the solution placed in a 24 mL-capacity screwcap glass vial. The solution was heated in an oven to 120 °C at a rate of 1.66 °C min^{-1}, held at 100 °C for a period of 24 hours and then cooled to 25 °C at a rate of 0.05 °C min^{-1}. This yielded fine, cream-coloured crystals of the title compound (112 mg, 0.26 mmol, 57% yield). CHNX expected: C 34.61%, H 2.72%, N 18.87%, Br 18.54 %; anal. found: C 35.34%, H 3.10%, N 17.73%, Br 19.27%.

(Yield and expected CHNX proportions based on a formula of **5.3·0.8DMF**, which gives best fit to the elemental analysis data, to the nearest tenth of an integer.)

[Zn(NO_2im)(Ibim)]·xH_2O·yDMF, 5.4·xH_2O·yDMF

Zinc nitrate hexahydrate (136 mg, 0.46 mmol), 2-nitroimidazole (80 mg, 0.70 mmol) and 5-bromobenzimidazole (54 mg, 0.46 mmol) were dissolved in 9 mL DMF, and the solution placed in a 24 mL-capacity screwcap glass vial. The solution was heated in an oven to 120 °C at a rate of 1.66 °C min^{-1}, held at 100 °C for a period of 24 hours and then cooled to 25 °C at a rate of 0.05 °C min^{-1}. This yielded fine, cream-coloured crystals of the title compound (97 mg, 0.18 mmol, 39% yield). CHN expected: C 30.88%, H 3.19%, N 16.43%; anal. found: C 31.11%, H 2.80%, N 15.81%.

(Yield and expected CHNX proportions based on a formula of **5.4·1.2H_2O·1.2DMF**, which gives best fit to the elemental analysis data, to the nearest tenth of an integer.)

5.2.2 Guest soaking experiments

Crystals of the as-synthesised **5.3·xH_2O·yDMF** were isolated from the mother liquor by filtering at the pump, and allowed to air-dry for at least ten minutes, before placing in a fresh 24 mL-capacity glass vial and adding 2 mL of either dichloromethane, or a 0.1 M solution of dibromomethane or diiodomethane in dichloromethane, and the vials were sealed and stored in a refrigerator (<5°C). The solvent was exchanged at least four times for fresh solvent, and the samples were allowed to soak for at least six weeks total before analysis. Samples were removed from the diohalomethane solvent no more than ten minutes before solid-state NMR analysis to prevent evaporation of dichloromethane.

5.2.3 Powder X-ray diffraction

The crystalline products were all ground in a pestle and mortar and packed in to 0.7 mm before data collection (borosilicate for phase purity checks and quartz for to heating studies). Phase purity checks were conducted at ambient temperature.

X-ray diffraction data for the phase purity checks of the as-synthesised **5.1·xH_2O·yDMF**, **5.2·xH_2O·yDMF**, **5.3·xH_2O·yDMF** and **5.4·xH_2O·yDMF** were collected at beamline I11 at Diamond Light Source at wavelength 0.825821 Å,[15,16] using a wide angle (90°) PSD detector comprising 18 Mythen-2 modules. A pair of scans was conducted, related by a 0.25 ° detector offset to account for gaps between detector modules. Five such scan pairs were collected at five seconds exposure per scan, whilst the sample capillary was spun about its axis to average beam exposure. These five pairs of scans were preceded and followed by a pair of one-second scans, to compare and therefore assess beam damage. No observable beam damage could be found, and the resulting patterns were summed to give the final pattern for structural analysis (total beam exposure time therefore 54 seconds).

X-ray diffraction data for the sample of **5.3·xH$_2$O·yDMF** heated *ex situ* were collected on a Cu Kα Bruker D8 ADVANCE X-Ray powder diffractometer (Cu Kα2). The instrument was fitted with a focusing Göbel mirror optic and a high-resolution energy-dispersive Lynxeye XE detector. Scans were collected over a range $3° \leq 2\theta \leq 40°$, using a step size of 0.01532° and step time of 20s giving a total exposure time of 13.5 h. The sample capillary was spun about its axis at a rate of 30 rev min^{-1}. For the samples **5.3·aDCM**, **5.3·aDCM·bDBM** and **5.3·aDCM·bDIM**, scans were collected over a range $3° \leq 2\theta \leq 30°$, using a step size of 0.01532° and step time of 8s giving a total exposure time of 3 h. The sample capillary was spun about its axis at a rate of 30 rev min^{-1}.

X-ray diffraction data for the *in situ* desolvation and heating of **5.3·xH$_2$O·yDMF** were collected (λ = 0.826210 (5) Å) at beamline I11 at Diamond Light Source,[15,16] using a wide angle (90°) PSD detector comprising 18 Mythen-2 modules. A pair of scans was conducted, related by a 0.25 ° detector offset to account for gaps between detector modules. Five such scan pairs were collected at five seconds exposure per scan, whilst the sample capillary was spun about its axis to average beam exposure. The resulting patterns were summed to give the final pattern for structural analysis (total beam exposure time therefore 50 seconds per measurement).

5.2.3.1 Phase purity check on the as-synthesised ZIFs

5.1·xH$_2$O·yDMF

Visual inspection of the pattern indicated the presence of a phase similar to that reported in the literature (CSD ref GITTUZ, hexagonal *P*6$_3$/*mmc*).[13] The reported unit cell of this material was used as the starting point for a Pawley refinement,[17] employing 487 parameters (10 background, 1 zero error, 5 profile, 2 cell, 469 reflections), resulting in final indices of fit R_{wp} = 7.981, $R_{wp'}$ = 35.31. Not all peaks were indexed. The unindexed peaks could not be attributed to any known ZIF phase corresponding to the components used in synthesis, nor to any of the individual reactants used in the synthesis.

[**5.1·xH$_2$O·yDMF**: *a* = *b* = 26.6888 (10) Å, *c* = 18.4922 (11) Å, *V* = 11407 (1) Å^3].

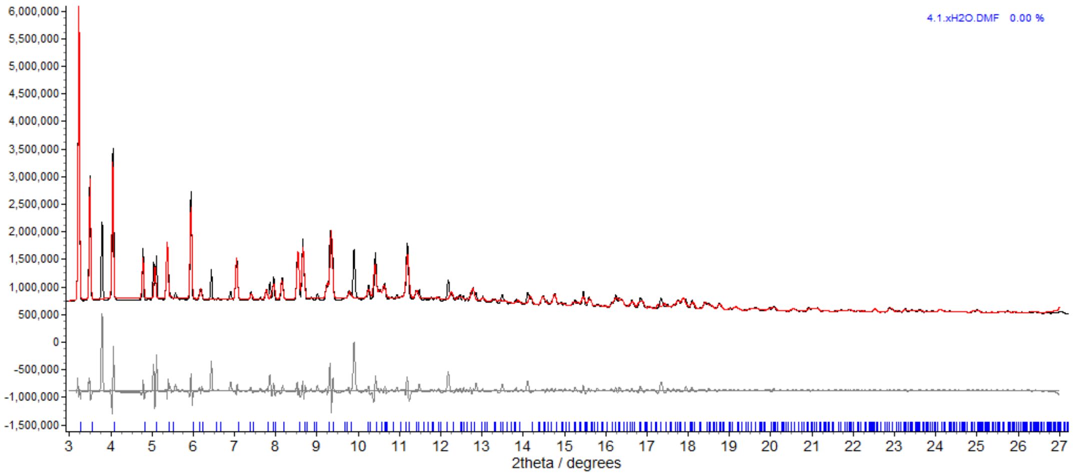

Figure 5.4. *Observed (black) and calculated (red) profiles and difference plot [I_{obs}-I_{calc}] (grey) of the Pawley refinement. (2θ range 3.0 - 27 °, d_{min} = 1.77 Å).*

5.2·xH$_2$O·yDMF

Visual inspection of the pattern indicated that the expected phase indicated in the literature (CSD ref YOZBOF, hexagonal *P*6$_3$/*mmc*) was not present, and instead a new phase (which did not correspond to any of the individual reactants used in the synthesis), which could not be indexed was formed.

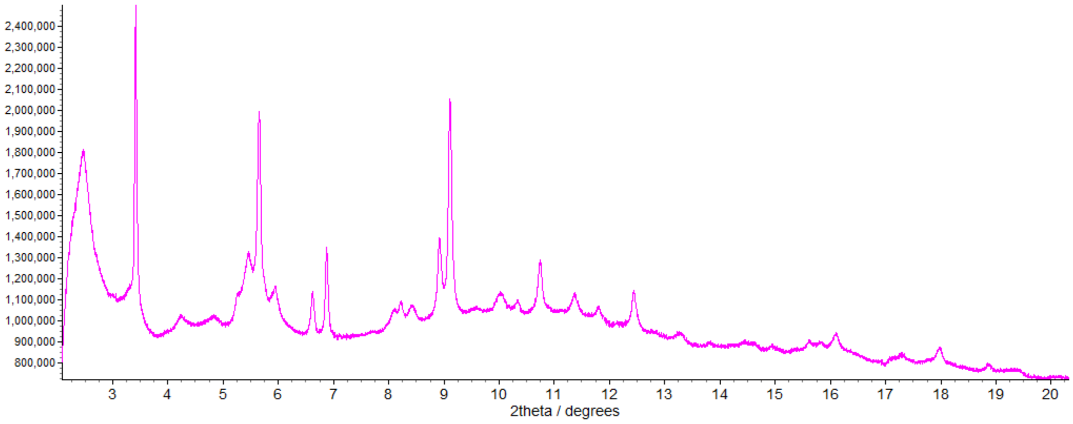

Figure 5.5. *Observed (pink) profile for the sample* ***5.2·xH$_2$O·yDMF****.*

5.3·xH$_2$O·yDMF

Visual inspection of the pattern indicated the presence of a phase similar to that in the literature (CSD ref YOZCAS, hexagonal $P6_3/mmc$).[13] The reported unit cell of this material was used as the starting point for a Pawley refinement,[17] employing 1095 parameters (10 background, 1 zero error, 5 profile, 2 cell, 1077 reflections), resulting in final indices of fit R_{wp} = 0.880, $R_{wp'}$ = 11.62.

[**5.3·xH$_2$O·yDMF**: $a = b$ = 26.1733 (3) Å, c = 19.6393 (3) Å, V = 11651.3 (3) Å^3].

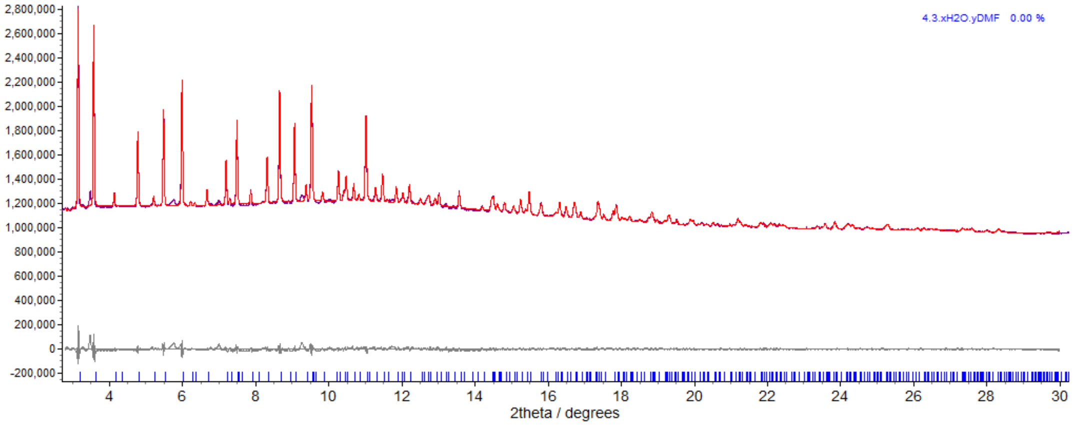

Figure 5.6. *Observed (purple) and calculated (red) profiles and difference plot [I_{obs}-I_{calc}] (grey) of the Pawley refinement. (2θ range 3.0 - 30 °, d_{min} = 1.60 Å).*

5.4·xH$_2$O·yDMF

Visual inspection of the pattern indicated that an isostructural ZIF to the brominated analogue was not formed (as shown in Figure 5.5), and instead a new phase, whose powder diffraction pattern largely matches that for **5.2·xH$_2$O·yDMF** was found.

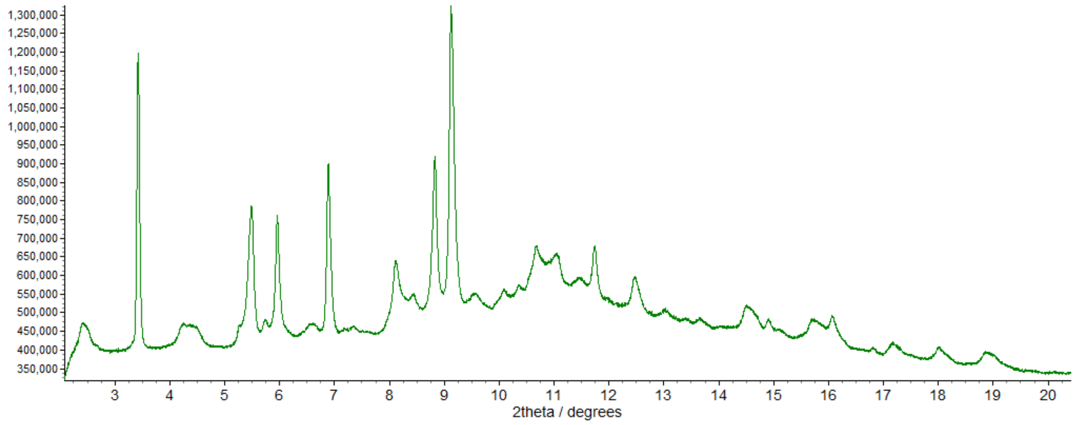

Figure 5.7. *Observed (green) profile for the sample* ***5.4·xH₂O·yDMF****.*

5.2.3.2 Phase purity checks on dihalomethane-soaked ZIF 5.3

5.3·aDCM

Visual inspection of the pattern indicated that the crystallinity of the sample had been degraded during the soaking, but that the key low-angle reflections corresponding to the established phase of **5.3·xH$_2$O·yDMF** still remained. The unit cell of this phase was used as the starting point for a Pawley refinement,[17] employing 116 parameters (8 background, 1 zero error, 5 profile, 2 cell, 100 reflections), resulting in final indices of fit R_{wp} = 12.33, $R_{wp'}$ = 25.09.

[**5.3·aDCM**: $a = b$ = 26.753 (3) Å, c = 19.168 (9) Å, V = 11811 (6) Å^3].

A reflection corresponding to an unknown phase, which was previously identified in the pattern corresponding to **5.3·xH$_2$O·yDMF** at 6.2° 2θ was also present, in addition to some further, small reflections at 10.2°, 12.25° and 18.8° 2θ. These were insufficient in number to permit indexing or further identification.

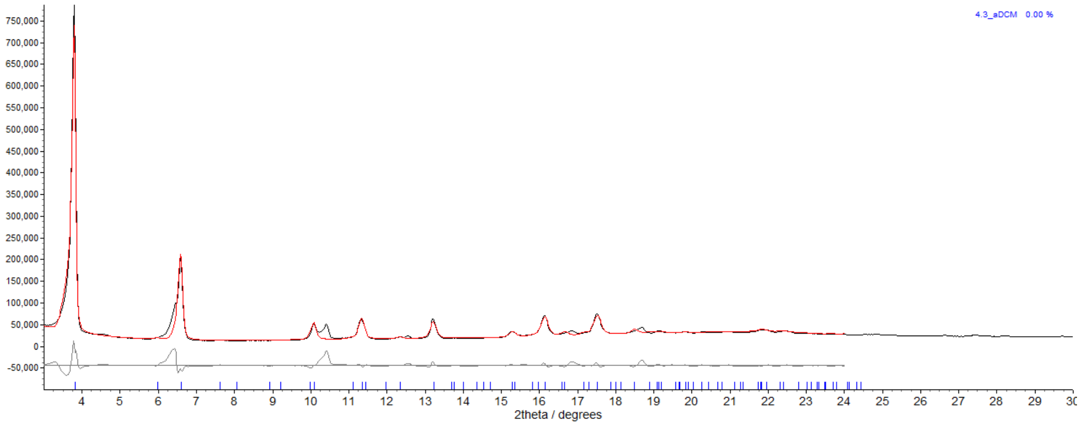

Figure 5.8. *Observed (black) and calculated (red) profiles and difference plot [I_{obs}-I_{calc}] (grey) of the Pawley refinement. (2θ range 3.0 - 30 °, d_{min} = 3.70 Å).*

5.3·aDCM·bDBM

Visual inspection of the pattern indicated that the crystallinity of the sample had been degraded during the soaking, but that the key low-angle reflections corresponding to the established phase of **5.3·xH₂O·yDMF** still remained. The unit cell of this phase was used as the starting point for a Pawley refinement,[17] employing 116 parameters (18 background, 1 zero error, 5 profile, 2 cell, 100 reflections), resulting in final indices of fit R_{wp} = 13.14, $R_{wp'}$ = 24.07.

[**5.3· aDCM·bDBM**: $a = b$ = 26.756 (3) Å, c = 19.186 (9) Å, V = 11895 (6) Å^3].

A reflection corresponding to an unknown phase, which was previously identified in the pattern corresponding to **5.3·xH₂O·yDMF** at 6.2° 2θ was also present, in addition to some further, small reflections at 10.2°, 12.25° and 18.8° 2θ. These were insufficient in number to permit indexing or further identification.

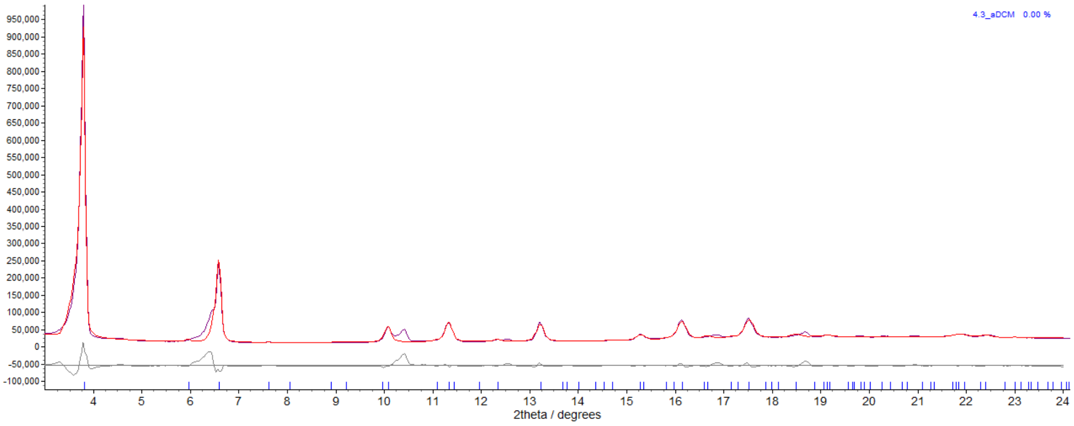

Figure 5.9. *Observed (purple) and calculated (red) profiles and difference plot [I_{obs}-I_{calc}] (grey) of the Pawley refinement. (2θ range 3.0 - 30 °, d_{min} = 3.70 Å).*

5.3·aDCM·bDIM

Visual inspection of the pattern indicated that the crystallinity of the sample had been degraded during the soaking, but that the key low-angle reflections corresponding to the established phase of **5.3·xH₂O·yDMF** still remained. The unit cell of this phase was used as the starting point for a Pawley refinement,[17] employing 116 parameters (8 background, 1 zero error, 5 profile, 2 cell, 100 reflections), resulting in final indices of fit R_{wp} = 9.981, $R_{wp'}$ = 20.08.

[**5.3·aDCM·bDIM**: $a = b$ = 26.741 (3) Å, c = 19.200 (8) Å, V = 11890 (5) Å^3].

A reflection corresponding to an unknown phase, which was previously identified in the pattern corresponding to **5.3·xH₂O·yDMF** at 6.2° 2θ was also present, in addition to some further, small reflections at 10.2°, 12.25° and 18.8° 2θ. These were insufficient in number to permit indexing or further identification.

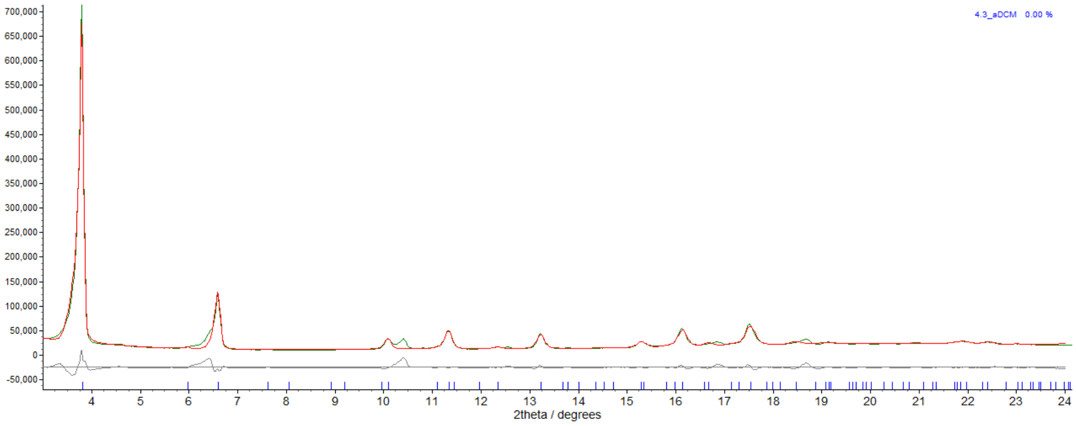

Figure 5.10. *Observed (green) and calculated (red) profiles and difference plot [I_{obs}-I_{calc}] (grey) of the Pawley refinement. (2θ range 3.0 - 30 °, d_{min} = 3.70 Å).*

5.2.3.3 *Ex situ* heating study on 5.3·xH$_2$O·yDMF

Crystals of the as-synthesised **5.3·xH$_2$O·yDMF** studied in section 5.2.3.1 were filtered at the pump and allowed to air-dry for a period of one hour, before heating in a tube furnace (under air) to 280°C for four hours. After the material had cooled to room temperature, the powder pattern of the resultant material was recorded.

Visual inspection of the resultant pattern indicated clearly that a phase change had taken place, but the pattern could not be successfully indexed to a single unit cell.

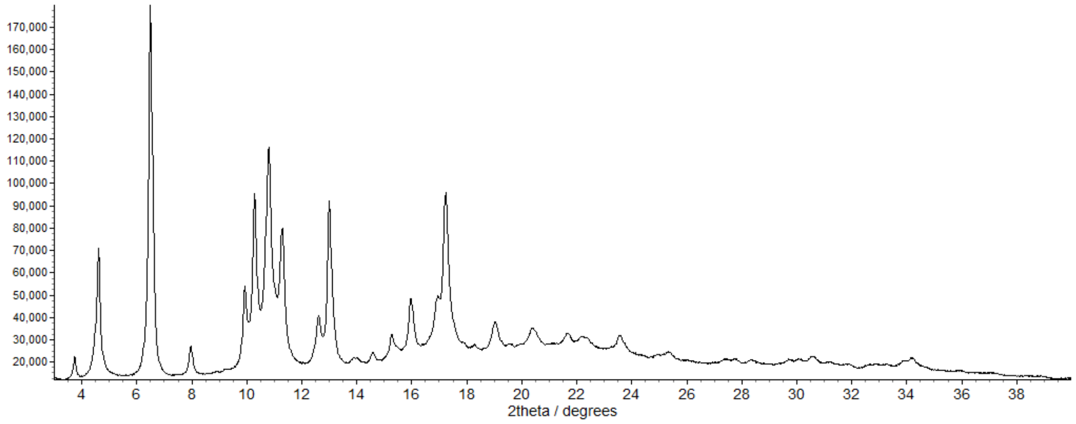

Figure 5.11. *Powder X-ray diffraction pattern for the new material "**5.5**".*

5.2.3.4 *In situ* heating study on 5.3·xH$_2$O·yDMF

Crystals of the as-synthesised **5.3·xH$_2$O·yDMF** studied in section 5.2.3.1 were filtered at the pump and allowed to air-dry for a period of one hour, before packing in the quartz capillary for study. Initially, one end of the capillary was left open and the other closed, for the initial phase purity check.

Initial pattern at ambient temperature

The unit cell of **5.3·xH$_2$O·yDMF** found in section 5.2.3.3 was used as the starting point for a Pawley refinement,[17] employing 369 parameters (8 background, 1 zero error, 5 profile, 2 cell, 353 reflections), resulting in final indices of fit R_{wp} = 6.625, $R_{wp'}$ = 32.37. Data were severely affected by bromine absorption/fluorescence at the wavelength (λ = 0.826210 (5) Å) used (see also chapter 3).

[**5.3·xH$_2$O·yDMF**: $a = b$ = 26.2098 (8) Å, c = 19.6392 (9) Å, V = 11683.7 (9) Å^3].

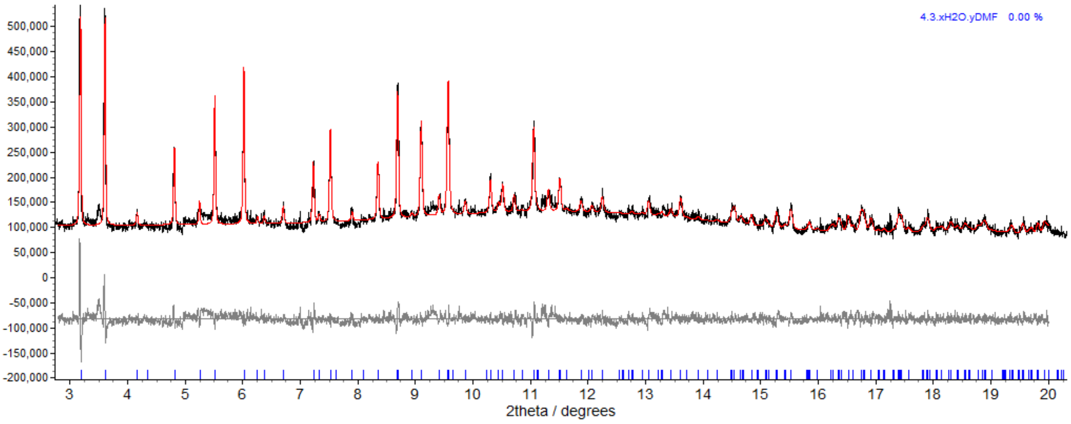

Figure 5.12. *Observed (black) and calculated (red) profiles and difference plot [I_{obs}-I_{calc}] (grey) of the Pawley refinement. (2θ range 2.8- 20 °, d_{min} = 2.37 Å).*

Pattern after 20 minutes of heating

The capillary was cut so as to be open at both ends (to allow flow of the hot N$_2$ stream and escape of solvent or gas. The capillary was heated using an Oxford Cryosystems Cryostream device, by ramping the temperature to 523 K. After 20 minutes, the gas stream temperature reached 523 K and the diffraction pattern was measured again.

The resultant powder pattern had lost a great deal of crystallinity, and the phase transformation to the new, unknown phase identified in section 5.2.3.8 had already occurred. Insufficient peaks could be identified in the pattern to facilitate indexing.

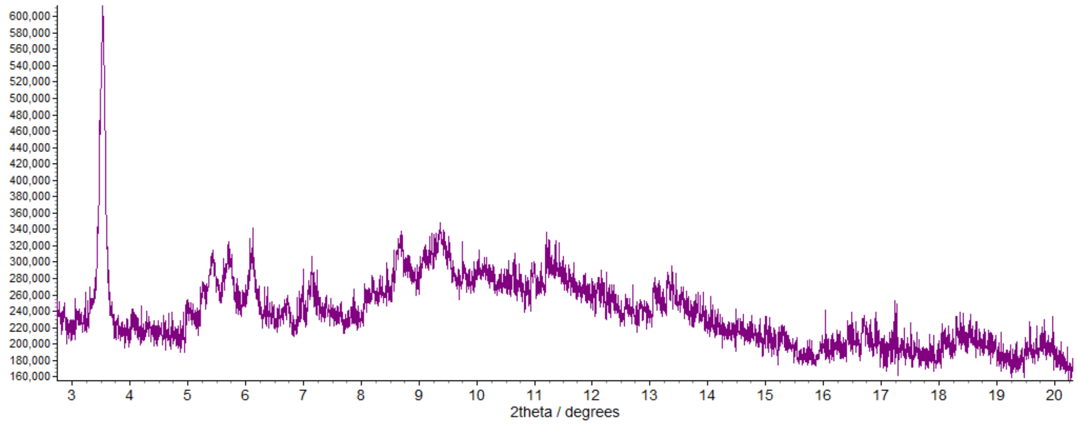

Figure 5.13. *Observed (purple) profile for the new material "**5.5**".*

5.2.4 Thermogravimetric analysis

5.2.4.1 As-synthesised 5.1·xH$_2$O·yDMF

The sample was heated from 25°C to 800°C, holding for 5 min at the start and end of the experiment. The initial mass loss of 16.7% corresponds to solvent loss. The rapid decrease in mass at 25 °C corresponds to loss of surface solvent on the crystals.

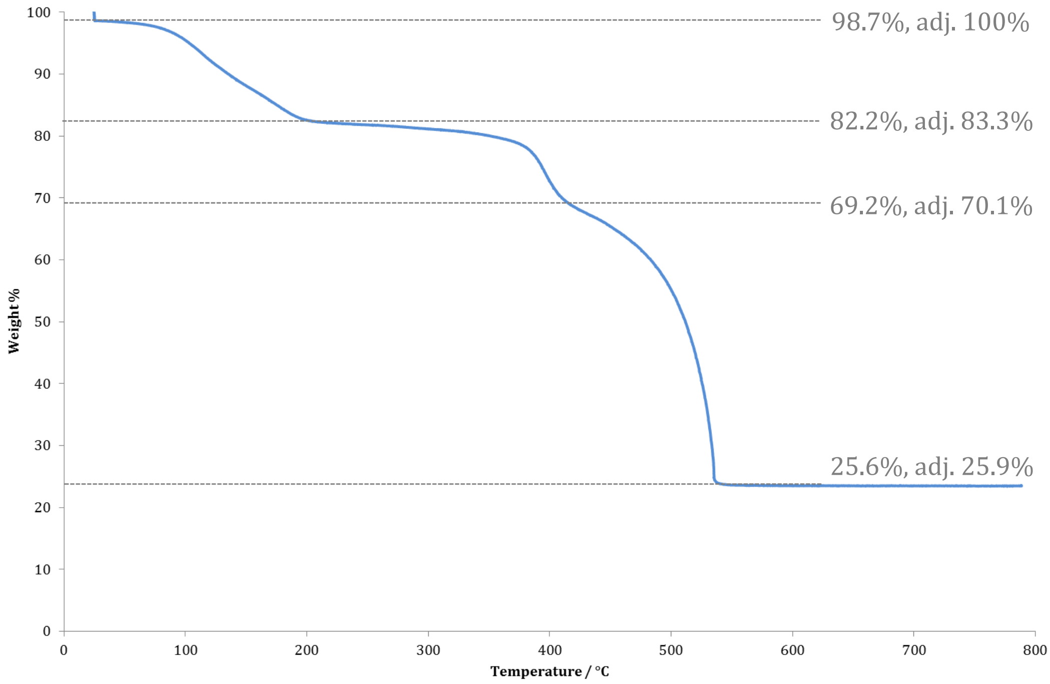

Figure 5.14. *Annotated thermogravimetric trace, for heating of the as-synthesised* ***5.1·xH$_2$O·yDMF****. "Adj." denotes mass % values adjusted for the initial loss of surface solvent on the crystals.*

5.2.4.2 As-synthesised 5.2·xH_2O·yDMF

The sample was heated from 25°C to 800°C, holding for 5 min at the start and end of the experiment. The initial mass loss of 14.1% corresponds to solvent loss.

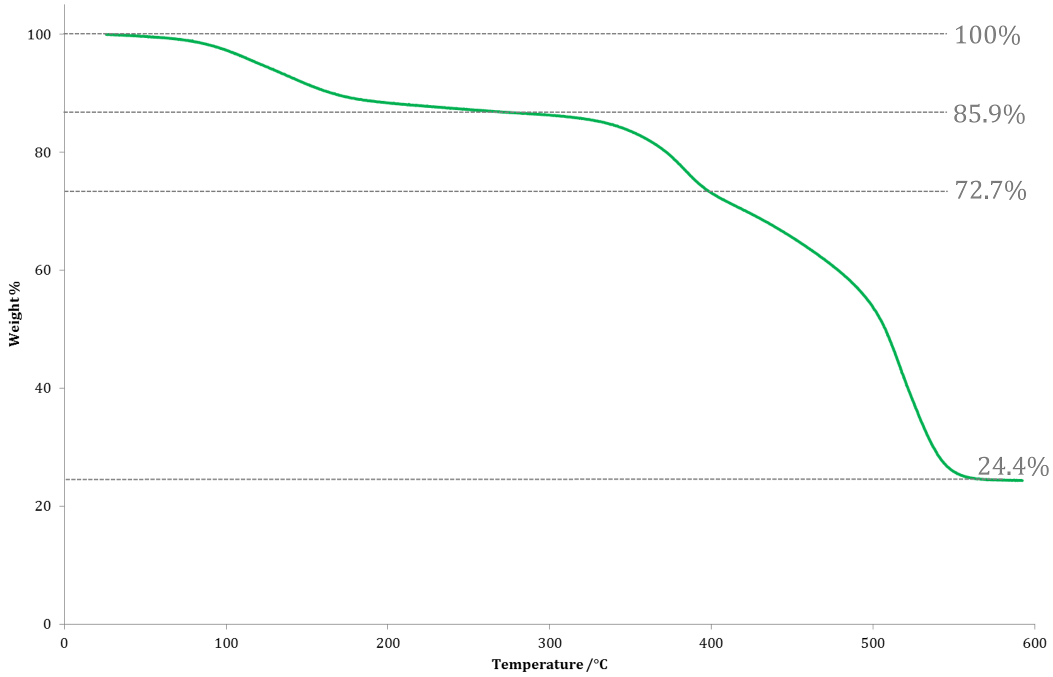

Figure 5.15. *Annotated thermogravimetric trace, for heating of the as-synthesised* ***5.2·xH_2O·yDMF****.*

5.2.4.3 As-synthesised 5.3·xH$_2$O·yDMF

The sample was heated from 25°C to 800°C, holding for 5 min at the start and end of the experiment. The initial mass loss of 19.7% corresponds to solvent loss.

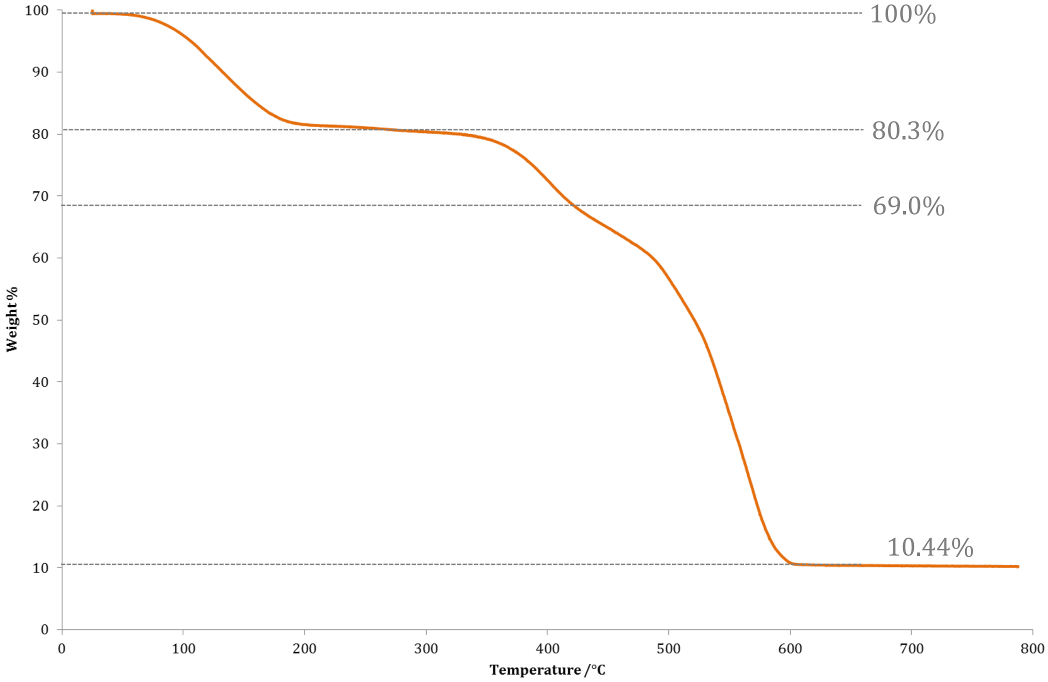

Figure 5.16. *Annotated thermogravimetric trace, for heating of the as-synthesised **5.3·xH$_2$O·yDMF**.*

5.2.4.4 As-synthesised 5.4·xH$_2$O·yDMF

The sample was heated from 25°C to 800°C, holding for 5 min at the start and end of the experiment. The initial mass loss of c.17.0% corresponds to solvent loss.

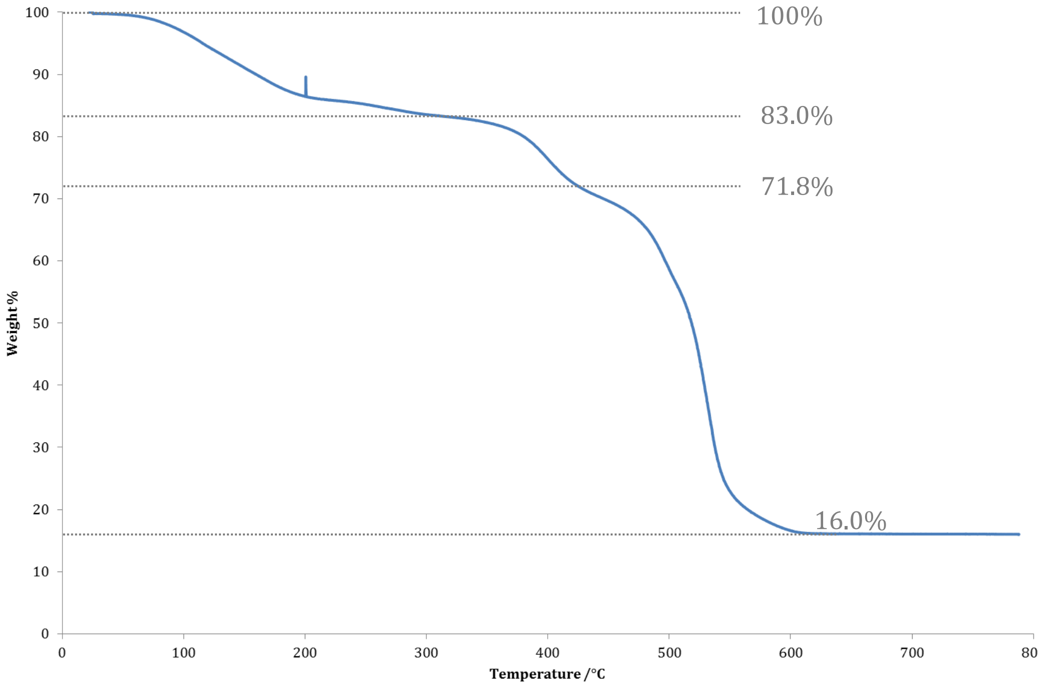

Figure 5.17. *Annotated thermogravimetric trace, for heating of the as-synthesised* ***5.4·xH$_2$O·yDMF****.*

5.2.5 Combined thermogravimetry-mass spectrometry (TGMS)

The crystalline **5.3·xH$_2$O·yDMF** was filtered from the mother liquor at the pump and were stored in sealed vials for at least one day before analysis. TGMS data were then collected using a Perkin–Elmer thermogravimetric analyser connected to a HPR20 QIC HIDEN mass spectrometer (ionisation method electron impact +). Samples were heated over the ranges specified in each case below, ramping at a rate of 5°C min^{-1}, under a flow of dry N$_2$ gas. TGMS traces are shown and discussed in section 5.3.3.1.

5.2.6 Solid-state NMR spectroscopy (SSNMR)

The crystalline solids of **5.3·aDCM**, **5.3·aDCM·bDBM** and **5.3·aDCM·bDIM** were filtered from the mother liquor at the pump and solid-state ^{13}C CP MAS NMR spectra were collected on a Bruker AV 500 MHz NMR spectrometer. In one instance, the cross-polarisation contact time was also allowed to vary and the spectrum recorded several times to study qualitatively the effect on signal intensity for the framework and guest(s). Annotated SSNMR spectra are shown and discussed in sections 5.3.2.1 and 5.3.2.3.

5.3 Results & discussion

5.3.1 Attempt to synthesise a family of isostructural ZIFs

Following the same synthetic conditions as used in the literature appeared to give not an isostructural series of ZIFs, and instead gave materials of unknown structure where the R- substituent on the benzimidazolate ligand was Me or I.

Using benzimidazole (synthesis of **5.1·xH$_2$O·yDMF**) or 5-bromobenzimidazole (synthesis of **5.3·xH$_2$O·yDMF**) as ligands in ZIF synthesis yielded the expected ZIF-69 topology (although **5.1·xH$_2$O·yDMF** was not phase-pure). However, using 5-methylbenzimidazole (synthesis of **5.2·xH$_2$O·yDMF**) or 5-iodobenzimidazole (synthesis of **5.4·xH$_2$O·yDMF**) appeared to give a new material of similar composition (given the presence of free ligand was not determined by assessing the powder diffraction patterns), but different crystalline phase.

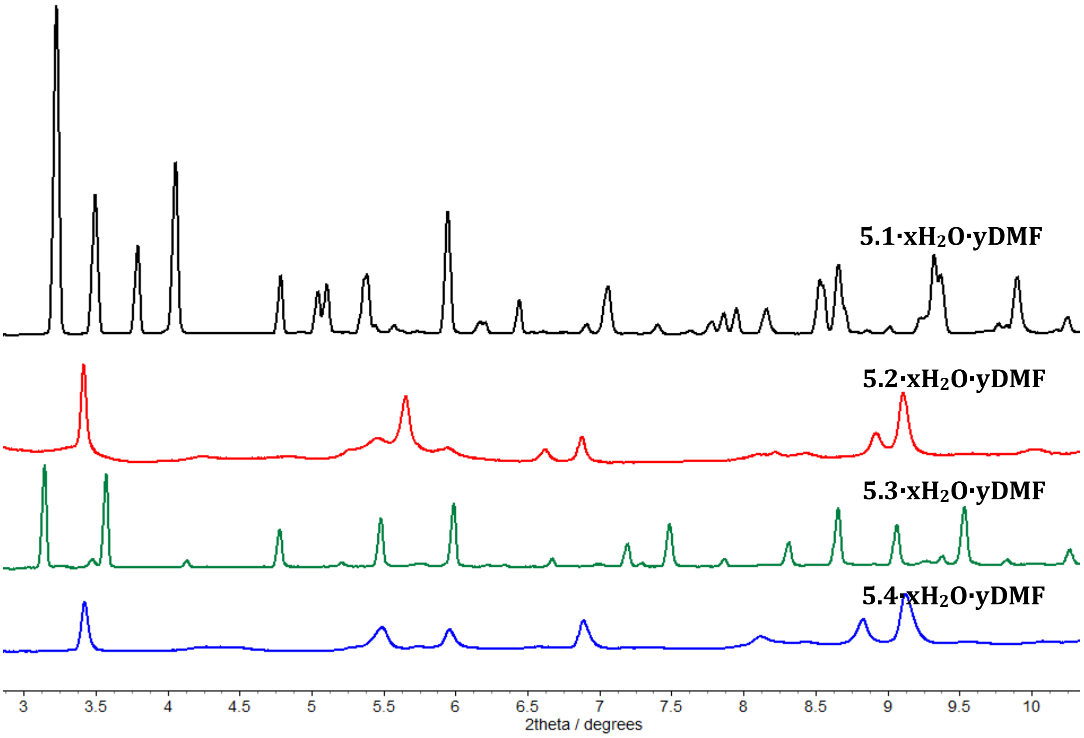

Figure 5.18. *Powder diffraction patterns of the as-synthesised* ***5.1·xH$_2$O·yDMF, 5.2·xH$_2$O·yDMF, 5.3·xH$_2$O·yDMF*** *and* ***5.4·xH$_2$O·yDMF****.*

The resultant materials **5.2** and **5.4** appeared to share largely the same powder diffraction patterns, and as such were thought to be the same phase. However, this material could not be indexed (too few reflections were found, crystallinity was low), and further structural studies could were not conducted. A small, unexpected peak at c. 3.5° 2θ in the powder pattern for **5.3** indicated the presence of a very small amount of this unknown phase.

Why the expected ZIF-69 phases could not be obtained is unknown. The literature procedure did not specify the heating and cooling times used for solvothermal synthesis, so whether this has any effect on the self-assembly of different ZIF topologies upon cooling is also unknown. In repeating exactly the procedure specified in section 5.2.1 consistent powder diffraction results (like those shown in Figure 5.18) were obtained, suggesting that minor fluctuations in individual experimental conditions are not likely to strongly affect the phases created.

As only the brominated ZIF **5.3** possessed the expected ZIF-69 topology, only this material was used for further guest uptake studies.

5.3.2 Dihalomethane uptake by 5.3, [Zn(NO_2im)(Brbim)]

The ability of the brominated ZIF **5.3** to uptake a series of dihalomethane guests was investigated, and the possibility of selective entrapment of diiodomethane or dibromomethane over dichloromethane was also explored. This was achieved by soaking crystals of the desolvated ZIF **5.3** in dichloromethane, a dichloromethane solution of dibromomethane or a dichloromethane solution of dioodomethane.

5.3.2.1 Solid state NMR

The presence of dihalomethane guests within the brominated ZIF **5.3** was successfully determined with solid state ^{13}C-SSNMR, and the annotated spectra are shown in Figures 5.19, 5.20 and 5.21.

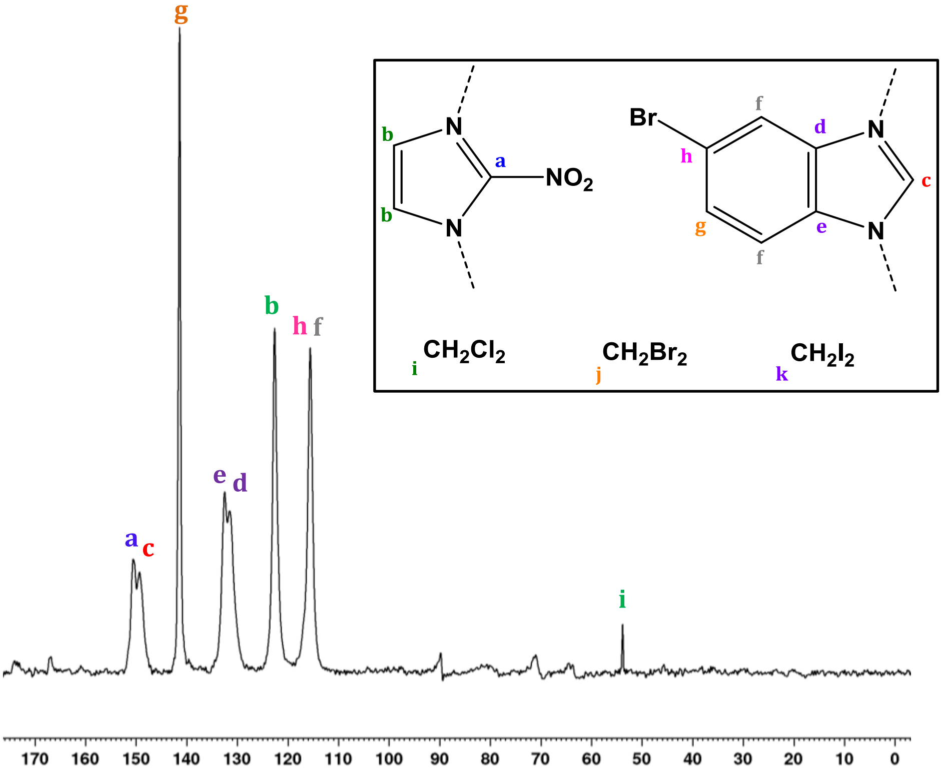

Figure 5.19. *Annotated solid-state CP-MAS* ^{13}*C-SSNMR of* ***5.3·aDCM****, after soaking crystals of* ***5.3*** *in dichloromethane. Notation for the assignment of signals is shown inset.*

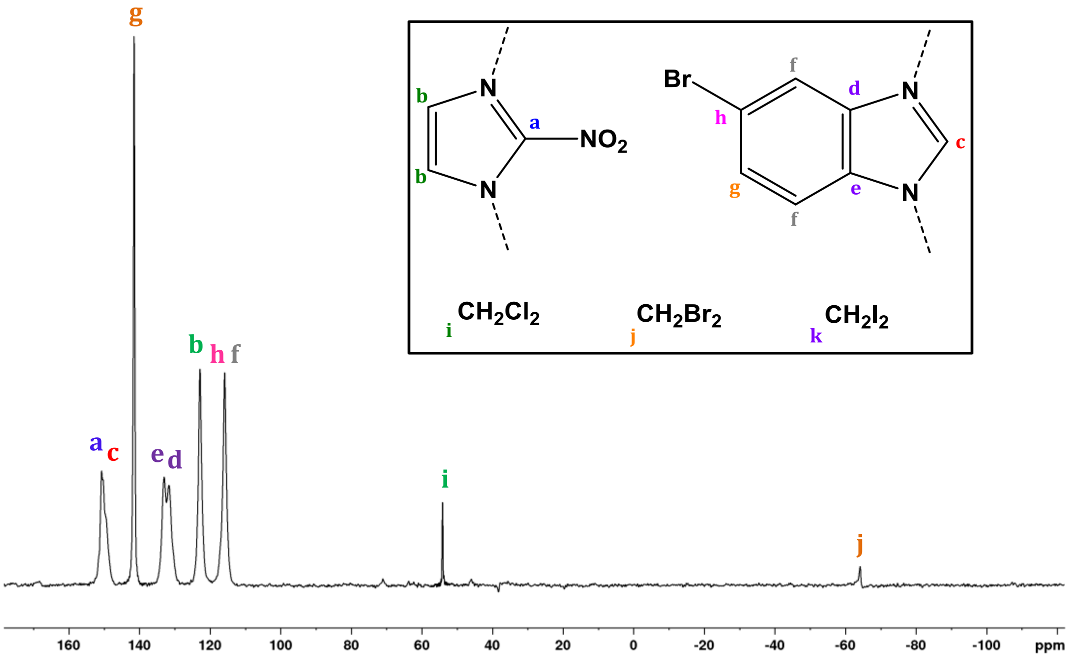

Figure 5.20. *Annotated solid-state CP-MAS* ^{13}*C-SSNMR of* ***5.3·aDCM·bDBM****, after soaking crystals of* ***5.3*** *in a dichloromethane solution of dibromomethane. Notation for the assignment of signals is shown inset.*

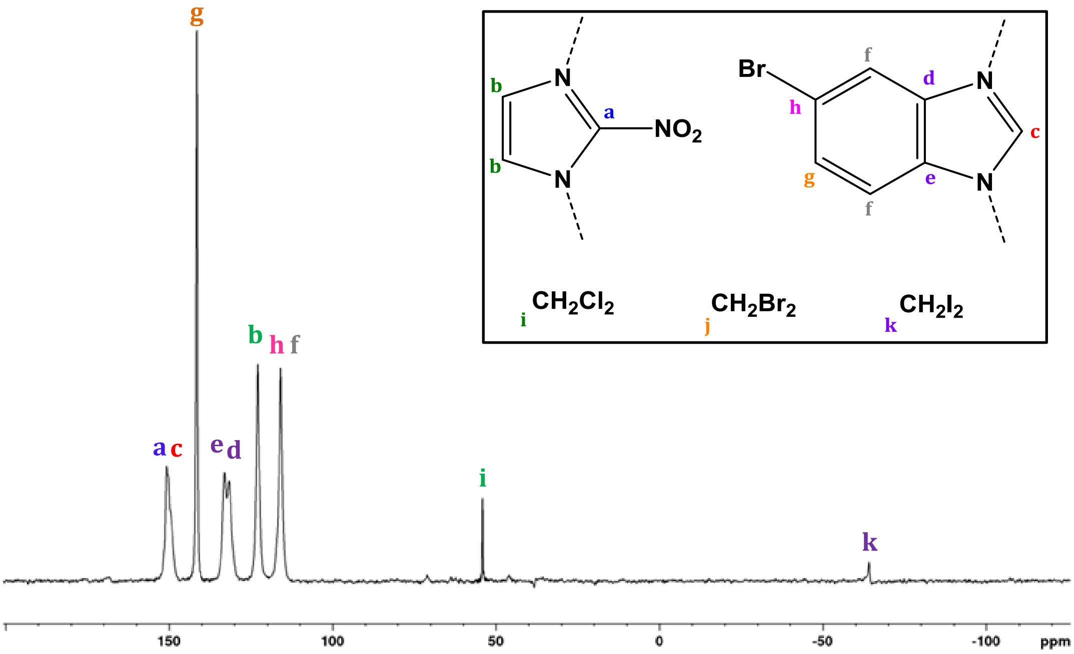

Figure 5.21. *Annotated solid-state CP-MAS ^{13}C-SSNMR of **5.3·aDCM·bDIM**, after soaking crystals of **5.3** in a dichloromethane solution of diiodomethane. Notation for the assignment of signals is shown inset.*

The SSNMR spectra show that all dihalomethane guests which the crystals of **5.3** were soaked in could be found within the framework, after soaking. This does not indicate that **5.3** is selective in its uptake of dihalomethane guests.

In the SSNMR, the intense and broad peaks for the framework ligands correspond well to rigid molecules, unable to easily undergo magnetic relaxation by rapid rotation (as in solution phase NMR). However the signals corresponding to solvent (i.e. in Figure 5.19, dichloromethane) are sharp, but weak. This indicates a guest which is more free to rotate and relax (more similar to conditions in the solution phase) on the timescale of the experiment. This indicates that the freely rotating dichloromethane is not bound rigidly to the surface of the pore through a particularly strong intermolecular interaction. The signals for the dibromomethane and diiodomethane guests are also weak, suggesting they are also not held in place strongly. The signals for dibromomethane and diiodomethane are, however, broader than those observed for dichloromethane within **5.3**.

5.3.2.2 Powder X-ray diffraction

The powder X-ray diffraction patterns of the materials **5.3·aDCM**, **5.3·aDCM·bDBM** and **5.3·aDCM·bDIM** (the materials resultant from dihalomethane soaking of framework **5.3**) were recorded, to determine the structural consequences of soaking. The powder diffraction patterns of the resultant materials (shown in section 5.2.3.2) do not indicate that a phase change takes place upon soaking ZIF **5.3** in dihalomethanes, and that the ZIF topology has been retained.

5.3.2.3 Variable contact time SSNMR spectroscopy

The usefulness of solid state NMR spectroscopy in probing the binding of guests within the host ZIF was investigated by running a variable contact-time cross-polarisation ^{13}C-SSNMR on **5.3·aDCM**. This was achieved by allowing different amounts of 'contact time' for transfer of polarisation to ^{1}H to ^{13}C, and recording the ^{13}C-SSNMR at these intervals. In comparing the relative intensities of signals obtained, the behaviour of the molecules in the solid state may be inferred. The resultant spectra are shown in Figure 5.22.

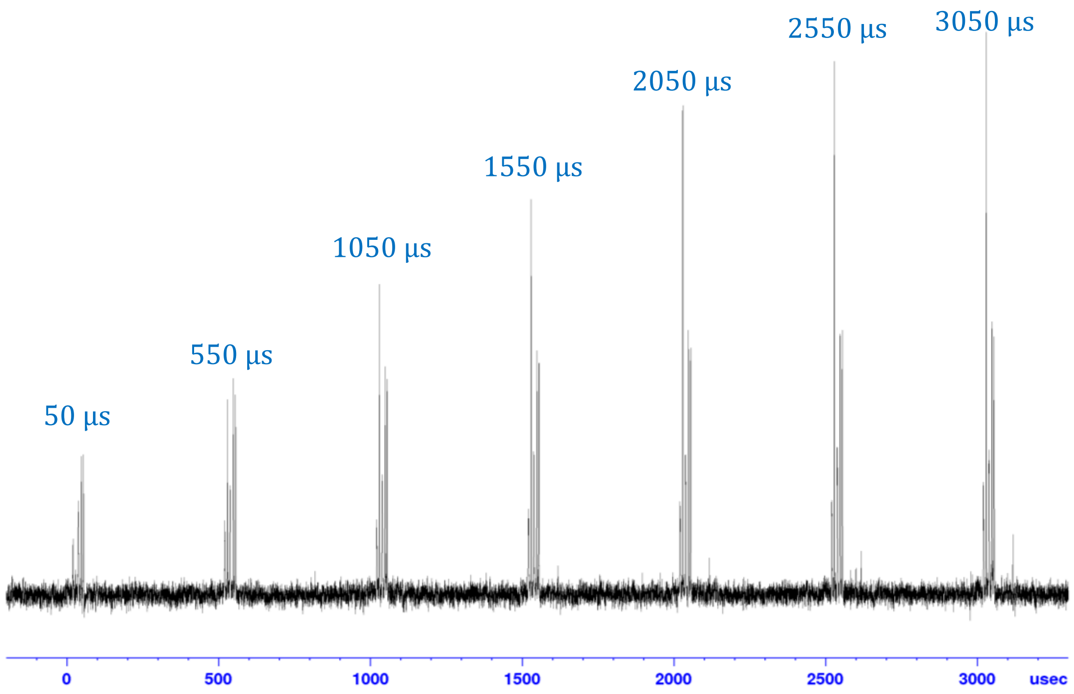

Figure 5.22. *Variable contact-time cross-polarisation ^{13}C-SSNMR of **5.3·aDCM** (therefore seven copies of the spectrum in Figure 5.19 are shown, at the relaxation times indicated above each spectrum here).*

To compare the growth of signals for the ZIF and the guest, the strongest, sharpest signal in the spectrum for the ligands was chosen for comparison. The relative intensity of the chosen signal corresponding to the framework (relative to its integral at 3050 μs contact time) was compared to that of the DCM carbon atom (relative to its integral at 3050 μs contact time). These integral values were plotted to demonstrate their growth with increasing contact time (shown in Figure 5.23).

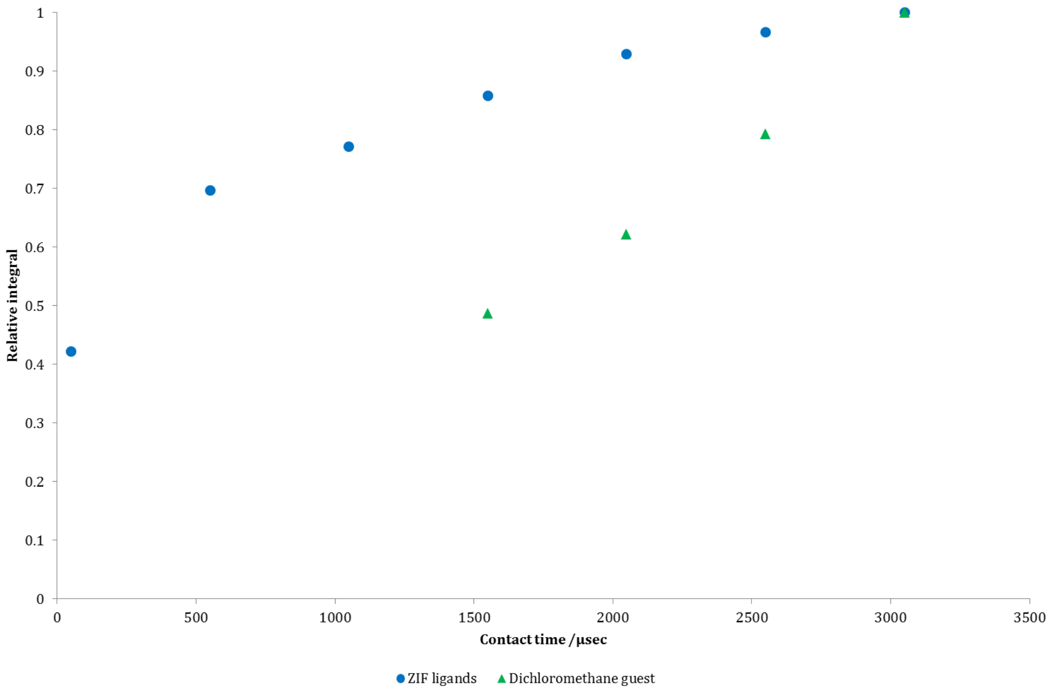

Figure 5.23. *Integral values for the strongest signal for the framework (relative to its integral value at 3050 μs contact time) and for the DCM carbon atom (relative to its integral value at 3050 μs contact time) in* ***5.3·aDCM****.*

The signals corresponding to the ZIF grow in rapidly in a natural logarithm-type profile, with the full set of expected ligand signals appearing after allowing just 550 μs of contact time. This suggests (as discussed in section 5.3.2.1) that there is a strong dipolar coupling between ligand ^{13}C atoms and neighbouring ^{1}H atoms, so cross-polarisation is rapid. Dipolar coupling of the ^{1}H and ^{13}C nuclei is weakened by distance and molecular motility. The ligands in the ZIF are not motile.

The slower, linear growth of the signal corresponding to DCM suggests much weaker dipolar coupling. It follows that, because the DCM guests within the pores are more motile (free to rotate and tumble in a 'liquid-like' fashion), their dipolar coupling is weaker. The ligands, being rigid and unable to move freely, therefore experience stronger dipolar coupling (and so faster polarisation transfer).

Due to the weak intensity of the DCM signal, this assessment may only be made qualitatively. If longer contact time was allowed (to give stronger signal growth and more data points), this could give better signal-to-noise ratios and would enable the plotting of more data points. In systems containing multiple guests (e.g. **5.3·aDCM·bDBM** and **5.3·aDCM·bDIM**), this could enable a comparison of the growth of the different guest signals.

5.3.3 Desolvation and thermal degradation of 5.3

Although thermogravimetric analysis is commonly used to demonstrate the desolvation of MOF materials, characterisation of the species being lost during desolvation is not common. In addition, complex features of thermogravimetric analysis traces such as mass losses possibly pertaining to loss of ligands or functional groups are difficult to correctly assign.

The thermogravimetric analysis trace for the as-synthesised **5.3·xH$_2$O·yDMF** displayed a mass loss of c. 19.7% (onset almost immediately at the start of the experiment), most likely corresponding to loss of DMF and water. A later mass loss of c. 11.3% (onset at c. 300°C) was observed. Based on the composition of the material, this corresponded well to the loss of NO_2, through denitration of the nitroimidazolate ligand (assuming the 19.7% mass loss is complete desolvation, NO_2 contributes c. 10% of the total sample mass).

To further characterise and remove ambiguity from these assignments, combined thermogravimetry-mass spectrometry, powder X-ray diffraction and infra-red spectroscopy were used. In particular the confirmation or rejection of the suggestion that **5.3** loses NO_2 upon heating was sought, given the notable health concerns of NO_2 release for human health.[18–22]

5.3.3.1 Combined thermogravimetry-mass spectrometry

A thermogravimetric analyser, from which the outgoing N_2 stream led to a mass spectrometer (EI+ ionisation) was used to characterise the mass fragments departing a sample of **5.3·xH$_2$O·yDMF**, heated gradually to 600°C. M/z ratios probed were 18 (for water), 46 (for NO_2) and 73 (for DMF). The set of combined TGMS traces are shown below, in Figures 5.24, 5.25 and 5.26.

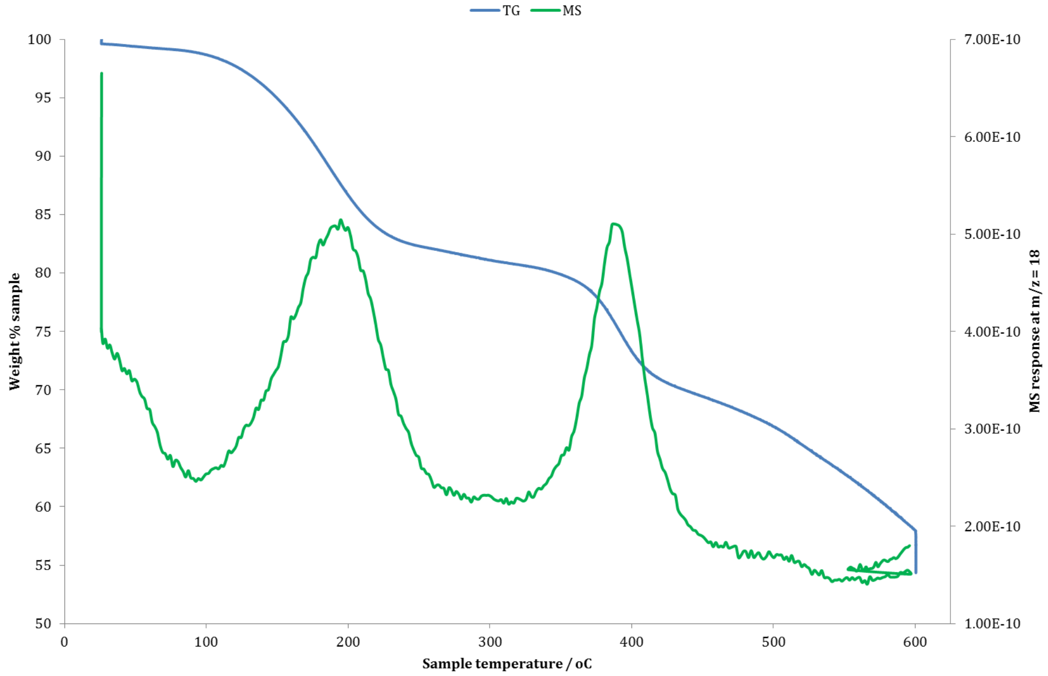

Figure 5.24. *TGMS trace for the as-synthesised* **5.3·xH_2O·yDMF**, *with mass spectrometer response at m/z 18 (water).*

There is a large mass spectrometer response for m/z 18 at the very beginning of the experiment, shown by the steep decline at T = 25°C, indicating a rapid loss of water. It also appears during the mass loss step up to c. 225°C. This could either be residual water within the material, or water as a potential breakdown product of DMF under electron impact. The large mass spectrometer response at c. 375°C is highly unlikely to correspond to water trapped in the framework, and is unexpected.

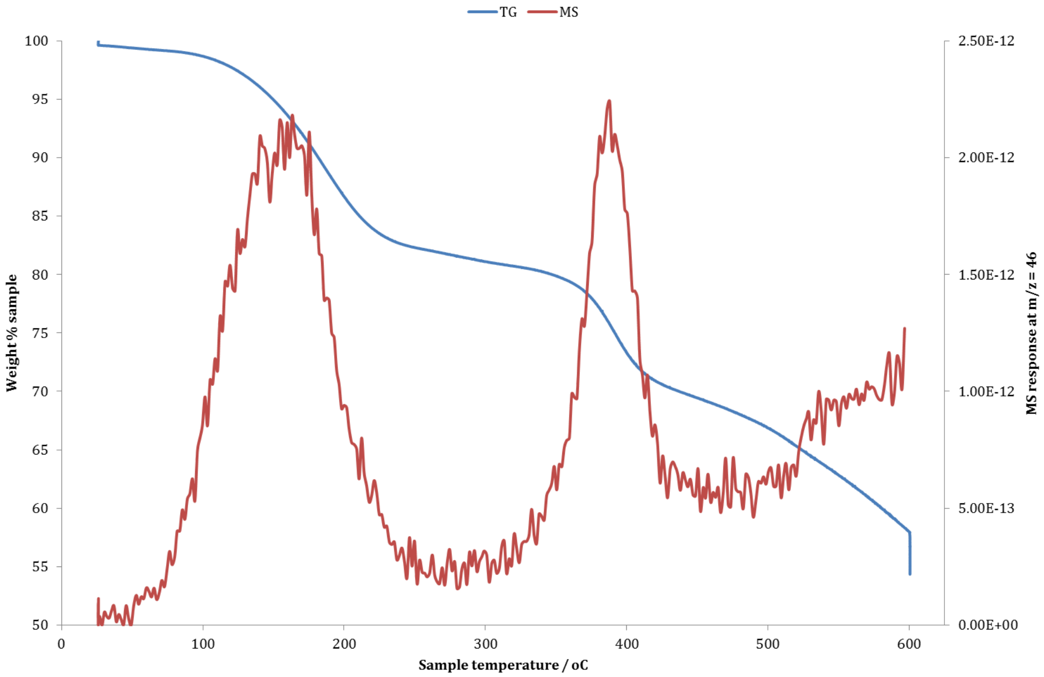

Figure 5.25. *TGMS trace for the as-synthesised* ***5.3·xH_2O·yDMF****, with mass spectrometer response at m/z 46 (NO_2).*

The mass spectrometer response for m/z 46 during the desolvation step may correspond to the hydrolysis of DMF, giving dimethylammonium ($H_2NMe_2^+$). This could be as a result of the DMF reacting with water as it departs the structure. The second, strong response during the mass loss onset at c. 350°C appears to suggest the evolution of NO_2, as previously hypothesised.

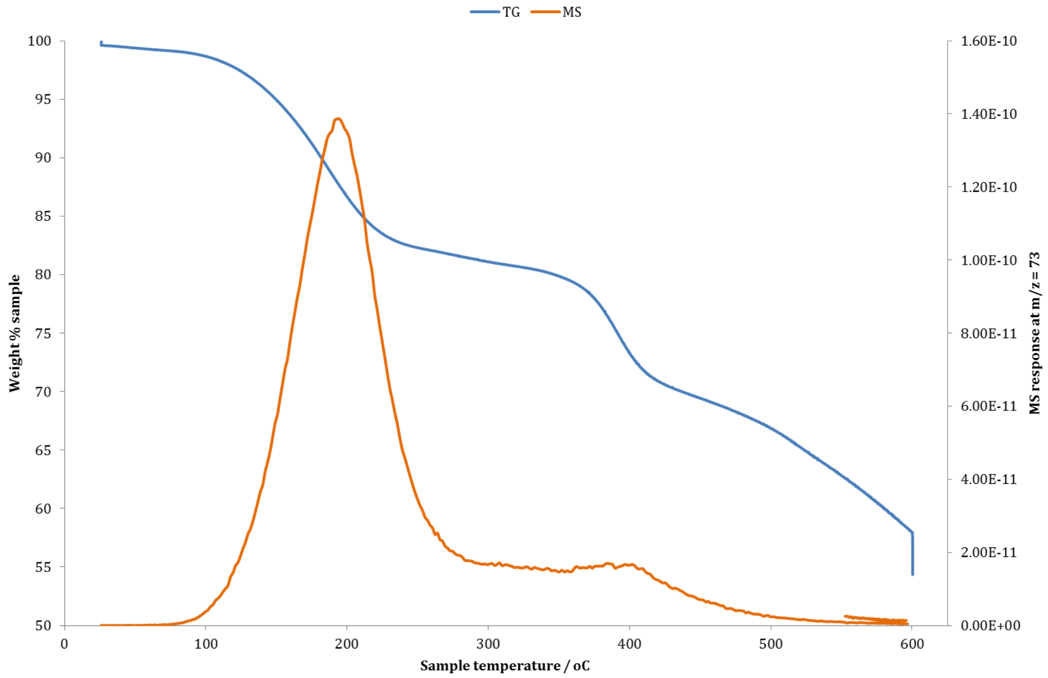

Figure 5.26. *TGMS trace for the as-synthesised* ***5.3·xH_2O·yDMF****, with mass spectrometer response at m/z 73 (DMF).*

As expected, a large loss of mass fragments of m/z 73 (corresponding to DMF) is found during the desolvation step. There appears not to be a significant mass spectrometer response at higher temperatures, though the observed mass spectrometer response for m/z 73 does not return to baseline levels until after 400°C. This could be caused by differential sample heating (i.e. the temperature across the whole sample may not be reflected by the recorded temperature), but is consistent across multiple samples, and multiple TGMS traces on the same sample.

The TGMS data demonstrated the loss of water and DMF during what was earlier identified as the desolvation step, and indicated that NO_2 was being lost during the mass loss after desolvation. However, the destructive electron-impact ionisation technique may have caused breakdown of larger molecules (solvent) which occlude these data. Further characterisation of the transformation taking place after desolvation was sought crystallographically and spectroscopically.

5.3.3.2 Following degradation of 5.3 with PXRD

In an attempt to further characterise this transformation, and to determine whether such a radical change to the ligand structure as a potential denitration would have further structural consequences on the ZIF, powder X-ray diffraction was used. Although heating framework materials to such high temperatures is not normally used, to prevent loss of crystallinity (see chapter 4 on desolvation and gas uptake in MOFs), some diffraction peaks were still observable.

Heating a sample of **$5.3{\cdot}xH_2O{\cdot}yDMF$** *ex situ* for four hours at 280°C (slightly lower than the observed onset temperature, to try to avoid loss of crystallinity) gave a material which was still crystalline. The powder X-ray diffraction patterns of the same batch of material before and after heating are shown in Figure 5.27.

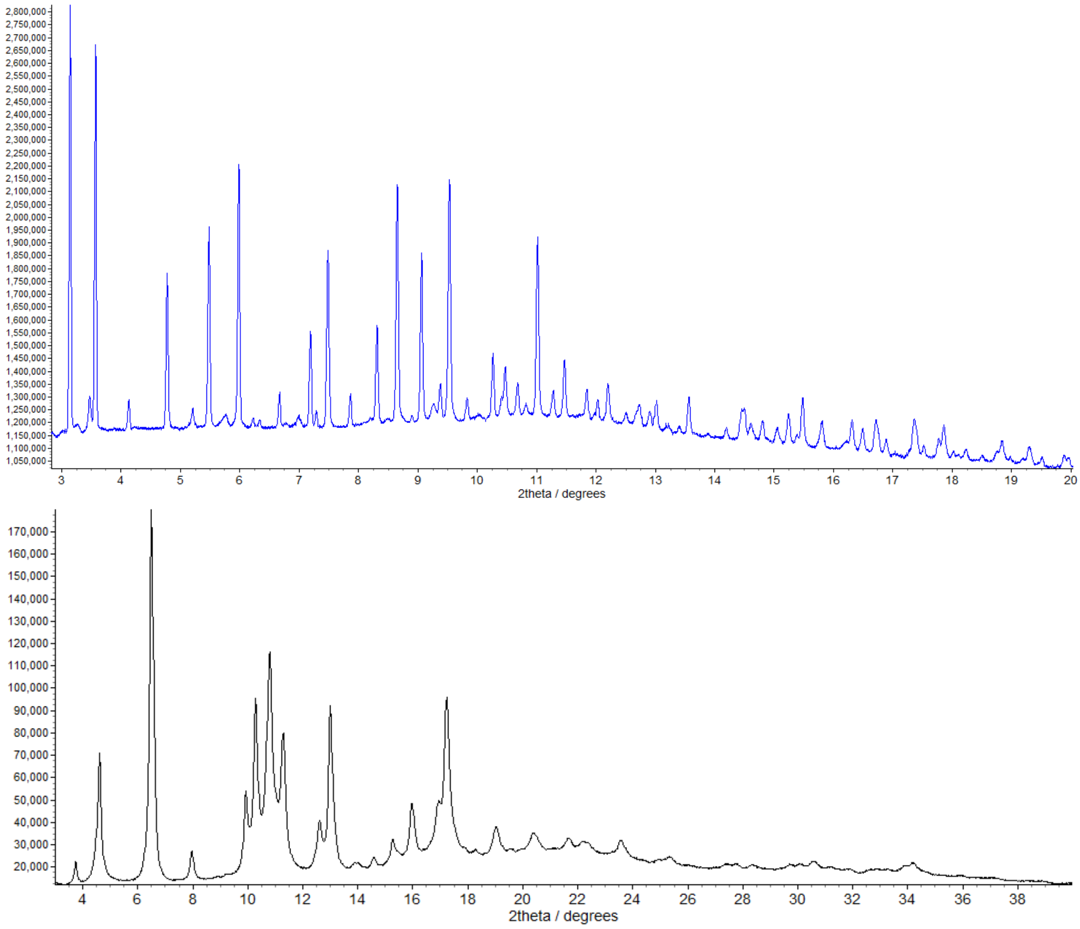

Figure 5.27. *Powder diffraction patterns of the as-synthesised* **$5.3{\cdot}xH_2O{\cdot}yDMF$** *before heating (top) and after heating (bottom).*

Clearly some phase transformation has taken place. However, the diffraction peaks for the new material whose pattern did not match any known ZIF phase, and could not be indexed to a sensible unit cell. This is likely because there are too few diffraction peaks (loss of crystallinity), but could alternatively be due to the presence of multiple crystalline phases. This hitherto unknown material is referred to as **"5.5"** from this point onward.

The structural rearrangement upon heating the ZIF to 280°C is not unexpected, as ZIF materials have been shown to be flexible in response to heat and cooling in the literature. Indeed, some ZIF materials are being explored as custom glasses due to their ability to form multiple distinct phases upon heating,[23–27] as characterised by ^{15}N-SSNMR data.

An *in situ* powder X-ray diffraction heating study was conducted to try to identify any intermediate phases formed upon NO_2 loss, and if the formation of the unknown phase was reproducible. The powder pattern progression is shown in Figure 5.28.

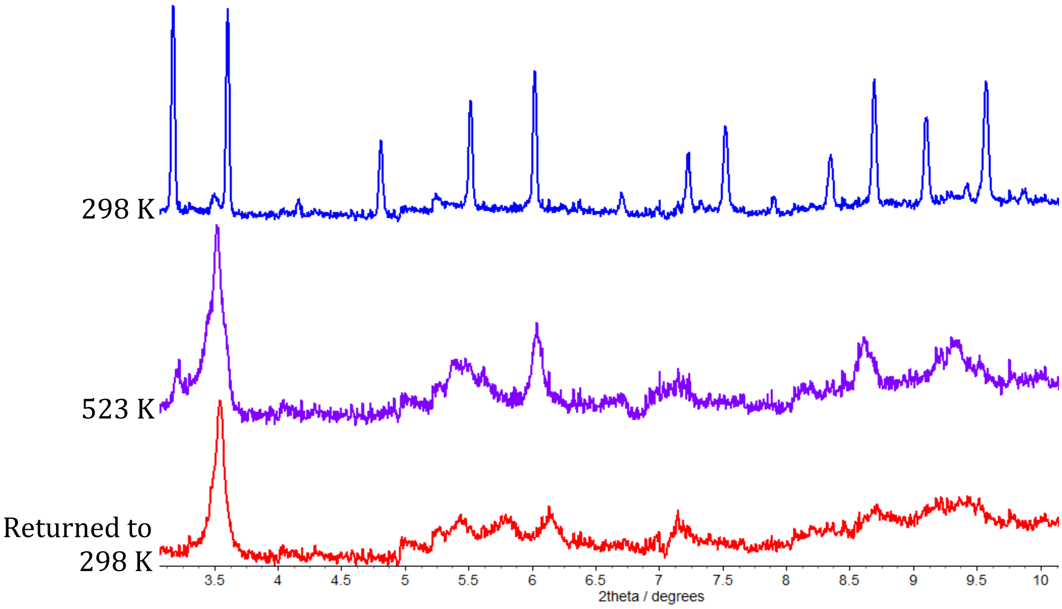

Figure 5.28. *X-ray powder diffraction pattern progression for the heating of* ***5.3·xH_2O·yDMF*** *to remove solvent and NO_2, forming an unknown phase.*

The phase change took place rapidly (less than 20 mins) and as such the presence of any intermediate phases was not identified. Crystallinity appeared to be worse than in the *ex situ* heating study, though whether this was due to the rapid heating or bromine X-ray fluorescence problems (as in the *in situ* study on compound **2.1** in chapter 3) is unknown.

5.3.3.3 Following degradation of 5.3 with IR spectroscopy

To attempt to further understand the structural consequences of the transformation taking place upon heating (and to confirm or refute the loss of NO_2), infra-red spectroscopy was used. The parent ZIF **5.3·xH_2O·yDMF** was heated at 280°C for four hours, and a second sample was heated to 400°C for one hour, and the infra-red spectra before and after heating were compared. The resultant spectra are shown in Figure 5.29.

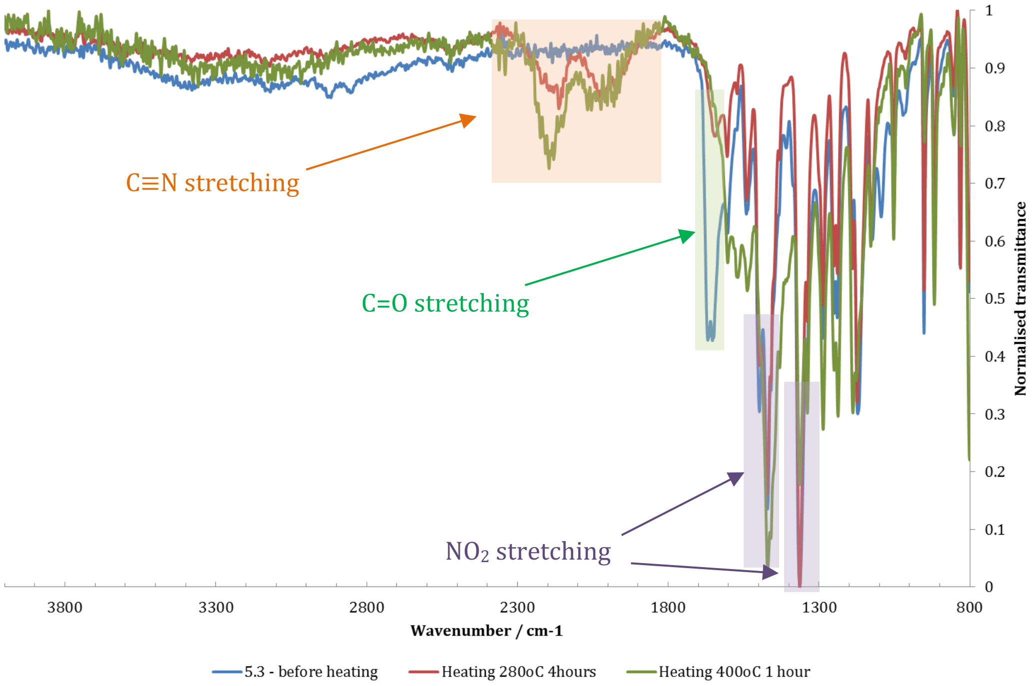

Figure 5.29. *Infra-red ATR spectra of **5.3·xH_2O·yDMF** (before heating, blue) and the resultant **"5.5"** (after heating a sample of **5.3·xH_2O·yDMF** to 280°C for four hours, red; or heating a separate sample to 400°C for one hour, green). Annotations indicating relevant IR regions are also added for discussion.*

The loss of intensity of the stretching band for C=O at 1668 cm^{-1} after heating represents the loss of the DMF solvent. However the strong N–O stretching bands for NO_2 (asymmetric 1470 cm^{-1}, symmetric 1365 cm^{-1}), matching closely to those for the free ligand,[28] were unchanged even by heating **5.3** to 400°C (forming **"5.5"** – the new material).

The growth of two broad bands in the C≡N stretching region may suggest that upon the phase change to **"5.5"**, the bonding character of some C–N bonds in the imidazolate ligands is increased as a result of the phase change. Details on the electron transfer necessary to achieve this, and structural implications for the framework are however unclear from the IR spectrum.

The identity of the mass fragment m/z 46, identified in the TGMS trace does not correspond to NO_2, based on the infra-red spectroscopy evidence. This could instead correspond to residual dimethylammonium (also m/z 46), also suggested to be present in the TGMS trace during desolvation. However without further characterisation the exact identity of this specie is still unknown.

5.4 Conclusions & Future work

5.4.1 Dihalomethane uptake in ZIFs

Two isostructural ZIF materials [Zn(NO_2im)(bim)] **5.1** and [Zn(NO_2im)(Brbim)] **5.3** based on substituted benzimidazolate ligands have been synthesised. Solid state NMR has been used to study the guest uptake of dihalomethanes within the phase pure **5.3**. Crystals of the halogenated ZIF material appeared by SSNMR to uptake all dihalomethanes that it was soaked in, with no apparent selectivity.

Future work on these materials would ideally proceed with an isostructural series of hosts so as to better understand the nature of any possible selectivity for different guests. The synthesis methods given in section 5.2.1 consistently gave the same unknown materials as opposed to those reported in the literature.

The variable contact-time cross-polarisation technique has been used to demonstrate in principle the identification of components which are rigid (ligands within a framework) and those which are flexible and liquid-like (guests weakly bound within a pore).

This technique could potentially be applied to the study of mixed-guest systems (for example, **5.3·aDCM·bDIM**) to study the nature of binding of different guests. If a guest is strongly bound to the walls of the host (i.e. stronger intermolecular interactions hold the guest in place, more rigidly) then the dipolar coupling of this would be stronger than a weakly held guest. Therefore there would be notable differences in the growth of the guest signals with increased contact time. Whether or not this would produce quantitative data would depend on the strength of the signals involved. In the case of materials such as **5.3·aDCM·bDIM**, this may require unfeasibly long experiments.

5.4.2 Characterising desolvation and degradation of ZIFs

The desolvation of brominated ZIF material **5.3·xH_2O·yDMF** was followed by TGMS, and the loss of DMF and water were successfully observed.

Mass spectrometry evidence initially suggested the loss of NO_2 upon the heating of **5.3**, due to the observation of a loss of ions of m/z 46, coincident with a mass loss in the thermogravimetric analysis trace that also suggested NO_2 loss. This was also shown to be accompanied by a phase change and a great degree of loss of crystallinity. The new phase formed upon degradation of framework **5.3** (the new phase named "**5.5**") did not match any of the existing ZIF phases noted in this chapter, or in the literature. Infra-red spectroscopy however suggested that loss of NO_2 from the nitroimidazolate ligands was not taking place during heating, and the identity of the species lost during the transformation could not be confirmed.

Further work at analysing the release of solvent, gases and mass fragments from MOF materials could utilise *in situ* infra-red spectroscopy. Through the use of a double-walled IR cell (see Figure 5.30), the evolution of IR-active gases with heat can be monitored *in situ* as they are generated. This has been successfully applied previously by the Brammer group to study the release of HCl and coordinated alcohol molecules as vapour from coordination polymers.[29,30]

Figure 5.30. *The double-walled IR gas cell for used in in-situ vapour/gas release studies.*

5.5 References

1 C. M. McGuirk, M. J. Katz, C. L. Stern, A. A. Sarjeant, J. T. Hupp, O. K. Farha and C. A. Mirkin, *J. Am. Chem. Soc.*, 2015, **137**, 919–925.

2 P. W. Siu, Z. J. Brown, O. K. Farha, J. T. Hupp and K. A. Scheidt, *Chem. Commun.*, 2013, **49**, 10920–10922.

3 X. W. Dong, T. Liu, Y. Z. Hu, X. Y. Liu and C. M. Che, *Chem. Commun.*, 2013, **49**, 7681–7683.

4 A. A. Tehrani, S. Abedi, A. Morsali, J. Wang and P. C. Junk, *J. Mater. Chem. A*, 2015, **3**, 20408–20415.

5 P. Borah, J. Mondal and Y. Zhao, *J. Catal.*, 2015, **330**, 129–134.

6 B. Chen, L. Wang, F. Zapata, G. Qian and E. B. Lobkovsky, *J. Am. Chem. Soc.*, 2008, **130**, 6718–6719.

7 Z. Zhao, J. Hao, X. Song, S. Ren and C. Hao, *RSC Adv.*, 2015, **5**, 49752–49758.

8 L. Liu, J. Hao, Y. Shi, J. Qiu and C. Hao, *RSC Adv.*, 2015, **5**, 3045–3053.

9 P. Kanoo, A. C. Ghosh, S. T. Cyriac and T. K. Maji, *Chem. Eur. J.*, 2012, **18**, 237–244.

10 M. Sadakiyo, T. Yamada and H. Kitagawa, *J. Am. Chem. Soc.*, 2011, **133**, 11050–3.

11 Q. Zhang, J. Yu, J. Cai, R. Song, Y. Cui, Y. Yang, B. Chen and G. Qian, *Chem. Commun.*, 2014, **50**, 14455–14458.

12 K. Tan, S. Zuluaga, Q. Gong, Y. Gao, N. Nijem, J. Li, T. Thonhauser and Y. J. Chabal, *Chem. Mater.*, 2015, **27**, 2203–2217.

13 R. Banerjee, A. Phan, B. Wang, C. Knobler, H. Furukawa, M. O'Keeffe and O. M. Yaghi, *Science*, 2008, **319**, 939–943.

14 T. Panda, K. M. Gupta, J. Jiang and R. Banerjee, *CrystEngComm*, 2014, **16**, 4677–4680.

15 S. P. Thompson, J. E. Parker, J. Potter, T. P. Hill, A. Birt, T. M. Cobb, F. Yuan and C. C. Tang, *Rev. Sci. Intrum.*, 2009, **80**, 075107.

16 S. P. Thompson, J. E. Parker, J. Marchal, J. Potter, A. Birt, F. Yuan, R. D. Fearn, A. R. Lennie, S. R. Street and C. C. Tang, *J. Synchrotron Rad.*, 2011, **18**, 637–648.

17 G. S. Pawley, *J. Appl. Crystallogr.*, 1981, **14**, 357–361.

18 J. M. Samet, F. Dominici, F. C. Curriero, I. Coursac and S. L. Zeger, *N. Engl. J. Med.*, 2000, **343**, 1742–1749.

19 B. Brunekreef and S. T. Holgate, *Lancet*, 2002, **360**, 1233–1242.

20 U. Ackermann-Liebrich, H. R. Anderson, T. Bellander, J. Brain, B. Brunekreef, A. Cohen, E. Dybing, F. Forastiere, J. Heinrich, U. Heinrich, S. T. Holgate, K. Katsouyanni, F. J. Kelly, M. Lippmann, R. Maynard, J. Pekkanen, A. Peters, R. Rapp, R. O. Salonen, J. Samet, B. Seifert, J. Sunyer, J. Vandenberg, H. Walton and H. E. Wichmann, *Health Aspects of Air Pollution with Particulate Matter, Ozone and Nitrogen Dioxide: WHO working group at Bonn*, 2003.

21 R. D. Brook, B. Franklin, W. Cascio, Y. Hong, G. Howard, M. Lipsett, R. Luepker, M. Mittleman, J. Samet, S. C. Smith Jr and I. Tager, *Circulation*, 2004, **109**, 2655–2671.

22 M. Kampa and E. Castanas, *Environ. Pollut.*, 2008, **151**, 362–367.

23 T. D. Bennett, A. L. Goodwin, M. T. Dove, D. A. Keen, M. G. Tucker, E. R. Barney, A. K. Soper, E. G. Bithell, J.-C. Tan and A. K. Cheetham, *Phys. Rev. Lett.*, 2010, **104**, 115503.

24 T. D. Bennett, P. Simoncic, S. A. Moggach, F. Gozzo, P. Macchi, D. a Keen, J.-C. Tan and A. K. Cheetham, *Chem. Commun.*, 2011, **47**, 7983–7985.

25 T. D. Bennett and A. K. Cheetham, *Acc. Chem. Res.*, 2014, **47**, 1555–1562.

26 E. F. Baxter, T. D. Bennett, C. Mellot-Draznieks, C. Gervais, F. Blanc and A. K. Cheetham, *Phys. Chem. Chem. Phys.*, 2015, **17**, 25191–25196.

27 M. T. Wharmby, S. Henke, T. D. Bennett, S. R. Bajpe, I. Schwedler, S. P. Thompson, F. Gozzo, P. Simoncic, C. Mellot-Draznieks, H. Tao, Y. Yue and A. K. Cheetham, *Angew. Chem. Int. Ed. Engl.*, 2015, **54**, 6447–6451.

28 L. V Epishina, V. I. Slovetskii, V. G. Osipov, O. V Lebedev, L. I. Khmel’nitskii, V. V Sveost’yanova and T. S. Novikova, *Kimya Geterotsiklicheskikh Soedinenii*, 1967, **3**, 716–723.

29 G. M. Espallargas, M. Hippler, A. J. Florence, P. Fernandes, J. Van De Streek, M. Brunelli, W. I. F. David, K. Shankland and L. Brammer, *J. Am. Chem. Soc.*, 2007, **129**, 15606–15614.

30 I. J. Vitórica-Yrezábal, S. Libri, J. R. Loader, G. Mínguez Espallargas, M. Hippler, A. J. Fletcher, S. P. Thompson, J. E. Warren, D. Musumeci, M. D. Ward and L. Brammer, *Chem. Eur. J.*, 2015, **21**, 8799–8811.

Metal pyrazolate coordination polymers:

Flexibility and hydrogen bonding

6

Chapter Six

6.1 Introduction

6.1.1 'Flexible' MOFs

Although many examples exist of the pore space of MOFs being modified (post-synthetic modification, see section 1.3.1.3),[1–4] change in the actual shape of the pore in response to a guest is still a relatively uncommon phenomenon in MOFs.[5–7] The notable examples in MOF research include the MIL (Materials Institute Lavoisier) series and the benzenedipyrazolate MOFs [M(bdp)].[8–12]

These MOFs show a responsiveness to the addition or removal of guest molecules (solvent or gas) accompanied by marked phase transitions. In perhaps the most well-known case, MIL-53, the empty MOF is found to abstract water from the air, facilitating a massive change in the profile of the one-dimensional channels (see Figure 6.1).[8]

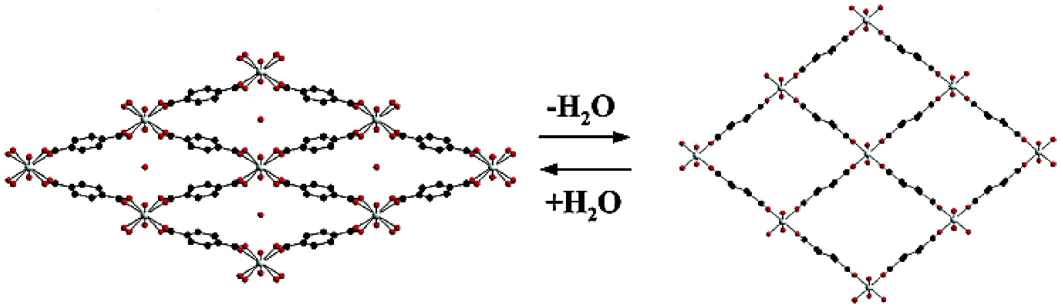

Figure 6.1. *Two of the phases of the flexible MOF MIL-53, [Cr^{III}(OH)(bdc)].guest. On the left, the hydrated phase, and on the right, the open-pore empty high-temperature phase. Figure reproduced from reference 8.*

This causes the framework to close, and once the solvent is removed thermally, the framework re-opens. Work to rationalise the effect of the water on the pore-opening/closing behaviour of these MOFs has shown that favourable host-guest interactions (hydrogen bonds) are formed.[9] These hydrogen bonds between water and the bdc ligands are what facilitate the closing of the framework, and therefore once the water is removed, no strong framework-framework interaction exists to hold the pore closed.

Depending on the metal ion used in the construction of the framework, the number of different phases accessible has also been shown to change. In the case of the analogous Fe^{III} framework, different levels of CO_2 uptake are shown to support at least four distinct phases of the MOF with different degrees of pore opening.[13] Different quantities of guest adsorbed engender different balances of interactions, where at lower CO_2 pressures framework-guest interactions are predominant, but at higher pressures, guest-guest interactions (as in solid CO_2) dominate.

The hydrophobic MOF [Co(bdp)]·guest has been shown by Long and co-workers to also display a guest-dependent flexibility.[11,12] Upon desolvation the pores of the MOF are shown to collapse (see Figure 6.2), facilitated by both twists in the ligand and a flattening of the coordination geometry about Co from tetrahedral to square planar.

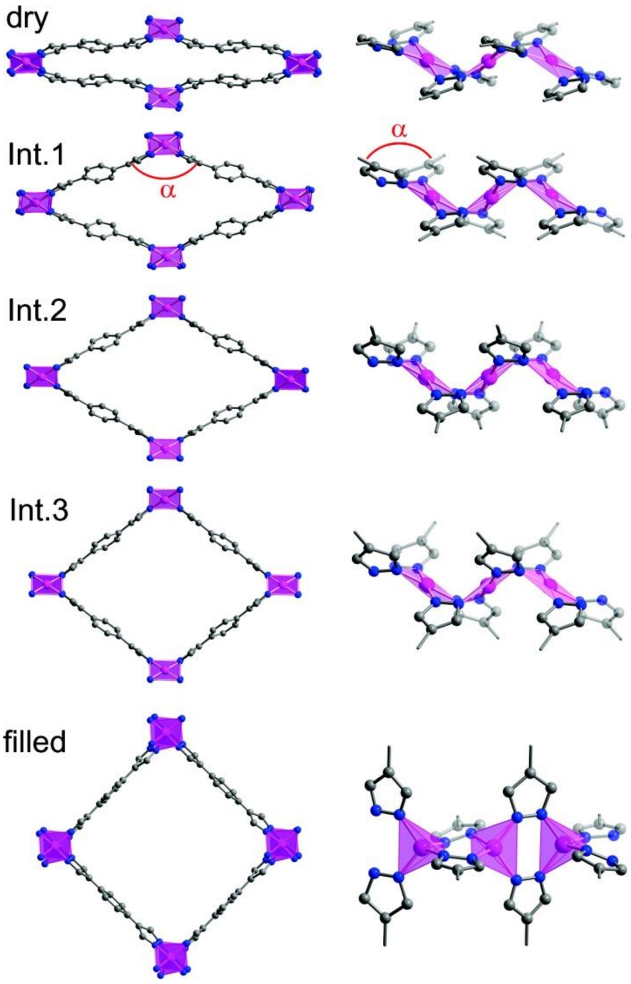

Figure 6.2. *Flexiblity of [Co(bdp)], showing five distinct crystallographic phases based on twisting of the ligands and flattening of the coordination environment around* Co^{II}*, during the uptake of* N_2*. Figure reproduced from reference 12.*

The [M(bdp)] (M = Zn, Ni) MOF system has also shown interesting activity in the uptake of volatile organic compounds (VOCs),[14] with the hydrophobic channels being capable of selective uptake of thiophene even in the presence of water. In these systems, the structural flexibility shown in [Co(bdp)] also appears to be present, however its role in the selectivity is not made clear.

Interestingly, the flexible behaviour of these two MOF systems appears to be limited to a ‘snapping’ behaviour – where a handful of discrete known phases exist for the MOFs, with different levels of pore openness. This is opposed to a continuous ‘breathing’ or ‘swelling’ motion. This may be due to the formation of favourable framework-guest or framework-framework interactions at each of these discrete steps/phases. To date, only one example of MOF flexibility which might be considered continuous is known, which is also from the MIL family of MOFs, MIL-88.[10] This material, as well as showing distinct and vastly different phases dependent upon the pore contents, also shows a continuous ‘swelling’ of some of these phases. With different solvent guests inside the pore (rather than different amounts of gas, or different amounts of the same solvent), structures of the same phase but slightly different pore openness were observed.

6.1.2 The bipyrazole ligand H_2bpz

The bipyrazole ligand 3,3’,5,5’-tetramethyl-4,4’-bipyrazole **H_2bpz** has been shown to be an interesting tecton for crystal engineering due to its twisted geometry, and its ability to donate and receive several hydrogen bonds. The crystal structure of the monohydrate, **H_2bpz·H_2O**, demonstrates these properties.[15] The steric bulk of the four methyl groups cause the ligand to twist about the central C–C bond. Hydrogen bonding between the ligands then leads to the formation of helices, as shown in Figure 6.3.

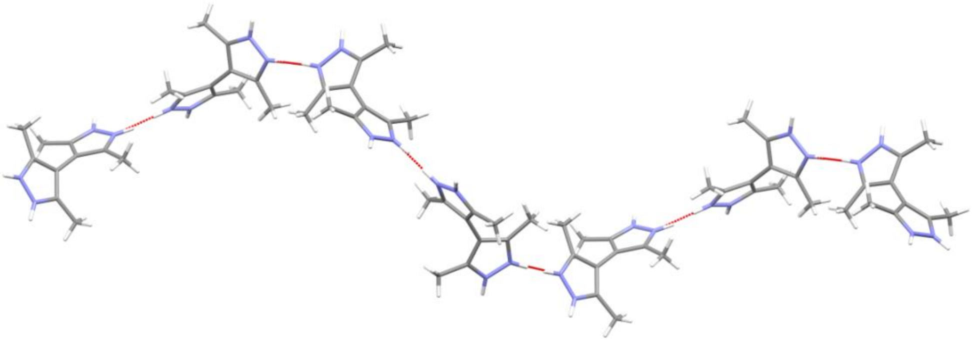

Figure 6.3. *Hydrogen-bonded helices of* ***H_2bpz*** *in the crystal structure of* ***H_2bpz·H_2O*** *(water molecules not shown for clarity). Note that disorder of the N–H protons exists across all four possible sites in the molecule.*

This hydrogen-bonding ability has also successfully been applied to the crystal engineering of coordination polymers, where **H_2bpz** was employed as a co-ligand to various dicarboxylates.[16–19] This has included the replacement (or partial replacement) of carboxylate ligands in well-known MOF systems (such as MOF-5),[17,19] and the cooperative inter- and intra-molecular hydrogen bonding within coordination polymers containing both **H_2bpz** and dicarboxylate ligands.[16,18] In one such piece of work, authors demonstrated the role of intramolecular hydrogen bonding by **H_2bpz** in directing the formation of different arrangements of the ligands about flexible d^{10} metal centres, supporting a paddlewheel secondary building unit (SBU) (as shown in Figure 6.4).

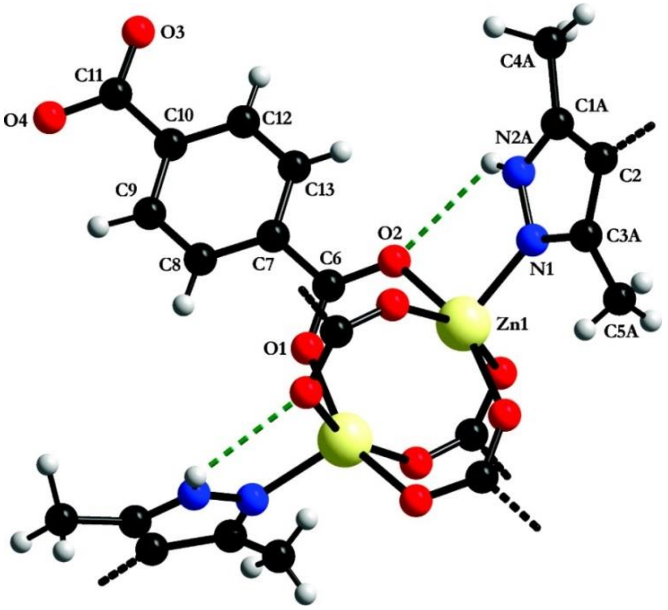

Figure 6.4. *Intramolecular hydrogen bonding by* ***H_2bpz*** *in the MOF [Zn_2(bdc)$_2$ (H_2bpz)], directing formation of the paddlewheel SBU. Figure reproduced from reference 18.*

These examples indicate that **H_2bpz** may be an interesting ligand to use for crystal engineering applications.

6.1.3 Chapter aims

Work in this chapter was aimed at synthesising MOF materials from **H_2bdp** and **H_2bpz**. The gas sorption properties of any MOFs synthesised were to be tested. The hydrogen-bonding capabilities of the **H_2bpz** ligand were to be explored through its use as a co-ligand with other functionalised dicarboxylate ligands not yet explored in the literature.

6.2 Experimental

6.2.1 Synthesis

All reactants were purchased from Fluorochem, Aldrich or Fisher Scientific and used as received without further purification. Where solvents were dried, this was accomplished by the Grubbs method,[20] and stored under nitrogen. NMR spectra and mass spectra for ligands can be found in appendix B.

Benzene dipyrazole, H_2bdp

The synthesis of benzene-1,4-dipyrazole was adapted from a literature procedure, avoiding use of perchlorate.[21] This greatly lowered the yield of the first step, to give salt **(a)**.

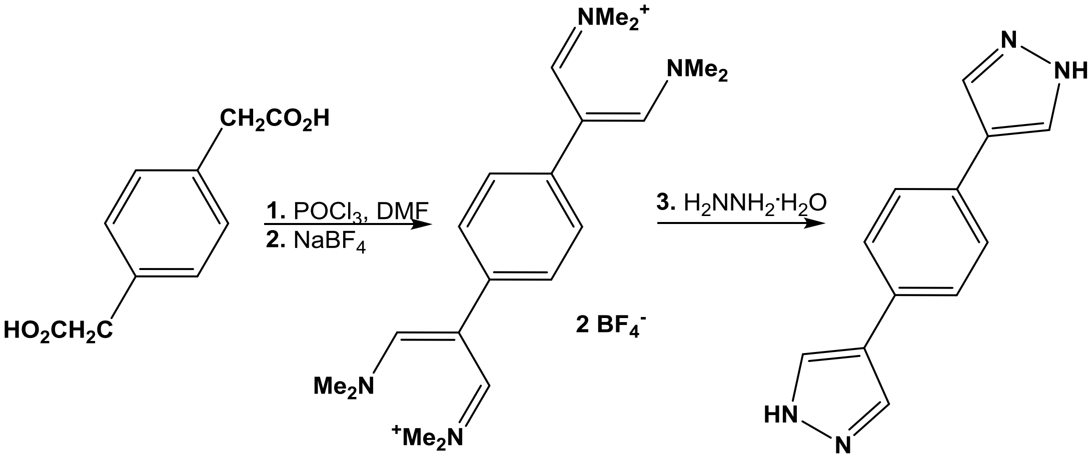

(a) 18 % **H_2bdp,** 67 %

Phosphorus oxychloride (3 mL, 12 mmol) was added dropwise to 12 mL cool, dry DMF under a nitrogen atmosphere and stirred for an hour. Solid para-phenylenediacetic acid (1 g, 5 mmol) was added in one portion, the mixture was heated at 95 °C for 2 hours, and then stirred at room temperature overnight. The reaction mixture was poured over 25 g crushed ice, and after 30 minutes a saturated aqueous solution of sodium tetrafluoroborate (3.3 g, 30 mmol) was added dropwise to effect precipitation of bis(tetrafluoroborate) salt **(a)** (400 mg, 0.9 mmol, 18 % yield).

Salt **(a)** (400 mg, 0.9 mmol) was added to a hot (90 °C) 0.5 M sodium hydroxide solution (5 mL). Upon complete dissolution, the solution was cooled to room temperature and was acidified to pH5 with 35% HCl. Hydrazine hydrate (0.20 mL, 5.5

mmol) was added immediately and the mixture stirred at room temperature for a further 24 hours. The cream-coloured precipitate was filtered, washed with cold water and dried under vacuum to give the title compound, which was used without further purification (123 mg, 67% yield, 10 % overall yield). ^{1}H-NMR (400 MHz, DMSO-d6): δ 7.55 (s, 4H, ArCH), 7.90 (s, 2H, pyrCH), 8.20 (s, 2H, pyrCH), 12.95 (s, 2H, NH). CHN expected: C 68.56%, H 4.79%, N 26.65%; anal. found: C 67.96%, H 4.70%, N 25.84%.

3,3',5,5'-tetramethyl-4,4'-bipyrazole monohydrate, H_2bpz·H_2O

The synthesis of 3,3',5,5'-tetramethyl-4,4'-bipyrazole was carried out according to a literature procedure.[22] The starting salt, sodium acetylacetonate monohydrate, may be purchased, or is readily prepared by mixing a methanolic solution of acetylacetone and NaOH.[22]

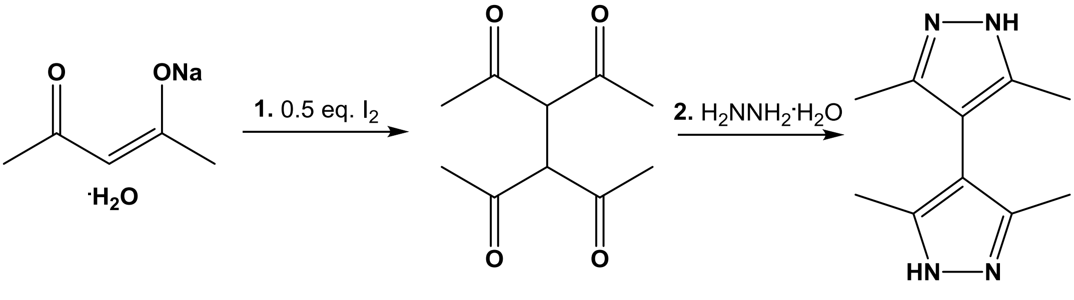

(b), 10 %   **H_2bpz**, 60 %

To a fine suspension of sodium acetylacetonate monohydrate (5.0 g, 36 mmol) in diethyl ether (100 mL) was added a solution of iodine (4.5 g, 18 mmol) in diethyl ether (100 mL), dropwise with vigorous stirring, over a period of 2 hours. The suspension was stirred for a further 4 hours. The ether was allowed to evaporate overnight and water (200 mL) was added to the brown residue and was chilled in a refrigerator overnight. The white precipitate was filtered, washed with cold water and recrystallised from MeOH to give **(b)** (710 mg, 3.6 mmol, 10% yield). MS (ES+): *m/z* = 199.1 [MH+], 221.1 [MNa+].

Crystals of **(b)** (300 mg, 1.5 mmol) were suspended in water (5 mL), slightly acidified with a few drops of acetic acid. Hydrazine hydrate (380 μL, 8 mmol) was added gently and the mixture was left to stir overnight. The white solid was filtered and recrystallised from water to give crystals of **H_2bpz** as its monohydrate (170 mg, 0.9 mmol, 60% yield). ^{1}H-NMR (400 MHz, DCl/D_2O): δ 0.97 (s, 12H, $-CH_3$). CHN expected (for **H_2bpz·H_2O**): C 57.67%, H 7.74%, N 26.90%; anal. found: C 57.18%, H 7.61%, N 26.58%. MS (ES+): *m/z* = 191.1 [MH+].

[Co(bdp)]·3DMF, 6.1·DMF

Cobalt (II) chloride hexahydrate (142 mg, 0.6 mmol) and **H_2bdp** (126 mg, 0.6 mmol) were mixed in 18 mL DMF in a 24 mL-capacity glass screwcap vial. Complete dissolution of **H_2bdp** could not be effected with sonication or gentle heating of the mixture. The vial was sealed and placed in an oven, then heated to 120 °C at a rate of 0.2 °C min^{-1}, held at 120 °C for 12 hours, then cooled to 25 °C at a rate of 0.5 °C min^{-1}. The mother liquor was decanted and purple crystals of the title compound (83 mg, 0.24 mmol, 40 % yield) were washed with a little fresh DMF and stored under more fresh DMF. CHN expected (for **[Co(bdp)]·2.15DMF·0.7H_2O**, best fit from least-squares fitting): C 58.27%, H 7.02%, N 22.65%; anal. found: C 58.23%, H 7.02%, N 22.76%.

[Zn(NH_2bdc)(H_2bpz)]·0.5H_2bpz, 6.2·H_2bpz

Zinc acetate dihydrate (220 mg, 1.0 mmol), aminoterephthalic acid (181 mg, 1.0 mmol) and **H_2bpz·H_2O** (95 mg, 0.46 mmol) were placed in a Teflon-lined 24 mL-capacity steel autoclave, along with 5 mL distilled water. The autoclave was sealed and heated in an oven to 150 °C at a rate of 12 °C hr^{-1}, held at 150 °C for 20 hours and then cooled to 25 °C at a rate of 5 °C hr^{-1}. The resulting cream/white solid was filtered, washed with distilled water (2 x 5 mL), giving an off-white crystalline solid (220 mg, 0.35 mmol, 152 % yield based on **H_2bpz**, assuming phase purity). CHN expected: C 52.28%, H 4.96%, N 18.55%; anal. found: C 48.99%, H 3.88%, N 16.43% (material is not phase pure, see sections 6.2.3 and 6.3.2.

6.2.2 Single crystal X-ray diffraction

Single crystal X-ray data were collected for compounds **6.1·DMF** and **6.2·H_2bpz** on Bruker *APEX-2* diffractometers, using Mo-Kα radiation. Data were corrected for absorption using empirical methods (*SADABS*), based on symmetry-equivalent reflections combined with measurements at different azimuthal angles.[23,24] Crystal structures were solved and refined against all F^2 values, using the *SHELXTL* program suite,[25] or using *Olex2*.[26] Non-hydrogen atoms were refined anisotropically (except as noted below), and hydrogen atoms placed in calculated positions refined using idealised geometries (riding model) and assigned fixed isotropic displacement parameters.

Due to small and weakly diffracting crystals, thermal parameters for atoms in the model for **6.1·DMF** could not be refined anisotropically. The results of the isotropic refinement are shown in Table 6.5.

Collection and refinement data for both collections may be found in Table 6.5. Crystallographic information files for all structures in Table 6.5 are provided in the digital appendix.

Table 6.5. *Data collection, structure solution and refinement parameters for crystal structures in chapter 6.*

	6.1·DMF	**6.2·H$_2$bpz**
Crystal habitat	Block	Plate
Crystal colour	Purple	Colourless
Crystal size (mm)	0.10 x 0.08 x 0.06	0.20 x 0.10 x 0.04
Crystal system	Monoclinic	Orthorhombic
Space group	$P\,2_1/c$	$P\,b\,c\,n$
a (Å)	13.299 (1)	15.698 (6)
b (Å)	14.116 (1)	17.929 (6)
c (Å)	26.461 (3)	17.962 (6)
α (°)	90	90
β (°)	101.025 (7)	90
γ (°)	90	90
V (Å^3)	4875.8 (8)	5055 (3)
Density (Mg m^{-3})	1.461	1.387
Temperature (K)	100	100
$\mu_{(Mo\text{-}Ka)}$ (mm^{-1})	1.389	1.014
θ range (°)	4.25 to 41.856	3.448 to 55.004
Reflns. collected	32984	51544
Independent reflns. (R_{int})	5058 [$R_{(int)}$ = 0.2576]	5768 [$R_{(int)}$ = 0.2570]
Reflns. used in refinement, n	5058	5768
LS parameters, p	237	323
Restraints, r	0	0
$R1$ (F)^a $I>2.0s(I)$	0.1433	0.0739
$wR2$ (F^2)^a, all data	0.3513	0.1721
$S(F^2)^a$, all data	1.178	0.997

[a] $R1(F) = \Sigma(|F_o| - |F_c|)/\Sigma|F_o|$; $wR2(F^2) = [\Sigma w(F_o^2 - F_c^2)^2/\Sigma wF_o^4]^{1/2}$; $S(F^2) = [\Sigma w(F_o^2 - F_c^2)^2/(n + r - p)]^{1/2}$

6.2.3 Powder X-ray diffraction

The crystalline products were all ground in a pestle and mortar and packed in to 0.7 mm capillaries before data collection (quartz for **6.1·DMF** and borosilicate for **6.2·H$_2$bpz**). In both cases, data were collected at ambient temperature.

X-ray diffraction patterns for the *in-situ* desolvation of **6.1·DMF** were collected (λ = 0.39986 (1) Å) at station ID31 (now ID22), at the European Synchrotron Radiation Facility (ESRF),[27] using a multi-analyser crystal (MAC) detector. Scans were collected over a range of $-2.5° \leq 2\theta \leq 18°$ (scan duration 2 mins), and were collected six times, spread over three different sample translations to average beam exposure to the sample and confirm phase purity along the capillary. Total sample exposure time was therefore 12 mins. The individual scans were compared and summed together to give the final patterns used for indexing and fitting.

X-ray diffraction data on **6.2·H$_2$bpz** were collected at beamline I11 (λ = 0.827124 (2) Å) at Diamond Light Source,[28,29] using a wide angle (90°) PSD detector comprising 18 Mythen-2 modules. A pair of scans was conducted, related by a 0.25 ° detector offset to account for gaps between detector modules. Six such scan pairs were collected at five seconds exposure, whilst the sample capillary was spun about its axis to average beam exposure. These six pairs of scans were preceded and followed by a pair of one-second scans, to compare and therefore assess beam damage. No observable beam damage could be found, and the resulting patterns were summed to give the final pattern for structural analysis (total beam exposure time therefore 64 seconds).

6.2.3.1 Sample of 6.1·DMF studied for desolvation.

The powder was filtered at the pump from the mother liquor and allowed to dry in air for 30 minutes to remove excess DMF. The sample was packed in a capillary as described above, and placed into a gas cell for desolvation. The sample was scanned under ambient conditions, and compared to the calculated pattern from single-crystal diffraction at 100 K.

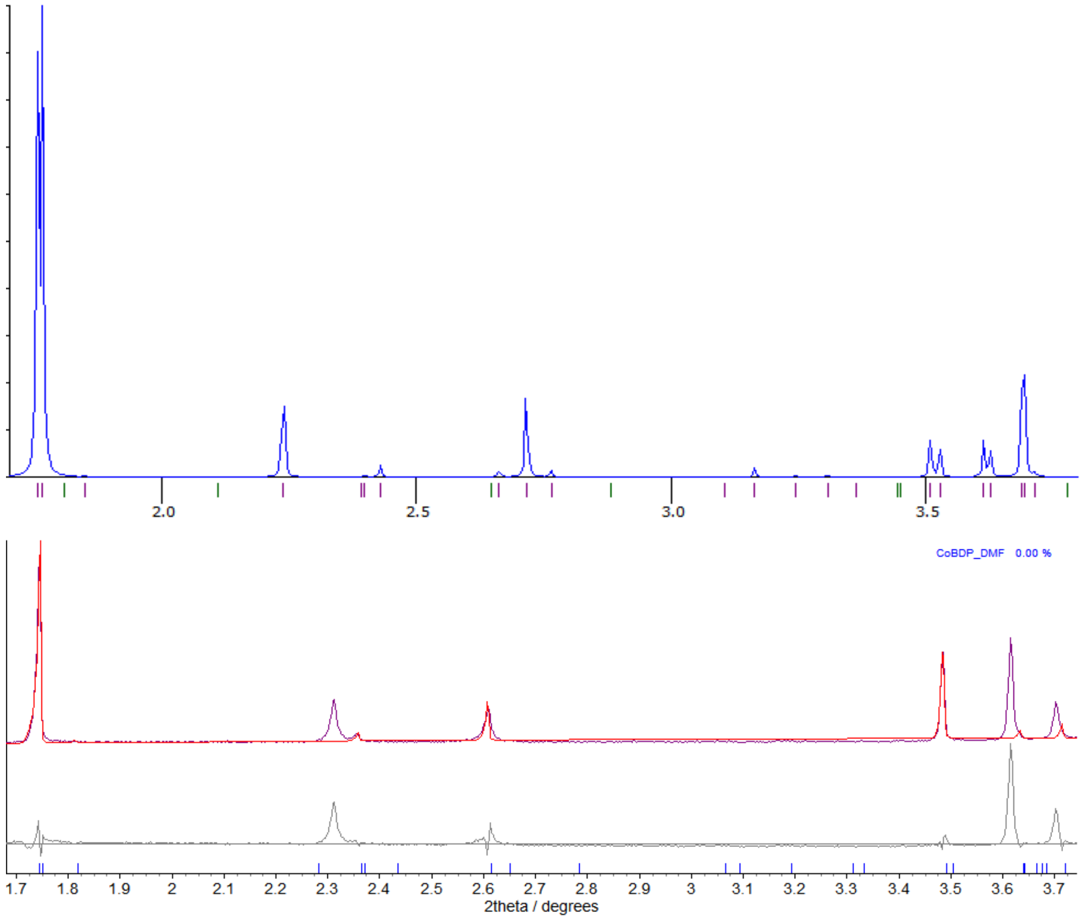

Figure 6.6. Top: *Calculated X-ray powder diffraction pattern at low angle, based on the structure solution for **6.1·DMF** at 100 K. **Bottom:** The result of an attempted Pawley fit on the observed powder X-ray diffraction pattern for **6.1·DMF** in the gas cell.*

Low-angle data appeared to suggest that some reflections show marked departures from their expected positions, much more so than would be typical of a temperature effect (with the exception of the (100) and (200) reflections at 2θ 1.74° and 3.49°). The pattern did not resemble that of any of the previously known phases of [Co(bdp)] (identified by Long and co-workers),[12] and attempts to apply the unit cells of these phases to Pawley refinement were unsuccessful.

In addition, the intensities of some reflections are drastically higher than expected, and this was also observed with other samples of simple organics and ligands also analysed on this particular synchrotron trip. This may indicate a sample averaging error or detector problem, which has caused ‘spikes’ or over-expression of some reflections. The results of the Pawley fit were as such:

The pattern at 298 K could not be indexed using the TOPAS programme.[30] Therefore, the unit cell that of **6.1·DMF** from single-crystal X-ray diffraction at 100 K was used as the starting point for a Pawley refinement,[31] employing 6392 parameters (6 background, 1 zero error, 5 profile, 4 cell, 6376 reflections), resulting in final indices of fit R_{wp} = 38.03, $R_{wp'}$ = 63.91.

[**6.1·DMF**: a = 13.2239 (2) Å, b = 14.3479 (2) Å, c = 26.5481 (3) Å, β = 98.539 (2)°, V = 4981.3 (1) Å^3].

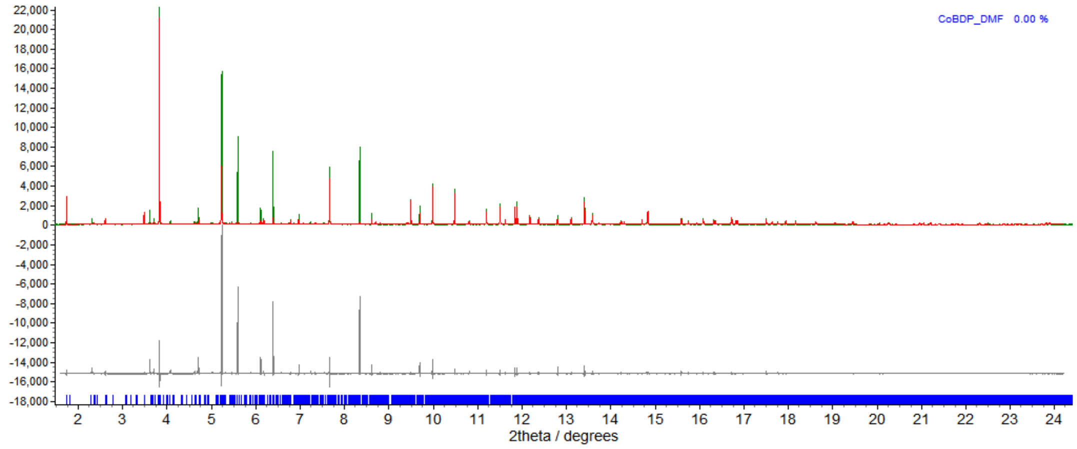

Figure 6.7. *Observed (green) and calculated (red) profiles and difference plot [I_{obs}-I_{calc}] (grey) of the Pawley refinement of **6.1·DMF**. (2θ range 1.6 – 24.2 °, d_{min} = 0.95 Å).*

The sample in the gas cell was then continuously pumped on at room temperature (pressure < 10^{-5} mbar), for a period of 15 hours. The peaks identified in Figure 6.8 (below) showed further departures from their expected positons from the calculated powder diffraction patterns, based on the single crystal structure of **6.1·DMF**.

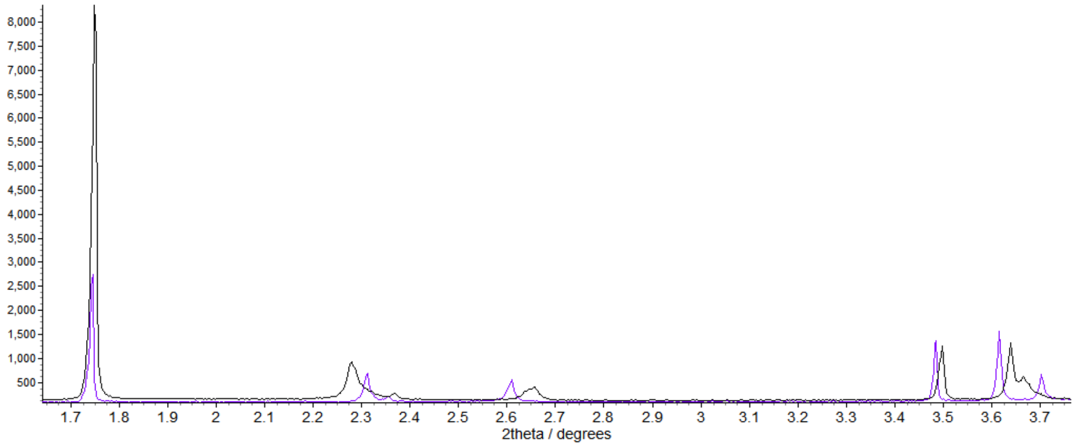

Figure 6.8. *Observed X-ray powder diffraction patterns for* ***6.1·DMF*** *before desolvation under vacuum (purple) and after 15 hours under vacuum (black). Note the distinct shift in low-angle reflections, suggesting flexibility of the MOF.*

The pattern measured after 15 hours under vacuum could also not be indexed directly using the TOPAS programme.[30] Therefore, the unit cell that of **6.1·DMF** from single-crystal X-ray diffraction at 100 K was used as the starting point for a Pawley refinement,[31] employing 841 parameters (6 background, 1 zero error, 5 profile, 4 cell, 825 reflections), resulting in final indices of fit R_{wp} = 22.14, $R_{wp'}$ = 45.57.
[**6.1·DMF**: a = 13.2948 (8) Å, b = 14.145 (1) Å, c = 26.464 (1) Å, β = 100.910 (8)°, V = 4886.6 (6) Å^3].

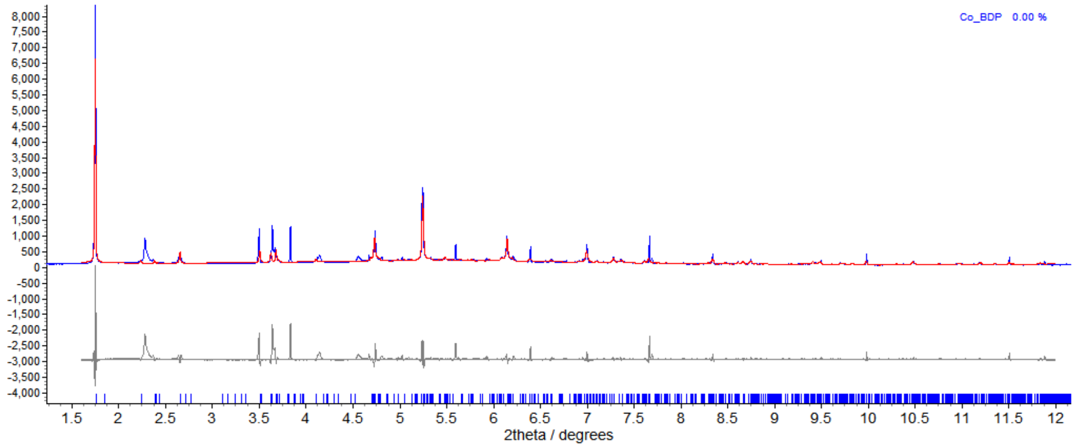

Figure 6.9. *Observed (blue) and calculated (red) profiles and difference plot [I_{obs}-I_{calc}] (grey) of the Pawley refinement of* ***6.1·DMF****. (2θ range 1.6 – 12.0 °, d_{min} = 1.90 Å).*

6.2.3.2 Sample of $6.2{\cdot}H_2bpz$, phase purity check

The pattern on the material at 298 K was compared with the calculated pattern for **$6.2{\cdot}H_2bpz$** from single-crystal X-ray diffraction at 100 K. A number of peaks belonging to another, unidentified phase were found. Indexing the peaks expected to correspond to **$6.2{\cdot}H_2bpz$** using TOPAS gave a unit cell similar to that of **$6.2{\cdot}H_2bpz$** at 100 K.[30] This cell was used as the starting point for a Pawley refinement,[31] employing 844 parameters (6 background, 1 zero error, 5 profile, 3 cell, 829 reflections), resulting in final indices of fit $R_{wp} = 12.79$, $R_{wp'} = 48.71$.

The starting model used for the Rietveld refinement,[32] also conducted using TOPAS, was the single-crystal structure of **$6.2{\cdot}H_2bpz$** collected at 100 K. Refinement employed 16 parameters (6 background, 1 zero error, 5 profile, 3 cell, 1 scale). Rietveld refinement converged to $R_{wp} = 13.93$, $R_{wp'} = 54.03$.

[**$6.2{\cdot}H_2bpz$**: a = 15.9513 (7) Å, b = 17.975 (1) Å, c = 17.8160 (7) Å, V = 5108.2 (4) Å^3].

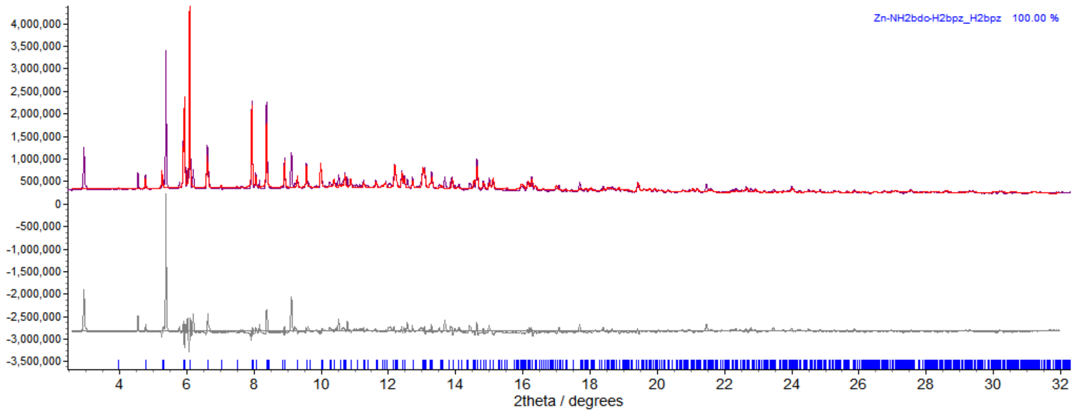

Figure 6.10. *Observed (purple) and calculated (red) profiles and difference plot [I_{obs}-I_{calc}] (grey) of the Rietveld refinement of* ***$6.2{\cdot}H_2bpz$****. (2θ range 1.6 – 12.0 °, d_{min} = 1.90 Å).*

6.3 Results & discussion

6.3.1 Benzene dipyrazolate MOF [Co(bdp)]

The flexible MOF [Co(bdp)] was sought as an initial synthetic target for study of pyrazolate MOFs due to its interesting gas sorption properties outlined in section 6.1.

Reaction of cobalt(II) chloride with benzenedipyrazole **H_2bdp** in dimethylformamide (DMF) under solvothermal conditions yields a metal-organic framework similar in structure to the previously published flexible MOF [Co(bdp)],[11,12] in this case as a DMF solvate, **6.1·DMF**. In the structure, each pyrazolate site on the benzenediprazolate ligands bridge cobalt(II) centres in infinite one-dimensional chains. The **bdp** ligand then also acts as a bridge between parallel chains of cobalt(II) centres, to give a MOF with one dimensional channels (see Figures 6.11 and 6.12).

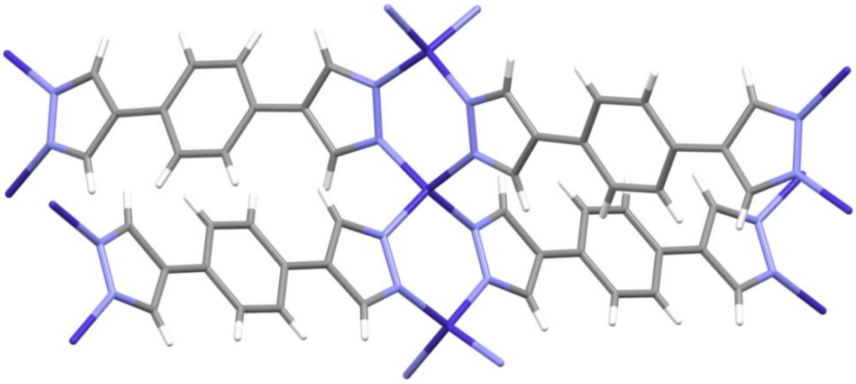

Figure 6.11. *Coordination environment within **6.1·DMF**, showing chains of Co(II) centres connected by pyrazolates along the crystallographic b-axis.*

The best fit to the crystallographic data suggested that **6.1·DMF** crystallises with three equivalents of DMF per formula unit, [Co(bdp)]·3DMF. These occupy the channels fully (see space-filling diagram in Figure 6.12). The solvent appears to show C–H···O hydrogen bonding both to other solvent molecules and to the framework of the MOF.

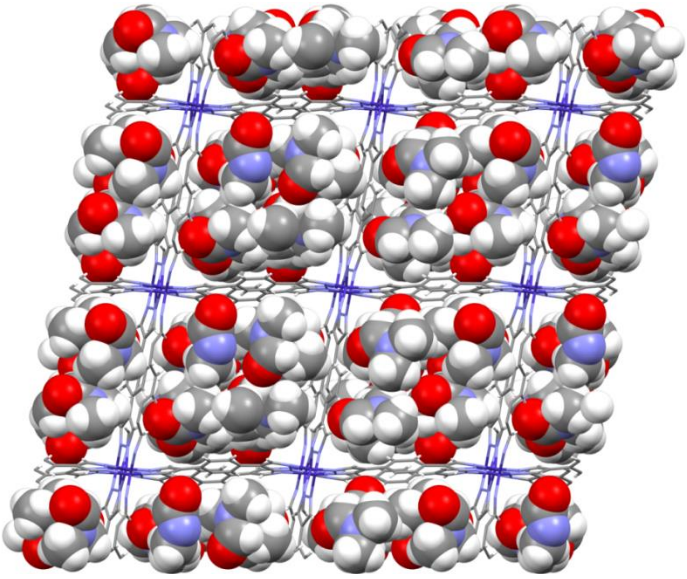

***Figure 6.12.** Channels in **6.1·DMF** shown with DMF solvent in spacefilling view.*

The MOF **6.1·DMF** crystallises in space group $P2_1/c$ (monoclinic), unlike the DEF/water solvate previously reported by Long and co-workers.[11,12] The previously reported [Co(bdp)]·xDEF·yH_2O crystallised in space group $P222_1$ (tetragonal), containing channels which are square in shape (see Figure 6.13), linked in the orthogonal directions by the **bdp** ligands as in **6.1·DMF**. However in **6.1·DMF**, distortion of the **bdp** ligands results in a lozenge-shaped channel (see Figure 6.13). The coordination environment around cobalt in both structures is tetrahedral.

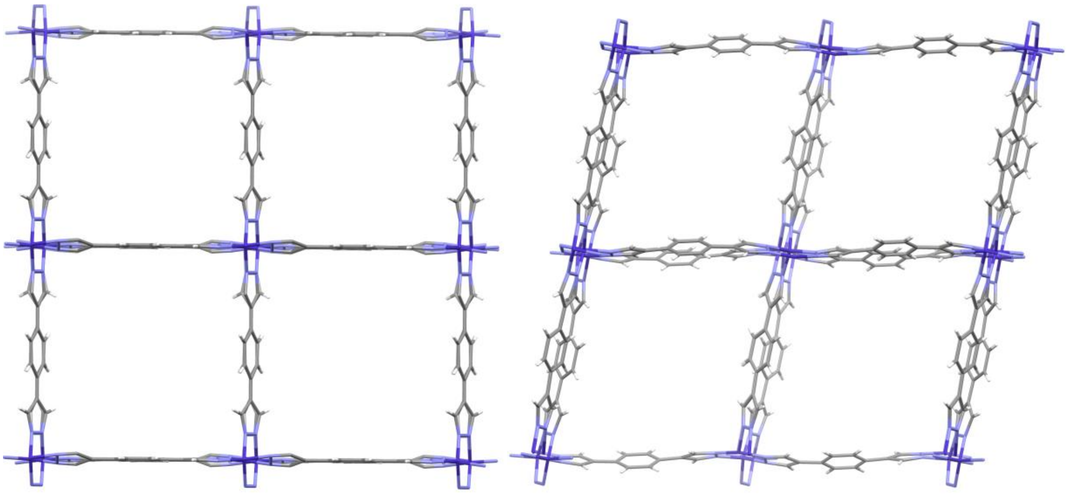

***Figure 6.13. Left:** Square-shaped channels in the tetragonal, previously-reported [Co(bdp)]·xDEF·yH_2O.[11,12] **Right:** The lozenge-shaped channels in the monoclinic **6.1·DMF**.*

The observed ligand distortion in the crystal structure of the as-synthesised **6.1·DMF**, leading to the lozenge-shaped pores as opposed to the square-shaped pores in the previously reported [Co(bdp)]·xDEF·yH_2O could be due to host-guest interaction. In studying the desolvation of the [Co(bdp)] MOF and its uptake of N_2, CH_4 and CO, the Long group suggested that interaction between the gaseous guests and the MOF led to different phases being formed. For example, when filling the desolvated MOF with N_2, four discrete phases were observed (in addition to the desolvated phase, as shown previously in Figure 6.2 and below in Figure 6.14) however when filling the desolvated MOF with CH_4 or CO at the same temperature, fewer of the phases (two for CH_4 adsorption, one for CO adsorption) were observed.[12] The role of solvent on the flexibility of [Co(bdp)] was also briefly explored by Long and co-workers. Exposure of the desolvated [Co(bdp)] to acetonitrile vapour led to the observed formation of only one of the four discrete phases identified during N_2 adsorption (see Figure 6.14).

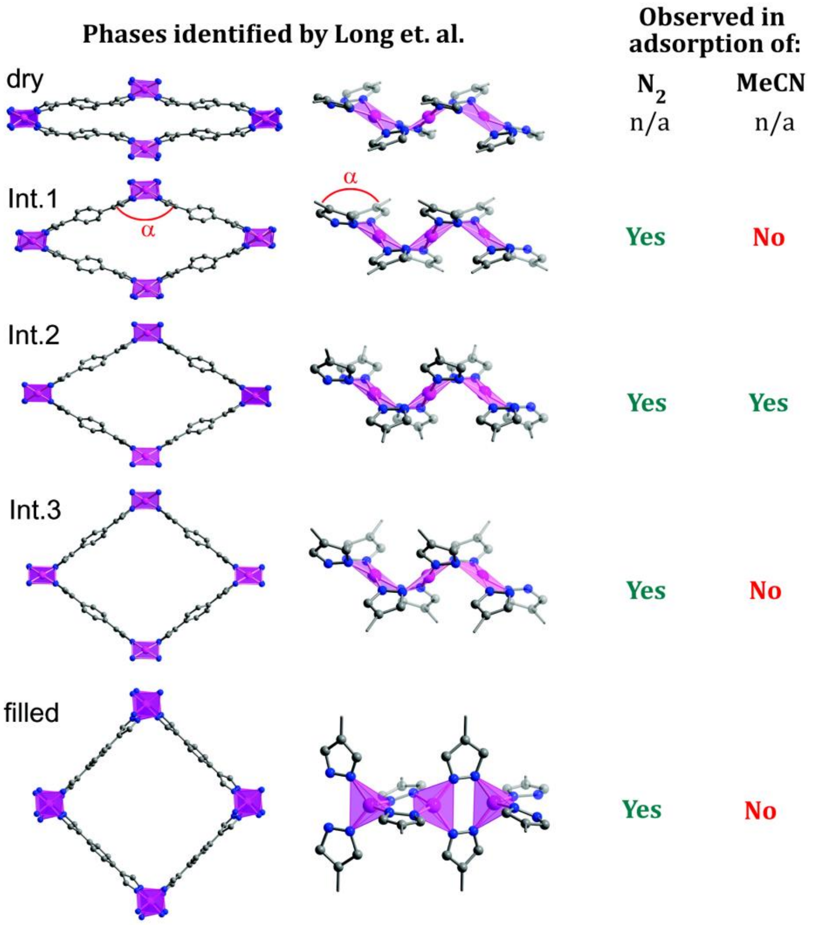

Figure 6.14. *Phases observed by Long and co-workers in the adsorption of nitrogen and acetonitrile vapour into the 'dry' framework [Co(bdp)].*[12] *Figure partially reproduced from reference 12.*

The demonstration of guest dependence of the pore shape may suggest that the shape of the pores could also depend upon the solvent within them after synthesis. However, a complete comparison of the effect of solvent on the pore shape of [Co(bdp)] is not possible, as the previously reported work with acetonitrile within the pores was conducted with acetonitrile in the vapour phase. The solvent present within the pores of the previously reported [Co(bdp)]·xDEF·yH_2O could not be found crystallographically. Further work with the [Co(bdp)] system in the literature has not further elucidated the role of solvent or gas upon the shape of the pores.

The phase purity of, and potential for desolvation of **6.1·DMF** was studied by X-ray powder diffraction, to determine its suitability for *in situ* gas uptake experiments (as shown on the MOFs in chapter 4), potentially further exploring its flexibility. A ground sample of the MOF was placed in a capillary and was pumped on at high vacuum power (c. 10^{-5} mbar) for 15 hours at ambient temperature. However, visual inspection of the powder pattern indicated that the sample was quite similar to the pattern calculated from the single crystal structure (see Figure 6.15 and experimental section 6.2.3.1 for attempts at fitting the data).

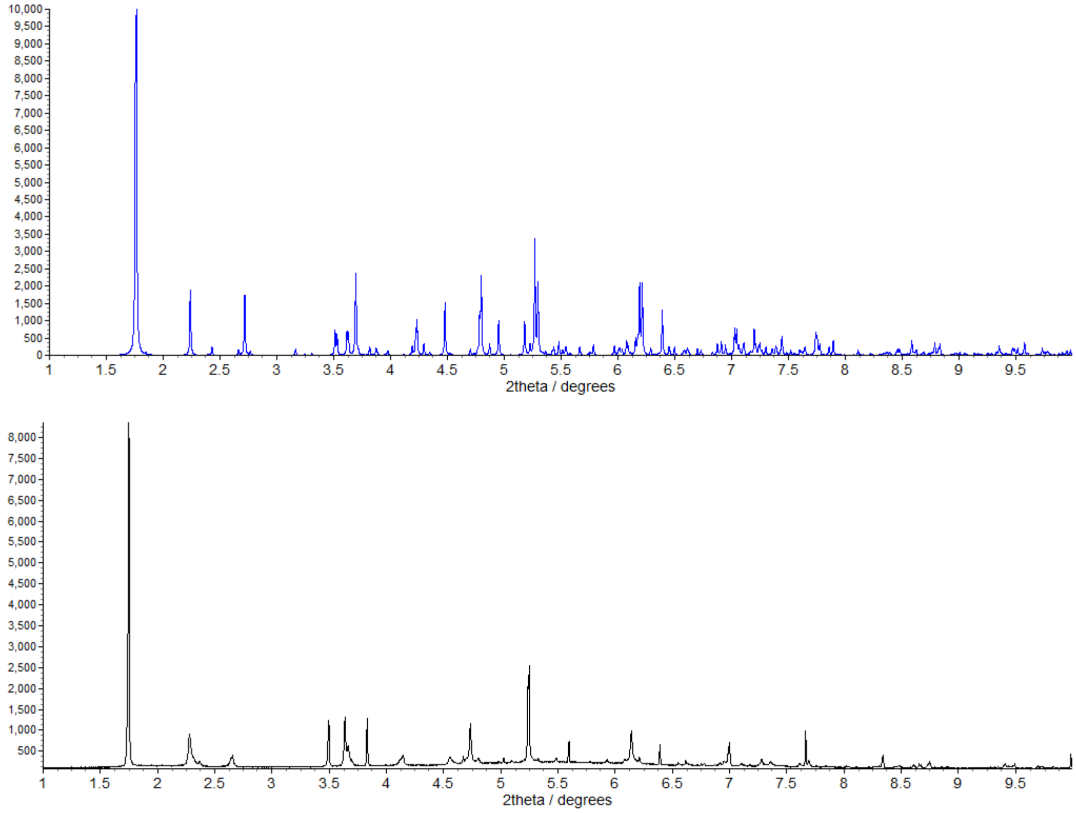

Figure 6.15. *(Top, blue) Calculated X-ray powder diffraction pattern for* ***6.1·DMF*** *based on the 100 K single crystal structure and (bottom, black) the observed powder diffraction pattern for* ***6.1·DMF*** *after pumping at 10^{-5} mbar for 15 hours.*

While initial visual inspection indicated there was little change, attempting to index the data did not give a unit cell that closely matched the structure from single crystal diffraction. Upon closer examination, key reflections such as the (1,0,-2) reflection at 2θ 2.25° in the calculated pattern, are shifted to different diffraction angle in the observed pattern after vacuum.

Attempts to fit the data with the unit cell of **6.1·DMF** from single crystal X-ray diffraction at 100 K did not give a sensible fit. Some peaks were matched quite well, whereas others were not matched (see fit in Figure 6.16). Attempts to allow the unit cell parameters of **6.1·DMF** to refine to the data over many iterations (by a simulated annealing approach, like as described for the attempts to find the structure of **2.1** in chapter 3) were also unsuccessful. Finally, the unit cells of the 'dry' desolvated [Co(bdp)], as well as the other four phases described in the previously published work by Long and co-workers were also used in attempted Pawley refinements,[12] but also did not fit the hitherto undescribed peaks in the powder pattern.

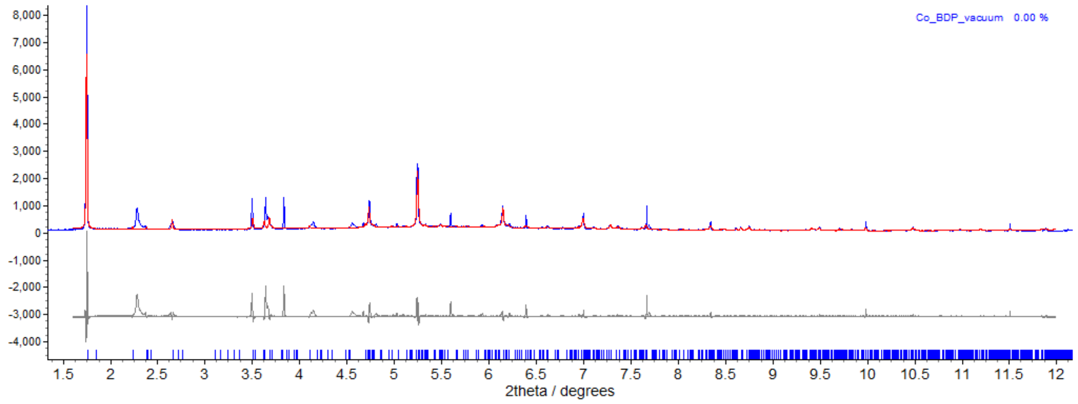

Figure 6.16. *The fitting result of Pawley refinement of the unit cell of* ***6.1·DMF*** *(from single-crystal X-ray diffraction) to the observed pattern, obtained by pumping on a sample of* ***6.1·DMF*** *at* 10^{-5} *mbar for 15 hours.*

This may indicate that a minor phase change has taken place upon (perhaps partial) desolvation, as is indicated by the phase changes observed and studied within this MOF in the literature.[12] However, the phase changes discussed in the literature are much more significant than that which appears to have taken place here. This instead may suggest a degree of flexibility in the MOF that is not fully described in the literature. This may indicate a degree of solvent-dependence on the desolvation and phase-change behaviour. It may be possible that the host-guest interactions in the DMF solvate **6.1·DMF** effect not only a different pore shape of the as-synthesised MOF, but a different desolvation pathway to that shown for the DEF/water solvate in the literature.

Because of time constraints in synchrotron work, the presence of an unknown phase upon desolvation and no understanding of whether or not the material was fully desolvated, the response of the new phase to gas was not tested.

6.3.2 A hydrogen-bonded coordination polymer of H_2bpz

As introduced in section 6.1.2, the ligand **H_2bpz** has been shown in the literature to be an interesting ligand for coordination polymer construction due to its 'twisted' geometry and its ability to form intramolecular hydrogen bonds as a ligand.[15,18] As part of a wider investigation into crystal engineering using pyrazole/pyrazolate ligands, a coordination polymer containing **H_2bpz** was found, displaying interesting hydrogen bonding properties in the solid state.

Reacting zinc acetate with 2-aminoterephthalic acid and **H_2bpz** under hydrothermal conditions afforded the 3D coordination polymer **6.2·H_2bpz**. As anticipated, the structure of **6.2·H_2bpz** is extensively hydrogen-bonded. The structure contains intramolecular hydrogen-bonds, intermolecular hydrogen bonding between interpenetrated coordination polymers and between guests and coordination polymers. It is analogous in many of its structural features to the previously identified [Zn(bdc)(H_2bpz)]·0.5H_2bpz,[16] but even more extensively hydrogen-bonded.

Unlike other carboxylate-based $M^{(II)}$ coordination polymers of **H_2bpz**, which are based on paddlewheel motifs,[18] [Zn(bdc)(H_2bpz)]·0.5H_2bpz and the isostructural **6.2·H_2bpz** are based around a single Zn(II) centre with two coordinated aminoterephthalate ligands, and two **H_2bpz** ligands. The twisted bipyrazole geometry facilitates the formation of a 3D coordination network, supported by intramolecular hydrogen bonding between the pyrazole proton and the non-coordinated carbonyl on the aminoterephthalate (see Figure 6.17). Two such 3D networks exist and are interpenetrated, as shown in subsequent Figures.

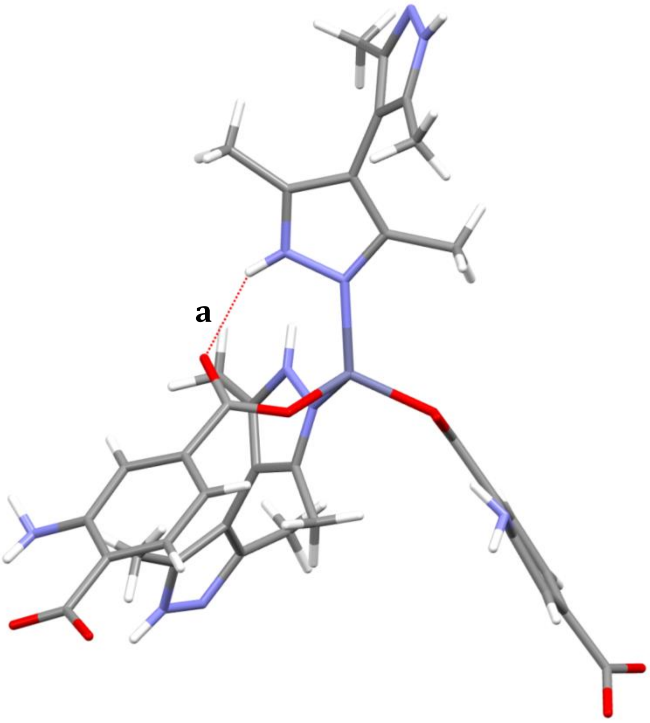

Figure 6.17. *Coordination environment around Zn(II) in **6.2·H_2bpz** and intramolecular hydrogen bonding (shown as red dashes) between coordinated **H_2bpz** and adjacent aminoterephthalate ligands.*

Additional intramolecular hydrogen bonds also exist within the aminoterephthalate ligands, between the non-coordinated carbonyl atoms and amino groups at the *ortho*-position (see Figure 6.18). This is naturally, due to its constrained nature, a short hydrogen bond, and likely has a less significant structural role on the packing of the material in the solid state than interaction '**a**', shown in Figure **6.17**.

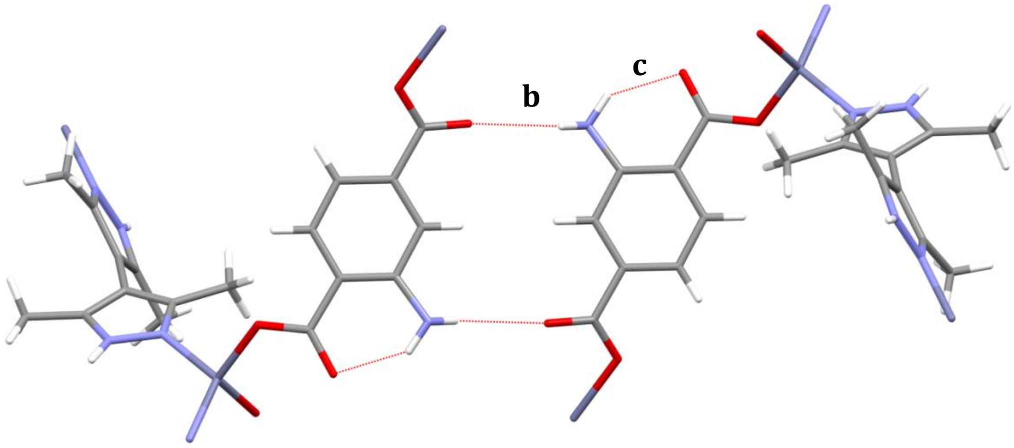

Figure 6.18. *Intramolecular hydrogen bonds (red dashes) within aminoterephthalate ligands in* ***6.2·H$_2$bpz*** *and intermolecular hydrogen bonds (red dashes) between adjacent coordination polymers of* ***6.2****.*

Intermolecular hydrogen bonded dimers of aminoterephthalate ligands bring adjacent interpenetrated coordination polymer networks into close contact. Each aminoterephthalate in the dimer receives and donates a hydrogen bond, again via the amine protons and carbonyl oxygen atoms. Inversion symmetry relates the two aminoterephthalate ligands comprising the hydrogen-bonded dimer, and as such it is described by just one notation, '**b**' in Table 6.22.

The interpenetrated networks of **6.2** also host guest molecules of **H$_2$bpz**. These guest molecules are themselves extensively hydrogen-bonded to the host frameworks. The guest **H$_2$bpz** N–H groups donate hydrogen bonds to those carbonyl oxygen atoms on the coordination polymer not already engaged in intramolecular hydrogen bonds. The guest **H$_2$bpz** non-protonated nitrogen atoms also accept hydrogen bonds from the **H$_2$bpz** ligands in the frameworks (see Figure 6.19). Each pyrazole moiety interacts with both of the interpenetrated coordination networks, as highlighted in Figure 6.20.

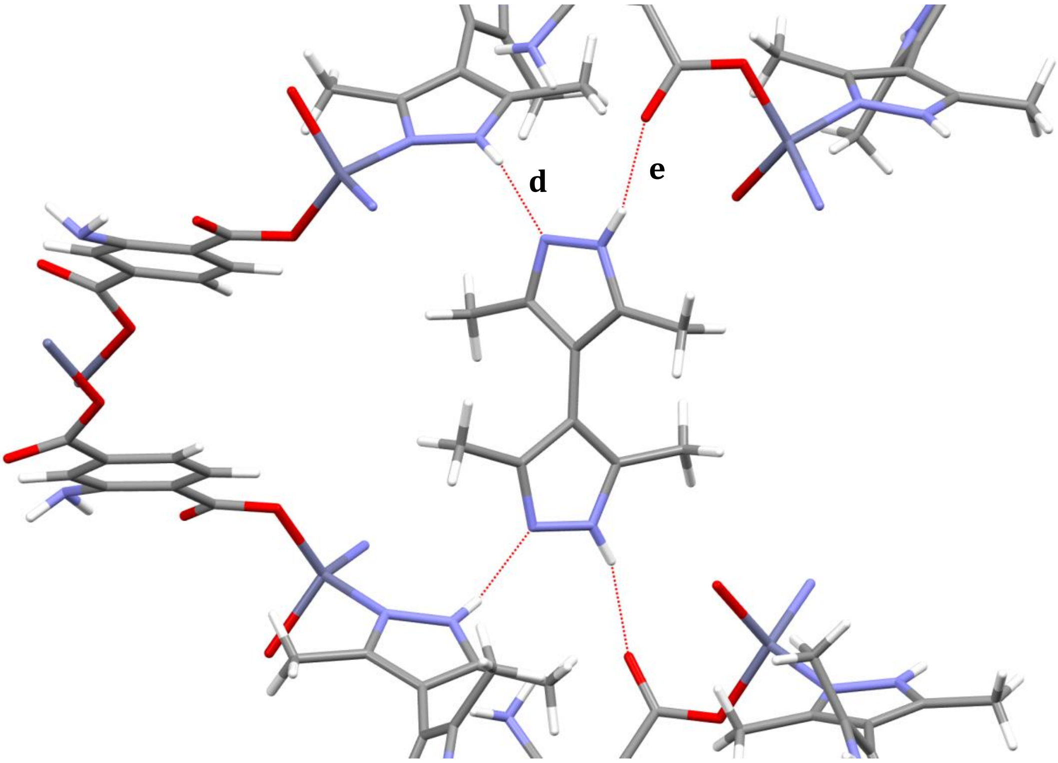

Figure 6.19. *Hydrogen bonding (red dashes) between guest* ***H_2bpz*** *molecules and the host framework* ***6.2****, in the crystal structure of* ***6.2·H_2bpz****.*

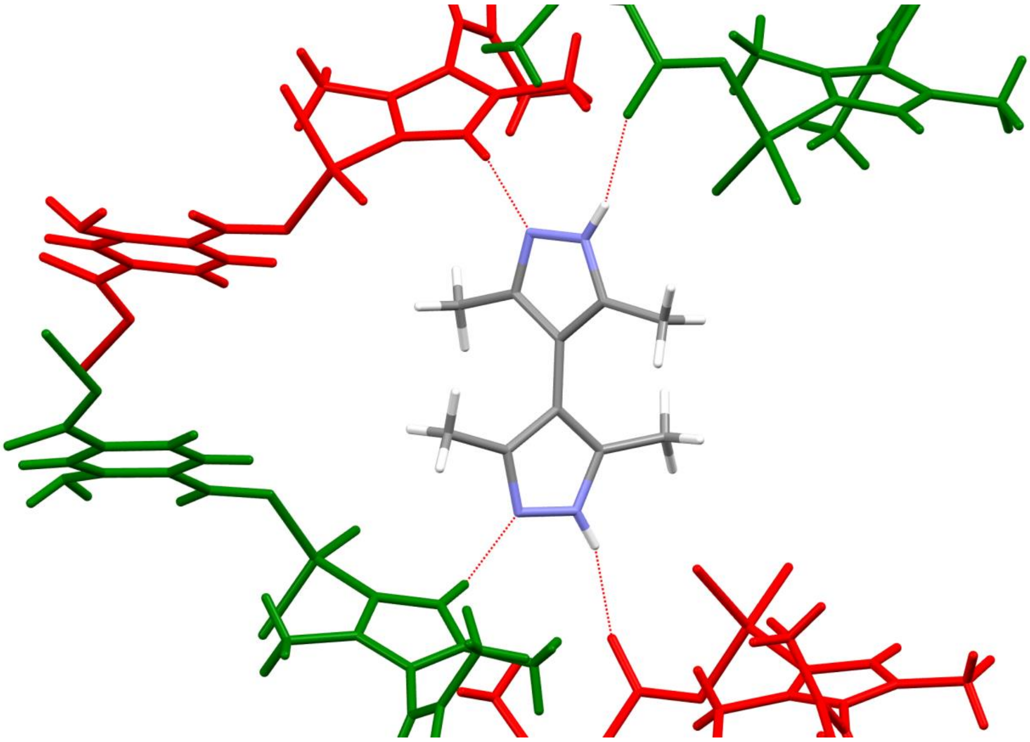

Figure 6.20. *The same view as Figure 6.17, with the two different interpenetrated coordination networks coloured in red and green, showing hydrogen bonding (red dashes) to the networks by each pyrazole ring.*

The guest **H_2bpz** stacks along one axis in the crystal structure, creating ‘channels’ of **H_2bpz** within the coordination networks (shown in Figure 6.21). Although these channels appear much like the MOF channels containing solvent in materials such as **6.1·DMF** (see Figure 6.12), each guest has strong hydrogen bonds to each wall of the channel.

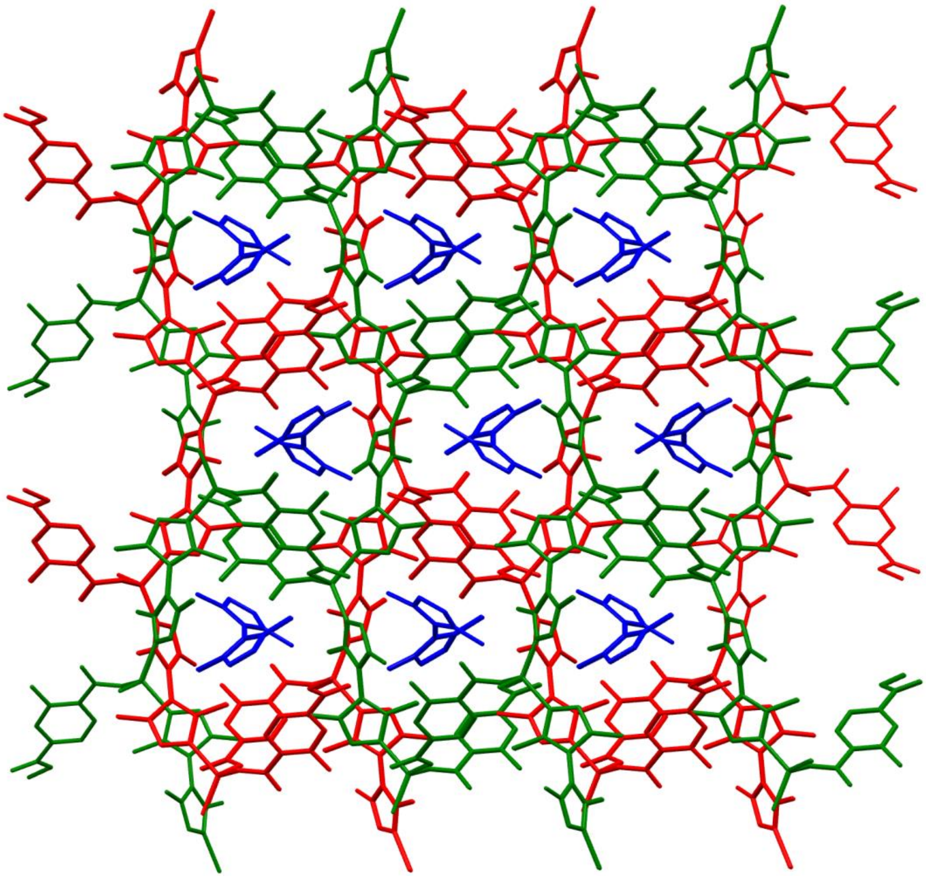

Figure 6.21. *‘Channels’ of guest **H_2bpz** (shown in blue) within the host framework **6.2** (interpenetrated networks shown in green and red), in the crystal structure of **6.2·H_2bpz**. Hydrogen atoms omitted for clarity.*

Table 6.22. *Hydrogen ("H-bond") geometries for compound **6.2·H₂bpz**. Interactions are listed as labelled in Figures 6.17, 6.18 and 6.19.*

Interaction		H···A (Å)	θ(N–H···A) (°)	θ(C–A···H) (°)	$r_H + r_A$ (Å)[a]	R_{HA}[a]
a H-bond*	N–H···O	1.938	137.36	127.11	2.72	0.71
b H-bond	N–H···O	2.280	125.92	143.60	2.72	0.84
c H-bond*	N–H···O	1.902	135.10	103.71	2.72	0.70
d H-bond	N–H···N	1.852	152.23	130.96	2.75	0.67
e H-bond	N–H···O	1.869	156.92	151.08	2.72	0.69

[a] *R_{XA} = d(H···A)/(r_H + r_A), where r_H and r_A are the van der Waals radii*[33] *of the hydrogen bond donor, H, and the acceptor, A (nitrogen or oxygen), respectively, following the definition of Lommerse et al.*[34] *Hydrogen bond lengths normalised to neutron diffraction values.*[35] *Asterisks (*) indicate intramolecular hydrogen bonds, between ligands comprising the same coordination polymer.*

Assessing the reduced interaction distances (R_{HA}, see Table 6.22) emphasises the importance of the guest **H_2bpz** in the structure of **6.2·H_2bpz**. The hydrogen bonds between the guest and the host coordination polymer are appreciably shorter than the intermolecular interactions between the interpenetrated networks, and are of comparable length to even the intramolecular hydrogen bonds in the framework. These strong hydrogen bonds indicate that the guest molecules may even be structurally integral to the coordination polymer architecture, and that their removal by heating or other means may facilitate the structural rearrangement of the material to compensate.

The isostructural [Zn(NH_2bdc)(H_2bpz)]·0.5H_2bpz reported in the literature had been investigated for its thermal stability.[16] The authors reported only a partial loss of H_2bpz guest upon heating to above 250°C, potentially indicating that the hydrogen bonds holding H_2bpz in the framework were strong enough to retain it until the material's eventual thermal decomposition. As the aminated **6.2·H_2bpz** analogue was found not to be phase pure (see experimental section 6.3.2.1), consistent thermogravimetric analysis traces could unfortunately not be obtained for comparison.

6.4 Conclusions & Future work

6.4.1 Solvent-dependence and desolvation of flexible MOFs

The structure of **6.1·DMF**, the dimethylformamide solvate of the previously reported flexible MOF [Co(bdp)] was determined. The distortion of the **bdp** ligands led to the altered shape of the pores, compared to the DEF/water solvate previously reported.[11] The role of solvent in the determination of the shape of the pores of [Co(bdp)] could not be directly determined, however.

The presence of an unknown phase (possibly the result of partial desolvation) in the powder pattern of the **6.1·DMF** material after exposure to high vaccum was observed, contrary to observations in the literature on deolvation of the DEF/water solvate of **6.1**. This suggests that the desolvation of flexible MOFs such as **6.1** may also be solvent-dependent. The amount of solvent present in the channels, or their identity, may lead to different desolvation pathways, and as such, different structures and response toward guests. Previously reported work with a variety of gaseous and vapour guests suggests that the flexibility of [Co(bdp)] does display a guest dependence.

Further work with this system should focus on properly characterising the desolvation of the MOF, including its synthesis from both DMF and from the DEF/water mixture previously reported. In addition, solvent exchange with more volatile solvents such as chloroform (as used in chapter 4) could also afford interesting avenues of study into its flexibility.

6.4.2 Hydrogen-bonded coordination polymers of H_2bpz

The extensively hydrogen-bonded structure of **6.2·H_2bpz** demonstrates that the ligand **H_2bpz** is a potentially useful tool in crystal engineering of hydrogen-bonded solids. Its ability to act as both a donor and acceptor of strong hydrogen bonds at four sites (as a guest in the crystal structure of **6.2·H_2bpz**) may also indicate that it is a good candidate for designed hydrogen-bonded co-crystals.

The extensive hydrogen bonding also indicates that its thermal properties may be interesting to study, as this may afford unexpected thermal stability that the material in its phase-pure form may possess.

The difficulty encountered in synthesising coordination polymers of **H_2bpz** in a phase-pure manner has prevented their further study. This may have arisen as a consequence of the many coordination polymer geometries that could be formed by the **H_2bpz** ligand (or by its spontaneous deprotonation, as shown in the literature). Following the synthetic strategy used to synthesise the non-amino equivalent of **6.2·H_2bpz**, [Zn(bdc)(H_2bpz)]·0.5H_2bpz could lead to a phase-pure sample of **6.2·H_2bpz** for further study. Thermogravimetry-mass spectrometry analysis, as shown previously in chapter 5, could also be useful in characterising the mass losses from guest containing materials such as [Zn(bdc)(H_2bpz)]·0.5H_2bpz and **6.2·H_2bpz**.

6.5 References

1 Z. Wang and S. M. Cohen, *Chem. Soc. Rev.*, 2009, **38**, 1315–1329.

2 S. C. Jones and C. A. Bauer, *J. Am. Chem. Soc.*, 2009, **131**, 12516–12517.

3 S. M. Cohen, *Chem. Sci.*, 2010, **1**, 32–36.

4 I.-H. Park, A. Chanthapally, H.-H. Lee, H. S. Quah, S. S. Lee and J. J. Vittal, *Chem. Commun.*, 2014, **50**, 3665–3667.

5 L. Sarkisov, R. L. Martin, M. Haranczyk and B. Smit, *J. Am. Chem. Soc.*, 2014, **136**, 2228–2231.

6 M. Alhamami, H. Doan and C.-H. Cheng, *Materials*, 2014, **7**, 3198–3250.

7 A. Schneemann, V. Bon, I. Schwedler, I. Senkovska, S. Kaskel and R. A. Fischer, *Chem. Soc. Rev.*, 2014, **43**, 6062–6096.

8 C. Serre, F. Millange, C. Thouvenot, M. Noguès, G. Marsolier, D. Louër and G. Férey, *J. Am. Chem. Soc.*, 2002, **124**, 13519–13526.

9 T. Loiseau, C. Serre, C. Huguenard, G. Fink, F. Taulelle, M. Henry, T. Bataille and G. Férey, *Chem. Eur. J.*, 2004, **10**, 1373–1382.

10 C. Serre, C. Mellot-Draznieks, S. Surblé, N. Audebrand, Y. Filinchuk and G. Férey, *Science*, 2007, **315**, 1828–1831.

11 H. J. Choi, M. Dincă and J. R. Long, *J. Am. Chem. Soc.*, 2008, **130**, 7848–7850.

12 F. Salles, G. Maurin, C. Serre, P. L. Llewellyn, C. Knöfel, H. J. Choi, Y. Filinchuk, L. Oliviero, A. Vimont, J. R. Long and G. Férey, *J. Am. Chem. Soc.*, 2010, **132**, 13782–13788.

13 N. Guillou, S. Bourrelly, P. L. Llewellyn, R. I. Walton and F. Millange, *CrystEngComm*, 2015, **17**, 422–429.

14 S. Galli, N. Masciocchi, V. Colombo, A. Maspero, G. Palmisano, F. J. López-Garzón, M. Domingo-García, I. Fernández-Morales, E. Barea and J. A. R. Navarro, *Chem. Mater.*, 2010, **22**, 1664–1672.

15 K. V. Domasevitch, I. Boldog, E. B. Rusanov, J. Hunger, S. Blaurock, M. Schröder and J. Sieler, *Z. Anorg. Allg. Chem.*, 2005, **631**, 1095–1100.

16 J. He, J.-X. Zhang, G.-P. Tan, Y.-G. Yin, D. Zhang and M.-H. Hu, *Cryst. Growth Des.*, 2007, **7**, 1508–1513.

17 L. Hou, Y.-Y. Lin and X.-M. Chen, *Inorg. Chem.*, 2008, **47**, 1346–1351.

18 J. Hunger, H. Krautscheid and J. Sieler, *Cryst. Growth Des.*, 2009, **9**, 4613–4625.

19 E. Q. Procopio, N. M. Padial, N. Masciocchi, S. Galli, J. E. Oltra, E. Barea and J. A. R. Navarro, *CrystEngComm*, 2013, **15**, 9352–9355.

20 A. B. Pangborn, M. A. Giardello, R. H. Grubbs, R. K. Rosen and F. J. Timmers, *Organometallics*, 1996, **15**, 1518–1520.

21 V. Lozan, P. Y. Solntsev, G. Leibeling, K. V. Domasevitch and B. Kersting, *Eur. J. Inorg. Chem.*, 2007, 3217–3226.

22 R. G. Charles, *Org. Synth.*, 1963, **4**, 869–870.

23 G. M. Sheldrick, *SADABS: Empirical absorption correction program (based on the method of Blessing), 1996*.

24 R. H. Blessing, *Acta Crystallogr. Sect. B*, 1995, **51**, 33–38.

25 G. M. Sheldrick, *Acta Crystallogr. Sect. C*, 2015, **71**, 3–8.

26 O. V. Dolomanov, L. J. Bourhis, R. J. Gildea, J. A. K. Howard and H. Puschmann, *J. Appl. Crystallogr.*, 2009, **42**, 339–341.

27 A. N. Fitch, *Res. Natl. Inst. Stand. Technol.*, 2004, **109**, 133–142.

28 S. P. Thompson, J. E. Parker, J. Potter, T. P. Hill, A. Birt, T. M. Cobb, F. Yuan and C. C. Tang, *Rev. Sci. Intrum.*, 2009, **80**, 075107.

29 S. P. Thompson, J. E. Parker, J. Marchal, J. Potter, A. Birt, F. Yuan, R. D. Fearn, A. R. Lennie, S. R. Street and C. C. Tang, *J. Synchrotron Rad.*, 2011, **18**, 637–648.

30 A. A. Coelho, *TOPAS Academic, version 4.1 (2007), see http://www.topas-academic.net*, .

31 G. S. Pawley, *J. Appl. Crystallogr.*, 1981, **14**, 357–361.

32 H. M. Rietveld, *J. Appl. Crystallogr.*, 1969, **2**, 65–71.

33 J. P. M. Lommerse, A. J. Stone, R. Taylor and F. H. Allen, *J. Am. Chem. Soc.*, 1996, **118**, 3108–3116.

34 A. Bondi, *J. Phys. Chem.*, 1964, **3**, 441–451.

35 F. H. Allen, *Acta Crystallogr. Sect. B*, 1986, **42**, 515–522.

Appendix A, Chapter 4:

NMR spectra and mass spectra for ligands *RR,SS*cbt and *RR*cbt

A1: ^{1}H-NMR spectrum for ***RR,SS*cbt**, 250 MHz in d6-DMSO

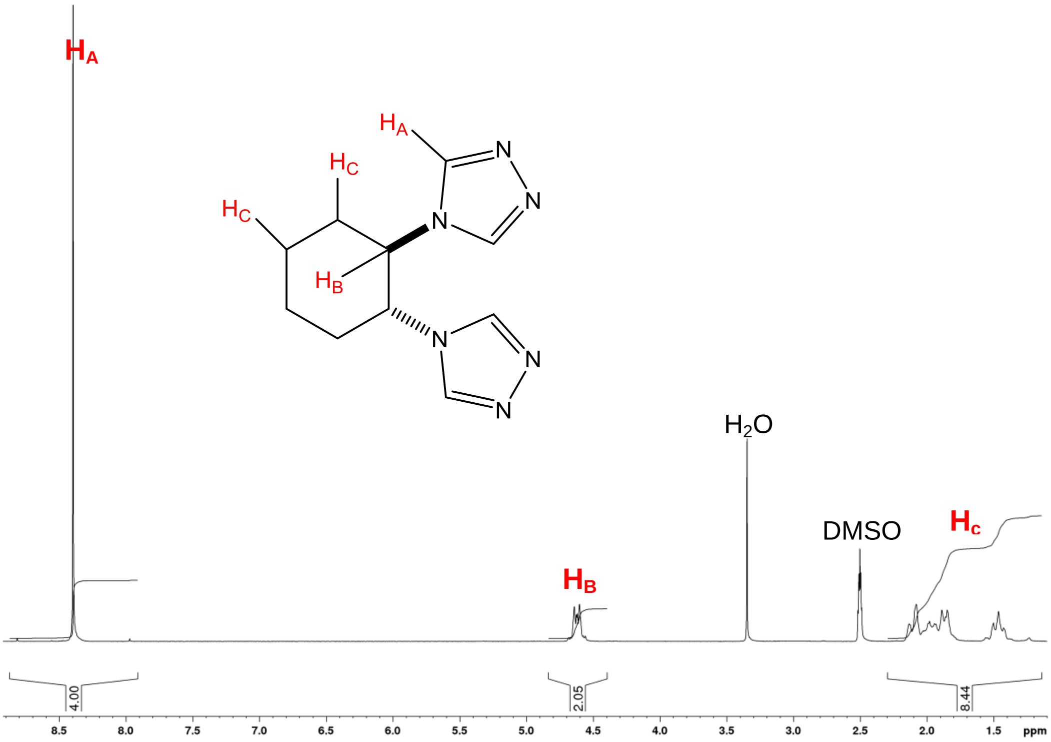

A2: TOF ES+ mass spectrum (from LC-MS) for ***RR,SS*cbt**

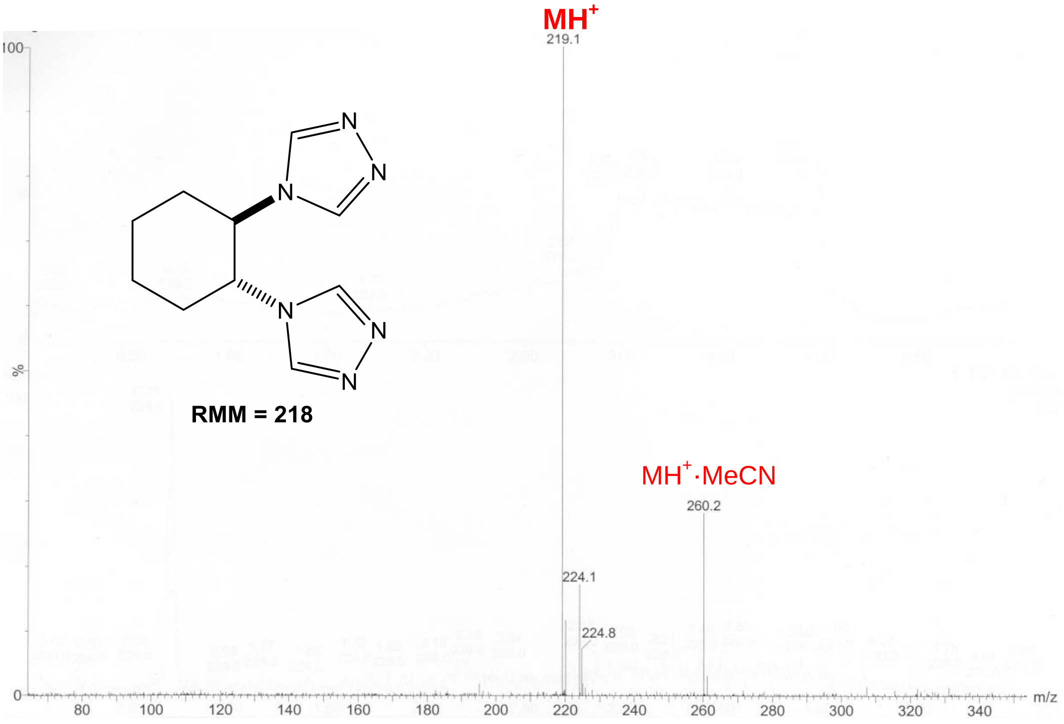

A3: ¹H-NMR spectrum for ***RR*cbt**, 400 MHz in d6-DMSO

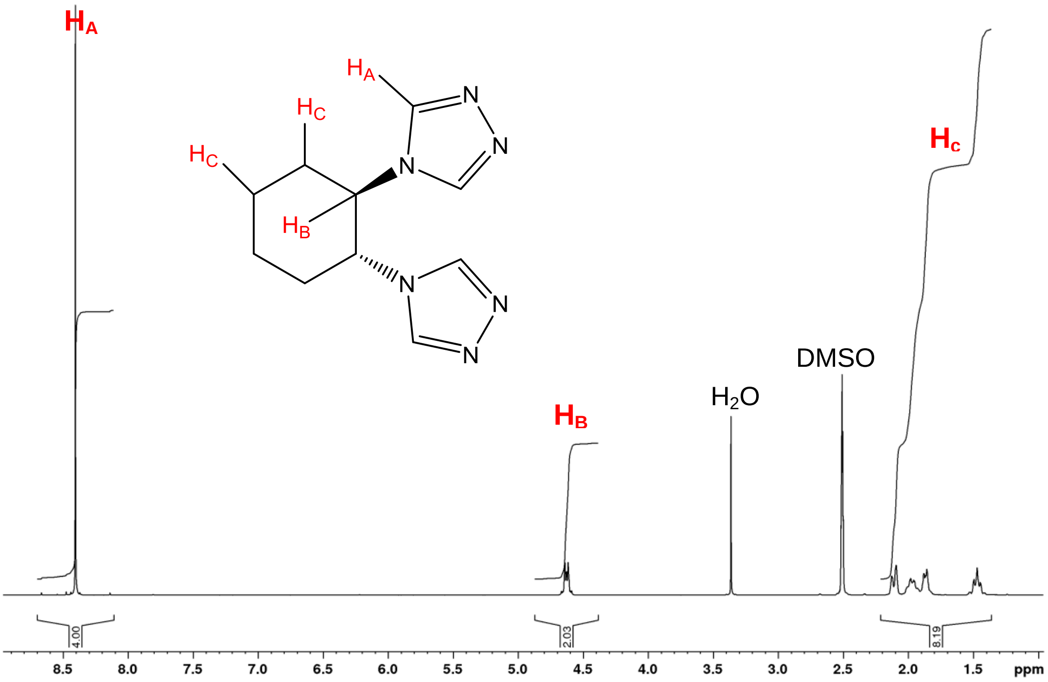

A4: ES+ mass spectrum for ***RR*cbt**

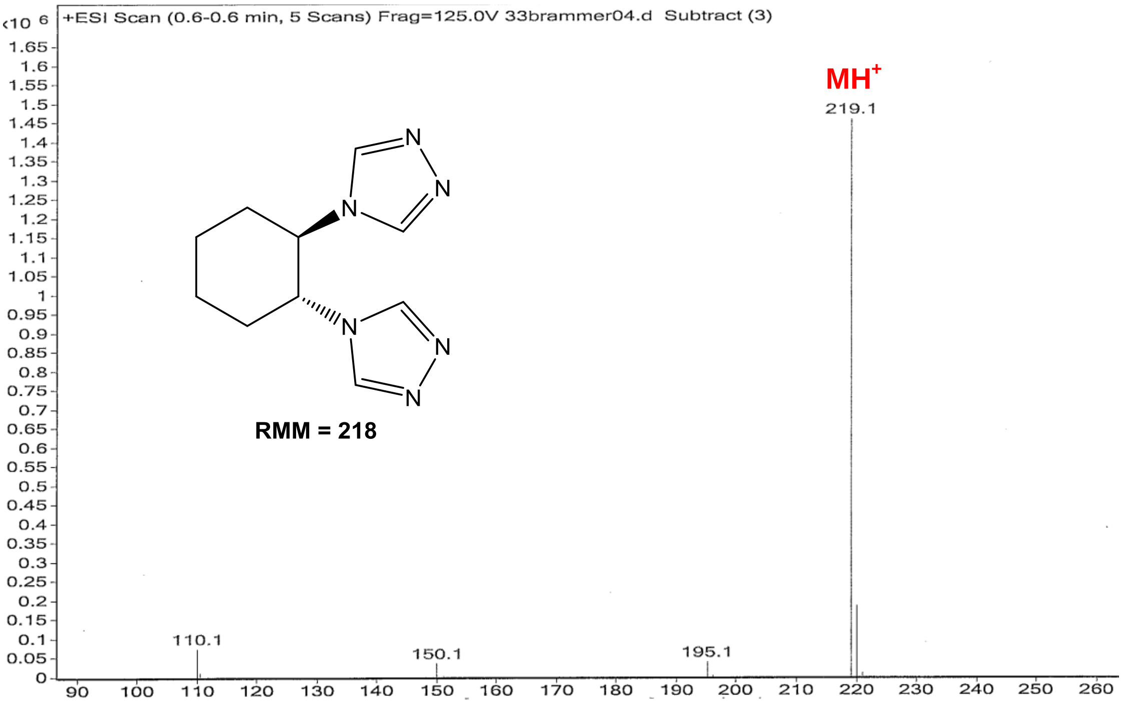

A5: Chiral gas chromatogram for phenylethanol-soaked **4.1·aPhCH$_2$(OH)Me**

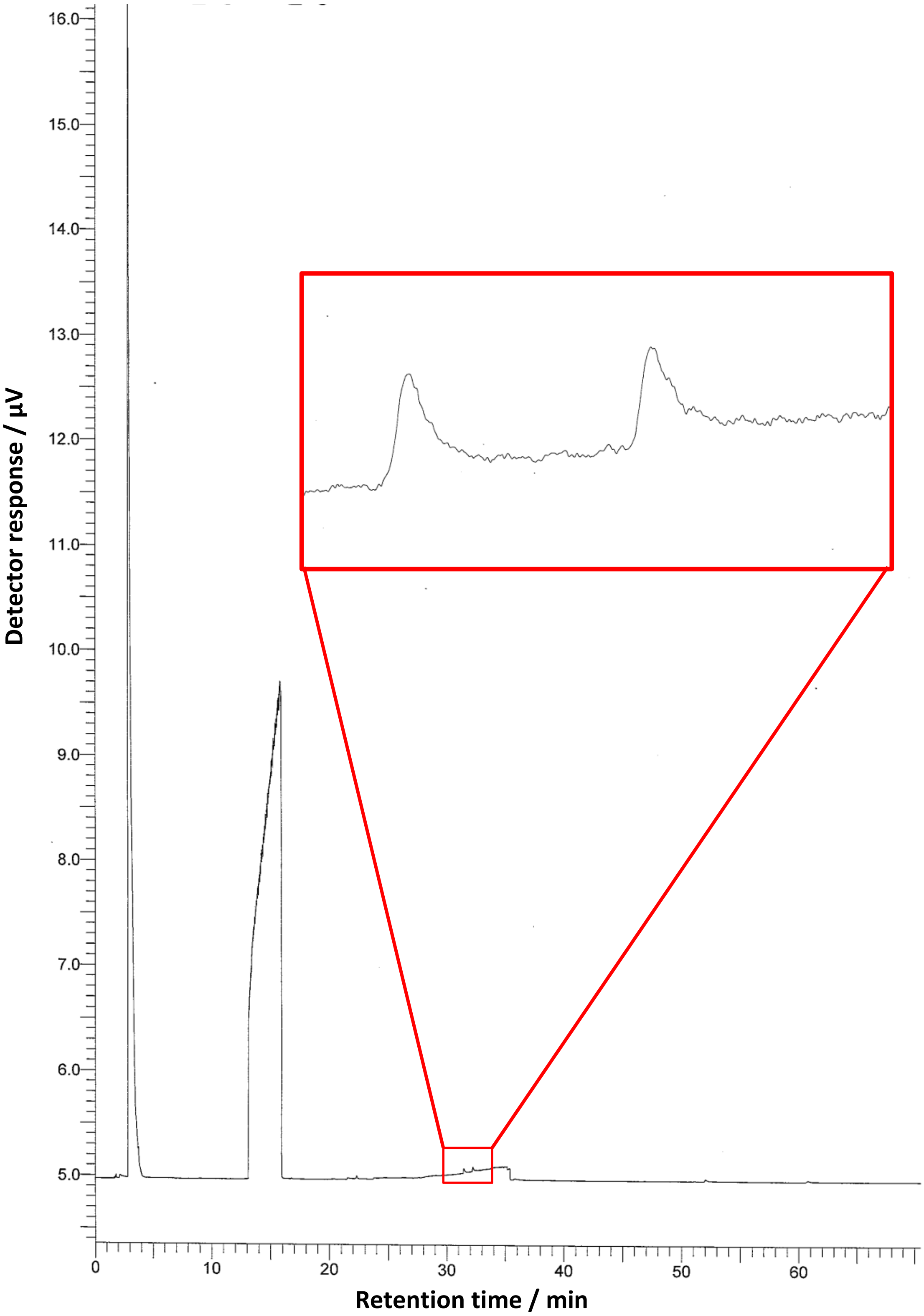

A6: Chiral gas chromatogram for phenylethanol-soaked **4.2·aPhCH$_2$(OH)Me**

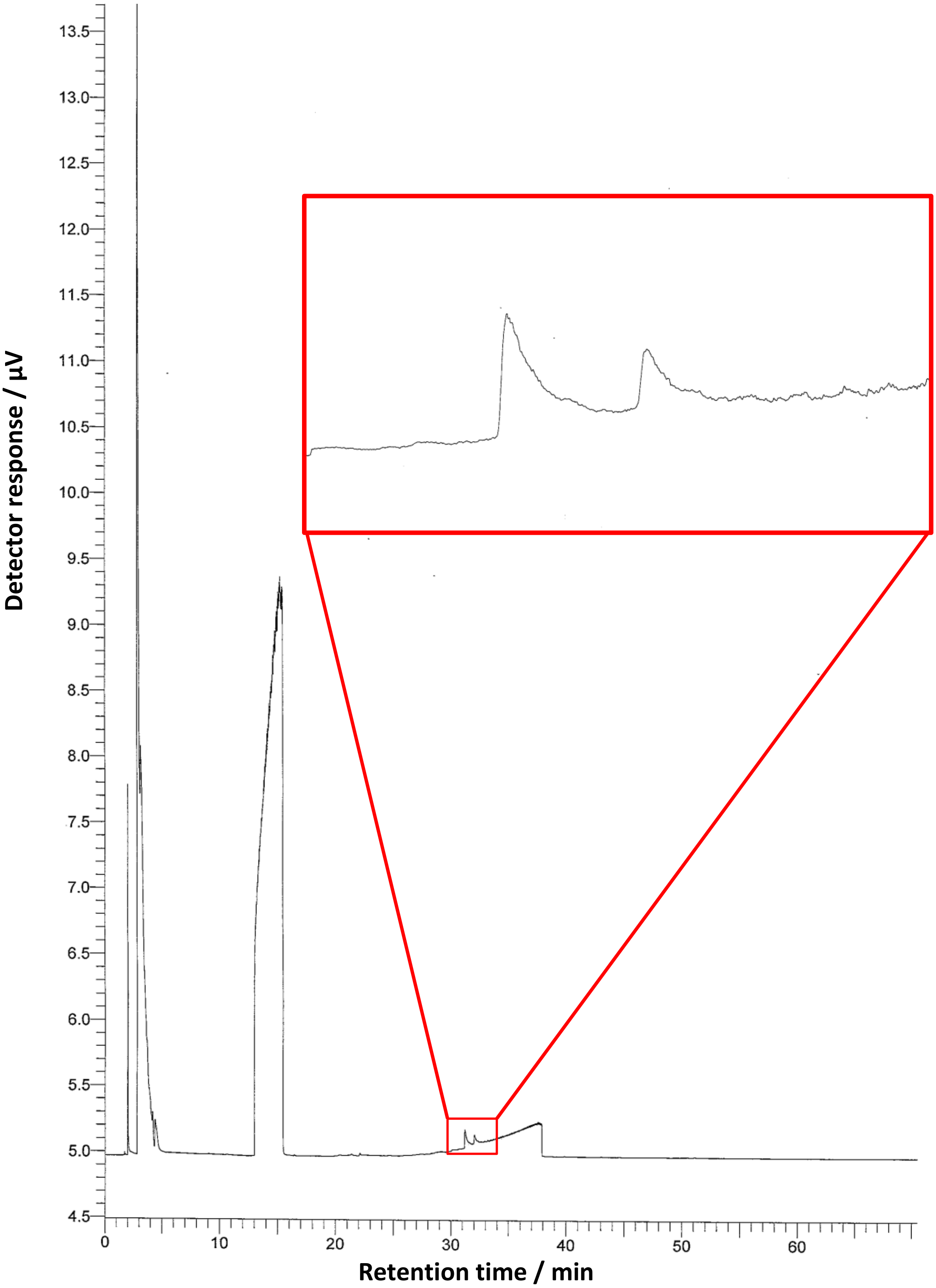

Appendix B, Chapter 6:

NMR spectra and mass spectra for ligands H_2bdp and H_2bpz

B1: ^{1}H-NMR spectrum for **H_2bdp**, 250 MHz in d6-DMSO
Due to poor sample solubility, the concentration is low – spectrum is zoomed in. Mass spectrometry could not be conducted due to low solubility.

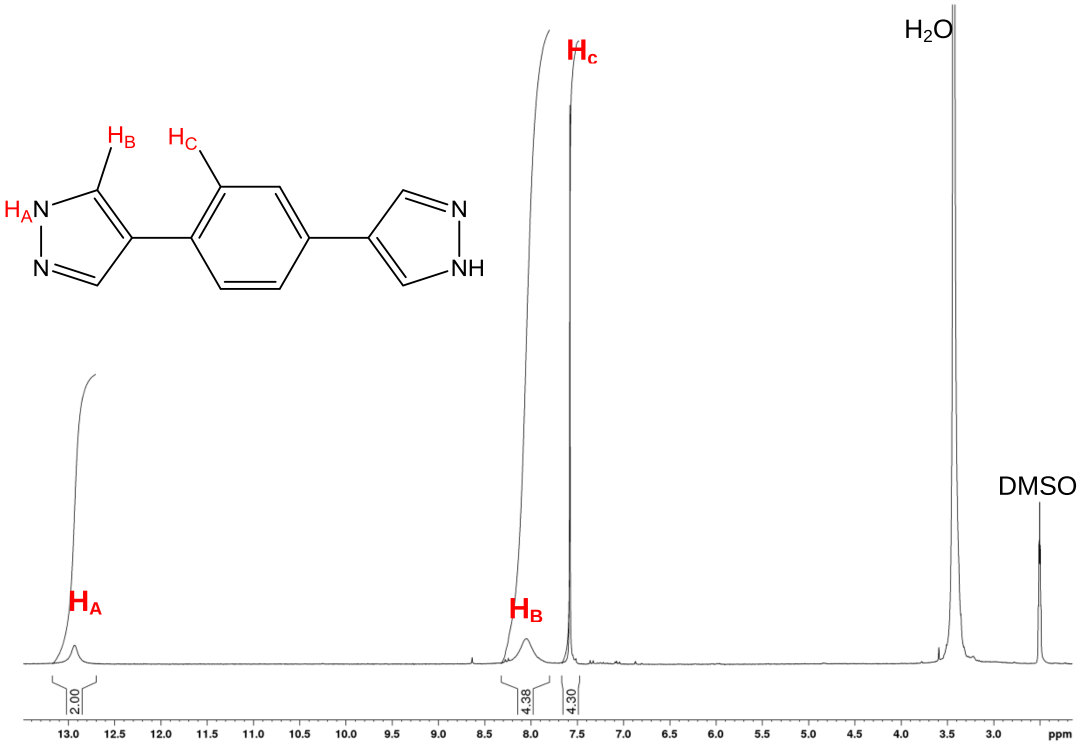

B2: ^{1}H-NMR spectrum for **H_2bpz**, 400 MHz in DCl/D_2O

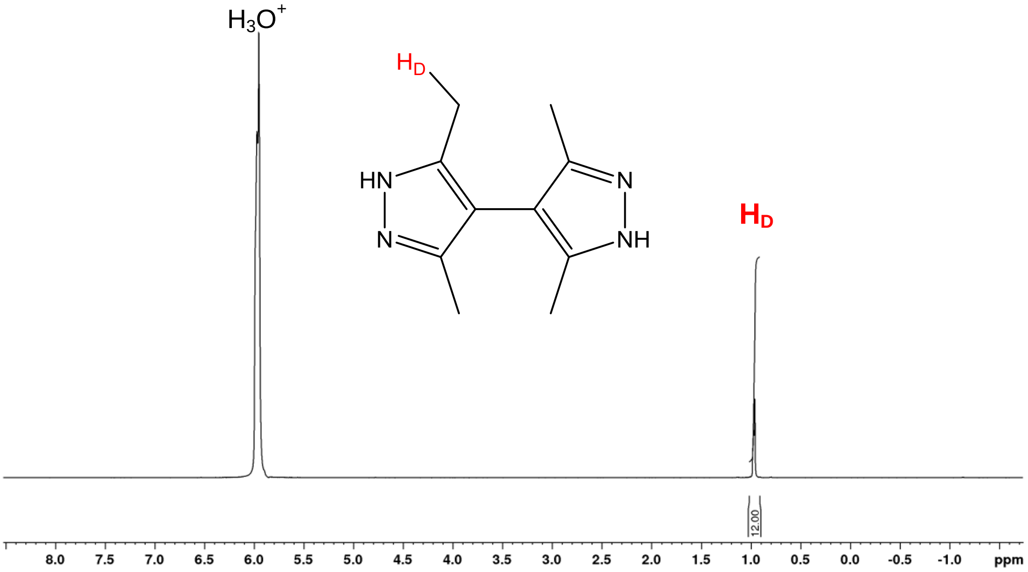

B3: ES+ mass spectrum for **H_2bpz**